VILNIUS UNIVERSITY
CENTER FOR PHYSICAL SCIENCES AND TECHNOLOGY

Laurynas
V E S E L I S

High energy hybrid femtosecond lasers based on Yb doped fibers and YAG crystals

DOCTORAL DISSERTATION

Natural sciences,
Physics (N 002)

VILNIUS 2021

This dissertation was written between 2016 and 2021 at the Department of Laser Technologies of the Center for Physical Sciences and Technology and the company *Ekspla*. The research was supported by the Research Council of Lithuania.

Academic supervisor:
Dr. Andrejus Michailovas (Center for Physical Sciences and Technology, Natural Sciences, Physics, N 002).

This doctoral dissertation will be defended in a public meeting of the Dissertation Defense Panel:
Chairman – Dr. Arūnas Varanavičius (Vilnius University, Natural Sciences, Physics, N 002).
Members:
Dr. Paulius Gečys (Center for Physical Sciences and Technology, Natural Sciences, Physics, N 002).
Dr. Pavel Loiko (Caen-Normandy University, Natural Sciences, Physics, N 002).
Prof. dr. Arkady Major (University of Manitoba, Natural Sciences, Physics, N 002).
Dr. Audrius Pugžlys (Vienna University of Technology, Natural Sciences, Physics, N 002).

The dissertation shall be defended at a public meeting of the Dissertation Defense Panel at 16:30 on 26th November 2021 in the hall of FTMC Institute of Physics.
Address: Savanoriu Ave. 231, LT-02300, Vilnius, Lithuania
Tel. +370 5 264 8884; e-mail: office@ftmc.lt

The text of this dissertation can be accessed at the libraries of Center for Physical Sciences and Technology and Vilnius University, as well as on the website of Vilnius University:
www.vu.lt/lt/naujienos/ivykiu-kalendorius

VILNIAUS UNIVERSITETAS
FIZINIŲ IR TECHNOLOGIJOS MOKSLŲ CENTRAS

Laurynas
V E S E L I S

Didelės energijos hibridiniai femtosekundiniai lazeriai Yb legiruotų šviesolaidžių bei YAG kristalų pagrindu

DAKTARO DISERTACIJA

Gamtos mokslai,
Fizika (N 002)

VILNIUS 2021

Disertacija rengta 2016– 2021 metais Fizinių ir technologijos mokslų centro Lazerinių technologijų skyriuje ir kompanijoje *Ekspla*. Mokslinius tyrimus rėmė Lietuvos mokslo taryba.

Mokslinis vadovas:
Dr. Andrejus Michailovas (Fizinių ir technologijų mokslų centras, gamtos mokslai, fizika, N 002).

Gynimo taryba:
Pirmininkas – Dr. Arūnas Varanavičius (Vilniaus universitetas, gamtos mokslai, fizika, N 002).
Nariai:
Dr. Paulius Gečys (Fizinių ir technologijų mokslų centras, gamtos mokslai, fizika, N 002).
Dr. Pavel Loiko (Normandijos Kano universitetas, Prancūzija, gamtos mokslai, fizika, N 002).
Prof. dr. Arkady Major (Manitobos universitetas, Kanada, gamtos mokslai, fizika, N 002).
Dr. Audrius Pugžlys (Vienos Universitetas, Austrija, gamtos mokslai, fizika, N 002).

Disertacija ginama viešame Gynimo tarybos posėdyje 2021 m. lapkričio mėn. 26 d. 16:30 val. FTMC Fizikos instituto salėje.
Adresas: Savanoriu pr. 231, LT-02300 Vilnius, Lietuva
Tel. +370 5 264 8884; el. paštas: office@ftmc.lt

Disertaciją galima peržiūrėti Fizinių ir technologijos mokslų centro bei Vilniaus universiteto bibliotekose ir VU interneto svetainėje adresu:
https://www.vu.lt/naujienos/ivykiu-kalendorius

TABLE OF CONTENTS

ACKNOWLEDGMENTS

ABBREVIATIONS

1D	one-dimensional
3D	three-dimensional
ACF	autocorrelation function
AOM	acousto-optic modulator
ASE	amplified spontaneous emission
CCD	charge-coupled device
CFBG	chirped fiber Bragg grating
CPA	chirped pulse amplification
CVBG	chirped volume Bragg grating
CW	continuous wave
DPSS	diode-pumped solid-state
FCPA	fiber chirped pulse amplification
FR	Faraday rotator
FROG	frequency resolved optical gating
FWHM	full width at half maximum
GD	group delay
GDD	group delay dispersion
GVD	group velocity dispersion
HWP	half-wave plate
LD	laser diode
Nd:YAG	neodymium-doped yttrium aluminum garnet
PTR	photo-thermo-refractive-glass
QWP	quarter-wave plate
ROC	radius of curvature
SESAM	semiconductor saturable absorber mirror
SCF	single crystal fiber
SCR	spectral chirp rate
SF	stretching factor
SPM	self-phase modulation
SSG	small-signal gain
SVWP	spatially variable wave-plate
TEC	thermoelectric cooler
TL	transform-limited
TOD	third-order dispersion
Yb:YAG	ytterbium-doped yttrium aluminum garnet

Introduction

Femtosecond high peak-power (TW/cm^2) and high repetition rate (MHz) laser systems are widely used in science, industry, and military sectors. The main mechanisms governing femtosecond pulse and material interactions are a multiphoton phenomenon and non-thermal processes that make them uniquely attractive for various applications [1,2]. Femtosecond lasers exhibit excellent capability in three-dimensional processing of transparent materials (e.g., fused-silica, sapphire, etc.), which makes them an outstanding tool for micromachining of optical fibers (e.g., fiber grating inscription), wafer dicing for the semiconductor industry, or forming widely-applicable S-waveplates, linear to radial (or azimuthal) polarization converters, birefringent phase gratings and holograms, rewritable 5D optical memory, spatial beam formation tools and many other [3–6]. Furthermore, the surfaces of solar panels could be altered by femtosecond lasers to increase solar cell efficiency [7]. Femtosecond lasers have also found unique applications in transient absorption spectroscopy – with the help of ultrashort probing pulses, fast evolution of photophysical and photochemical reactions can be tracked in real-time within biological material [8]. These are but just a few of the application areas advanced by femtosecond laser systems, but the magnitude is sufficiently illustrated by the examples provided.

However, the generation of femtosecond pulses is a challenge – direct amplification of high peak-power femtosecond pulses is limited by nonlinear effects such as self-phase modulation, self-focusing, Raman scattering, etc. [9,10]. These non-desirable and limiting effects are efficiently mitigated with chirped pulse amplification (CPA) technique [11], where pulses are stretched in time (chirped), amplified, and then compressed to achieve high-peak-power laser pulses by avoiding mentioned non-desirable effects. Pulse stretching and compression are usually realized with diffraction grating setups of matched chromatic dispersion profiles [12,13]. However, if pulses are chirped to few hundreds of picoseconds or longer duration, such CPA systems become impractical due to the size of required gratings.

Ultrafast fiber laser technologies could offer a substantial solution. Fiber-based oscillators used as seed sources for femtosecond lasers are a promising approach – a substitution of diffraction grating-based pulse stretcher by chirped fiber Bragg grating helps alleviate size issues [14,15]. Furthermore, the implementation of chirped volume Bragg gratings (CVBG) as a pulse compressor showed increasing interest in the last decade [16–18]. Improvements in the holographic recording of the gratings as well as in homogeneity of photorefractive glass allowed to demonstrate high

compression efficiency while also preserving good beam quality [16,17]. Moreover, a compressor based on CVBG is very compact, simple to align, and much less sensitive to misalignment than a diffraction grating compressor. These properties are very desirable for industrial ultrafast lasers. Furthermore, fiber-based laser sources offer many other practical advantages, including diffraction-limited beam quality, compact and robust design, and maintenance-free operation. Additionally, a broad emission spectrum of ytterbium (Yb^{3+}) doped fused-silica fibers allows for amplification of ultrashort pulses.

The major drawback of fiber-based laser systems in achieving high peak power is the relatively small mode area of single-mode fibers ($\sim 95\ \mu m^2$) and long interaction length causing a significant impact of nonlinear effects. When pulses are stretched even up to the practical limit of $1\ ns$, the achievable peak power is still limited by the most dominant nonlinear effect – self-phase modulation (SPM). It was investigated that SPM-induced nonlinear phase shift of more than $1\ rad$ affects pulse compression and results in temporal broadening and a reduction of the peak power of the recompressed pulses [19]. Large mode area (LMA) fibers with core diameter up to $30\ \mu m$ could be an alternative. However, to achieve strictly fundamental mode operation, advanced fiber designs, such as photonic crystal fibers, have to be used, which is somewhat impractical in building industrial-grade laser systems [20,21]. This suggests that although fiber lasers offer considerable advantages, they alone are not sufficient, and additional free-space solid-state amplification cascades are necessary, where mode area is sufficiently enlarged and interaction length is reduced to avoid nonlinear limiting factors.

The proper design of diode-pumped solid-state (DPSS) amplification cascades relies on the choice of the amplification medium. To amplify broadband laser pulses (which can then be compressed to femtosecond pulse durations), an amplification medium with a bandwidth broader than the spectral width of the laser pulse is necessary. Additionally, both good thermo-optical and mechanical properties of gain medium are preferred. Excellent candidates for DPSS amplifiers are ytterbium (Yb^{3+}) doped laser crystals (e.g., Yb:YAG, Yb:KGW, Yb:CaF$_2$, etc.). They possess some highly desirable properties, like a low quantum defect, broad amplification bandwidth, low excited state absorption, for efficient generation of ultrashort pulses [22–24]. However, reaching high optical-to-optical efficiency at room temperature requires high peak-power pumping due to the quasi three-level nature of Yb^{3+} ions. Cryogenically cooled systems were proposed as a solution, reaching record-high power scalability, but they add considerable complexity,

bulkiness and cost which is disadvantageous for industrial applications [25–27]. Diode-pumped thin-disk regenerative amplifier designs were also proposed as a viable option [28,29]. However, the main issue with such methods is that pulse injection, and ejection require Pockels cell and a Pockels cell driver with a low switching time (below resonator round-trip time) and precision. In case of imperfect switching, satellite pulses could arise, degrading overall pulse contrast, which requires an additional pulse picker for sufficient suppression of pre- or post-pulses, thus increasing the overall complexity of the design. Also, the average power is limited by the power capability of the Pockels cell itself. A possible alternative is a multi-pass DPSS amplifier, where a fixed number of passes through the gain medium are arranged with a set of mirrors [30,31]. However, such a design becomes complicated and somewhat hard to align if the number of passes is high. The recent introduction of commercially available high brightness ($NA < 0.22$) based pump diode lasers [32] would in principle enable reaching sufficient power extraction from pumped bulk crystals at room temperatures even with minimal number of passes through gain medium.

A prominent drawback of the highly-pumped gain medium in solid-state amplifiers is the significant power loss via depolarization [33–37]. Thermal gradients in gain medium lead to detrimental effects, including aberrations and stress-induced birefringence. Many techniques for mitigating problems related to thermal stress were proposed. For optically isotropic gain medium, such as Yb:YAG, depolarization loss can be minimized by using a classic depolarization compensation layout where two identical amplifier modules are put on after another with polarization rotation and relay imaging between them [38,39]. The basic idea of such compensation methods is to inverse polarization states across the beam profile before entering the second active element and cancel accumulated phase difference between radial and tangential polarizations. Some research was performed with different crystal cut directions demonstrating reduction of depolarization in Yb:YAG and Nd:YAG cases [40–42]. All these methods work to some extent, however posing some serious drawbacks – either depolarization is not fully compensated, is susceptible to thermal effects, requires precise alignment and similar pumping conditions, suffer from nonlinear interaction (self-focusing, spectrum modulation), or is somewhat too sensitive to crystal configuration and alignment (different cut crystals).

Considering the advantages and disadvantages of proposed fiber and DPSS amplifier designs, a hybrid CPA approach seems to be a viable option for building a compact and cost-effective femtosecond laser solution. The main goal of my doctoral work was to design and validate solid-state gain medium

configurations seeded by specifically designed by Ekspla Yb^{3+} doped all-in-fiber oscillators (thus the term *hybrid*) to search for the most effective hybrid laser system suitable for applications in the industrial market. Configuration simplicity and practicality were the main criteria.

Initially, for DPSS amplifier design, different host materials were theoretically investigated, and Yb:YAG was chosen as the most promising material. Furthermore, numerical modeling software for the DPSS amplifier was developed and validated in the case of the axis-symmetric situation (1D). It was used to optimize the parameters (e.g., length, dopant concentration, signal, and pump spot diameters, etc.) of the amplifier for a few practical scenarios. Two concepts of hybrid CPA systems were experimentally investigated by applying knowledge gathered from numerical simulations, targeting high-energy and high average power laser systems. The numerical model was additionally expanded to a three-dimensional (3D) situation to account for non-symmetrical effects (e.g., bi-focusing, depolarization) arising in the end-pumped gain medium. Knowledge gathered from such simulations was used to design a novel depolarization compensation technique in a highly pumped double-pass DPSS amplifier configuration. Finally, the whole gathered experience was realized in developing and experimentally validating a high average power hybrid sub-picosecond laser system for a broad application capability in the industrial and scientific market.

Scientific Novelty

The major drawback of fiber-based laser systems in achieving high peak power is the relatively small mode area of single-mode fibers ($\sim 95 \ \mu m^2$) and long interaction length causing a significant impact of nonlinear effects [19]. As a result, additional free-space solid-state amplification cascades are necessary, where mode area is sufficiently enlarged and interaction length is reduced to avoid nonlinear limiting factors. On the other hand, prominent drawbacks of the highly-end-pumped Yb:YAG crystal amplifiers (chosen as the basis for this work) are significant power loss via depolarization, polarization-dependent astigmatism, and beam deterioration due to thermal effects [33–37], which limit achievable output power from such amplifiers. Additionally, reaching sufficient power extraction from pumped bulk crystals at room temperatures even with a significant number of passes through the gain medium is problematic. Furthermore, pulse stretching and compression in femtosecond laser systems are quite impractical if pulses in the CPA schematic are stretched to a few hundred picoseconds or longer duration [12,13]. Thus, considering the advantages and disadvantages of fiber and

DPSS amplifier designs, a hybrid CPA approach seems to be a viable option for building a compact and cost-effective femtosecond laser solution. In this regard, the scientific novelty of my work lies in the effective combination of already established fiber and solid-state technologies in the mission to solve such arising problematics, aided by the developed numerical model:

1. A new and computationally efficient numerical model for three-level gain medium continuous-wave amplifier modeling was developed and experimentally validated. To the best of my knowledge, such a modeling approach was never publicly presented before.

2. A compact ultrafast laser system based on fiber seed laser and Yb:YAG crystal double-pass power amplifier was developed, which operated at room temperature. The key novelty of the system was the application of CFBG stretcher and CVBG compressor with matched dispersion which enabled to obtain nearly bandwidth-limited compressed femtosecond pulses. Proposed laser architecture enabled the construction of truly compact and robust high-energy ultrashort pulse laser.

3. Method to minimize depolarization and polarization-induced astigmatism by the use of the spatially variable waveplate (SVWP) in end-pumped Yb:YAG crystal amplifier was numerically investigated and applied experimentally. To the best of my knowledge, this method was applied for the first time. In my opinion, such laser system demonstration provides sufficient proof that end-pumped double-pass Yb:YAG amplifier configuration, together with SVWP, is a rather simplistic and efficient technology for peak power scaling, being more advantageous compared to other technologies, such as thin-disk or crystal fiber [43,44].

Practical value

The development of compact, robust, and cost-effective femtosecond laser systems is rapidly advancing for use in scientific and industrial markets. Femtosecond lasers exhibit excellent capability in various applications - three-dimensional processing of transparent materials (e.g., fused-silica, sapphire, etc.), wafer dicing for the semiconductor industry, forming widely-applicable S-waveplates, linear to radial (or azimuthal) polarization converters, birefringent phase gratings and holograms, rewritable 5D optical memory, spatial beam formation tools and many other [1–6]. Adopting a hybrid laser system approach, which is based on the fiber chirped pulse amplification (FCPA) laser as seeder and additional DPSS amplifiers as the means for

further peak-power scaling leads to a practical realization of such femtosecond laser systems. Thus, this doctoral work has a practical significance in several aspects:

1. The developed numerical model for three-level gain medium continuous-wave amplifier modeling enabled to rapidly design, optimize and test various configurations of end-pumped Yb:YAG laser amplifiers, suitable for developing femtosecond laser systems. Developed modeling software is currently used in the company *Ekspla*.

2. Application of CFBG as pulse stretcher and CVBG or four-pass diffraction-grating setup as pulse compressor with matched dispersion enabled to construct compact ultrafast laser system based on fiber seed laser and Yb:YAG crystal double-pass power amplifier, and obtain nearly bandwidth-limited compressed femtosecond pulses. Implementation of such an approach led to the development of the commercial laser system *FemtoLux 30* at company *Ekspla*.

3. A novel method for depolarization compensation using SVWP was experimentally confirmed and realized in a hybrid laser system, incorporating fiber seed source and a two-cascade DPSS amplifier system. Such laser system demonstration provided practical means for peak power scaling, being more advantageous compared to other technologies, such as thin disk or crystal fiber [43,44].

Statements to defend

S1. Axis-symmetric (1D) numerical model for three-level gain medium continuous-wave amplifier, which incorporates signal beam propagation by Hankel transform, pump beam shape calculation by ABCD matrix method, gain medium parameters – thermal conductivity, thermo-optic coefficient, spectroscopic cross-sections – dependency on temperature, spectroscopic cross-section value dependency on wavelength, and operates in the iterative algorithm, where convergence parameters are end-pumped gain medium temperature (single-pass) and output power (double-pass), is capable to accurately predict amplifier output power, gain narrowing effect, amplified beam shape, and wave-front distortions.

S2. Application of CFBG as pulse stretcher and CVBG as pulse compressor with matched dispersion in the hybrid laser system, consisting of FCPA laser as a seed source and double-pass end-pumped Yb:YAG amplifier for further peak-power scaling, enables to construct a compact hybrid laser

system, delivering nearly bandwidth-limited compressed femtosecond pulses.

S3. Incorporation of a pair of quarter-wave plates in an end-pumped double-pass Yb:YAG amplifier, placed before and after gain medium, and oriented in a way that enables amplification of circularly polarized signal beam inside the gain medium, provides practical means to significantly minimize amplified beam astigmatism induced by bi-focusing, enabling to achieve diffraction-limited beam quality after amplification in end-pumped Yb:YAG amplifier.

S4. Implementation of SVWP enables significant reduction of thermally-induced depolarization and astigmatism in double-pass end-pumped Yb:YAG amplifier configuration.

Authors' contribution

All the research presented in the thesis was performed by the author except the work mentioned in the Co-authors' contribution section. The author developed the modeling software described in Chapter 2 and Chapter 5 of this thesis and performed all the numerical calculations and theoretical analysis presented in Chapter 3 and article A3. The author designed, constructed, and experimentally realized the laser systems described throughout the work and in articles A1, A2, and A4. The author developed and experimentally realized a two-cascade Yb:YAG amplifier laser system and performed part of the experiments for depolarization compensation, which is presented in article A3. The author prepared manuscripts A1-A4.

Co-authors' contribution

- Dr. Andrejus Michailovas was the supervisor of the authors' Ph.D. studies and was the initiator for developing the depolarization compensation method presented in article A3, shared valuable insights for the preparation of article A2, and significantly contributed to the overall preparation of this thesis.
- Dr. Nerijus Rusteika was the main initiator for developing DPSS amplifiers based on Yb:YAG as the gain medium, provided significant ideas for developing the numerical algorithm of the presented model, made a great contribution in preparing the manuscript for A1 publication.
- Dr. Tadas Bartulevičius experimentally realized the majority of FCPA laser seed sources throughout this thesis, helped to realize pulse

compression with CVBG (presented in article A1), and consulted regarding FROG measurements.

- Raimundas Burokas experimentally realized depolarization compensation as presented in publication A3.
- Karolis Madeikis consulted and greatly contributed to various electric/electronics related tasks.
- Dr. Audrius Zaukevičius shared his experience and knowledge in numerical beam propagation analysis and provided overall invaluable consultations regarding modeling.
- Dr. Mikhail Grishin shared his experience and knowledge in the numerical analysis of thermal effects in the end-pumped gain medium. In addition to this, part of the optical design for the double-pass amplifier presented in articles A2 and A3 was based on his initial suggestions.

Scientific papers

Publications related to the topic of the thesis:

A1. **L. Veselis**, T. Bartulevičius, K. Madeikis, A. Michailovas, and N. Rusteika, "Compact 20 W femtosecond laser system based on fiber laser seeder, Yb:YAG rod amplifier and chirped volume Bragg grating compressor", Opt. Express **26** (24), 31873-31879 (2018). https://doi.org/10.1364/OE.26.031873

A2. **L. Veselis**, R. Burokas, A. Michailovas, "Numerical model of end-pumped Yb:YAG double-pass laser amplifier experimentally validated at 129 W output power", Lith. J. Phys. **61**(4), accepted, will be published in 2021.

A3. **L. Veselis**, R. Burokas, O. Ulčinas, T. Gertus, K. Michailovas, and A. Michailovas, "Depolarization compensation with spatially variable waveplate in 116 W, 441 fs, 1 MHz Yb:YAG double-pass laser amplifier", Appl. Opt. **60**, 7164-7171 (2021). https://doi.org/10.1364/AO.432573

A4. **L. Veselis**, T. Bartulevičius, K. Madeikis, and A. Michailovas, „Generation of 40 W, 400 fs pulses at 1 MHz repetition rate from efficient, room temperature Yb:YAG double-pass amplifier seeded by fiber CPA system", Proc. SPIE 11259, Solid State Lasers XXIX: Technology and Devices, 1125925 (2020). https://doi.org/10.1117/12.2545473

Other publications:

A5. T. Bartulevičius, **L. Veselis**, K. Madeikis, A. Michailovas, and N. Rusteika, "Compact femtosecond 10 µJ pulse energy fiber laser with a CFBG stretcher and CVBG compressor", Opt. Fiber Technol. **45**, 77-80 (2018).
https://doi.org/10.1016/j.yofte.2018.06.006

A6. P. M. Dansette, R. Burokas, **L. Veselis**, A. Zaukevičius, A. Michailovas, and N. Rusteika, "Peculiarities of Second Harmonic Generation with Chirped Femtosecond Pulses at High Conversion Efficiency", Opt. Commun. **455**, 1224462 (2019).
https://doi.org/10.1016/j.optcom.2019.124462

A7. T. Bartulevičius, K. Madeikis, **L. Veselis**, V. Petrauskienė, and A. Michailovas, "Active fiber loop for synthesizing GHz bursts of equidistant ultrashort pulses", Opt. Express **28**(9), 13059-13067 (2020).
https://doi.org/10.1364/OE.389056

Conference presentations

C1. **L. Veselis**, T. Bartulevičius, K. Madeikis, R. Danilevičius, A. Michailovas, and N. Rusteika, *Compact High Average Power High Energy CPA Laser System Based on Yb Fiber Seeder and Yb:YAG Amplifier*, CLEO 2018, San Jose, CA, USA, May 13-18, 2018. [poster presentation]
https://doi.org/10.1364/CLEO_AT.2018.JTh2A.154

C2. **L. Veselis**, T. Bartulevičius, K. Madeikis, A. Michailovas, and N. Rusteika, *Compact CPA Laser System Based on Yb Fiber Seeder and Yb:YAG Amplifier*, International Conference "Laser Optics 2018", St. Petersburg, Russia, June 4-8, 2018. [oral presentation]
https://doi.org/10.1109/LO.2018.8435748

C3. **L. Veselis**, T. Bartulevičius, K. Madeikis, R. Danilevičius, A. Michailovas, and N. Rusteika, "Compact CPA Laser System Based on Yb Fiber Seeder and Yb:YAG Amplifier", Laser Precision Microfabrication Symposium 2018. [poster presentation]

C4. **L. Veselis**, T. Bartulevičius, K. Madeikis, R. Danilevičius, A. Michailovas, and N. Rusteika, *Ultrafast CPA laser system based on Yb fiber seeder and Yb:YAG amplifie*r, 8th EPS-QEOD EUROPHOTON Conference "Solid State Lasers", Barcelona, Spain, September 02-07, 2018. [poster presentation]

C5. **L. Veselis**, T. Bartulevičius, K. Madeikis, A. Michailovas, ir N. Rusteika, *Femtosekundinė lazerinė sistema, paremta skaiduliniu užkrato šaltiniu, Yb:YAG kietakūniu stiprintuvu ir čirpuotos tūrinės Brego gardelės impulsų spaustuvu*, FizTeCh: 8-oji Fizinių ir technologijos mokslų centro doktorantų ir jaunųjų mokslininkų konferencija, 2018 m. spalio 17-18 d., Vilnius, Lietuva. [oral presentation]

C6. **L. Veselis**, T. Bartulevičius, K. Madeikis, R. Danilevičius, N. Rusteika, A. Michailovas, *CPA laser system based on Yb fiber seeder and two cascade Yb:YAG amplifier for compact OPCPA pump source*, CLEO/Europe-EQEC 2019, Munich, Germany, June 23-27, 2019. [poster presentation]
https://doi.org/10.1109/CLEOE-EQEC.2019.8871833

C7. **L. Veselis**, T. Bartulevičius, K. Madeikis, A. Michailovas, *Generation of 40 W, 400 fs pulses at 1 MHz repetition rate from efficient, room temperature Yb:YAG double-pass amplifier seeded by fiber CPA system*, Frontiers in Optics 2019, Washington, DC, USA, September 15-19, 2019. [poster presentation]
https://doi.org/10.1364/FIO.2019.JW3A.44

C8. **L. Veselis**, T. Bartulevičius, K. Madeikis, A. Michailovas, *40 W, 400 fs 1 MHz impulsų generacija iš efektyvaus, kambario temperatūros Yb:YAG dvigubo lėkio stiprintuvo, paremto visiškai skaiduline CPA sistema*, 43-oji Lietuvos nacionalinė fizikos konferencija, Kauno technologijos universitetas, 2019 m. spalio 3-5 d., Kaunas, Lietuva. [oral presentation]

C9. **L. Veselis**, T. Bartulevičius, K. Madeikis, A. Michailovas, *35 W, 350 fs,1 MHz impulsų realizacija iš efektyvaus, kambario temperatūros Yb:YAG dvigubo lėkio tiesinio stiprintuvo*, FizTeCh: 9-oji Fizinių ir technologijos mokslų centro doktorantų ir jaunųjų mokslininkų konferencija, 2019 m. spalio 23-24 d., Vilnius, Lietuva. [oral presentation]

C10. **L. Veselis**, T. Bartulevičius, K. Madeikis, A. Michailovas, *CPA laser system based on Yb fiber seeder and two cascade Yb:YAG amplifier for compact OPCPA pump source*, Siegman International Summer School on Lasers 2019, Rochester, NY, USA, July 27 – August 03, 2019. [poster presentation]

Additionally, during the doctorate studies, 19 conference reports not related directly to the thesis, were co-authored.

The structure of the thesis

The material of the thesis is divided into six main parts. First, materials, methods, and technologies relevant to this work are presented in Chapter 1. The following chapters cover the modeling and experimental part of the thesis. Chapter 2 is dedicated to describing and experimentally validating numerical model dedicated to the three-level gain medium amplifiers. Numerical optimization of critical amplifier parameters, such as crystal doping concentration and crystal length, are presented in Chapter 3. Chapter 4 is dedicated to the experimental realization of femtosecond laser systems based on FCPA laser as a seed source and pre-modeled end-pumped Yb:YAG crystal amplifier for further peak power scaling. Additionally, problematics arising in such configurations are reviewed, including beam quality and depolarization degradation due to thermal effects of the end-pumped gain medium. Finally, Chapter 5 is dedicated to solving these issues. An extended numerical model with bi-focusing and depolarization effects included is presented. The novel depolarization compensation method is experimentally validated in a two-cascade Yb:YAG amplifier system. The last chapter is dedicated to the comparison of the presented laser systems to the others.

1. Literature overview

1.1. Yb³⁺ as an activator ion

The most promising activator ion that is used in non-Nd based DPSS amplifiers in the same range of emission wavelength of $\sim 1\,\mu m$ is Yb^{3+} [22,45]. This dopant has a simple electronic level structure consisting of only two state manifolds: the $^2F_{7/2}$ ground state and the $^2F_{5/2}$ excited state. Thus, Yb^{3+} doped materials are free of parasitic effects such as up-conversion, excited state absorption (which reduces effective laser cross-section) and crossed relaxation. Typical absorption and emission transition lines for Yb^{3+} and Nd^{3+} are shown in Fig. 1.1 [45].
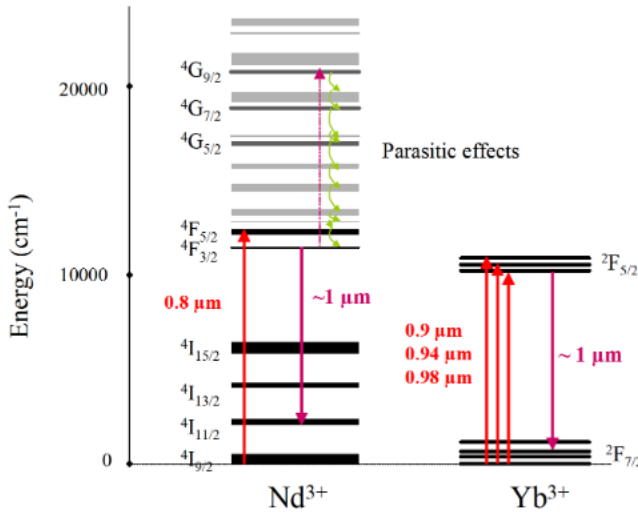
Fig. 1.1 Nd^{3+} and Yb^{3+} energy levels. Typical transition lines for pump absorption (solid red arrows) and laser emission (solid purple arrows) are shown. Green lines indicate non-radiative transitions [45].

The narrow and intense Yb^{3+} absorption lines are not well-suited for conventional broadband flash-lamp pumping as compared to Nd^{3+} which has many absorption lines and a four-level laser energy structure. However, with the dawn of high brightness semiconductor (e.g., InGaAs/GaAs) narrow-band diode lasers, efficient pumping of Yb^{3+} doped gain medium became possible [32]. High intensity of such pump diodes enabled to reach sufficient population inversion to avoid reabsorption losses at laser wavelength (due to quasi-three level nature), and sufficient to yield practical amplification levels. Additionally, the Stokes shift between absorption and emission lines is significantly lower for Yb^{3+} (~8.7% at 940 nm pumping or ~5.9% at 969 nm

pumping) versus Nd^{3+} (~24.8% at 800 nm pumping) doped gain medium. This naturally reduces the thermal loading of the gain material leading to higher extractable power from amplifiers. The relaxation processes present in Nd^{3+} doped gain media are non-radiative, which means they further contribute to the thermal load, whereas in the case of Yb^{3+} it is negligible. Finally, typical upper state lifetime for Yb^{3+} ions is longer (~1 ms) than Nd^{3+} (~0.25 ms), which may allow for a better storage of the pump energy.

In conclusion, even though Nd^{3+} has already shown and is continuing to show its potential in building high-power picosecond laser systems, Yb^{3+} doped materials are of special interest for femtosecond pulse generation/amplification due to the broader bandwidth of the emission lines (~1.3 nm vs. ~9 nm respectively at room temperature) [46,47]. For this reason, Yb^{3+} doped gain medium was chosen as a backbone for building DPSS amplifier laser systems, which is covered in this thesis.

1.2. Overview of different Yb³⁺ doped gain media

In this section, properties of several commercially available Yb^{3+} doped host materials were investigated. Of particular interest are:

(1) yttrium aluminum garnet Yb:YAG suitable for high-power operation at 1030 nm;

(2) monoclinic potassium double tungstates Yb:KGW and Yb:KYW with a good combination of the broad emission spectrum and high emission cross-section;

(3) borate Yb:BOYS with broadband emission;

(4) Yb:CALGO with very broadband and smooth emission cross-section and high thermal conductivity;

(5) calcium fluoride Yb:CaF₂ with relatively broad emission spectrum;

(6) yttrium vanadate Yb:YVO₄ with broad and smooth emission spectrum;

(7) sesquioxides yttria Yb:Y₂O₃, scandia Yb:Sc₂O₃, and lutetia Yb:Lu₂O₃ with high thermal conductivity suitable for high-power operation;

(8) Yb:LuAG, which offers similar properties to Yb:YAG, yet is somewhat less commercially available;

(9) fluoride Yb:YLF with the broad emission spectrum.

Parameters of interest for different materials used in this analysis are shown in Table 1.1 and Table 1.2.

Table 1.1 Summarized characteristics of selected Yb^{3+} doped gain media. The nonlinear refractive index n_2 is in $10^{-20} m^2 W^{-1}$, thermal conductivity k is in $W m^{-1} K^{-1}$, thermal expansion coefficient α_T is in $10^{-6} K^{-1}$, thermal shock parameter R_s is in $W cm^{-1}$, bandwidth $\Delta\lambda$ is in nm (at negligible inversion level), and lifetime τ_f is in ms. All parameters except for bandwidth and lifetime are for undoped materials. Materials are presented in no particular order.

Material	n_0	n_2	k	α_T	R_s	$\Delta\lambda$	τ_f	Ref.
Yb:YAG	1.82	6.2	10.7	6	10.4	9	0.95	[47–51]
Yb:KGW	2.0	15	3.8	16	4	20	0.40	[50–52]
Yb:KYW	2.0	8.7	2.7	10	-	16	0.36	[50–52]
Yb:BOYS	1.74	6.6	1.8	19.5	-	40	1.1	[50,51,53,54]
Yb:CALGO	1.91	9.6	6.9	35	6.4	50	0.4	[50,55,56]
Yb:CaF$_2$	1.43	1.3	9.7	-18	1.7	30	1.9	[47,50]
Yb:YVO$_4$	1.96	1.9	7.0	-	11.3	30	0.3	[50,57]
Yb:Y$_2$O$_3$	1.92	11.6	12.8	25.5	12	15	0.85	[50,58–60]
Yb:Sc$_2$O$_3$	1.93	11.5	16.5	27	13	18	0.80	[50,58–60]
Yb:Lu$_2$O$_3$	1.93	8.6	12.2	24	12	20	0.82	[50,58,60]
Yb:LuAG	1.84	-	7.2	6.1	-	6	0.85	[47,50]
Yb:YLF	1.45	1.7	6.0	13	1.8	25	2.1	[50,52]

Table 1.2 Summarized cross-sections of selected Yb^{3+} doped gain media at room temperature. Values are indicated for usual emission and pumping lines. Units for spectral lines are in nm, and for spectroscopic cross-sections in $10^{-24} m^2$. * marks calculated parameters – signal saturation intensity for optimal amplification I_{sat} in $kW cm^{-2}$, and minimum pump intensity required to achieve transparency at the laser wavelength I_{min} in $kW cm^{-2}$. Materials are presented in no particular order.

Material	λ_L	$\sigma_a(\lambda_L)$	$\sigma_e(\lambda_L)$	λ_P	$\sigma_a(\lambda_P)$	$\sigma_e(\lambda_P)$	I_{sat}*	I_{min}*	Ref.
Yb:YAG	1030	0.12	2.20	940	0.82	0.15	8.8	1.3	[47]
Yb:KGW	1023	0.2	2.8	981	10	12	16.2	0.3	[52]
Yb:KYW	1025	0.3	3.0	981	12	14	16.3	0.4	[52]
Yb:BOYS	1025	0.03	0.3	975	0.92	0.8	53.4	1.7	[53]
Yb:CALGO	1043	0.05	0.7	980	1.0	1.5	63.5	3.2	[55]
Yb:CaF$_2$	1047	0.02	0.3	980	0.58	0.03	31.2	1.1	[47]
Yb:YVO$_4$	1008	0.2	1.25	984	7.0	9.5	45.3	1.3	[57]
Yb:Y$_2$O$_3$	1030	0.1	1.0	976	2.0	1.8	20.6	1.0	[59]
Yb:Sc$_2$O$_3$	1042	0.1	1.2	976	3.1	2.7	18.3	0.6	[59]
Yb:Lu$_2$O$_3$	1033	0.1	1.0	976	2.9	2.3	21.3	0.7	[60,61]
Yb:LuAG	1030	0.15	2.8	940	0.73	0.8	7.7	1.6	[47]
Yb:YLF	1017	0.08	0.71	971	1.10	0.33	11.8	0.9	[52]

An evaluation of various material properties suitable for defining DPSS amplifier performance is presented below based on data retrieved from the literature.

The thermal performance of gain media is of significant importance for high average power and high repetition rate DPSS amplifier systems. Key parameters are thermal conductivity k and thermal shock resistance parameter

R_s ($R_s = \frac{\sigma_f k f(v)}{E \alpha_T}$, where σ_f is the maximal strain supported by the material, $f(v)$ is a function of the Poisson coefficient, E is the Young modulus, k is the thermal conductivity of the material, α_T is the thermal expansion coefficient [62]), which both describe how efficiently the heat from pumping is dissipated and how resistant the material is to thermal gradients resulting from pumping of the gain medium. Materials with high thermal shock resistance parameters and high thermal conductivity are preferable. These parameters were chosen as a figure of merit, and a graph illustrating this is shown in Fig. 1.2.
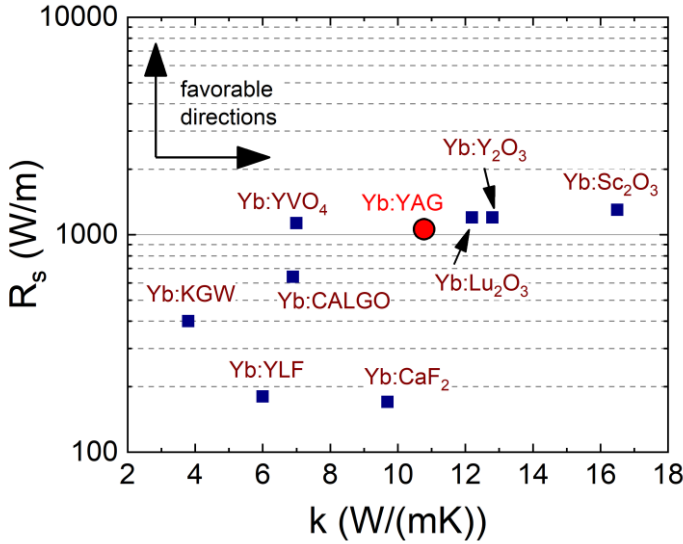
Fig. 1.2 Thermal shock resistance parameter R_s dependence on thermal conductivity k for various gain media. High R_s and k are preferable.

Data indicates that *sesquioxides* (Yb:Sc$_2$O$_3$, Yb:Y$_2$O$_3$, and Yb:Lu$_2$O$_3$) are in the lead, with well-established Yb:YAG not far behind. The lowest performance in terms of thermal properties manifests Yb:KGW and Yb:YLF.

Another important aspect in choosing a suitable material for DPSS amplifier systems is the amplification bandwidth (the highest value is preferable). A suitable figure of merit for comparison is the saturation fluence, which is a criterion for efficient energy extraction. Low values are preferable, however, at too low, amplified spontaneous emission (ASE) also starts to extract energy, competing with the amplification of signal. At too high levels, on the other hand, laser-induced damage (LIDT) of material coatings (or material itself) would be reached before efficient energy extraction can be achieved. A comparison of mentioned parameters is shown in Fig. 1.3.
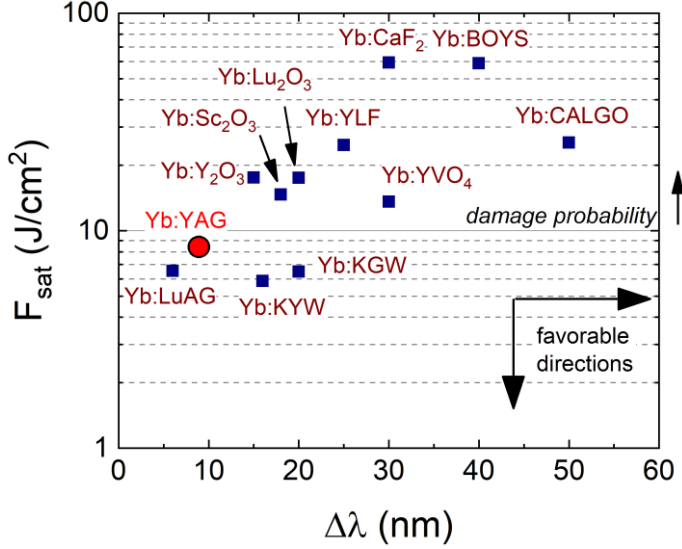
Fig. 1.3 Total bandwidth $\Delta\lambda$ (FWHM, at room temperature; horizontal axis) and saturation fluence F_{sat} (vertical axis) of the selected gain materials. High $\Delta\lambda$ and low F_{sat} are preferable.

Nonlinear refractive index n_2 of gain material is another classification parameter related to high peak-power laser systems. B-integral parameter relates n_2 to total nonlinear phase accumulated as pulse travels along the gain medium. Accumulated nonlinear phase distorts pulse temporal (pulse contrast, defined as Strehl ratio) and spatial (degrades beam quality parameter M^2) characteristics. A rule of thumb is to keep B-integral values in the laser system below 1 rad [19,30].

To calculate B-integral values for different materials, a set of parameters were chosen for this analysis: pulse duration $\tau_p = 100\ ps$ and pulse repetition rate $f = 100\ kHz$. The reasoning behind this is that in CPA systems pulses are usually temporally stretched to durations of 100 ps - in case of diffraction grating setup, system size is still convenient, and in the case of CFBG, manufacturing of such fibers is comfortably below manufacturers technology limits (e.g., *TeraXion*). Additionally, pulse repletion rate in the range of hundreds of kilohertz was chosen as it is very practical in various material processing [1-10]. B-integral was estimated as phase (in radians) accumulated per centimeter of propagation in analyzed material, where peak intensity was chosen based on saturation intensity I_{sat} of material (intensity required for achieving most of the possible output intensity of analyzed material; gain is reduced to half of the small-signal gain value). B-integral is expressed as $\beta_{int} = \frac{2\pi}{\lambda} \int n_2 I(z)dz$, where λ is the signal wavelength, and $\int I(z)dz$ is

integrated peak intensity along propagation distance ($\int I(z)dz = I\,L$, where L is total propagation distance). In the case of Gaussian envelope pulses, peak power can be expressed as $P_p = 0.94\frac{E_p}{\tau_p}$, where pulse energy E_p can be defined via saturation power P_{sat} as $E_p = \frac{P_{sat}}{f}$, where f is pulse repetition rate. For Gaussian beams, peak intensity is defined as $I_p = \frac{2P_p}{A}$, where A is beam cross-section area. This yields peak intensity of $I_p = \frac{1.88 I_{sat}}{f\tau_P}$, and in propagation distance of $L = 0.01\,m$ ($1\,cm$), B-integral can be expressed as $\beta_{int}(rad/cm) = \frac{3.76\pi}{\lambda} n_2 \frac{I_{sat}}{f\tau_P}$, where n_2 is the nonlinear refractive index of the analyzed material. B-integral value as compared to materials' saturation intensity value I_{sat} is presented in Fig. 1.4. Both low β_{int} and I_{sat} are preferred.
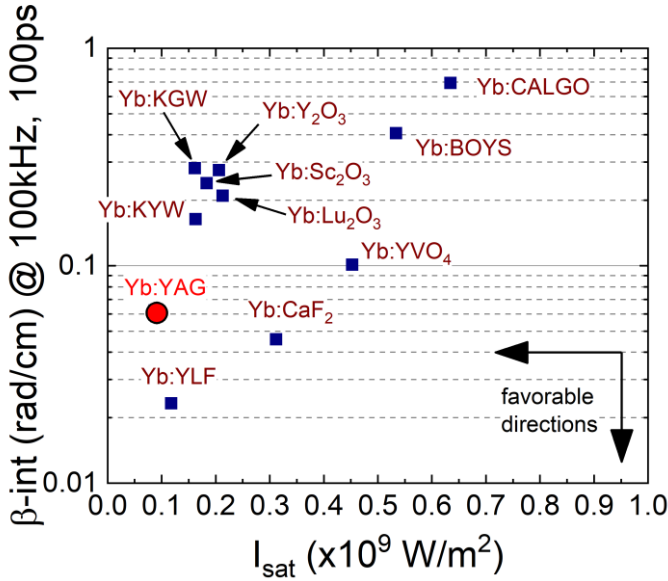
Fig. 1.4 B-integral β_{int} versus saturation intensity I_{sat} of analyzed materials for $100\,ps$ pulses at $100\,kHz$ pulse repetition rate. Low values of β_{int} and I_{sat} are preferred.

Leading candidates in case of low B-integral and saturation intensity are Yb:YLF and Yb:YAG, whereas for Yb:CALGO (with the highest amplification bandwidth as seen in Fig. 1.3) figure-of-merit is the worst.

The final evaluation of material performance was based on the minimum pump intensity I_{min} required to achieve transparency at the signal wavelength and signal saturation intensity I_{sat} for optimal amplifier configuration. I_{min} is defined as $I_{min} = \frac{\sigma_a}{\sigma_e + \sigma_a} \frac{hc}{\lambda\pi\sigma_{ap}\tau}$, where σ_a, σ_e is the absorption and emission

cross-section at the signal wavelength, σ_{ap} is the absorption cross-section at the pump wavelength, τ is the upper-state lifetime, λ is the signal wavelength, h is Planck's constant, c is the speed of light. Saturation intensity I_{sat} is defined as $I_{sat} = \frac{hc}{\lambda(\sigma_a + \sigma_e)\tau}$, where σ_a, σ_e is the absorption and emission cross-section at the signal wavelength. Results of this comparison are shown in Fig. 1.5.
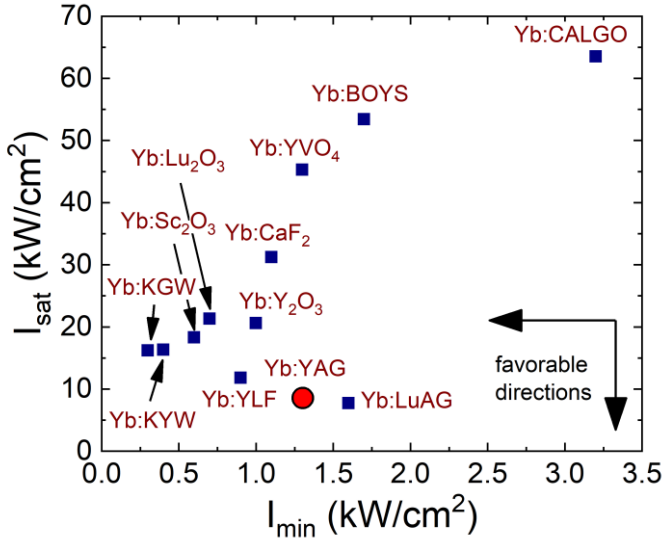
Fig. 1.5 Signal saturation intensity I_{sat} versus minimum required pump intensity I_{min} to achieve transparency at the signal wavelength. Low values of I_{sat} and I_{min} are preferred.

A good combination of parameters is achieved in most materials. In this comparison Yb:CALGO stands out as the material having the worst figure-of-merit, even though it would allow amplification of wide bandwidth signal pulses.

In conclusion, considering all the mentioned parameters, the most promising Yb-doped material is Yb:YAG for high repetition-rate and high peak-power DPSS amplifier systems. It features a low non-linear refractive index n_2, leading to low accumulated nonlinear phase during signal propagation in amplification medium. Additionally, as was seen in Fig. 1.2, it has a high thermal conductivity k and a thermal shock resistance parameter R_s, which are both crucial in efficiently and safely pumping gain medium, leading to low thermal gradients and consequently thermal distortions of the amplified beam. Additionally, comparatively low values of signal saturation intensity I_{sat} and minimum pump intensity I_{min} to achieve transparency at the

signal wavelength proves Yb:YAG to be sufficiently easy to use in simplistic amplifier environments without the need for multi-pass or regenerative amplifier setups. The major drawback, however, is the amplification bandwidth $\Delta\lambda = 9\ nm$ supported by this material, as compared to such material as Yb:CALGO ($\Delta\lambda = 50\ nm$). Still, a theoretically achievable pulse duration of $\tau = 174\ fs$ (Gaussian pulse) is possible, which makes this material suitable for a wide range of applications in the industrial and scientific market. For these reasons Yb:YAG was chosen as a host material for the development of DPSS amplifier systems in my thesis.

1.3. Depolarization compensation techniques

Even though Yb-doped materials have a quite small quantum defect (<10 %), thermal effects in the highly pumped gain medium cause significant power losses via depolarization if a laser system contains polarization-sensitive elements (e.g., Brewster plates, Faraday rotators, polarizers) [33,34]. In end-pumped geometry (which is the major focus in my thesis) and side cooling of the gain medium, a characteristic temperature distribution with its maximum in the center of the element (coincides with pumping region) and minimum at the medium outer surface results in axially symmetric temperature gradients. These gradients induce mechanical stresses in pumped crystal, which lead to correlated gradient distribution of refractive indexes and birefringence over the cross-section of gain medium [35]. For [111]-cut Yb:YAG crystal, birefringence axes are oriented in the radial and tangential directions to this gradient field (crystal axis of symmetry), leading to a common "clover leaf" depolarized beam shape of initially linearly-polarized light at the input of amplifier [33]. Thermally-induced stresses not only affect spatial beam profile (via depolarized part that is lost) but also result in bi-focusing, which spoils beam focusability [63]. Many techniques for mitigating problems related to thermal stress were proposed. In this section, I review a few of them that illustrates the main principle behind such techniques. Furthermore, a novel technique of depolarization compensation used in this thesis is briefly presented (more information is found in Chapter 5).

For optically isotropic gain medium, such as Yb:YAG, depolarization loss can be minimized by using a classic depolarization compensation layout where two identical amplifier modules are put one after another with polarization rotation and relay imaging between them [33,38,39]. Additionally, instead of placing two active elements in a row, scheme with a $\lambda/4$ waveplate (with the principal axis parallel to the incident polarization)

and flat reflective mirror can be employed. Principal schematics for both techniques are shown in Fig. 1.6.
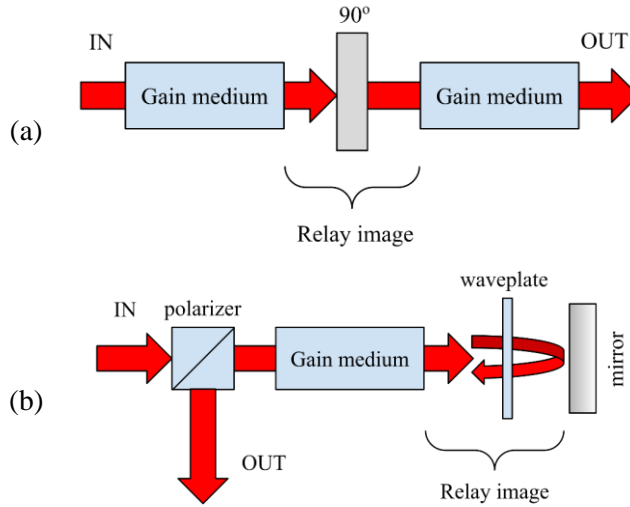
Fig. 1.6 The depolarization compensation schematics. (a) scheme with a 90-degrees polarization rotator; (b) scheme with $\lambda/4$ waveplate with the principal axis parallel to the incident polarization.

The basic idea of these compensation methods is to inverse polarization states across the beam profile before entering the second active element (or identical in double-pass setup) and, in this way, cancel accumulated phase difference between radial and tangential polarizations. The most serious shortcoming of the method in Fig. 1.6 (a) is that two identically thermally loaded and cooled gain media must be used, which is often impossible or impractical to implement. In the second method with quarter waveplate, depolarization is compensated in the same gain medium via double-pass configuration at low heat power levels only. It was shown that the compensated depolarization part is proportional to the fourth power of absorbed heat (at low heat power density), whereas the uncompensated depolarization part is proportional to the second power [33,37]. At high heat generation rates, depolarization decreases only slightly.

A traditional approach using Faraday rotator before reflecting mirror (instead of quarter waveplate in Fig. 1.6 (b)) is also possible and demonstrates good results [36,64]. However, the main drawback of this method is the Faraday rotator's susceptibility to thermal and nonlinear effects, which makes it unsuitable for high average power applications.

Some research was performed with different crystal cut directions demonstrating reduction of the depolarization in Yb:YAG and Nd:YAG

crystals [40–42]. In the work of *D. Albach et al.*, for example, a theoretical and experimental investigation was carried out for [111], [001], and [110] cut directions Yb:YAG crystals, where the input beam angle of incidence was fixed to 0 and 13 degrees. A resulting depolarization map for such a case, where linearly polarized input signal polarization orientation is varied, is shown in Fig. 1.7.
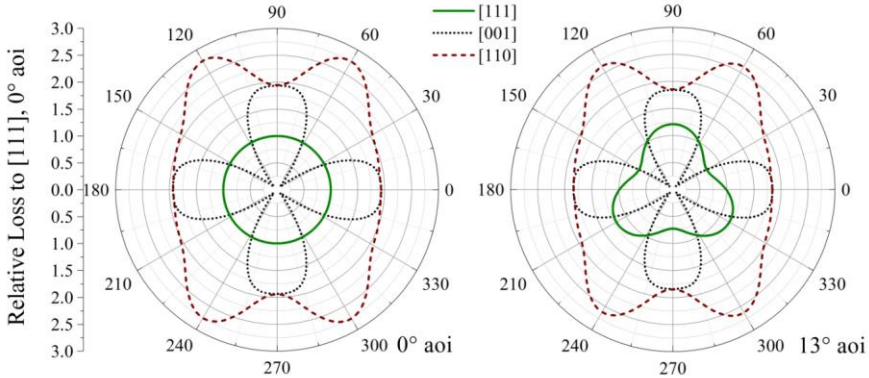
Fig. 1.7 Calculated angular depolarization loss maps for an Yb:YAG crystal carrying three types of orientations. The left map is obtained for a double-pass extraction beam propagating through the disk at normal incidence (AOI 0°), whereas a 13° AOI is depicted on the right map. Data and graphs were taken from the work of *D. Albach et al.* [42].

Graphs in Fig. 1.7 clearly illustrate theoretically possible depolarization minimization when Yb:YAG crystal is cut in [001] direction, and input signal polarization is oriented at 45 degrees. However, this method poses some practical shortcomings, like crystal and signal polarization orientations must be precisely oriented, whereas, in the case of [111] crystal cut direction, no dependency of input signal polarization orientation is seen at small angle of incidence. This reason encouraged me to search for a novel yet practical approach to reducing depolarization in a highly pumped gain medium.

A very promising technology, which allows mimicking birefringence of thermally stressed Yb:YAG crystals, is one of inscription by femtosecond laser of self-assembled periodic sub-wavelength structures ("nanogratings") in optically transparent materials, e.g., fused silica [65–67]. These modifications exhibit optical anisotropy (birefringence), allowing the fabrication of different unique optical elements. Worth mentioning are S-waveplates, linear to radial or azimuthal polarization converters, birefringent phase grating and holograms, rewritable 5D optical memory, spatial beam formation tools, and many others, all exhibiting high damage threshold of bulk fused silica glass [5,6]. The main feature of such nanogratings is that, by choosing a certain parameter range of fabricating ultrafast laser, one can

precisely point-by-point induce birefringence and orient local principal polarization axes across area-of-interest [6]. In fact, with sufficient knowledge of depolarization level in Yb:YAG amplifier, its origin, and amplified beam parameters (shape and initial polarization state), one could, in principle, reproduce and fabricate depolarization pattern in fused silica glass with opposite phase, which would theoretically fully compensate depolarization loss. This, to the best of my knowledge, novel approach was applied in my thesis for compensation of depolarization in highly end-pumped Yb:YAG amplifier. Theoretical calculations and experimental data are presented in Chapter 5.

1.4. Pulse stretching and compression

In this section, I review relevant to this thesis pulse stretching and compression techniques in the CPA scheme, including corresponding limitations.

As was mentioned in the introductory section, an attractive approach in designing a high-power ultrafast laser system is using a hybrid laser system approach, where the initial seed source for the DPSS amplifier is fiber-based. Substitution of conventional diffraction grating-based pulse stretcher by chirped fiber Bragg grating (CFBG) is then possible [14,15], which offers various advantages, such as system compactness, robustness, industrial-grade performance without the need of free-space alignment.

The working principle of the CFBG stretcher is based on Fresnel reflection, where light traveling between media of different refractive indices may both reflect and refract at the interface. In CFBG, a periodically varying refractive index modulation (grating) is inscribed into silica fiber core, generating a wavelength-sensitive mirror for different segments of CFBG [68]. At different segments of CFBG, the Bragg condition is satisfied for different wavelengths (where the reflected wavelength is $\lambda_B = 2n_e\Lambda$; n_e is effective index of refraction of fiber core, and Λ is local grating period), thus providing temporal pulse stretching (chirping) due to different optical paths that these wavelengths travel before and after reflection. The principal scheme of CFBG is shown in Fig. 1.8.
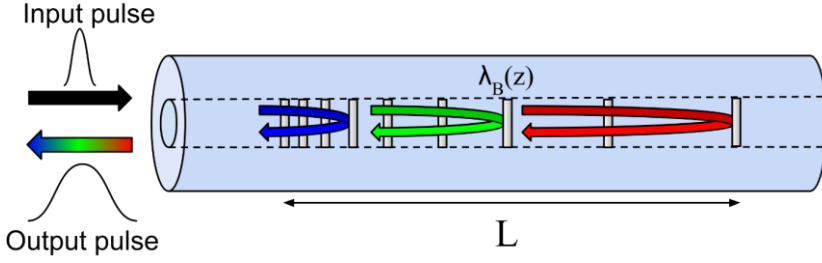
Fig. 1.8 The schematic of CFBG (not to scale). $\lambda_B(z)$ denotes varying Bragg wavelength along the fiber, and L denotes a hypothetical length of CFBG inside the fiber. Differently colored arrows show the hypothetical reflection of different wavelengths from different segments of CFBG.

The design of the CFBG stretcher accounts for dispersion that laser pulse acquires propagating within laser system, including fibers, free-space components, and dispersion of designed pulse compressor. The dispersion of the pulse stretcher is usually specified in terms of the Taylor expansion coefficients of its optical phase $\phi(\omega)$ [69]:

$$\phi(\omega) = \sum_{n=0}^{\infty} \frac{\beta_n}{n!} (\omega - \omega_c)^n, \qquad (1.1)$$

where ω is the optical frequency, and coefficients β_n are the derivatives of the phase at the center frequency ω_c. These coefficients are typically expressed in ps^n, i.e., for second-order dispersion, they are in ps^2 (can be converted to $\frac{ps}{nm}$ by $D_2(\frac{ps}{nm}) = \frac{2\pi c}{\lambda^2} \beta_2$; for $\lambda = 1\ \mu m$, the coefficient is $D_2\left(\frac{ps}{nm}\right) \approx 1.78\ \beta_2$), third-order in ps^3 and so on. For optimal and practical CFBG stretcher design, up to the fourth-order dispersion is typically specified.

The performance of the CFBG stretcher is mainly limited by manufacturing errors due to instabilities while inscribing, particles on the fiber, heterogeneity of the fiber, etc. [69]. Due to these imperfections, group delay (GD) ripples translate into a pedestal or side pulses accompanying the main compressed pulse. However, high fidelity femtosecond pulses are still achievable, as was presented by *Bartulevičius et al.*, where a compression ratio of ~1100 employing CFBG was demonstrated to obtain compressed 208 fs pulses at the output of the system [15]. This proves that such technology is also suitable for high-power femtosecond laser system design, which concept was applied in the experimental part of this thesis (see Chapter 4).

For the purpose of pulse compression, chirped volume Bragg grating (CVBG) technology is promising for its' compactness and ease of alignment, as was discussed in the introductory section of my thesis. The working

principle of this device is identical to CFBG, except for CVBG being a free-space device, typically with apertures up to $10 \ mm$. The basic parameter that defines the CVBG properties is spectral chirp rate (SCR), determined as [70]:

$$SCR = \frac{d\lambda}{dz} = 2n\frac{d\Lambda}{dz},$$ (1.2)

where $\frac{d\Lambda}{dz}$ is grating period, n is the average index of refraction. The total spectral width of CVBG is the product of the spectral chirp rate and CVBG thickness $\Delta\lambda = SCR \times L$, and total delay time (maximum temporal compression) between spectral components corresponding to the front and back ends of a CVBG is defined as $t = \frac{2nL}{c}$. The delay between spectral components of a laser pulse then determines the stretching factor SF of this device, which, for CPA systems, can conveniently be expressed in $\frac{ps}{nm}$ as [70]:

$$SF\left(\frac{ps}{nm}\right) = \frac{t}{\Delta\lambda} = \frac{100}{SCR,(nm/cm)}.$$ (1.3)

The principal scheme of CVBG is shown in Fig. 1.9.
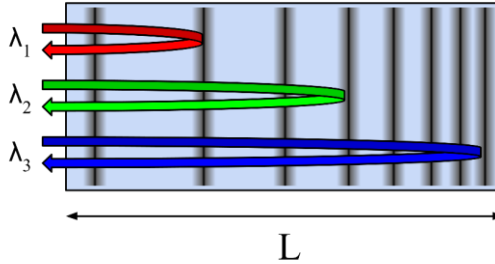
Fig. 1.9 The scheme of CVBG (not to scale). $\lambda_1 > \lambda_2 > \lambda_3$ denotes different wavelength reflection from segments of CVBG, L is CVBG thickness.

In an ideal case, the delay of the different spectral components is a linear function of wavelength. However, the material dispersion of the photosensitive material (photo-thermo-refractive-glass (PTR) used for CVBG) along with its imperfections, including precision of the hologram recording system for CVBG (which is the method for inscription of spatially varying refractive index modulations into the PTR glass), cause deviations from such linear function. This leads to additional higher-order terms of dispersion profile (e.g., the third-order dispersion), causing imperfect compression of the laser pulse, which could become problematic for large bandwidth laser pulses if left unaccounted for. Additionally, CVBG in PTR glass features wavelength-dependent scattering and absorption due to the

material structure, with shorter wavelengths being more susceptible to such loss resulting in CVBG efficiency loss (for example, 30% for $800\ nm$, and almost lossless for $2\ \mu m$) [70]. This, along with the quality of optical material, leads to beam quality degradation. Due to these reasons, practical parameter of CVBG in the vicinity of $1\ \mu m$ wavelength and bandwidth of $10\ nm$ (which is the Yb:YAG amplifier case), is stretching factor of $30\ \frac{ps}{nm}$, which yields a maximum stretched pulse duration of $300\ ps$ [70]. CVBG compressor is very promising in CPA systems, considering the advantages of compactness and ease-of-alignment as compared to conventional diffraction grating pulse compressor, and was the reason to apply it in the hybrid CPA laser system, which is presented in Chapter 4 of this thesis.

Another, more conventional approach in compressing laser pulses is based on diffraction grating compressor setups [13]. Despite its complexity in alignment [71], it is still a method of choice for compressing pulses to the record high peak powers due to the relatively straightforward scaling of the size of the grating [44]. A folded configuration of Treacy pulse compressor, employing 4-pass single transmission diffraction grating, which is more compact compared to double diffraction grating setup, was employed in this thesis (see Chapter 4) [72]. A principal layout of the pulse compressor is shown in Fig. 1.10.
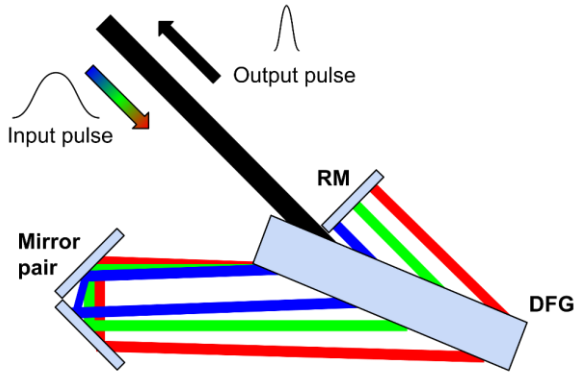
Fig. 1.10 The principal layout of 4-pass diffraction grating pulse compressor (not to scale). Differently colored arrows indicate different wavelengths of the input pulse. DFG is transmission diffraction grating, RM is the reflective mirror for beam reflection after 2-passes via diffraction grating, mirror pair is for compressor folding.

Dispersion parameters of grating pair compressor for a given length L of the compressor (the optical path length that central wavelength of the pulse travels in two passes) are then given by (for near Littrow angles) [13]:

$$GDD(\lambda) = -\frac{\lambda^3 L \cos\theta_{diff}}{\pi c^2 d^2}\left[1 - \left(\frac{\lambda}{d} - \sin\theta\right)^2\right]^{-1.5}, \qquad (1.4a)$$

$$\theta_{diff} = \arcsin\left(\frac{\lambda}{d} - \sin\theta\right), \qquad (1.4b)$$

$$TOD(\lambda) = -\frac{3\lambda}{2\pi c} GDD \frac{1 + \frac{\lambda}{d}\sin\theta - \sin^2\theta}{1 - \left(\frac{\lambda}{d} - \sin\theta\right)^2}, \qquad (1.4c)$$

where GDD and TOD are the second and third-order dispersion values, λ is central pulse wavelength, L is the optical length of the compressor, c is the speed of light, d^{-1} is grooves density of diffraction grating, θ is the angle of incidence, and θ_{diff} is the diffracted beam's angle.

The advantage of diffraction grating pulse compressor is the ability to fine-tune second-order dispersion by tuning incidence angle θ of the beam and the length of compressor L. This becomes important if, for example, the CFBG stretcher was manufactured without accounting for additional system dispersion arising from, e.g., fibers. Let us consider a practical case, where CFBG stretcher dispersion orders were designed to be compensated by pulse compressor using diffraction grating of $1600 \, mm^{-1}$ grooves density, beam incidence angle at Littrow condition ($\theta \approx 55.5°$), and $L = 100 \, mm$. In that case, second and third-order dispersion values that such compressor compensates are $GDD = -3.086 \, ps^2$ and $TOD = 0.026 \, ps^3$. Let us then assume that silica fiber of $50 \, m$ length was inserted into the system, adding the second-order $18.9 \cdot 10^{-3} \, ps^2/m \times 50 \, m = 0.945 \, ps^2$ and the third-order $4.12 \cdot 10^{-5} \, ps^3/m \times 50 \, m = 0.002 \, ps^3$ dispersion [73]. Pulse compressor must then be tuned to compensate the new dispersion values of $GDD = -2.155 \, ps^2$ and $TOD = 0.028 \, ps^3$. A convenient figure of merit for optimal pulse compression in such case is the ratio $\frac{TOD}{GDD} = -13 \, fs$ (original compressor design is $\frac{TOD}{GDD} = -8.4 \, fs$) – by tuning and fixing the beam's angle of incidence θ at which ratio $\frac{TOD}{GDD}$ is matched to the new design, we can correct GDD value just by changing compressor's optical path length, while the ratio $\frac{TOD}{GDD}$ remains constant. A graph portraying GDD, TOD and ratio $\frac{TOD}{GDD}$ dependence on beam's angle of incidence θ for this specific scenario is illustrated in Fig. 1.11 (left). The dependence of these parameters at fixed θ on L is shown in Fig. 1.11 (right). To compensate for such deviation from designed values, diffraction grating compressor could be tuned to the another

angle of incidence $\theta = 49.5°$ and to compressor length $L = 0.046\ m$, yielding correct dispersion values.
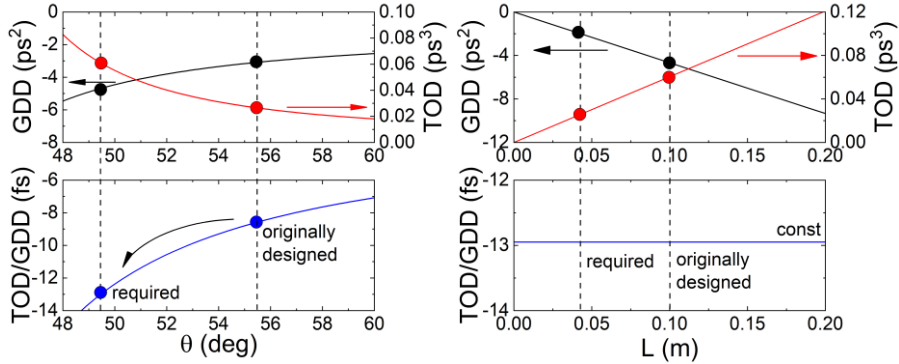
Fig. 1.11 <u>**Left:**</u> dispersion parameters GDD, TOD and $\frac{GDD}{TOD}$ dependency on beam's angle of incidence θ to diffraction grating at fixed compressor optical length $L = 0.1\ m$. <u>**Right:**</u> dispersion parameters dependency on compressor optical length L at optimized incidence angle $\theta = 49.5°$. Diffraction grating grooves density is set to $1600\ mm^{-1}$.

In conclusion, both pulse compression methods, combined with pulse stretching with CFBG, offered substantial advantages, and were implemented in a developed hybrid laser system, as reviewed in the experimental part of the thesis (see Chapter 4 and Chapter 5).

1.5. Overview of the recent advancements in Yb:YAG DPSS amplifier systems

Demand for high peak power femtosecond lasers has been investigated in various fields in science and industry, as was reviewed in the introductory section of the thesis [1–8]. In this subsection, I review recent advancements in various configurations of DPSS amplifiers based on Yb:YAG as the gain medium that were built for different purposes. A summary of reviewed configurations and target amplifier parameters developed in this thesis is presented.

One of the promising amplifier configurations using Yb:YAG as the gain medium is the single-crystal fiber (SCF) technology. It has shown promising results in amplifying laser pulses to high peak power levels [43,74–76]. SCF amplifier is a hybrid laser architecture between conventional bulk laser crystals and active optical fibers. The SCFs diameter is typically less than 1 mm while the length is several tens of millimeters [74]. Due to the high surface-to-volume ratio, SCF provides means for excellent thermal management, allowing efficient operation at room temperatures. An advantage against conventional rod crystal is that in SCF amplifier pump

radiation is confined by the guiding capacity of SCF (signal beam is in free propagation), giving relatively higher gain. Signal beam usually propagates in double-pass configuration, whereas pump radiation in single-pass. As an example, using a well-established *Taranis* module (developed by *Fibercryst*), *X. Delen et. al.* has developed a CPA based hybrid single-cascade amplifier system, providing $\tau = 380\,fs$ duration, $1\,mJ$ energy pulses at pulse repetition rate (PRR) of $10\,kHz$, reaching peak power of $2.5\,GW$ [75]. An interesting example is a system developed by *F. Lesparre et al.*, employing three cascades of Yb:YAG SCF amplifiers to reach $\tau = 750\,fs$ duration, $5\,\mu J$ energy pulses at pulse repetition rate (PRR) of $20\,MHz$ (corresponding to an average power of $100\,W$), reaching peak power of $6\,MW$ in an entirely non-CPA configuration [76].

Another promising DPSS amplifier technology that is based on Yb:YAG as the gain medium is *InnoSlab* (IS; developed by *Amphos*) [30,77,78]. An IS amplifier consists of a longitudinally, partially pumped slab crystal. Pump radiation is focused to form a line segment inside the slab crystal, whereas signal beam propagation is arranged in multi-pass configuration, where each pass propagates at a different segment of the crystal. Setup is arranged in a way that the signal beam is expanded after each pass to balance the increase of power and intensity. The thickness of the slab is usually in the order of $1\,mm$. The short distance between the pumped gain volume and the large cooled mounting surfaces allow for efficient heat removal. A good example of the capabilities of such technology was presented by *P. Russbueldt et al.* in a two-cascade non-CPA IS amplifier setup [77]. In this work, they managed to achieve $\tau = 615\,fs$ duration, $55\,\mu J$ energy pulses at a pulse repetition rate (PRR) of $20\,MHz$ (corresponding to an average power of $1100\,W$), reaching a peak power of $84\,MW$.

Yb:YAG bulk-crystal multi-pass (bulk and thin-disk) technology has also proved its ability in amplifying laser pulses to high peak power levels [44,79–82]. In the multi-pass configuration, signal beam propagation is arranged so that it passes multiple times end-pumped Yb:YAG crystal at a small angle (via mirrors), each time being reflected by a mirror placed close to the pump gain medium and at the opposite side of input direction. Outcoupling of the amplified beam is realized via the geometry of configuration. Excellent results using this technology were presented by *G. Figueira et al.* [79]. In this work, they achieved $\tau = 730\,fs$ duration, $106\,mJ$ energy pulses at a pulse repetition rate (PRR) of $1\,Hz$ (corresponding to average power of $106\,mW$), reaching a peak power of $136\,GW$, based on CPA technology. For higher pulse repetition rates reaching $1\,kHz$ level, cryogenically cooled Yb:YAG gain medium was

employed to reach $\tau = 6\,ps$ duration, $70\,mJ$ energy pulses at a pulse repetition rate (PRR) of $1\,kHz$ (corresponding to average power of $70\,W$), reaching a peak power of $11\,GW$ in non-CPA configuration.

An interesting solution was demonstrated by *J. Pouysegur et al.*, using divided-pulse amplification configuration with an end-pumped bulk Yb:YAG crystal for efficient energy scaling [83]. When operated in a double-pass regime, divided pulse amplification was implemented with a free-space delay line made of two thin-film polarizers to generate sufficient delay between pulse replicas (directed to the amplifier) to avoid any temporal overlap of the two pulses in the gain medium. In this way, laser peak power was significantly reduced in the amplifier module. After amplification, pulses were coherently recombined using the same delay line with an efficiency of $> 90\%$. The result was $\tau = 523\,fs$ duration, 2.2mJ energy pulses at a pulse repetition rate (PRR) of $10\,kHz$ (corresponding to an average power of $22\,W$), reaching a peak power of $4\,GW$.

A different category of developed Yb:YAG DPSS amplifier systems worth mentioning are code-named The-High-Energy-Class Diode-Pumped-Solid-State-Lasers (HEC-DPSSL) [84–88]. They feature a low pulse repetition rate ($\sim 1\,Hz$), but high pulse energy ($1\,J$ level) system parameters, with pumping of multi-kW levels (pulsed). Multi-cascade, with combinations of cryogenic regenerative and multi-pass amplifiers were employed to reach mind-blowing peak powers of TW level. Despite low repetition rates, which are unsuitable for industrial environment, such laser systems proved to be applicable in scientific environment, such as plasma physics and electron acceleration [89,90].

A short summary of the main parameters achieved by different technologies for Yb:YAG DPSS amplifier systems is presented in Table 1.3 and Fig. 1.12.

Table 1.3 Summary of main parameters achieved in different Yb:YAG DPSS amplifier systems. SCF – single crystal fiber, IS – InnoSlab, MP – multipass, HEC-DPSLL – high energy class DPSLL, τ – achieved pulse duration, PRR – pulse repetition rate, P_{peak} – achieved maximum pulse peak power, η_{eff} – optical-to-optical efficiency, M^2 – beam quality parameter. In the case of different units for parameters, they are specified separately.

	Technology	τ (ps)	PRR (MHz)	P_{peak} (GW)	η_{eff} (%)	M^2	Year	Ref.
1	SCF (non-CPA)	0.75	20	0.006	22.7	1.3	2015	[76]
2	SCF (CPA)	0.86	0.1	0.069	15	1.24	2017	[74]
3	SCF (CPA)	0.38	0.01	2.5	28.5	1.1	2013	[75]
4	SCF (non-CPA)	0.8	83.4	0.002	36.8	1.9	2015	[43]
5	IS (non-CPA)	0.68	76	0.007	49	1.4	2009	[30]
6	IS (non-CPA)	0.62	20	0.084	43	2.1	2016	[77]

7	IS (CPA)	0.83	0.013	22.65	40	1.25	2011	[78]
8	MP (thin-disk, regen., CPA)	0.62	0.003	26	42	1.5	2016	[44]
9	MP (bulk, cryogenic CPA)	6	0.001	11	21	1.17	2015	[80]
10	MP (bulk, CPA)	0.73	1 Hz	136	7.5	-	2017	[79]
11	MP (thin-disk, non-CPA)	6.5	0.3	0.31	30	2.3	2016	[81]
12	MP (bulk, non-CPA)	5.5	78	0.001	40	1.95	2009	[82]
13	HEC-DPSLL (CPA, thin-disk, cascaded multi-pass)	0.74	1 Hz	1270	21	-	2014	[84]
14	HEC-DPSLL (CPA, slab, cascaded cryogenic multi-pass)	10 ns	1 Hz	0.95	22	-	2012	[85]
15	HEC-DPSLL (CPA, thin disk, cascaded multi-pass)	8 ns	2 Hz	1.65	17	-	2013	[86]
16	HEC-DPSLL (CPA, thin-disk, cascaded regen. + multi-pass)	2	100 Hz	150	14	1.1	2009	[87]
17	HEC-DPSLL (CPA, cascaded cryogenic regen.)	10	100 Hz	94 TW	-	-	2008	[88]
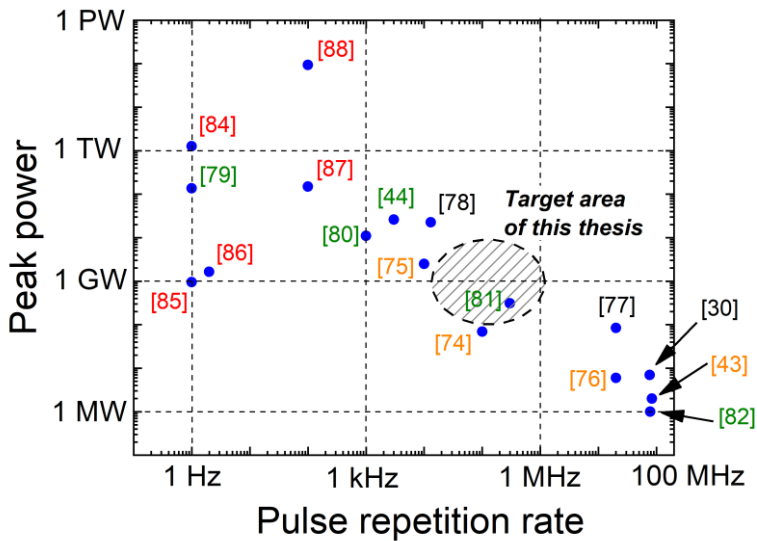
Fig. 1.12 Summarized graph showing peak power and pulse repetition rate for different Yb:YAG DPSS amplifier systems as reviewed in the literature. Numbered insets correspond to literature as indicated in the bibliography of this thesis. Different colors correspond to used technology/type: red – HEC-DPSSL, green – MP, orange – SCF, black – IS (see Table 1.3). The dashed area highlights the targeted range of parameters that were demonstrated in the experimental part of this thesis.

In conclusion, a broad range of parameters were demonstrated and presented in the literature using Yb:YAG as the gain medium. However, most technologies featured multi-pass or regenerative amplifier configurations, which are complicated to align and use a tremendous amount of space. *InnoSlab* and *Taranis* modules, while proved to be efficient solutions, are state-of-the-art technologies, which might prove to be not cost-efficient in building independent amplifier systems. Additionally, cryogenic cooling, which was presented as a solution for some systems, adds considerable complexity, bulkiness, and cost. These reasons encouraged us to search for and develop a compact, cost-effective, and operating at a room-temperature solution for DPSS amplifier system suitable for industrial applications, which is based on a well-established Yb:YAG gain medium. The main parameter range targeted in this thesis is shown in Fig. 1.12, which covers pulse repetition rates between $10\ kHz - 1\ MHz$, and peak powers in the range of $0.1 - 1.2\ GW$.

2. Numerical model for the end-pumped three-level gain medium

Modeling methods related to this Chapter were partly published in A2

2.1. Introduction

The key benefit of any numerical modeling attempt is the ability to predict system performance prior to experimental investigation. By running a series of calculations, one could beforehand choose optimal system parameters and conduct considerably fewer experiments, thus saving time. The more precise the model is, the fewer experiments are required, suggesting that model validation from experimental data is needed.

The aim of this section is thus to provide the necessary theoretical background and used principles of the numerical model suitable for end-pumped three-level gain medium amplifiers. Yb:YAG was selected as a reference material for model validation. A series of experiments were conducted, and results were compared to numerical data, all of which are presented in this Chapter.

The model was fully written in a *Matlab* environment without the need for additional external software (or non-standard modules of *Matlab* itself). Modular program structure was chosen as a backbone of the numerical model, providing the ability to easily add or remove various effects arising in end-pumped gain medium (thermal lensing, heat dissipation, propagation, etc.).

This section is divided into subsections by their purpose:

2.2. Quasi-Three-Level rate equations.
2.3. Thermal analysis of end-pumped Yb:YAG crystal rod.
2.4. Pump beam propagation analysis.
2.5. Signal beam propagation analysis.
2.6. Material parameter definition.
2.7. Physical model grid definition.
2.8. Physical model algorithm.
2.9. Experimental validation.
2.10. Conclusions.

This numerical model is based on radial symmetry ignoring non-symmetrical effects arising in end-pumped gain medium (e.g., stress-induced bi-focusing). For most of this thesis, the approximation is sufficient. In Chapter 5, where non-symmetrical effects are analyzed, the numerical model is expanded to a full three-dimensional concept, however, at the cost of calculation time.

At the end of each section, a brief discussion related to the modeling part is presented. Finally, a short review of the full model is presented, and the overall performance of the physical model is discussed in the concluding section.

2.2. Quasi-Three-Level rate equations

Yb:YAG amplifiers operating at $1 \ \mu m$ and room temperature exhibit a quasi-three energy level dynamics, as Yb-doped materials are free of parasitic effects such as upconversion, excited-state absorption, and crossed relaxation [45]. The multi-phonon transition between the highest energy Stark level manifolds (3→2) is usually strong, therefore the highest energy level population density N_3 will be small (except for extremely high pump intensities) due to rapid excited ions transition from level 3 to level 2. It is thus valid to neglect the population in level 3 and corresponding transitions starting from that level. In such case, the rate equation system obtained is the following [91]:

$$\frac{\delta N_2}{\delta t} = -A_{21} N_2 + \frac{\sigma_{12} I_p}{h\nu_p} N_1 - \frac{\sigma_{21} I_p}{h\nu_p} N_2 + \frac{\sigma_{12} I_s}{h\nu_s} N_1 - \frac{\sigma_{21} I_s}{h\nu_s} N_2, \qquad (2.1)$$

$$\frac{\delta N_1}{\delta t} = +A_{21} N_2 - \frac{\sigma_{12} I_p}{h\nu_p} N_1 + \frac{\sigma_{21} I_p}{h\nu_p} N_2 - \frac{\sigma_{12} I_s}{h\nu_s} N_1 + \frac{\sigma_{21} I_s}{h\nu_s} N_2, \qquad (2.2)$$

where N_i indicate a fractional level population of level i ($N_1 + N_2 = 1$), parameter A_{ij} indicates spontaneous transition rate from level i to j (inverse upper-state lifetime $\frac{1}{\tau}$), σ_{ij} correspond to transition cross-sections, I_s and I_p are the optical intensities at the signal and pump wavelength, and $h\nu$ are corresponding photon energies.

In this thesis, I do not analyze the temporal evolution of population densities as it is usually impractical for amplifiers pumped with continuous wave (CW) diodes. It is then convenient to produce an analytical expression for steady-state ($\frac{\delta N}{\delta t} = 0$) population density for given pump and signal intensities:

$$N_2 = \frac{\dfrac{\sigma_{12} I_p}{h\nu_p} + \dfrac{\sigma_{12} I_s}{h\nu_s}}{A_{21} + \dfrac{(\sigma_{12} + \sigma_{21}) I_p}{h\nu_p} + \dfrac{(\sigma_{12} + \sigma_{21}) I_s}{h\nu_s}}, \qquad (2.3)$$

The steady-state gain coefficient g and power amplification factor G is expressed as:

$$g = (N_2\sigma_{21} - N_1\sigma_{12})L, \tag{2.4}$$

$$G = \exp(g), \tag{2.5}$$

$$P_{out} = P_{in}G, \tag{2.6}$$

where L is the length of the gain medium, P_{in} is the input power, P_{out} is the output power. By following these equations, we can calculate steady-state values of signal and pump intensities given that we have gain medium and input beam parameters.

Previously discussed equations considered monochromatic situations only. For a more realistic scenario, to include signal and pump spectrum profiles, the spectrum profile is divided into a finite number of spectral channels with corresponding central wavelength at each channel. A summation across all spectral components is performed, and population density N_2 is expressed as an average across the full spectrum. Updated terms of equations (2.3-2.6) are shown in Table 2.1.

Table 2.1 Monochromatic (left) and polychromatic (right) description of rate equation terms. λ is the corresponding central wavelength at spectrum channel, W is the integer number of spectral channels used in calculations, N_{2A}, N_{1A} are averaged population densities across spectral width of signal and pump radiation.

Monochromatic	Polychromatic
$\dfrac{\sigma I}{h\nu}$	$\displaystyle\sum_{i=1}^{W} \dfrac{\sigma(\lambda)I(\lambda)}{h\frac{c}{\lambda}}$
$g = (N_2\sigma_{21} - N_1\sigma_{12})L$	$g(\lambda) = (N_{2A}\sigma_{21}(\lambda) - N_{1A}\sigma_{12}(\lambda))L$
$P_{out} = P_{in}G$	$P_{out}(\lambda) = P_{in}(\lambda)G(\lambda)$
P_{out}	$\displaystyle P_{out} = \sum_{i=1}^{W} P_{out}(\lambda)$

It is important to note that in these equations only the spontaneous emission (SE) term is included and the amplified spontaneous emission (ASE) term is omitted. Brief reasoning for this is provided further.

The emission of a spontaneously emitted photon that occurs at any point in the pumped volume will experience an amplification factor $G_{ASE} = \exp(\sigma_{ASE}N_2L_c)$, where L_c is the characteristic length of the system [92]. In principle, ASE becomes relevant either if the population density is high (high-gain amplifiers) or if the characteristic length where the gain is experienced is large (e. g., case of uncoated crystal faces, allowing partially reflected ASE photons to oscillate and amplify within a gain medium). Stable oscillations of ASE can occur if the total gain per round-trip exceeds 1 (amplification in the pumped area and reflection losses at the end-faces of crystal rod). The term $A_{21} = \frac{1}{\tau}$ from equation (2.3) then reads $A_{21} = \frac{1}{\tau}\exp(\sigma_{ASE}N_2L_c)$. This

correction reflects that effective upper-state lifetime is reduced due to ASE. In a simple case, if we neglect ASE absorption in unpumped area, the total gain would be expressed as [93]:

$$G_{ASE} = R \exp(g_0 L_c), \tag{2.7}$$

where R is the reflectivity of end-faces of crystal rod.

The typical reflectivity of anti-reflection (AR) coated crystal rod end-faces used in my work is $R = 0.002$ ($< 0.2\%$). Based on a simple assumption that ASE experiences the same gain coefficient $g_0 L_c$ as the signal, we can find the threshold for the onset $g_0 L_c$ of parasitic oscillations and find to which signal gain this onset corresponds. Parameter $g_0 L_c$ and corresponding signal gain was compared to different values of end-face reflectivity R and the worst-case scenario of the uncoated case when characteristic reflectivity of air/YAG interface is $R = 0.086$ (Fig. 2.1).
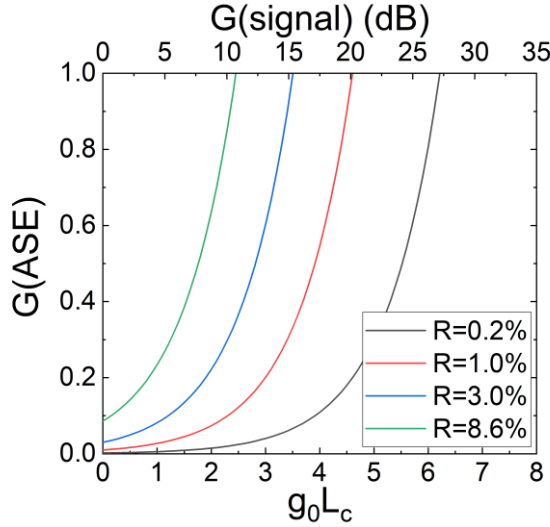
Fig. 2.1 Total ASE gain G_{ASE} dependency on the characteristic gain coefficient $g_0 L_c$. The top axis displays corresponding signal gain (in decibels) at different values of the parameter $g_0 L_c$. Parasitic ASE oscillations start when $G_{ASE} > 1$.

The calculation shown in Fig. 2.1 reveals that the threshold for parasitic ASE oscillations is obviously reduced with AR coating – in the case of uncoated YAG crystal oscillations could start at the signal gain of 11 dB (~12 times) whereas with coating of $R = 0.002$ (actual coating used in the experimental part of this thesis) threshold signal gain value is 27 dB (~500 times). Such suppression of possible parasitic ASE effects is practically enough in moderate-gain Yb:YAG amplifier systems. Furthermore, if we consider reabsorption of ASE radiation within the gain medium, this value

additionally shifts towards higher values of signal gain, making this issue even less relevant in the considered amplifier system.

The real influence of ASE parasitic effects on population inversion can only be calculated with a proper 3D ray-tracing amplification simulation, which was not the scope of this thesis.

2.3. Thermal analysis of end-pumped Yb:YAG crystal rod

The calculation of pump light absorption via rate equations provides sufficient data to calculate dissipated pump power within the crystal. It is assumed that dissipated pump power heats crystal due to the quantum defect only. In this section, I present analytical expressions for the calculation of temperature gradient arising due to dissipated pump power within the crystal rod. Proposed expressions consider pump beam shape, which is of practical interest for building optimal amplifier configurations. Additionally, assumptions and limitations are reviewed.

In order to obtain the required analytical expressions, we assume the following: (1) crystal rod is a radially symmetric (cylinder shape); (2) pump profile is axisymmetric; (3) no heat flow along beam propagation direction; (4) no heat transfer from end-faces of crystal rod; (5) no mechanical deformations of crystal rod end-faces; (6) crystal is homogenous in all directions (no parameter dependency on angular coordinate, e. g. thermal conductivity); (7) heating of crystal is due to the quantum defect only. The geometry of the crystal assumed in our numerical model is displayed in Fig. 2.2.
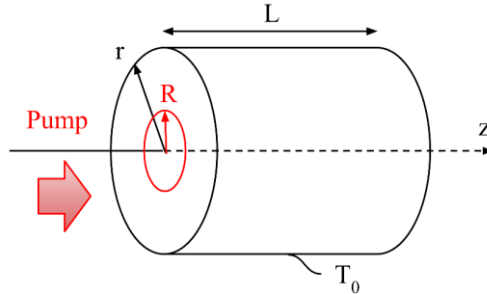
Fig. 2.2 Geometry of the crystal for temperature distribution calculations. r is the radial coordinate of crystal rod, R is the radial coordinate of pump beam intensity profile (red circle displays the edge of the pumped region inside crystal rod), T_0 is the boundary temperature of the crystal rod (cooling temperature), z denotes the axis of beam propagation direction.

Following previous assumptions, equations governing temperature distribution within cylindrical crystal rod can then be expressed as follows [30,45,94]:

$$T(r,z) = -\int_0^r \frac{h(r_1,z)}{k(T)}\,dr_1 + T_0, \qquad\qquad (2.8\ a)$$

$$h(r,z) = \frac{1}{Lr}\int_0^r I(r_1,z)r_1\,dr_1, \qquad\qquad (2.8\ b)$$

$$P(r,z) = 2\pi\int_0^R I(r_1,z)r_1\,dr_1, \qquad\qquad (2.8\ c)$$

where h is the heat flux (W/m^2), L is the rod length, r is the radial coordinate, I is the pump beam intensity, P is the heating power at the radial coordinate (due to the quantum defect), k is the thermal conductivity coefficient ($W/(m \cdot K)$), T_0 is the crystal rod temperature at the boundary (cooling temperature), and T is the temperature distribution in the crystal rod across the radial direction. By numerically integrating across the radial coordinate, the temperature distribution in the crystal rod is retrieved with pump beam shape considered. Initially, it is assumed that the contact between the crystal rod boundary and the heat sink is ideal, producing no additional temperature rise.

The shape of the pump beam intensity profile is of importance regarding the overall temperature distribution within the crystal rod. Initial modeling was performed using equations (2.8) in two cases: when pump intensity distribution is Gaussian and when it is flat-top. Crystal length was set to $L = 10\ mm$, crystal width $2\ mm$, thermal conductivity $k = 10\ W/(m \cdot K)$, absorbed pump power $100\ W$ (heating power $P = 8.7\ W$ due to quantum defect of 8.7 %), and pump beam radius at $1/e^2$ maximum intensity level $R = 0.25\ mm$. Modeling results are displayed in Fig. 2.3.
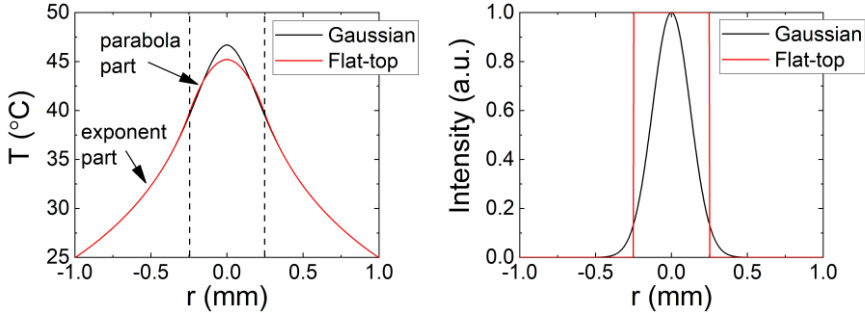
Fig. 2.3 <u>Left:</u> radial temperature distribution in crystal, pumped by $100\ W$ of power (heating power $P = 8.7\ W$ due to quantum defect of 8.7 %). Crystal length $L = 10\ mm$, width $2\ mm$, thermal conductivity $k = 10\ W/(m \cdot K)$, pump beam radius at $1/e^2$ level $R = 0.25\ mm$. Dashed lines indicate the edges of the pump beam at $1/e^2$ maximum intensity level. Characteristic parabolic and exponential parts of temperature gradient are depicted with arrows. <u>Right:</u> pump beam intensity profiles in case of Gaussian and flat-top distribution. Beam radius is the same at $1/e^2$ maximum intensity level. Both intensity profiles were normalized to the maximum value.

It is considered that the crystal is end-pumped by a fiber-coupled diode, which produces a nearly flat-top pump intensity distribution at the end of the fiber. However, as the beam propagates, the intensity distribution evolves to Gaussian intensity distribution, which is analogous to the case of super-Gaussian intensity distribution beams. From modeling results, we see that the flat-top pump intensity profile is more favorable than Gaussian – the peak temperature is $T(0) = 46.7°C$ in case of Gaussian distribution and $T(0) = 45.2°C$ for flat-top distribution. The overall lower peak temperature leads to higher pump absorption and higher signal amplification simply because transition cross-sections are temperature-dependent (with higher temperatures, their value decrease). However, in practice, it is impossible to keep flat-top pump intensity distribution along the whole crystal, as the radiation that is emitted from the fiber-end has a finite numerical aperture. Due to the super-Gaussian nature of pump radiation, flat-top intensity distribution could be formed at some part of the crystal, whereas at other parts, this distribution would evolve to Gaussian-like. The best practice is to relay image fiber-end (flat-top) at the front segment of crystal, where pump absorption is highest. This would theoretically yield the lowest possible peak temperature rise with the same pump absorption. More information regarding pump beam propagation and intensity distribution evolution is provided in the next section.

In practice, crystals are mounted in some sort of heatsink (e.g., copper mount). An interface between the heatsink and the actual crystal is used. This interface is of finite thickness and thermal conductivity, producing additional temperature shift of boundary condition $T_0 = T_0 + \Delta T_{int}$. The practical requirements of interface material are its "softness" (to avoid mechanical impact on crystal rod, leading to initial depolarization or fracture when the crystal is pumped) and good thermal conductivity. A good candidate for such application is thermally conductive silicone CV-2946 from NuSil, with thermal conductivity parameter $k_I = 1.49 \, W/(m \cdot K)$. Our analytical model can be extended, and temperature rise at crystal boundary due to the thermal resistance of silicone interface can analytically be expressed as [94]:

$$\Delta T_I = \frac{P \delta r_I}{k_I A_I}, \tag{2.9 a}$$

$$T_0 = T_0 + \Delta T_I, \tag{2.9 b}$$

where P is the deposited heat onto the silicone layer surface (W), δr_I is the interface layer thickness (m), k_I is the thermal conductivity of the interface material $(W/(m \cdot K))$, $A_I = 2\pi r L$ is the surface area of the interface (m^2), and T_0 is the heatsink temperature. In the numerical model, it is assumed that

deposited heat onto the interface layer is $P = P_{pump\,absorbed} \times (quantum\,defect)$. An assumption is made that the remaining unabsorbed power, e.g., in terms of spontaneous emission, exits the crystal without reabsorption at the interface layer.

We can deduct from equation (2.9) that we could minimize temperature rise due to interface layer by increasing surface area of the crystal rod – either by increasing aperture dimensions or length of the crystal. However, as is seen from equations (2.8), an increase of radial dimension of crystal leads to an increase of peak temperature of crystal rod. On the other hand, we could increase crystal length, but the longer gain path for signal could lead to nonlinearities (e.g., the rise of B-integral), which deteriorate beam and pulse quality [6]. Additionally, spontaneous emission, which is emitted in all possible directions (when the crystal is pumped), has a lower chance of exiting the crystal rod without reabsorption at the crystal and heatsink interface if the length of the crystal rod is large, leading to additional heat dissipation. This suggests that there must be an optimal geometry of the crystal rod in terms of temperature distribution.

Although the task is rather complex and multidimensional, we can gather some initial insights into what the influence of the interface layer between the crystal and heatsink is. Let us consider a case where pump beam radius is fixed and set to $R = 0.25\,mm$ (flat-top), absorbed pump power in the crystal is $100\,W$ (heating power $P = 8.7\,W$ due to quantum defect of 8.7 %, e.g., pumping is centered at $940\,nm$), crystal thermal conductivity $k = 10\,W/(m \cdot K)$, interface layer thermal conductivity $k_I = 1.49\,W/(m \cdot K)$. The resulting temperature rise due to heating with and without interface layer at different values of crystal length and crystal width is plotted in Fig. 2.4. Three practical interface layer thickness values of $\delta r = 100\,\mu m, 200\,\mu m, 300\,\mu m$ are considered. Crystal width is varied from $1\,mm$ to $11\,mm$, and crystal length is varied from $5\,mm$ to $15\,mm$ (practical values that are covered within this thesis).
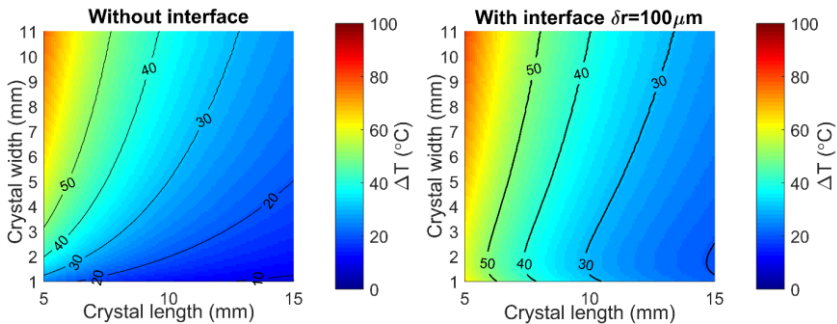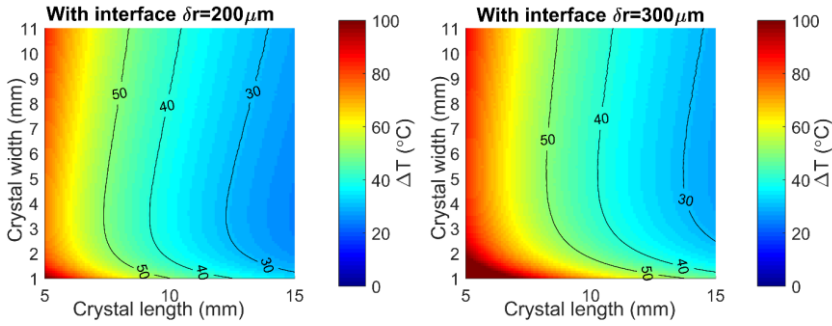
Fig. 2.4 Peak temperature rise within crystal rod due to heating induced by absorbed pump power. Black lines indicate isotherms with corresponding temperature values displayed as a label. Crystal rod is pumped by $100\ W$ of power (heating power $P = 8.7\ W$ due to quantum defect of 8.7 %), crystal thermal conductivity $k = 10\ W/(m \cdot K)$, pump beam radius at $1/e^2$ level $R = 0.25\ mm$ (flat-top), interface layer thermal conductivity $k_I = 1.49\ W/(m \cdot K)$. **From top left to bottom right:** case without interface layer; case when the interface layer thickness is $\delta r = 100\ \mu m$; case when the interface layer thickness is $\delta r = 200\ \mu m$; case when the interface layer thickness is $\delta r = 300\ \mu m$.

Results indicate that the inclusion of interface layer introduces significant peak temperature rise in crystal rod when crystal width is minimal (corresponding to the lowest surface area from which heat can dissipate from layer to heatsink). On the other hand, when crystal width is large, the influence of the interface layer is minimal, resulting in peak temperature rise mostly due to absorbed pump radiation heating of crystal. Additionally, as interface layer thickness δr is increased, the peak temperature rise is even more prominent at low values of crystal width, whereas at high values of crystal width, peak temperature is less affected. It is interesting to note that when interface layer is introduced, peak temperature varies less at fixed crystal length when crystal width is changed (e.g., case of layer thickness $\delta r = 300\ \mu m$, crystal length $L = 11\ mm$ – when crystal width is varied, peak temperature stays within $40\ °C$ across the most range). Also, the influence of the interface layer is minimal in large apertures and long crystal rods. However, practical crystal width in Yb:YAG amplifier systems is within $5\ mm$, suggesting that thickness of interface layer becomes non-negligible at determining peak temperature rise due to end-pumping of crystal rod. Typical achievable interface silicone layer thickness is $\delta r = 100\ \mu m$, indicating a rather wide range of practical crystal geometries for the purpose of building end-pumped crystal rod amplifier systems. There are additional factors influencing optimal crystal geometry, which are presented in the next sections throughout this thesis.

2.4. Pump beam propagation analysis

In simple cases, one can assume that the pump beam shape does not change as the beam propagates along the crystal. However, in end-pumped Yb:YAG amplifier systems pump beam must be focused to a tight beam spot to achieve a sufficient amplification level [30]. When beam Rayleigh length is compared to the length of the pumped crystal, it is observed that pump beam size (and shape) changes significantly across the crystal rod, suggesting that pump beam propagation characteristics must be accounted for precise numerical modeling.

In this thesis, numerical calculation of pump beam shape and propagation along the crystal rod is based on the ABCD matrix method [91]. Paraxial and thin lens approximation is assumed. Usually, the coherence length of pump beam radiation is short, thus this method is in good agreement with experimental observations, as is presented further.

In experiments throughout this thesis, pump radiation is outcoupled from the fiber-end to air, collimated with a collimating lens, and then focused to the crystal rod with a focusing lens to form the required pump beam diameter at crystal plane. Throughout experiments, and for the purposes of numerical model validation, a high-brightness fiber-coupled ($NA = 0.22$) diode from *nLight* was used, with fiber core/cladding diameter of $105/125 \, \mu m$. The principle optical scheme of pump beam shaping is displayed in Fig. 2.5.
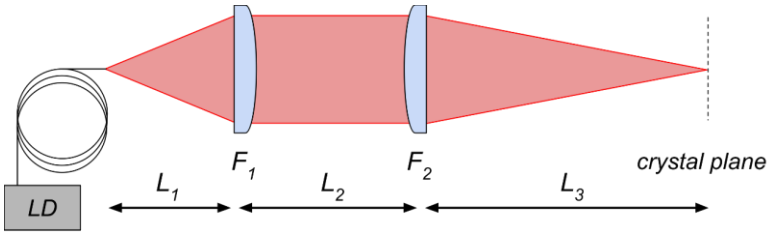
Fig. 2.5 Principal optical scheme of pump beam shaping emanating from the fiber-coupled laser diode. Lenses of focal lengths $F_1 = 25 \, mm$, $F_2 = 200 \, mm$ are used. Distances between lenses are set to $L_1 = 23 \, mm$, $L_2 = 320 \, mm$, $L_3 = 300 \, mm$, magnifying output beam from fiber with core diameter $105 \, \mu m$ to $\sim 600 \, \mu m$ at crystal plane. Fiber-end is relay imaged to crystal plane. *LD* is a fiber-coupled diode.

ABCD matrix of such optical setup can be expressed as:

$$\begin{pmatrix} r_{out} \\ \theta_{out} \end{pmatrix} = \begin{pmatrix} 1 & L_3 \\ 0 & 1 \end{pmatrix} \cdot \begin{pmatrix} 1 & 0 \\ -\frac{1}{F_2} & 1 \end{pmatrix} \cdot \begin{pmatrix} 1 & L_2 \\ 0 & 1 \end{pmatrix} \cdot \begin{pmatrix} 1 & 0 \\ -\frac{1}{F_1} & 1 \end{pmatrix} \cdot \begin{pmatrix} 1 & L_1 \\ 0 & 1 \end{pmatrix} \cdot \begin{pmatrix} r_{in} \\ \theta_{in} \end{pmatrix}, \qquad (2.10)$$

where r_{in} – ray exiting from the fiber at a particular radial position, θ_{in} – the tangent angle of ray at a radial position that is exiting fiber, L_1 is the distance

from fiber to collimating lens, F_1 is the focal length of collimating lens, L_2 is the distance between collimating lens and focusing lens, F_2 is the focal length of focusing lens to crystal plane, L_3 is the distance from focusing lens to crystal, r_{out}, θ_{out} is resulting ray radial position and its tangent angle.

Rays that are leaving fiber-end can be described as an intensity function that is dependent on radial coordinate r, and angular coordinate θ, expressed as $I(r, \theta)$. If we assume that the angular distribution of each ray is identical, we can conveniently express intensity function as a convolution of two functions – spatial and angular intensity distributions:

$$I(r, \theta) = f(r) \cdot g(\theta), \tag{2.11}$$

where $f(r)$ is spatial intensity distribution and $g(\theta)$ is angular intensity distribution. It must be noted that both functions are two-dimensional.

To calculate beam intensity profile at crystal plane, the distance of ray between its radial coordinate and optical axis r_{out} is required, whereas ray angle θ_{out} is not important. From the ABCD matrix of equation (2.10), we can calculate:

$$r_{out} = k_r(L_3)r_{in} + k_\theta(L_3)\theta_{in}, \tag{2.12}$$

where

$$k_r = 1 - \frac{L_3}{F_2} - \left[\left(1 - \frac{L_3}{F_2}\right)L_2 + L_3\right]\frac{1}{F_1}, \tag{2.13 a}$$

$$k_\theta = \left[1 - \frac{L_3}{F_2} - \left((1 - \frac{L_3}{F_2})L_2 + L_3\right)\frac{1}{F_1}\right]L_1 + \left(1 - \frac{L_3}{F_2}\right)L_2 + L_3. \tag{2.13 b}$$

Following equations and assumptions made previously, we can derive that beam intensity profile at crystal plane is then a convolution of two resulting circles with radiuses $|k_r|r$ and $|k_\theta|\theta$. To calculate the resulting pump beam intensity profile, a convolution of two functions $f(k_r r)$ and $g(k_\theta \theta)$ is performed:

$$I(r) = f(k_r r) * g(k_\theta \theta). \tag{2.14}$$

The principal geometrical model of rays exiting fiber with spatial and angular intensity distributions is displayed in Fig. 2.6.
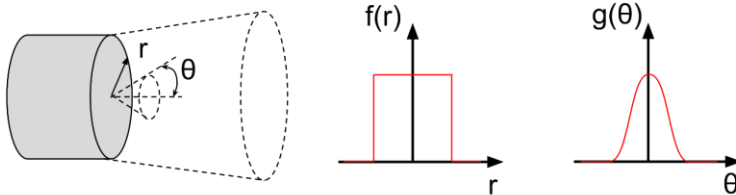
From experimental observations, it was deducted that spatial intensity distribution (near-field beam profile) can best be approximated with flat-top intensity profile, whereas angular (far-field beam profile) – by Gaussian intensity profile. For practical reasons, these functions can conveniently be expressed as a function of radial coordinate r only:

$$f(r) \propto \exp\left(-2\left(\frac{r}{|k_r|\omega_0}\right)^n\right), \tag{2.15 a}$$

$$g(r) \propto \exp\left(-2\left(\frac{r}{|k_\theta|NA}\right)^2\right), \tag{2.15 b}$$

where r is the radial coordinate, n is the order of super-Gaussian beam distribution (to generate flat-top intensity profile $n = 1000$ was used), ω_0 is the initial beam radius at fiber-end, NA is the numerical aperture of beam exiting fiber, k_r and k_θ are functions as described in Eq. (2.13).

To validate this assumption, an experiment was carried out employing the principal scheme shown in Fig. 2.5. Pump radiation exiting a fiber was collimated and then refocused with a pair of lenses. Focused pump beam intensity distribution was then captured with a CCD camera, and beam diameter at a 4-sigma intensity level was estimated. Beam diameter evolution as the beam propagates was measured via the z-scan technique, where the camera is translated along the beam propagation direction, and resulting beam intensity profiles are captured at each position. Experimental and modeling results are shown in Fig. 2.7, Fig. 2.8, and Fig. 2.9.
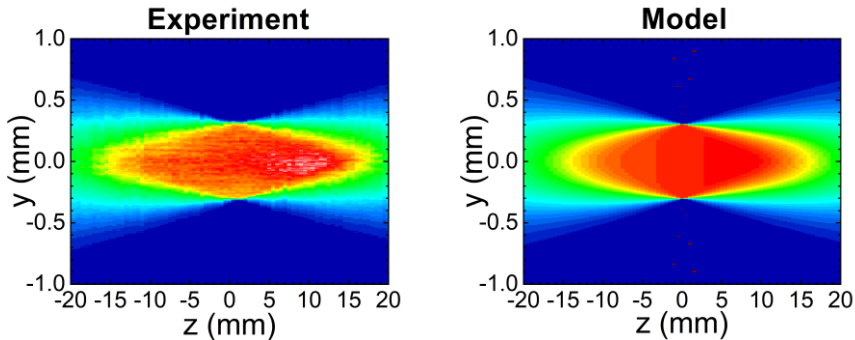
Fig. 2.7 2D beam intensity cross-section colormap of experimental measurement (left) and numerical calculations (right). z corresponds to beam propagation direction, y is lateral coordinate. The numerical aperture of fiber was set to $NA = 0.15$. Colormap range is identical in both cases.
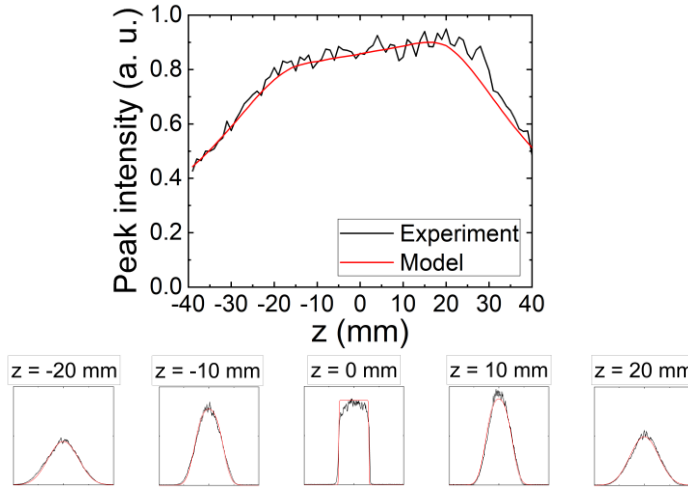
Fig. 2.8 Pump beam peak intensity evolution as it propagates. The solid black line indicates experimental data, and the red curve indicates modeling data. At the bottom, beam cross-sections at different propagation distances are plotted.
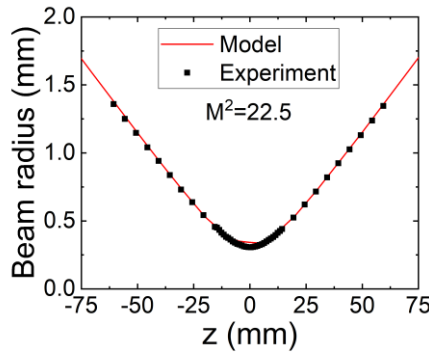
Fig. 2.9 Beam radius evolution measurement along beam propagation direction (black marks – experimental data, red curve – modeling data). Beam quality parameter M^2 was estimated from the fit of data. The measured value corresponds to NA = 0.15.

Experimental and modeling data comparison indicates a nearly perfect match. Beam cross-section in the fiber-end image plane (flat-top intensity distribution) from experimental data shows a somewhat parabolic intensity profile at the top of intensity distribution, although from modeling data, I predict an ideal flat-top intensity profile at this plane. The reason for this could be due to mode-filling of fiber, producing non-ideal flat-top intensity distribution of beam exiting fiber-end. However, by tuning expression $f(r)$ in Eq. (2.15), I could practically get a perfect match to experimental data. Nonetheless, overall pump beam propagation prediction with the model is satisfactory.

It must be noted that in this model, the numerical aperture of the beam exiting the fiber must be tuned to $NA = 0.15$ to best match the experimental data. The actual fiber numerical aperture is $NA = 0.22$. However, according to the datasheet of the fiber-coupled diode from *nLight*, 95% of beam power exiting the fiber is within $NA = 0.15$, whereas the remaining 5% are within $NA = 0.22$. It is then practical to assume a numerical aperture of $NA = 0.15$. However, caution must be taken if long fiber ($> 5\ m$) of different NA is spliced to diode fiber, as eventually beam numerical aperture will match the additional fibers.

Additionally, maximum peak intensity position along the propagation direction of focused pump beam does not necessarily coincide with relay image of fiber-end (flat-top position), as was seen in Fig. 2.8 ($z = 0\ mm$) and is dependent on distances between the lenses. If distances between the lenses are chosen to match the focal length of corresponding lenses (e.g., $L_1 = F_1, L_2 = F_1 + F_2, L_3 = F_2$), total symmetry of maximum peak intensity distribution along propagation direction is achieved. This is important to consider if the pump beam propagation path is sufficiently large within the crystal rod as that could influence overall amplifier performance.

2.5. Signal beam propagation analysis

The Hankel transform method proves to be an efficient and reliable solution for the propagation of optical beams through systems with cylindrical symmetry [95,96]. It is an analogy of the well-known Fourier transform method in the two-dimensional domain. Hankel transform (HT) and the inverse Hankel transform (IHT) can be expressed as:

$$f_2(\nu) = 2\pi \int_0^\infty f_1(r) J_p(2\pi\nu r) r\, dr, \qquad\qquad \text{(2.16 a)}$$

$$f_1(r) = 2\pi \int_0^\infty f_2(\nu) J_p(2\pi r\nu) \nu\, d\nu, \qquad\qquad \text{(2.16 b)}$$

where J_p is the p-th order Bessel function of the first kind, r is the radial coordinate, ν is the spatial frequency, and $f_1(r), f_2(\nu)$ are the real and complex functions. Integrals in equations (2.16) are difficult to compute because of the oscillatory behavior of the Bessel function and the infinite length of the interval. However, by introducing a pre-calculated transformation matrix C for function transformation forward and backward from Fourier (Hankel) plane, and assuming that the transformed functions are distributed in a limited region ($0 \le r \le R,\ 0 \le \nu \le V$), a computationally-efficient set of functions can be derived [95]:

$$F_2(m) = \sum_{n=1}^{N} C_{mn} F_1(n), \qquad\qquad (2.17\ a)$$

$$F_1(n) = \sum_{m=1}^{N} C_{nm} F_2(m), \qquad\qquad (2.17\ b)$$

where

$$F_1(n) = f_1\left(\frac{j_n}{2\pi V}\right)\left|J_1^{-1}(j_n)\right|R, \qquad\qquad (2.18\ a)$$

$$F_2(m) = f_2\left(\frac{j_m}{2\pi R}\right)\left|J_1^{-1}(j_m)\right|V, \qquad\qquad (2.18\ b)$$

$$C_{mn} = \frac{2}{j_{N+1}} J_0\left(\frac{j_n j_m}{j_{N+1}}\right)\left|J_1^{-1}(j_n)\right|\left|J_1^{-1}(j_m)\right|, \qquad\qquad (2.18\ c)$$

$$n, m = 1, \dots, N, \qquad\qquad (2.18\ d)$$

where j_n, j_m are the positive roots of the zero-order Bessel function, J_1 is the first-order Bessel function, R is the maximum value of radial distance ($0 \leq r \leq R$), V is the maximum value of spatial frequency ($0 \leq v \leq V$), C_{mn} is the transformation matrix, and N is the maximum value of points for discretization in the radial direction. More information can be found in the work of *Yu et al.* [95].

To account for diffraction in free-space after distance dz, complex function in Fourier (Hankel) plane is multiplied by a factor [97]:

$$F(k_r, dz) = F(k_r)\exp(-ik_z dz), \qquad\qquad (2.19)$$

where $F(k_r)$ is complex function before propagation, $F(k_r, dz)$ is complex function after propagation distance dz, k_r and k_z are beam wavevector projections in radial and beam propagation directions ($k_0^2 = k_z^2 + k_r^2$, where $k_0 = \frac{v_0 n(v_0)}{c}$, v_0 is wave frequency, $n(v_0)$ is the refractive index at the frequency v_0, c is the speed of light). To retrieve the real function of the diffracted beam that propagated distance dz in free-space, an inverse Hankel transform of function $F(k_r, dz)$ is performed.

To account for a case when the beam passes thin lens, a real function is multiplied by a factor (no Hankel transform necessary):

$$F(r) = F_0(r)\exp\left(-ik_0\frac{r^2}{2f}\right), \qquad\qquad (2.20)$$

where $F_0(r)$ is real function before the lens, $F(r)$ is real function after lens, r is radial coordinate, f is the focal length of a thin lens. To consider thermal

lens arising in end-pumped Yb:YAG crystal rod due to the refractive index change of pumped gain medium, multiplication factor becomes [98]:

$$F(r) = F_0(r)\exp\left(-i\frac{2\pi}{\lambda}\frac{dn}{dT}\Delta T(r)dz\right), \tag{2.21}$$

where $\frac{dn}{dT}$ is the thermo-optic coefficient of gain material, λ is the wavelength of beam, $\Delta T(r)$ is the temperature difference from initial temperature due to pumping at the radial position, dz is the material thickness at which thermal lens is calculated.

It must be noted that this method for signal beam propagation is valid for monochromatic wave propagation.

2.6. Material parameter definition

In this subsection, critical material parameters that are dependent on temperature are defined with the sources provided.

For the simulation and design of diode end-pumped amplifiers, data on gain medium absorption and emission cross-sections are essential. Moreover, temperature dependency of cross-sections is required for precise modeling. In the numerical model, cross-section, as measured by *Koerner et al.*, was used [47]. Absorption and emission cross-sections at room temperature of $T = 20°C$ are displayed in Fig. 2.10.
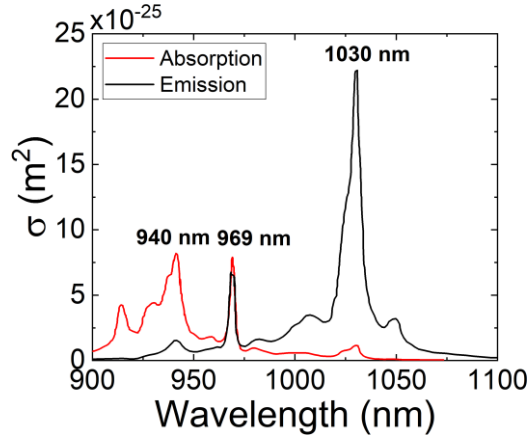
Fig. 2.10 Absorption (solid red line) and emission (solid black line) cross-section of Yb:YAG at room temperature of $T = 20°C$.

In the numerical model, wavelength ranges for pump ($940\ nm$ or $969\ nm$) and signal ($1030\ nm$) are discretized in a finite number of wavelength channels, with each channel having a central wavelength λ_c assigned.

Typically, for precise modeling range of $\pm 40\,nm$ is sufficient, with 200 discretization points. Additionally, each wavelength has a corresponding absorption cross-section $\sigma(\lambda_c)$ assigned to it.

To consider temperature dependency of cross-sections, peak absorption and emission-cross section dependency on temperature were used (Fig. 2.11 and Fig. 2.12). A whole range of cross-sections is scaled accordingly [47].
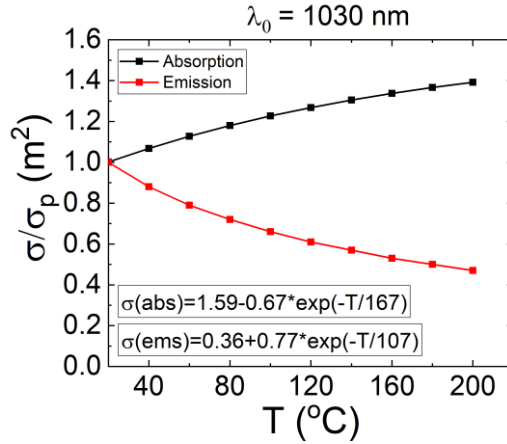
Fig. 2.11 Relative change in peak absorption and emission cross-sections for Yb:YAG at $1030\,nm$. σ_p is the absolute value of peak absorption or emission cross-section. Exponential decay fit was performed with corresponding functions displayed as an inset.
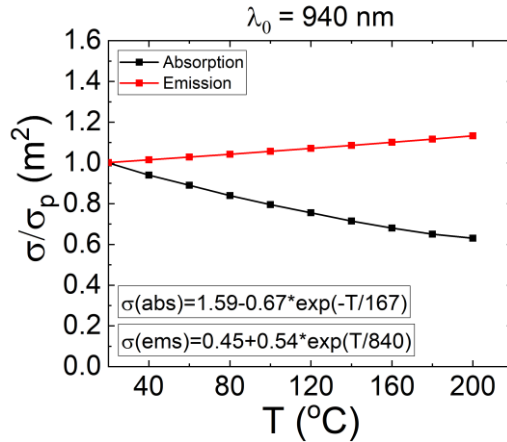
Fig. 2.12 Relative change in peak absorption and emission cross-sections for Yb:YAG at $940\,nm$. σ_p is the absolute value of peak absorption or emission cross-section. Exponential decay fit was performed with corresponding functions displayed as an inset.

Two other parameters with dependency on temperature that were considered in the numerical model are (1) thermo-optic coefficient $\frac{dn}{dT}(T)$ and

(2) thermal conductivity $k(T)$. Values with corresponding fit functions are displayed in Fig. 2.13 and in Fig. 2.14 [48,49].
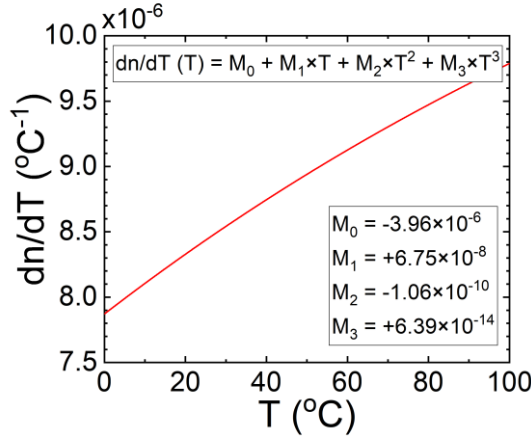
Fig. 2.13 Temperature dependence of the thermo-optic coefficient $\frac{dn}{dT}(T)$ of an undoped YAG crystal. **Note:** the value of temperature in the fit function is in Kelvins [48].
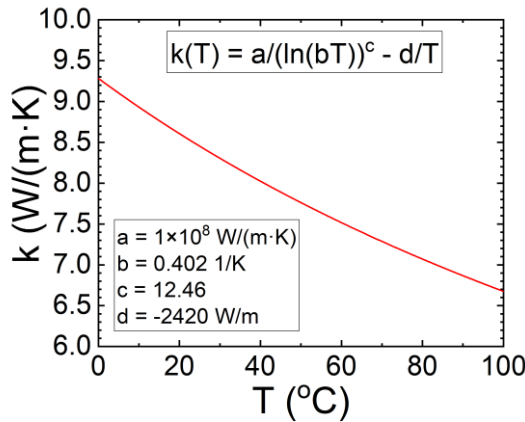
Fig. 2.14 Thermal conductivity $k(T)$ of Yb:YAG (2% doping) as a function of temperature. **Note:** the value of temperature in fit function is in Kelvins [49].

Other parameters for modeling which dependency on temperature was not accounted for are provided in the experimental validation subsection.

2.7. Physical model grid definition

In this subsection, the grid definition for radially symmetric numerical calculations is explained. The principal schematic of such grid is shown in Fig. 2.15.
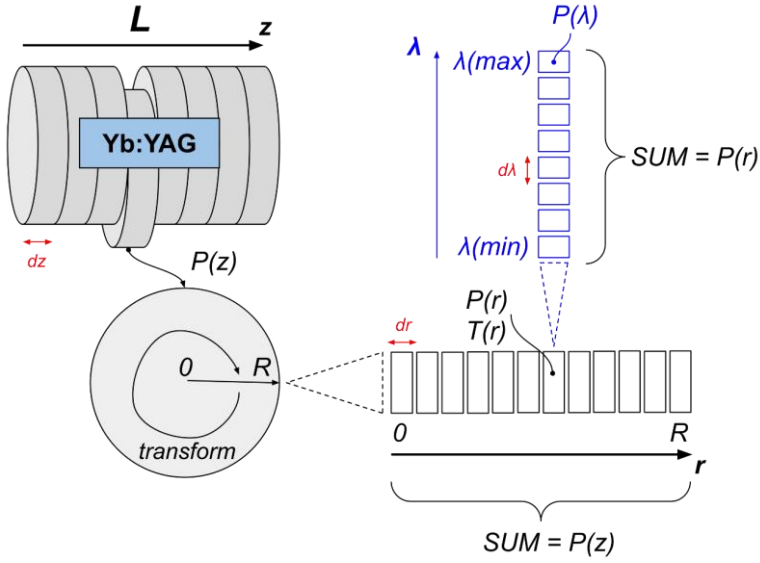
Fig. 2.15 Grid schematic for radially symmetric numerical calculations. L denotes Yb:YAG crystal rod length, $P(z)$ is total power in particular slice at propagation position z, dz is slice thickness, R is the total radius of crystal rod, $transform$ denotes required transformation for two-dimensional intensity (or power) distribution conversion to radial symmetry (see equations (2.17)), r is radial coordinate, dr is radial slice thickness, $P(r)$ is total power in radial slice, $T(r)$ is the temperature at the radial slice, $\lambda(\min)$ is starting wavelength in wavelength range, $\lambda(\max)$ is ending wavelength in wavelength range, $d\lambda$ is the width of wavelength channel, λ is the direction for wavelength scanning (from minimal to maximal value), $P(\lambda)$ is total power in wavelength channel.

In the physical model, the crystal rod is divided into a finite number of slices along the beam propagation direction. Each slice is of equal length with thickness dz. dz is set to a value that is considerably shorter than Rayleigh length z_R of signal beam, satisfying $dz \ll z_R$. This ensures that beam change is minimal between adjacent slices. dz is also defined, so that maximum temperature (due to heating of crystal) at the center of neighboring slices is much lower than total longitudinal temperature gradient of crystal, ensuring that effectively there is no heat flow along beam propagation direction within adjacent slices (assumption made in Section 2.3). Additionally, the small-signal gain condition must be satisfied [99]. Additional tuning of discretization parameters was completed for a balance of calculation speed and solution convergence.

Initial definitions of signal and pump beam in the two-dimensional case are then transformed to radial dimension using the matrix, as denoted in Eq. (2.17). Further calculations are based fully on a radially symmetric case.

Each crystal rod slice, which is one-dimensional after transformation, is then divided into the finite number of radial slices of thickness dr. Each slice holds a unique power value of $P(r)$ (updated as the signal beam is amplified, or pump beam is absorbed) and calculated temperature $T(r)$ (see Section 2.3). The number of slices in the radial direction is also of equal length. Thickness dr is defined so that satisfactory sampling of propagating signal and pump beam is achieved. This parameter is usually tuned before calculations to achieve optimal value. Setting this value to too small as compared to crystal rod radius R would require tremendous computational resources of user's hardware. By adding each radial slice power value $P(r)$, a power value $P(z)$ of the crystal slice at propagation distance z is retrieved.

Each radial slice is then divided into a finite number of wavelength slices. Each wavelength slice is of equal thickness $d\lambda$. The range of wavelength slices is set from $\lambda(min)$ to $\lambda(max)$ to cover corresponding spectral widths of signal and pump radiation. $d\lambda$ is set to sufficiently sample features of each spectrum. Each wavelength channel is attributed to a specific power value of $P(\lambda)$ so that it accommodates for spectral shape of the signal and pump radiation. By adding each wavelength slice power value $P(\lambda)$, a power value $P(r)$ of the radial slice at radial position r is retrieved.

2.8. Physical model algorithm

In this subsection physical model algorithm suitable for end-pumped Yb:YAG crystal is described. It is assumed that continuous-wave (CW) radiation is propagating in the crystal. Modeling of signal beam propagation and amplification in crystal rod is based on an iterative procedure, iterating through crystal slices consecutively in forward and backward directions to complete double-pass amplifier configuration, whereas pump beam propagates in the forward direction only. The principle scheme considered in this model is displayed in Fig. 2.16.
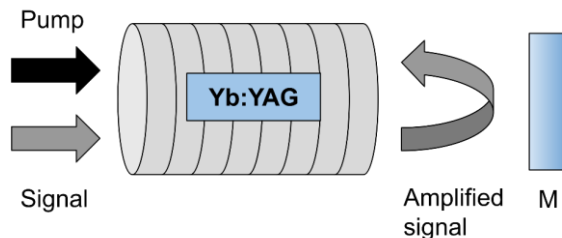

Fig. 2.16 Schematic of signal and pump radiation propagation in the double-pass amplifier configuration. M denotes a hypothetical mirror for amplified signal reversing to complete double-pass configuration.

Primarily, crystal rod sampling is defined - a number of crystal slices, radial slices, and a number of wavelength channels are set (as defined in subsection (2.7)). Then, before the iterative procedure is started, initial modeling parameters are defined: **(1)** signal and pump power distribution functions (e.g., beam diameters, total power) and focusing positions within the crystal, i.e. $P_{signal}(r)$ and $P_{pump}(r)$; **(2)** pump distribution at each crystal slice $P_{pump}(r, z)$ is pre-calculated (see Section 2.4) and it is assumed that the pump beam does not experience lensing effects within the crystal; **(3)** initial temperature map $T_0(r, z)$ across the whole crystal rod (cooling temperature); **(4)** cross-section values across the whole crystal, at each radial position, and through all considered wavelength range based on the initial temperature $T_0(r, z)$ - $\sigma_{absoprtion}(\lambda, r, z)$ and $\sigma_{emission}(\lambda, r, z)$ for signal and pump separately; **(5)** crystal geometry (length L and radius R); **(6)** crystal doping concentration (%) and upper-state lifetime τ; **(7)** unperturbed refractive index of the material $n_0(r, z)$.

The modeling algorithm of signal beam propagation through the gain medium is based on an iterative procedure, where the algorithm convergence parameter is crystal rod temperature. The algorithm is iterated enough times until the subsequent peak temperature value of the crystal rod is within the error margin (algorithm convergence parameter) as compared to the peak temperature value retrieved in the previous iteration.

The iterative procedure starts with the first pass through the gain medium. Single iteration in a numerical model is defined as a situation when calculations across all crystal slices are finished (single- or double-pass). Initially defined parameters are used to calculate amplification parameters at the first crystal slice, which is divided into a finite number of radial slices. Calculations are performed at each radial slice independently. The average value of population densities N_2 and N_1 at each radial slice is calculated by integrating through all wavelength channels (see formulas in subsection (2.2) and Table 2.1). Gain coefficients $g(\lambda) = \sigma_{emission}(\lambda) \cdot N_2(average) - \sigma_{absorption}(\lambda) \cdot N_1(average)$ at each wavelength channel in this radial slice are calculated for the signal and pump radiation. Afterward, a calculation of respective power change $P_{out}(\lambda) = P_{in}(\lambda)\exp(g(\lambda))$ at each wavelength channel is performed. By summing all $P_{out}(\lambda)$ values across wavelength range, a total power $P_{out}(r)$ at radial slice is retrieved. This is repeated across all radial slices, yielding a total relative profile of amplification (or absorption) at the crystal slice. By summing all $P_{out}(r)$ power values, we can retrieve the total resulting power $P_{out}(z)$ at crystal slice. Furthermore, absorbed pump power $P_{pump\_absorbed}(r)$ is retrieved, crystal heating power (at each radial

slice) due to quantum defect is calculated, and temperature $T(r)$ due to heating of crystal at calculated crystal slice is stored for next numerical iteration.

After amplification calculation, the signal beam is propagated through a crystal slice with thickness dz. In the first iteration signal beam is propagated through the gain medium without considering any change of unperturbed refractive index $n_0(r)$ due to thermo-optic response of pumped gain medium, whereas subsequent model iterations consider this change due to updated full temperature map $T(r, z)$.

With updated (scaled) power values of signal and pump, the procedure is repeated with the next slice – newly retrieved power values at each radial slice r (which contain independent power values $P(\lambda)$ at each wavelength channel) are fed to subsequent slice, and amplification parameters are again calculated. The signal beam is then again propagated through a crystal slice with thickness dz. This iterative procedure is repeated until the last slice is reached.

After iteration of the first pass is finished, a new temperature map $T(r, z)$ of the crystal rod is retrieved based on modeling data. Spectroscopic cross-sections $\sigma(T)$ and refractive index distribution $n(T)$ are updated accordingly. An iterative procedure is repeated with newly updated parameters, as described previously. The algorithm for the first-pass repeats itself until the difference between the newly retrieved temperature map values and previous values are within the error margin.

Second pass modeling is started by retrieving calculated signal and pump power values $P(\lambda, r, z)$ across the crystal rod. Then the signal beam is relay-imaged from and back to crystal to compensate for the lensing effect resulted in the first pass through the gain medium. Iterative procedure for the second pass is then started, which is analogous to the first pass, but with retrieved first pass power values $P(r, z)$ used as additional input parameters for the calculation of population densities, gain coefficients and fractional power change. The convergence parameter for the second pass is the output power of signal – if the difference between new and previously retrieved power values is above the error margin, the algorithm is repeated starting with the first pass but with signal and pump power values from the second pass used as additional input parameters for the first pass. The resulting temperature map $T(r, z)$ is also retrieved, and temperature-dependent parameters are updated accordingly. When convergence is reached, the algorithm is stopped, and the solution of amplification is determined. The principal schematic drawing of the algorithm is displayed in 2.17.
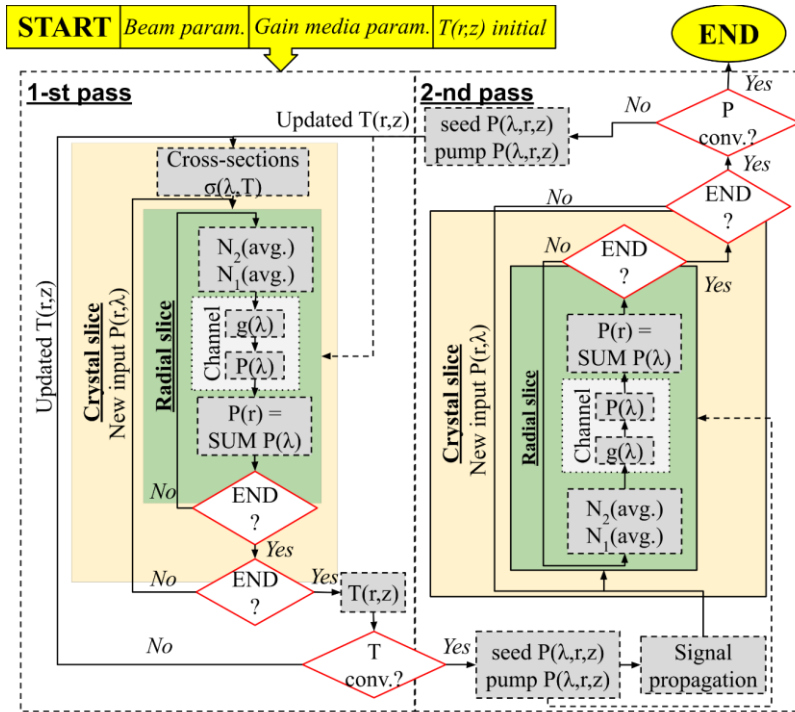
Fig. 2.17 Schematic drawing of the iteration algorithm for solving signal beam amplification in the end-pumped Yb:YAG gain medium.

2.9. Experimental validation

In this section, a series of experiments that were carried out to validate the numerical model are presented. The optical setup used for the experiments is shown in Fig. 2.18.
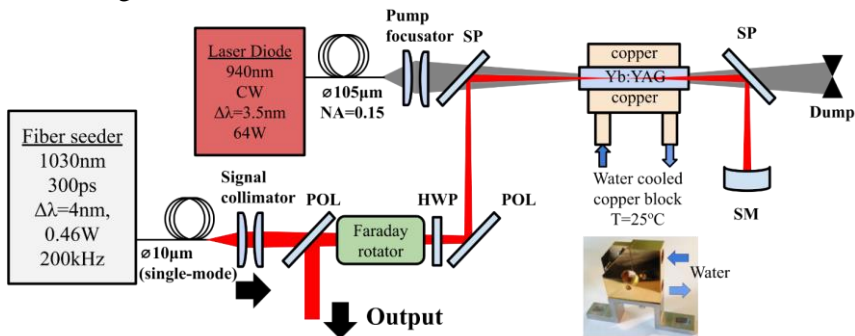
Fig. 2.18 Principal layout of the experimental setup for model validation. Fiber seeder was used as a seed source, emanating temporarily chirped $300\,ps$ pulses at $\lambda_s = 1030\,nm$ ($\lambda(FWHM) = 4\,nm$) with a maximum power of $P_s = 0.46\,W$. The pulse repetition rate was set to $200\,kHz$. Fiber-coupled (core diameter $105\,\mu m$, $NA = 0.15$) laser diode was used as a pump source, with maximum power $P_p = 64\,W$ ($\lambda_p = 940\,nm$, $\lambda(FWHM) = 3.5\,nm$). POL – polarizer, HWP – half-wave plate, SP – pump and signal beam separator, SM – spherical

64

mirror for signal beam returning. **Inset:** actual Yb:YAG crystal as mounted in the copper block with silicone interface. Cooling water runs a loop around the crystal, as is shown in the inset.

Two different geometry and doping concentration of c-cut ([111]) Yb:YAG crystals were tested: (1) $2x2x20\ mm^3$ with Yb^{3+} doping concentration of 2%, and (2) $2x2x13\ mm^3$ with Yb^{3+} doping concentration of 3.6%. Crystals featured square aperture and were mounted into copper blocks. Each copper block consisted of two L-shaped copper parts, which, when connected, formed a square hole, with the aperture size matching the crystal aperture size, and the length of the hole slightly shorter than the length of the crystal (Fig. 2.17). Thin silicone layer was applied on the inside surface of the hole prior to mounting the crystal. The gain medium was then carefully placed onto one of the L-shape parts, and then the second L-shape part was connected so that the gain medium was evenly pressed from all the side surfaces. The interface between crystal and copper was high-thermal conductivity silicone ($k_I = 1.49\ W/(m \cdot K)$.) with $100\ \mu m$ thickness (measured under the microscope). The fiber seeder coupled to a single-mode fiber (core diameter was $10\ \mu m$) was used as a seed source for end-pumped Yb:YAG amplifier. It generated the maximum output power of $0.46\ W$ at $1030\ nm$ central wavelength with a spectral bandwidth of $4\ nm$ at a full-width half-maximum intensity level (FWHM). Signal pulses emanating from the fiber seeder were temporarily chirped to $300\ ps$. The pulse repetition rate of the fiber seeder was set to $200\ kHz$. Continuous-wave (CW) fiber-coupled (core diameter $105\ \mu m$, $NA = 0.15$) laser diode was used as a pump source. It emanated the maximum power of $64\ W$ at $940\ nm$ central wavelength with a spectral bandwidth of $3.5\ nm$ at FWHM.

Signal and pump beams were tightly focused to beam diameters of $0.4\ mm$ and overlapped in the crystal rod. The resulting unabsorbed pump power was outcoupled via separator SP and dumped, whereas the signal beam was reflected and directed to spherical convex mirror SM with radius $R = -50\ mm$, which returned the signal beam via same optical path for double-pass configuration. The signal beam was outcoupled from the double-pass amplifier via polarization, as is seen in Fig. 2.18.

The output power and signal gain dependency in 1-pass and 2-pass configuration versus input signal power were measured. Additionally, resulting unabsorbed pump power was registered (at maximum input signal power). Furthermore, output power at maximum input signal power dependency on crystal cooling temperature was measured in the range of 15℃ to 35℃ to validate spectroscopic transition cross-section dependency on temperature influence on amplification. To validate thermo-optic coefficient

influence on the change of beam focusing and intensity distribution, beam cross-section and its dependency on propagation distance were measured at the output of crystal rod (after single-pass). Additionally, the value of pump-induced thermal-lens was measured via the z-scan method (by registering the change in the beam caustic). All experimental results were plotted against modeling data. Parameters used for the experiments and modeling are provided in Table 2.2.

Table 2.2 Modelling and experimental parameters and material properties of end-pumped Yb:YAG crystal rod.

	Symbol	Value	Unit	Ref.
Signal wavelength	λ_s	1030	nm	
Signal spectral width @ FWHM	$\lambda_s(FWHM)$	4	nm	
Signal power	P_s	0-0.46	W	
Signal beam diameter @ $1/e^2$ level	ω_s	0.4	mm	
Pump wavelength	λ_p	940	nm	
Pump spectral width @ FWHM	$\lambda_p(FWHM)$	3.5	nm	
Pump power	P_p	64	W	
Pump beam diameter @ FWHM	ω_p	0.4	mm	
Absorption cross-section at λ_s	$\sigma_{abs}(\lambda_s)$	Fig. 2.11		[47]
Emission cross-section at λ_s	$\sigma_{ems}(\lambda_s)$	Fig. 2.11		[47]
Absorption cross-section at λ_p	$\sigma_{abs}(\lambda_p)$	Fig. 2.12		[47]
Emission cross-section at λ_p	$\sigma_{ems}(\lambda_p)$	Fig. 2.12		[47]
Unperturbed refractive index	n_0	1.82		
Thermo-optic coefficient	$\delta n/\delta T$	Fig. 2.13		[48]
Thermal conductivity	k	Fig. 2.14		[49]
Excited state lifetime	τ	1.0	ms	[100]
Density of Yb^{3+} ions	N_t	1.3745	10^{26} m^{-3}	[101]
Rod length	L	13 & 20	mm	
Rod width & height	a	2	mm	

Experimental and modeling amplification data in case of $2x2x20\ mm^3$@2.0% Yb:YAG crystal for single- and double-pass are displayed in Table 2.3.

Table 2.3 Modelling and experimental amplification results for $2x2x20\ mm^3$@2.0% Yb:YAG crystal rod for single- and double-pass configurations. **From top to bottom:** output power dependency on input signal power; signal gain dependency on input signal power (logarithmic scale); output power dependency at maximum input signal power on crystal copper block cooling temperature.

Yb:YAG $2x2x20\ mm^3$@2.0%	
1-st pass	2-nd pass

Pump unabsorbed at max. signal power
($T = 25°C$): (experiment) **4.90W**;
(model) **6.73W**

Pump unabsorbed at max. signal power
($T = 25°C$): (experiment) **3.96W**;
(model) **5.50W**
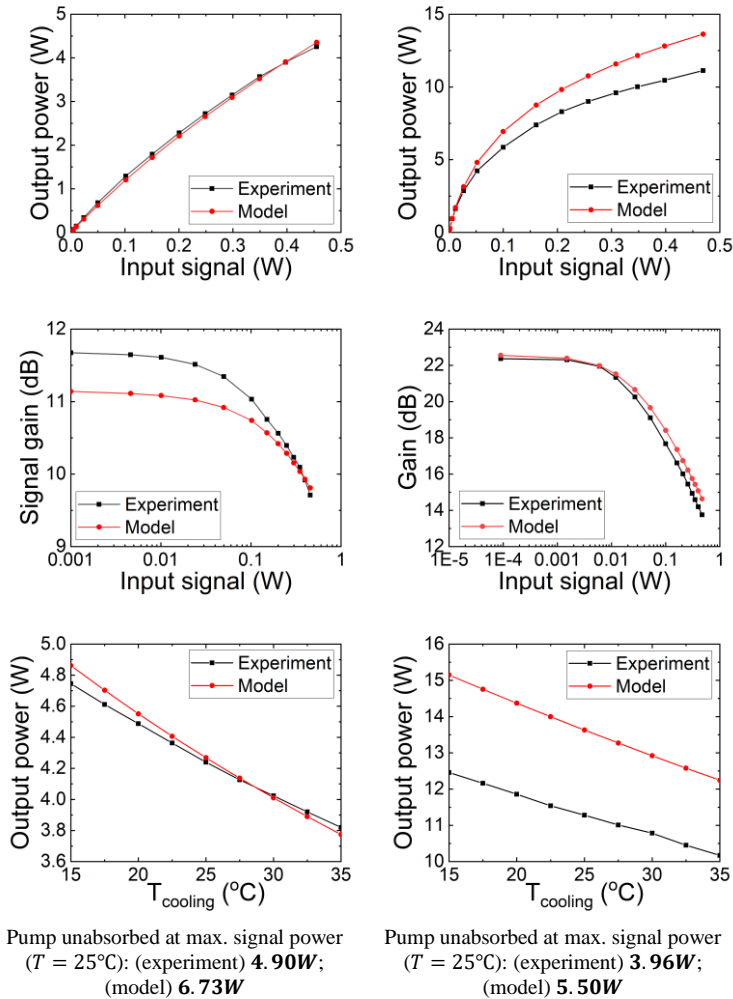
Results indicated an almost perfect match between experimental and modeling amplification in a single-pass regime when input signal power is at the maximum value ($0.46\,W$). Unabsorbed pump power as measured in the experiment was $4.9W$ whereas modeling predicts $6.73W$ (absorbed pump power difference was 2.8%), which also matches well. The small-signal amplification regime modeling predicted somewhat lower amplification than was measured in the experiment (by 5%), however, the error margin is well within tolerable levels. Furthermore, the output power dependency on crystal holder cooling temperature also showed well-match to modeling data. This trend is also similar between experimental and modeling data in the double-pass regime.

In the double-pass regime, at the highest values of input signal power, the model predicts higher amplification than measured in the experiment by 12%, whereas the small-signal gain value differed by 3%. Absolute transition cross-section values or actual doping concentration of Yb:YAG crystal (used in the experiment) might be the cause, as measured unabsorbed pump power in double-pass regime was $3.96\,W$ as compared to modeling value of $5.5\,W$ (difference of absorbed pump power in crystal rod is 2.4%). This indicates possibilities that either: (1) absolute pump absorption cross-section value is higher and signal emission cross-section value is lower, or (2) crystal doping concentration is higher, but signal emission cross-section value is still lower. Additional effects, such as fluorescence heating of crystal rod, could be the cause, which increases overall crystal temperature, thus lowering amplification. As this effect was not considered in the model, no data is provided. However, it was decided not to tune modeling parameters to fit experimental data as that requires careful re-estimation and re-analysis of various experimental and modeling parameters (e.g., actual crystal doping concentration, measurement of spectroscopic cross-sections, etc.), which was not the scope of this thesis. Despite this, the overall precision of modeling was more than satisfactory.

Amplified signal beam propagation after single-pass was characterized via the z-scan technique. The amplified signal beam was separated from the unabsorbed pump beam, collimated with lens, and refocused with an additional lens. The CCD camera was translated at finite propagation steps near signal waist position, and beam intensity cross-section at each step was captured. The optical setup for this task is displayed in Fig. 2.19.
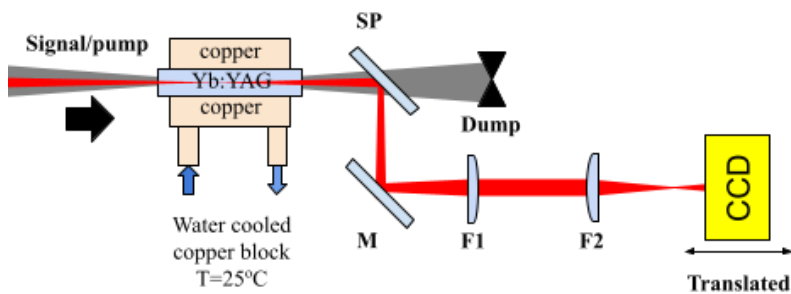
Fig. 2.19 Optical layout for beam characterization via z-scan technique after single-pass. Distance from fiber to the collimating lens $F_1 = +500\,mm$ was $660\,mm$, distance between lenses $770\,mm$, focusing lens $F_2 = +200\,mm$, distance from the lens to waist position $180\,mm$ (z-scan performed in this region). SP is a signal/pump beam separator, M is a mirror with a high-reflection coating for signal beam, CCD is a camera used for beam cross-section recording.

The results of the z-scan measurement are displayed in Table 2.4. The value of pump-induced thermal-lens was also measured via the z-scan method, by registering the change in the beam caustic (Fig. 2.20).

Table 2.4 Beam intensity cross-section as measured via z-scan technique at different propagation distances (black curve). The red curve indicates modeling data. Insets indicate propagation distance near waist position, where $0\ mm$ indicates waist position.

Yb:YAG $2x2x20\ mm^3$@2.0%

Fig. 2.20 The results of thermal lens measurement at different pump power (top axis) and corresponding crystal heating power due to the quantum defect (bottom axis). The black curve indicates experimental data, and the red curve indicates the modeling data. Maximum pumping power directed to the crystal rod was $64\ W$.

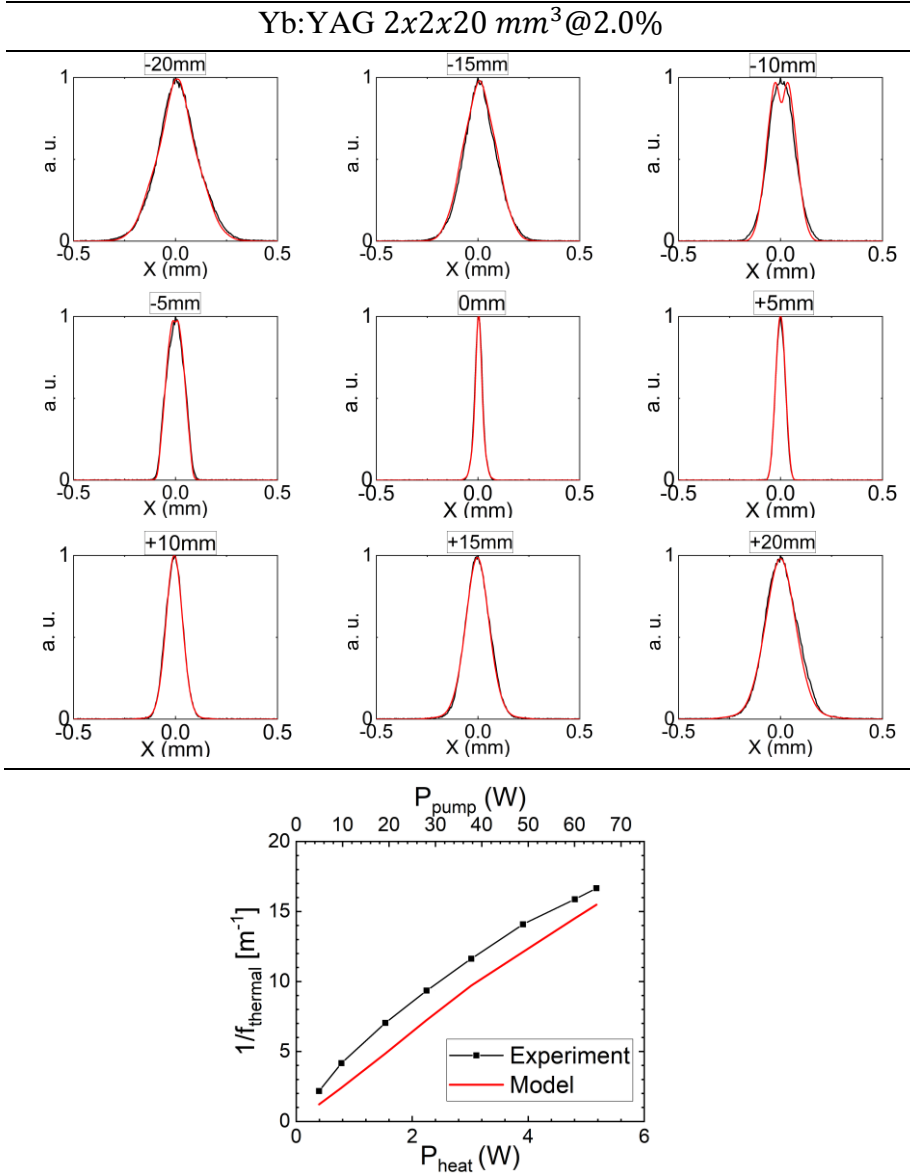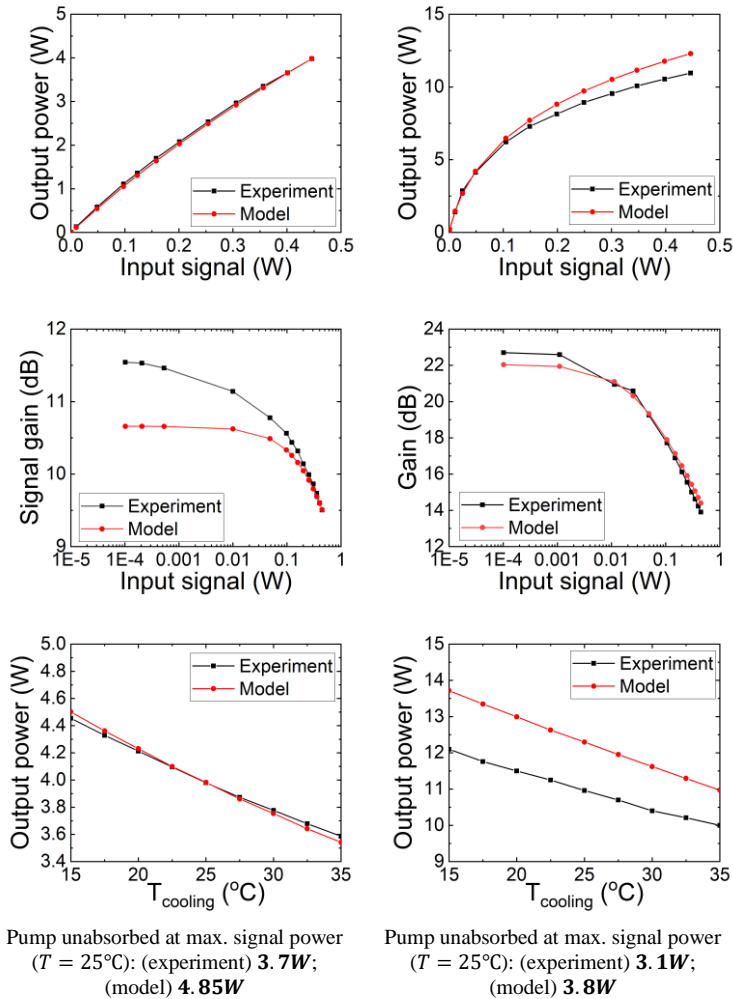Beam intensity cross-section degradation due to the amplification and thermal-lensing effects are well reflected in the modeling data. One beam intensity cross-section feature, which was not measured in the actual experiment and was predicted in the model, was a "dip" at the peak of intensity cross-section, which can be seen at propagation position of $-10\ mm$ (Table 2.4). Modeling indicated that tuning of temperature dependency of $\frac{dn}{dT}(T)$ would resolve this issue, and a nearly perfect match to experimental data would be achieved.

The modeling prediction of the thermal lens value slightly differed from the experimental results ($\sim 8\%$ at $64\ W$ of pump power), indicating that the thermo-optic coefficient $\frac{dn}{dT}$ and thermal conductivity k could be slightly off. In the model I have used the values of $\frac{dn}{dT}$ for an undoped YAG crystal, whereas the values of k were for the Yb:YAG crystal with 2 % doping (Fig. 2.13 and Fig. 2.14), which could explain the observed difference, mainly due to the used values of $\frac{dn}{dT}$. Unfortunately, at the time of modeling, the only values of $\frac{dn}{dT}$ dependence on temperature were found for undoped YAG crystal, hence they were used. Additionally, in the model I didn't include the influence of mechanical deformations (end-bulging) on the thermal lens [45]. This effect is quite important, but the architecture of my program didn't allow for an easy integration of such an effect. However, the overall modeling predictions of the thermal lens were satisfactory, nonetheless.

Identical measurements and modeling were performed for $2x2x13\ mm^3$@3.6% Yb:YAG crystal. Results are displayed in Table 2.5 and Table 2.6.

Table 2.5 Modelling and experimental amplification results for $2x2x13\ mm^3$@3.6% Yb:YAG crystal rod for single- and double-pass configurations. **From top to bottom:** output power dependency on input signal power; signal gain dependency on input signal power (logarithmic scale); output power dependency at maximum input signal power on crystal copper block cooling temperature.

Yb:YAG $2x2x13\ mm^3$@3.6%	
1-st pass	2-nd pass

Pump unabsorbed at max. signal power
($T = 25°C$): (experiment) **3.7W**;
(model) **4.85W**

Pump unabsorbed at max. signal power
($T = 25°C$): (experiment) **3.1W**;
(model) **3.8W**

Comparison of modeling and experimental data showed similar differences to previously analyzed crystal. In single-pass configuration, the small-signal gain value differed by 7%. Unabsorbed pump power as measured in the experiment was 3.7 W whereas modeling predicts 4.85 W (absorbed pump power difference 1.8%), which also matched well. The trend of output power dependency on crystal holder cooling temperature is also similar between experimental and modeling data for both – single and double-pass regimes.

In the double-pass regime, at the highest values of input signal power, the model predicts higher amplification than measured in the experiment by 12%. The measured unabsorbed pump power was 3.1 W as compared to modeling value of 3.8 W (difference of absorbed pump power in crystal rod is 1.1%). The small-signal gain value difference was 3%. Overall, modeling prediction

of amplification was like the previous crystal, indicating sufficient precision of calculations.

Results of z-scan measurement after single-pass are displayed in Table 2.6.

Table 2.6 Beam intensity cross-section as measured via z-scan technique at different propagation distances (black curve). The red curve indicates modeling data. Insets indicate propagation distance near waist position, where $0\ mm$ indicates waist position.

Yb:YAG $2x2x13\ mm^3$@3.6%
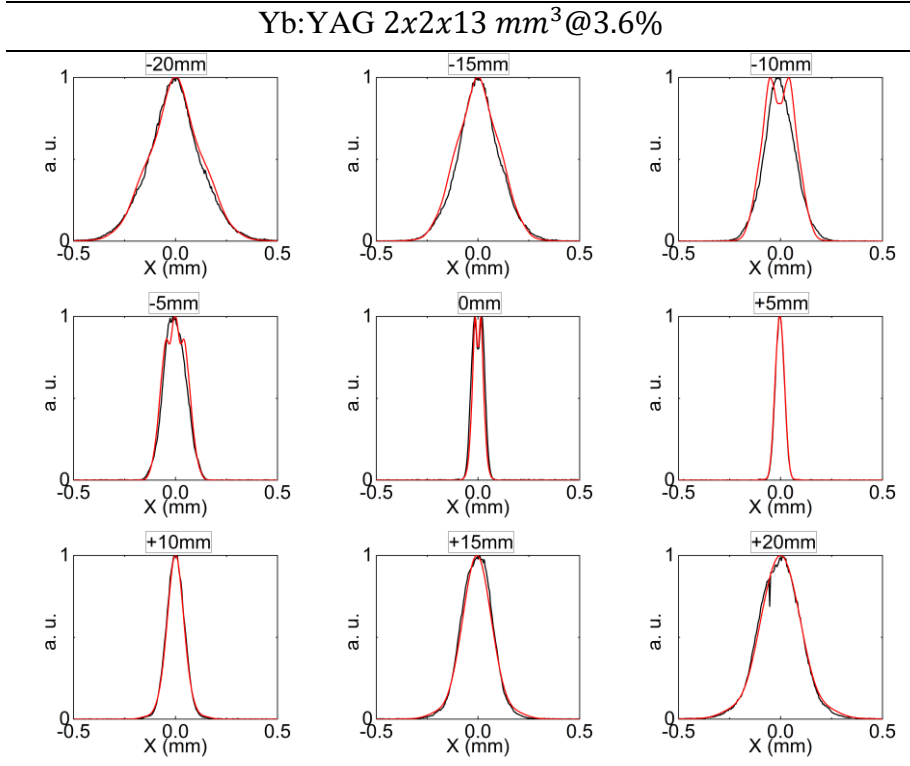
Modeling data fits well on experimentally measured intensity cross-sections at different beam propagation distances. Artificial feature, as seen at a distance $-10\ mm$ (Table 2.6) was still present (as discussed above in the case of the previous crystal). Overall, model performance is satisfactory and identical to the previous crystal.

Spectral width narrowing due to gain narrowing effect was analyzed in the case of $2x2x20\ mm^3$@2% Yb:YAG crystal. Spectral width was measured experimentally with a spectrum analyzer at different signal gain values in single- and double-pass regimes. In the model, it was assumed that signal spectral shape was ideal Gaussian, which is close to experimental observations. Experimental data were compared to modeling results and are displayed in Fig. 2.21.
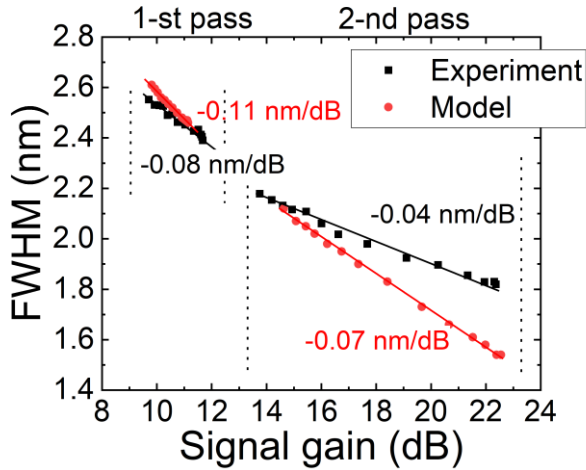
Fig. 2.21 Spectral width at FWHM dependency on the signal gain in single- and double-pass regimes. In this experiment $2x2x20\ mm^3$@2% Yb:YAG crystal was used. Inset numbers in (nm/dB) indicate the slope of each curve. Input signal spectrum FWHM is $4\ nm$.

Results show similar absolute spectral width values at different signal gain values. However, the dependency slope is different – in the single-pass regime, the slope is $-0.08\ nm/dB$ for experiment and $-0.11\ nm/dB$ for the model. In the case of the double-pass regime, these values are $-0.04\ nm/dB$ and $-0.07\ nm/dB$ correspondingly. It must be noted that in the experiment, the whole beam was fed into the spectrum analyzer, and an averaged spectrum across the whole beam was measured. In modeling data, the case is different – plotted values in Fig. 2.21 are for beam peak intensity cross-section position, where the gain is naturally the highest, resulting in the biggest change of spectral width due to signal gain. If, for example, in a single-pass regime, modeled spectrum values are taken as an average between spectral width at beam peak intensity cross-section position and at $1/e^2$ position, the slope would yield $-0.06\ nm$ trend, which is closer to the experimental data. However, to achieve maximum precision, each spectral shape at every beam's intensity cross-section value of the modeled beam must be considered and averaged. This was not attempted in this thesis, as an overall result is well-matched to experimental data, and additional calculations would make the model unnecessarily complex.

2.10. Summary

In this section, the description of the physical model for the end-pumped double-pass Yb:YAG amplifier was presented. To validate the model experimentally, different Yb:YAG crystal configurations were used -

$2x2x20\ mm^3$ with Yb^{3+} doping concentration of 2%, and $2x2x13\ mm^3$ with Yb^{3+} doping concentration of 3.6%, which were end-pumped by $64\ W$ of the pumping power (pump diameter $0.4\ mm$), and seeded by the maximum signal power of $0.46\ W$ (signal diameter $0.4\ mm$). In both cases, the error between experimental and modeling amplification values was below 7% in the small-signal gain regime and below 12% in the high input signal power regime. It was discussed that errors most likely arise due to the selection of modeling parameters, such as transition cross-section, thermo-optic coefficient, and thermal conductivity values and their dependency on temperature. Additionally, analysis and comparison of the experimental beam propagation characteristics (including thermal lens) after the end-pumped Yb:YAG amplifier showed a good-match to modeling data – beam degradation features due to amplification and thermal effects were sufficiently reflected in the modeling results. It was discussed that the slight offset of the measured and modeled thermal lens value (~8% difference at $64\ W$ of pump power) was mainly due to the used thermo-optic coefficient $\frac{dn}{dT}$ values – these values were taken for an undoped Yb:YAG crystal, since only such a dependence on the temperature was found in the literature at the time. Finally, investigation of gain narrowing effect due to amplification was also well predicted by model – spectral width at FWHM was reduced from $2.6\ nm$ to $1.8\ nm$ in experimental measurements (signal gain range of $9.5 - 22.5\ dB$), and from $2.7\ nm$ to $1.5\ nm$ in numerical calculations. In conclusion, the presented physical model for the end-pumped double-pass Yb:YAG amplifier proved to be a sufficiently accurate tool for numerical calculations.

3. Numerical optimization of the double-pass Yb:YAG DPSS amplifier

3.1. Introduction

This chapter is dedicated to numerical optimization of the end-pumped double-pass Yb:YAG bulk crystal amplifier configuration that would act as a base for experimental development of GW level peak power laser system. Optimization of crystal length, active ion doping concentration, beam focusing parameters are performed, and the influence of signal spectral parameters are investigated. Useful insights and discussions for similar systems development are also provided. All numerical simulations are based on developed modeling software described in Chapter 2.

The central wavelength of signal radiation was chosen to be $\lambda_s = 1030\ nm$ with a spectral width of $\Delta\lambda_s = 4\ nm$ (Gaussian shape), which corresponds to transform-limited Gaussian pulse with a duration of $\tau_{TL} = 390\ fs$. The spectral width of signal radiation was chosen to be around half of the emission bandwidth of Yb:YAG (see Table 1.1) to avoid a large influence of gain narrowing effect, but with sufficient bandwidth for the possibility to compress amplified pulses to sub-ps duration. The influence of signal spectral width and central wavelength on amplification characteristics is also discussed later in this chapter. Signal average power was varied depending on the task reviewed but initially was set to a lo0w value for the realization of a small-signal gain regime.

Pump power and beam size was varied to realize different pump intensities in the range of $I_p = 25\ldots125\ kW/cm^2$, which is sufficient to cover the practical pumping intensity range for the end-pumped systems [74,75]. Other parameters for pump radiation were based on commercially available fiber-coupled diode model from *nLight*, except for numerical aperture, which was experimentally measured to be $NA = 0.15$ (see Fig. 2.9 in Chapter 2). Central wavelength for pump radiation was set to $940\ nm$ instead of zero-phonon line at $969\ nm$, because the narrow width of zero-phonon line makes it impractical for diode pumping [102,103].

As discussed in Chapter 2, the interface between the crystal and heatsink was chosen to be silicone with a practical thickness of $\delta = 100\ \mu m$, which corresponded to the achieved values in experiments. Heatsink temperature was constant with the value $T_c = 25°C$ (boundary condition).

To realize the double-pass configuration for signal beam, a convex spherical mirror with a specific radius of curvature R was placed at the

required distance L_x from the crystal to compensate a thermal lens of the end-pumped Yb:YAG gain medium. Values of R and L_x for each modeling configuration were chosen to be equal to the focal length of the thermal lens. In such a configuration, the signal beam is relay-imaged back to the crystal. Pump beam experiences only a single pass through Yb:YAG crystal. Beam sizes for signal and pump beams was chosen to be equal.

A principal schematic of the double-pass amplifier under optimization is shown in Fig. 3.1, and a summary of the initial parameters is provided in Table 3.1.
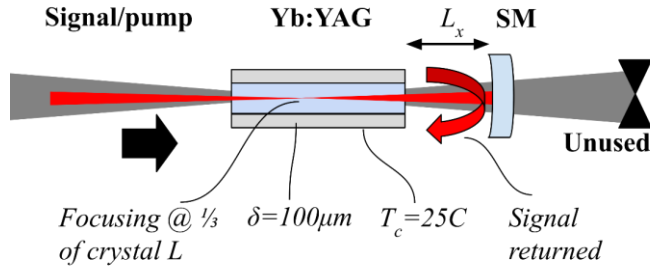

Fig. 3.1 The principal schematic of the double-pass Yb:YAG amplifier under consideration. Red line indicates signal beam propagation, grey line – pump beam. *SM* is a convex spherical mirror with specific radius R, and placed at required L_x distance (for thermal lens compensation) to correctly image signal beam back to the crystal. Both signal and pump beams are focused at 1/3 of crystal length L. The thickness of the interface between crystal and heatsink was chosen to be $\delta = 100\ \mu m$. Heatsink temperature is $T_c = 25°C$ (boundary condition).

Table 3.1 Modelling parameters and material properties for double-pass Yb:YAG amplifier under consideration.

	Symbol	Value	Unit
Signal wavelength	λ_s	1030	nm
Signal spectral width @ FWHM	$\lambda_s(FWHM)$	4	nm
Signal power	P_s	varied	W
Signal beam diameter @ $1/e^2$ level	ω_s	varied	mm
Pump wavelength	λ_p	940	nm
Pump spectral width @ FWHM	$\lambda_p(FWHM)$	3.5	nm
Pump power	P_p	100	W
Pump beam diameter @ FWHM	ω_p	varied	mm
Pump radiation numerical aperture	NA	0.15	-
Absorption cross-section at λ_s	$\sigma_{abs}(\lambda_s)$	Fig. 2.11	
Emission cross-section at λ_s	$\sigma_{ems}(\lambda_s)$	Fig. 2.11	
Absorption cross-section at λ_p	$\sigma_{abs}(\lambda_p)$	Fig. 2.12	
Emission cross-section at λ_p	$\sigma_{ems}(\lambda_p)$	Fig. 2.12	
Unperturbed refractive index	n_0	1.82	-
Thermo-optic coefficient	$\delta n/\delta T$	Fig. 2.13	

Thermal conductivity	k	Fig. 2.14	
Excited state lifetime	τ	1.0	ms
Density of Yb^{3+} ions	N_t	1.3745	10^{-26} m^{-3}
Ions doping concentration	X	varied	%
Rod length	L	varied	mm
Rod width & height	a	2	mm
Thermal conductivity of interface layer	k_I	1.5	W/(m K)
Thickness of interface layer	δ	100	μm
Heatsink temperature (boundary condition)	T_c	25	ºC
Spherical mirror radius of curvature	R	varied	mm
Distance between crystal and spherical mirror	L_x	varied	mm

3.2. Crystal length and doping concentration optimization

In a quasi-three-level system, pump absorption and signal reabsorption need to be balanced against each other since too high doping levels or too long gain medium would lead to excessive reabsorption losses [104]. This section is thus dedicated to crystal length and ion doping concentration optimization, which corresponds to the highest gain. General parameters are taken from Table 3.1. Modeling is performed for several different pump intensity values, where pump beam diameter and pump power are varied correspondingly. The ratio of pump and signal beam size was fixed to 1 (identical). Initially, signal beam power was fixed at the level which corresponded to a small-signal gain (SSG) regime. At each modeled configuration, spherical mirror radius R and its distance to the crystal L_x is adjusted to account for thermal lens. Modelling parameters of interest that were covered in this section are displayed in Table 3.2.

Table 3.2 Modelling parameters for crystal length and doping concentration optimization.

	Symbol	Value	Unit
Signal/pump beam diameter at 4-sigma level (signal Gaussian, pump flat-top)	ω_s, ω_p	0.2; 0.3; 0.4; 0.5	mm
Signal power for SSG regime	P_{SSG}	1	μW
Pump beam intensity (flat-top)	I_P	25; 50; 75; 100; 125	kW/cm^2
Spherical mirror radius of curvature	R	varied	mm
Distance between crystal and spherical mirror	L_x	varied	mm

Signal gain maps at different pump intensities with varied pump/signal beam diameters were calculated at the SSG regime. An illustratory example with pump intensity of $I_P = 75\ kW/cm^2$ is shown in Fig. 3.2.
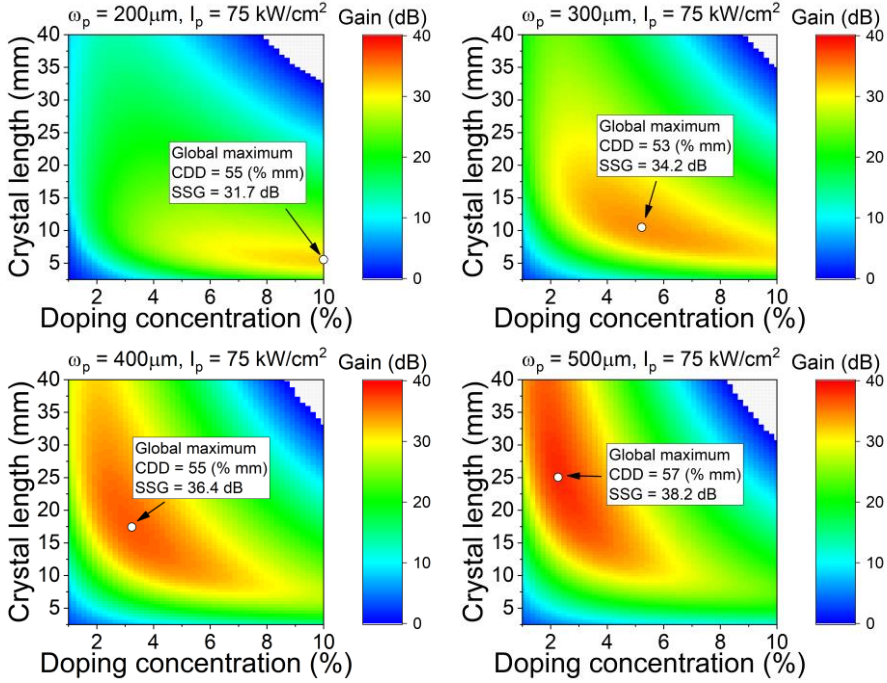

Fig. 3.2 Numerical calculation results of gain dependency on the combination of crystal length and doping concentration at pump intensity of $I_P = 75\ kW/cm^2$. From top to bottom – results retrieved for an increased increment of pump and signal beam diameters (displayed as title for each graph). White circles with an arrow pointing to them pinpoint global optimum (in terms of gain) at specific configuration. A grid of 10x16 (doping concentration x length; 160 points) was retrieved, and intermediary points were interpolated with spline function to the total grid of 50x80. CDD corresponds to the product of doping concentration and crystal length (columnar doping density). A white dotted area depicts a configuration where the signal is absorbed instead of amplified.

The first observation when varying doping concentration X and crystal length L was that almost identical product of $X \times L$ at fixed pump intensity corresponded to the global gain maximum at each modeled pump beam diameter. Therefore the so-called area or columnar doping density CDD is introduced, which is then the main parameter in the context of optimizing signal gain at different pump intensities, independently on pump beam diameter [104]. Gain maps were retrieved for other pump intensities (see Table 3.2). Parameter CCD dependence on pump intensity at different pump beam diameters is shown in Fig. 3.3.
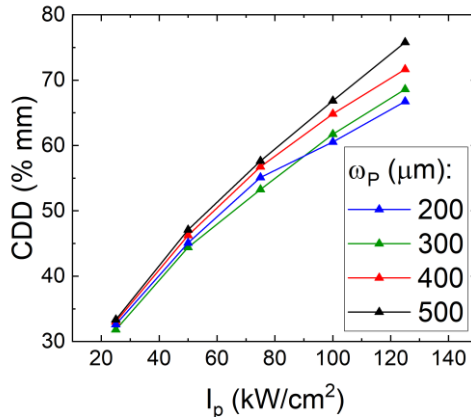
Fig. 3.3 Columnar doping density (CDD) dependence on pump intensity at different modeled pump beam diameters. Signal beam diameter was equal to pump beam diameter in each case.

Retrieved results indicated that optimal parameter CDD increased with increasing pump intensity – from 32 at $I_P = 25 \ kW/cm^2$ to around 70 at $I_P = 125 \ kW/cm^2$. This increment of CDD can be explained as follows. Firstly, high pump intensity contributes to a significant degree of excitation of the amplifier medium active ions. Thus, the absorption is then saturated to some extent, simply because the density of ions in the ground state, from where they can absorb light, is depleted. Secondly, higher absorbed pump power leads to temperature rise in the gain medium, reducing pump absorption cross-section (see Chapter 2). To overcome this, longer crystal or higher doping concentration is thus needed.

Another observation from modeling was that essentially higher gain could be achieved with a larger pump beam diameter at identical pump intensity. This is due to finite brightness of pump radiation – larger pump beam diameter is less divergent, thus leading to relatively higher pump intensity along the gain medium.

Furthermore, in a quasi-three-level system, pump absorption and signal reabsorption need to be balanced against each other since too high doping level or too long crystal leads to excessive reabsorption losses (Fig. 3.2, white dotted areas). Typically, crystal length and doping concentration had to be optimized to leave around 5% of unabsorbed pump power at the output of gain medium.

Additionally, optimal crystal length dependency on pump beam diameter for each different pump intensity level was retrieved, and results are shown in Fig. 3.4.
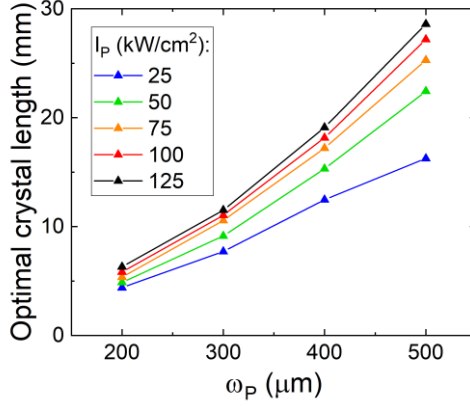
Fig. 3.4 Optimal crystal length dependence on pump beam diameter ω_P at different pump intensities I_P.

These results show that even though optimal parameter $CDD = L \cdot X$ is mainly dependent on pump intensity level, optimal crystal length L still depends on pump beam diameter ω_P. Short optimal crystal length corresponds to a small pump beam diameter. This is mainly due to the divergence of the pump beam, which limits the effective length of the crystal within which sufficient pump intensity is maintained to achieve transparency and amplification at the signal wavelength. It was found that the optimal ratio of crystal length L and pump Rayleigh length z_R is in the range of $L/z_R \sim 2 - 3$. This ratio increases with increasing pump intensity.

It must be noted that such optimal parameter scan was performed when input signal power is low, corresponding to the small-signal gain regime. However, in practice, input signal power is usually set higher to achieve practical output power. At high input signal power, considerable Yb^{3+} upper-state manifold depletion happens, leading to an increase of pump power absorption due to the three-level nature of Yb^{3+} ions. Thus, optimal parameter CDD becomes lower – either crystal length or active ions doping concentration should be reduced to counter increased pump absorption.

Input signal power was thus set to saturation power P_{sat} at each modeled signal beam diameter (coincides with modeled pump beam diameter), which determines the amount of input power of an amplifier required for achieving most of the possible output power. Pump intensity was varied in the range $I_P = 25 - 125 \ kW/cm^2$, and pump beam diameter was again varied in the range $\omega_P = 200 - 500 \ \mu m$. Crystal length L was set to the optimum global value found in the previous modeling in the SSG regime. Optimal parameter CDD was calculated at each pump intensity by changing crystal doping

concentration X to avoid the influence of pump beam divergence. Results are shown in Fig. 3.5.
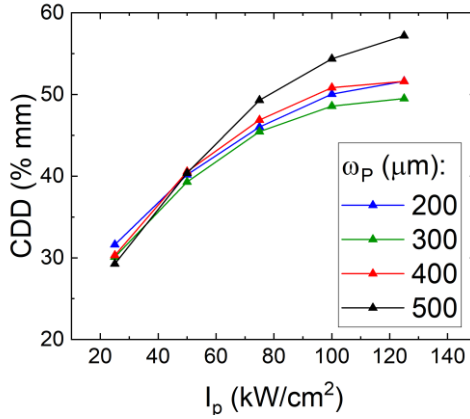

Fig. 3.5 Columnar doping density (CDD) dependence on pump intensity at different modeled pump beam diameters. Signal beam diameter was equal to pump beam diameter in each case. Signal power was set to signal saturation power at each modeled signal beam diameter: $P_{sat} = 1.3; 2.9; 5.2; 8.1\ W$ at signal/pump beam diameter of $\omega = 200; 300; 400; 500\ \mu m$.

As expected, the observation when varying doping concentration X at previously optimized crystal length L with input signal power set to saturation power was that the optimal parameter CDD was noticeably lower compared to the case when input signal power is low (small-signal gain regime). Additionally, such impact is greater at higher pump intensities - at $I_P = 25\ \frac{kW}{cm^2}$ the difference is between $CDD = 32\ (\%\ mm)$ and $CDD = 30\ (\%\ mm)$ (~6.7 % difference), whereas at $I_P = 125\ \frac{kW}{cm^2}$ $CDD = 70\ (\%\ mm)$ and $CDD = 51\ (\%\ mm)$ (~27.1 % difference). The reason is that at high pump intensity, larger relative excitation of the amplifier medium active ions happens. This leads to a relatively larger change in increased pump absorption along the gain medium in the case when input signal power is sufficient to deplete the population inversion. Therefore, crystal doping concentration (or crystal length) must be reduced more at high pump intensities to avoid amplified signal reabsorption at the end of the pumped crystal (due to insufficient pump intensity to reach transparency at signal wavelength), leading to a larger decrease in optimal parameter CDD.

In conclusion, with the help of numerical modeling, guidelines for optimal crystal length and doping concentration combination were deduced, in the case of an end-pumped Yb:YAG gain medium pumped at $940\ nm$ wavelength and seeded at $1030\ nm$ wavelength. Investigated pump intensity values were

in the range of $I_P = 25 - 125 \frac{kW}{cm^2}$, and pump diameter values were in the range of $\omega_P = 200 - 500 \, \mu m$, which cover a truly wide and practical range of possible amplifier scenarios. Numerical investigation showed that parameter $CDD = L \cdot X$ conveniently describes the optimal gain medium configuration, as it is mainly dependent on pump intensity only. It was found that signal gain regime has an influence on determining optimal gain medium parameters – in the case when the input signal is weak (small-signal gain regime), the optimal parameter is $CDD = 32 - 70 \, (\% \, mm)$, and in the case when input signal power equals signal saturation power, such parameter becomes $CDD = 30 - 51 \, (\% \, mm)$ in the investigated pump intensity range. Furthermore, it was found that optimal crystal length correlates to the divergence of pump radiation. In described scenarios, the optimal ratio of crystal length and pump radiation Rayleigh length was found to be in the range of $L/z_R \sim 2 - 3$. In the author's opinion, such guidelines would prove to be useful in the preliminary determination of optimal parameters for the end-pumped Yb:YAG amplifier system.

3.3. Signal spectrum bandwidth considerations

In any gain media with finite gain bandwidth an amplified pulse spectrum inevitably changes. The primary reason for the amplified signal spectrum bandwidth change is the bandwidth reduction due to signal gain, the effect called "gain narrowing" [105,106]. This statement stands if nonlinear effects are not significant to cause spectral broadening due to self-phase modulation (SPM). The amount of gain narrowing is proportional to the total gain of the amplifier. The reason is that an amplifier with a finite gain bandwidth amplifies wavelengths at the peaks of its bandwidth with a higher probability than at "wings", thus resulting in signal bandwidth reduction. As a consequence, gain narrowing has a direct effect on the transform-limited pulse duration of the amplified signal.

As a figure of merit for numerical estimation, the ratio of initial and amplified signal transform-limited pulse duration $\frac{\tau_{in}}{\tau_{out}}$ was chosen, assuming that the initial signal pulse is unchirped. If we consider initial pulse is amplified by total gain Γ in an amplifier with a Lorentzian atomic transition with bandwidth $\Delta\omega$, the resulting amplified signal transform-limited pulse duration τ_{out} can be expressed as [99]:

$$\tau_{out} = \sqrt{\tau_{in}^2 + \frac{16 \ln 2 \ln \Gamma}{\Delta\omega^2}}, \tag{3.1}$$

$$\Delta\omega = \frac{2\pi c \Delta\lambda}{\lambda_0{}^2}, \tag{3.2}$$

where $\Delta\lambda \approx 5.3\ nm$ (at FWHM) is the effective gain bandwidth of Yb:YAG [28], λ_0 is the center wavelength of input pulse, and c is the speed of light. Parameter $\frac{\tau_{in}}{\tau_{out}}$ dependency on initial transform-limited pulse duration, expressed in terms of bandwidth $\Delta\lambda$ (Gaussian pulse shape assumed), was calculated for several amplifier gain values Γ, and results are displayed in Fig. 3.6.
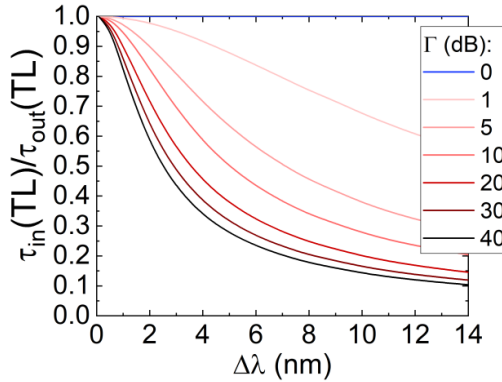

Fig. 3.6 Ratio of initial and amplified signal transform-limited pulse duration $\frac{\tau_{in}}{\tau_{out}}$ dependency on initial spectral bandwidth at FWHM level $\Delta\lambda$. Corresponding gain level Γ (in dB; constant across curve) is indicated in the legend.

Results indicate that in general, the most straightforward way to reduce gain narrowing effect arising in Yb:YAG amplifier is to: (1) operate in a low gain regime (e.g., choose sufficient initial signal intensity to operate in a highly saturated gain regime, by the use of pre-amplifiers), or (2) choose initial signal spectrum bandwidth as narrow as possible. In a more practical sense, to determine optimal initial signal spectral bandwidth for a wide range of gain regimes, transform-limited pulse duration of $< 1\ ps$ was chosen as a target, which is optimal for a number of applications, as reviewed in Chapter 1 of this thesis. In such case, when the initial signal bandwidth is $\Delta\lambda = 4.0\ nm$ (corresponds to $\tau_{TL} = 390\ fs$), the amplified signal transform-limited pulse duration is still within $< 1\ ps$ – in high gain $g = 30\ dB$ regime $\tau_{TL} = 1000\ fs$, and in low gain $g = 5\ dB$ regime this value is $\tau_{TL} = 546\ fs$. This indicates that the initial signal bandwidth of $\Delta\lambda = 4.0\ nm$ is optimal for operation in the sub-ps regime.

An interesting possibility to counter the gain narrowing effect is to shift the initial signal central wavelength from the peak emission line of the gain

medium [107]. In the case of Gaussian-shaped signal spectrum, an amplification dynamic could be reached when the peak part of the initial signal spectral is amplified by weaker part of Yb:YAG emission spectrum by the same amount as the lower spectral intensity part of the signal, which coincides with peak emission line of Yb:YAG. In such a case, larger initial bandwidth of signal could be preserved, leading to a somewhat weaker gain narrowing effect. However, the absolute value of gain would drop, but if the actual resulting peak power is taken as a figure of merit, a compromise could maybe be reached. As an illustration, numerical modeling of such central wavelength shifting was performed, and the resulting peak intensity change was recorded. Two extreme cases of signal gains were considered - 5 dB and 30 dB at initial signal Gaussian bandwidth of $\Delta\lambda = 4\ nm$ (at FWHM). Central wavelength was shifted in the range of $\lambda = 1020 \ldots 1040\ nm$.

At first, small-signal gain spectrum profiles $g_0(\lambda)$ for Yb:YAG at different excitation levels were calculated by [108]:

$$g_0(\lambda) = \sigma_e(\lambda)N_2 - \sigma_a(\lambda)N_1, \tag{3.3}$$

where σ_e, σ_a are emission and absorption cross-sections of Yb:YAG, and N_2, N_1 are population densities of the upper and lower manifolds. Excitation level is defined as $\beta = \frac{N_2}{N_T}$, where N_T is the total population density at a specified doping concentration. Spectrum profile $g_0(\lambda)$ for 1 % doping and at different excitation levels β is shown in Fig. 3.7.
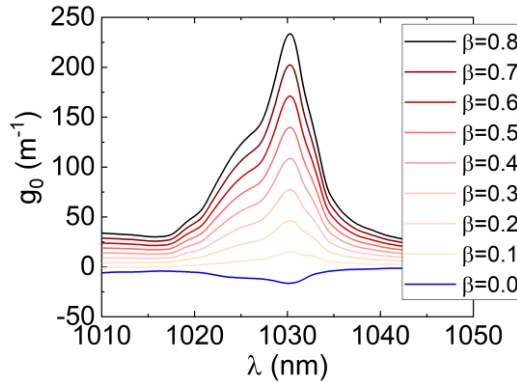

Fig. 3.7 Calculated small-signal gain spectrum $g_0(\lambda)$ of 1 % doped Yb:YAG for several excitation levels β. If $\beta = 0$, signal absorption is visible due to the three-level nature of Yb:YAG.

The resulting signal spectrum component amplification (in case of small-signal gain, no saturation) can then be expressed via amplification factor (gain) by [109]:

$$P(\lambda) = P_0(\lambda)\Gamma(\lambda) = P_0(\lambda)\exp(g_0(\lambda)dz), \qquad (3.4)$$

where $P_0(\lambda)$ is the spectral power of the initial signal, $P(\lambda)$ is the amplified spectral power of the signal, and dz is the length of the gain medium. Arbitrary excitation value of $\beta = 0.5$ was taken, and dz was varied so that different maximum gain values at peak emission line $\Gamma(\lambda = 1030\ nm)$ were retrieved. Resulting gain profiles $\Gamma(\lambda)$ at different maximum gain values (normalized to peak gain, expressed in times) are plotted in Fig. 3.8.
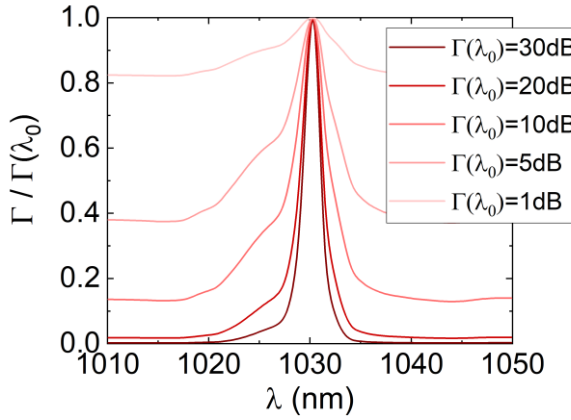

Fig. 3.8 Calculated amplification factor Γ (normalized to $\Gamma(\lambda_0)$; in times) profile at different gain values. Legend display gain values at λ_0, expressed in dB.

This, in principle, illustrates the gain narrowing effect – in the case of low signal gain, relative spectral gain across spectral components is more evenly distributed, whereas for high gain, only the band that corresponds to the peak emission line of Yb:YAG is effectively amplified.

Initial signal with Gaussian spectral shape with a bandwidth of $\Delta\lambda = 4\ nm$ (at FWHM), and peak centered at the wavelength range of $\lambda = 1020\dots1040\ nm$, was then fed to the gain media with different relative gain profiles at $\Gamma(\lambda_0) = 5;\ 30\ dB$ (low gain and high gain) and amplified. Resulting relative total gain values $\Gamma = \dfrac{P}{P_0}$ and spectral profiles were recorded. Amplified signal bandwidth-limited pulse duration was estimated by performing a Fourier transform of the amplified signal spectrum. At each case change in transform-limited pulse duration $\dfrac{\tau_{in}}{\tau_{out}}$, gain Γ (in times) and peak

power change $\gamma = \Gamma \frac{\tau_{in}}{\tau_{out}}$ (in times) was calculated. Relative change of such parameters depending on central wavelength shift and resulting spectrum profiles are displayed in Fig. 3.9 (high gain) and in Fig. 3.10 (low gain).
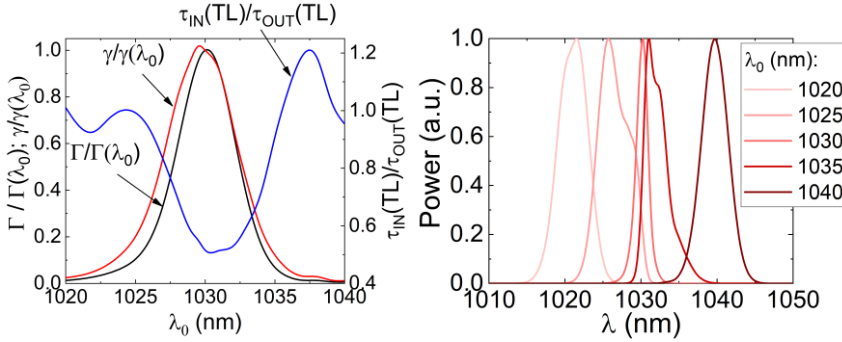

Fig. 3.9 <u>Left:</u> calculated amplification factor Γ (normalized to $\Gamma(\lambda_0)$; in times), peak power change factor γ (normalized to $\gamma(\lambda_0)$; in times) and pulse duration change $\frac{\tau_{in}}{\tau_{out}}$ dependency on central wavelength shift λ_0. $\Gamma(\lambda_0) = 459\ times\ (26.6\ dB)$, $\gamma(\lambda_0) = 236\ times\ (23.7\ dB)$. **<u>Right:</u>** amplified signal spectrum profiles at different central wavelengths.
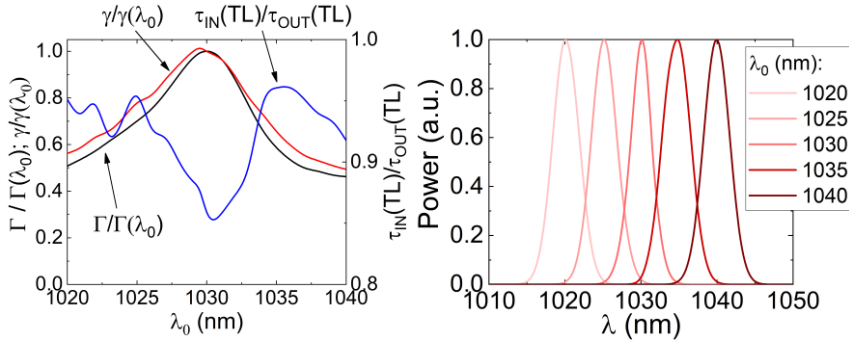

Fig. 3.10 <u>Left:</u> calculated amplification factor Γ (normalized to $\Gamma(\lambda_0)$; in times), peak power change factor γ (normalized to $\gamma(\lambda_0)$; in times) and pulse duration change $\frac{\tau_{in}}{\tau_{out}}$ dependency on central wavelength shift λ_0. $\Gamma(\lambda_0) = 2.64\ times\ (4.2\ dB)$, $\gamma(\lambda_0) = 2.27\ times\ (3.6\ dB)$. **<u>Right:</u>** amplified signal spectrum profiles at different central wavelengths.

Results indicate that slight shifting of central signal wavelength to $\lambda_0 = 1029\ nm$ would yield the same amount of peak power increase (due to broader preserved amplified signal bandwidth), even though gain itself drops. As an example, at high gain and at $\lambda_0 = 1029\ nm$, gain drops from $\Gamma(1030\ nm) = 459\ times$ to $\Gamma(1029\ nm) = 393\ times$, and resulting transform-limited pulse duration changes to $\tau_{out}(1030\ nm) = 757\ fs$, and $\tau_{out}(1029\ nm) = 672\ fs$ (from original $\tau_{in} = 390\ fs$), yielding almost identical peak power change (proportional to $\Gamma \frac{\tau_{in}}{\tau_{out}}$) but with shorter resulting

transform-limited pulse duration at shifted central wavelength. This change in transform-limited duration is due to the resulting shape of the spectrum itself – in the case of the shifted central wavelength, parts of the original spectrum are amplified more than the peak of the signal spectrum, resulting in a broader preserved amplified signal bandwidth. If Fourier transform is applied to calculate resulting bandwidth-limited pulse duration, a shorter value could be retrieved, limited by the bandwidth and the shape of the spectrum. A similar effect applies to the low gain situation, the difference being that peak power change is less severe at shifted signal central wavelength (more even gain profile across the spectral range).

It is interesting to analyze the situation when the resulting amplified signal transform-limited pulse duration is expected to be lower than the initial signal. According to calculations, this could happen at high gain with shifted original signal central wavelength to $\lambda_0 = 1037\ nm$ (Fig. 3.9), but obviously at the cost of a significant gain drop. Initial signal and amplified signal spectrum profiles were retrieved, and calculated transform-limited pulse shapes are plotted in Fig. 3.11.
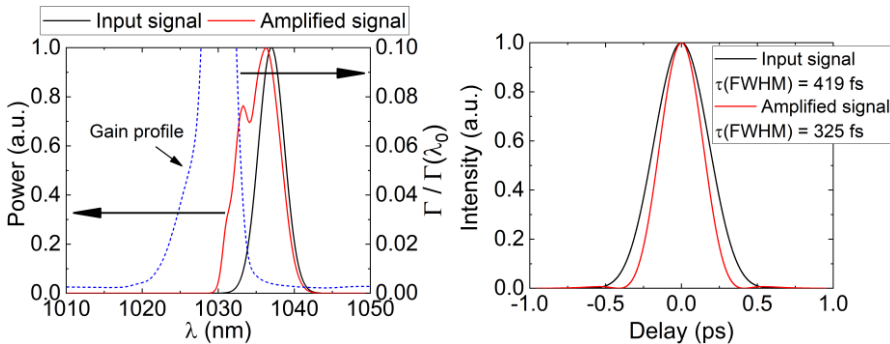

Fig. 3.11 <u>Left:</u> calculated spectral profiles of initial (solid black line) and amplified (solid red line) signal. Gain profile at $\Gamma(\lambda_0) = 26.6\ dB$ is plotted as a blue dashed line. **<u>Right:</u>** calculated pulse shape by performing Fourier transform of the spectrum.

As seen from Fig. 3.11, spectral reshaping of amplified signal beam is the reason for lower transform-limited pulse duration after amplification. This significant reshaping is in effect because the lower wavelength wing of the initial signal corresponds to increasing gain values, whereas the higher wavelength part experiences relatively lower total gain, and as a result forming closer to flat-top spectral profile as compared to Gaussian input signal. However, as mentioned before, this comes at the cost of total gain, which would prove to be very impractical.

In conclusion, results indicate that in general, the most straightforward way to reduce gain narrowing effect arising in Yb:YAG amplifier is to: (1) operate

in a low gain regime (e.g., choose sufficient initial signal intensity to operate in the highly saturated gain regime, by the use of pre-amplifiers), or (2) choose initial signal spectrum bandwidth as narrow as possible. In a more practical sense, to determine optimal initial signal spectral bandwidth for a wide range of gain regimes, transform-limited pulse duration of $< 1\,ps$ was chosen as a target, which is optimal for a number of applications, as reviewed in Chapter 1 of this thesis. In such case, when the initial signal bandwidth is $\Delta\lambda = 4.0\,nm$ (corresponds to $\tau_{TL} = 390\,fs$), the amplified signal transform-limited pulse duration is still within $< 1\,ps$ – in high gain $g = 30\,dB$ regime $\tau_{TL} = 1000\,fs$, and in low gain $g = 5\,dB$ regime this value is $\tau_{TL} = 546\,fs$. This indicates that the initial signal bandwidth of $\Delta\lambda = 4.0\,nm$ is optimal for operation in the sub-ps regime. Additionally, central signal wavelength shifting to lower wavelength region by $\sim 1\,nm$ seems to be another option to counter gain narrowing, at least to some extent. Total system gain would drop, but resulting transform-limited pulse duration would decrease, yielding practically the same resulting peak power. However, in this thesis, this scenario was not attempted due to the limited possibility of shifting the initial signal central wavelength.

3.4. Optimal pump beam focusing position

As was discussed in Chapter 1 of the thesis, in the end-pumped Yb:YAG amplifier systems pump beam must be focused to a tight beam spot to achieve sufficient amplification level [30]. When beam Rayleigh length is shorter than the length of the pumped crystal, it is observed that pump beam size (and shape) changes significantly across the crystal rod, suggesting that there must be an optimal focusing position for the pump beam to achieve maximum signal amplification. On one hand, focusing the pump beam too close to the front part of the crystal would yield pump intensity insufficient to reach amplification at the end of the gain medium. On the other hand, if the pump beam is focused at the end of the crystal, the frontal part of the gain medium would yield lower amplification (due to lower pump intensity) than would be optimally possible.

The optimal pump focusing position inside the end-pumped gain medium was extensively studied by *Chen et al.* and verified by *Kim et al.* [110,111]. They used Nd:YAG as the gain medium, but their findings are also applicable to Yb:YAG, as presented later. Chen's proposed analytical model reported that the optimal (highest efficiency) focusing position of the pump beam was only dependent on the pump absorption rate inside the gain medium, expressed as:

$$z_{optimal} = \frac{\ln(2)}{\alpha},\qquad\qquad(3.5)$$

where α is the pump absorption coefficient in mm^{-1}, which can be approximately estimated by $\alpha = N_d\sigma_a$, where N_d is the doping concentration of active ions in the gain medium, and σ_a is the absorption cross-section of the pump radiation. In principle, a larger absorption coefficient leads to the optimum pump beam focusing position closer to the incident surface of the active medium.

Such a proposition was numerically tested in the model. Double-pass Yb:YAG configuration was used as a reference, with a medium length of $L = 30\ mm$, and pump beam diameter of $\omega_p = 0.4\ mm$. Yb:YAG doping concentration was varied to match the tested pump absorption coefficient, and in each case, the pump beam focusing position was varied to find the highest efficiency. Additionally, the proposition was tested experimentally with three different Yb:YAG crystal configurations - $2x2x12\ mm^3$ with Yb^{3+} doping concentration of 3.6% ($\alpha = 0.396\ mm^{-1}$), $2x2x20\ mm^3$ with Yb^{3+} doping concentration of 2% ($\alpha = 0.22\ mm^{-1}$), and $4x4x30\ mm^3$ with Yb^{3+} doping concentration of 1% ($\alpha = 0.11\ mm^{-1}$). At each case, the pump beam waist was imaged onto the beam profiler (CCD camera), which was placed after the pump and signal beam separator (see Fig. 2.17 in Chapter 2, in the experimental validation of the model). Initially, the pump beam waist position was adjusted to coincide with the entrance face of the crystal rod (the entrance face position was found by slightly clipping the side of the crystal with the pump beam, and finding the position of the sharpest image of the crystal edge). The pump beam focusing position was then varied (by linearly translating the pump collimator) to find the highest efficiency in the double-pass configuration. More information regarding the other experimental conditions can be found in Chapter 2, Chapter 4 and Chapter 5 of this thesis.

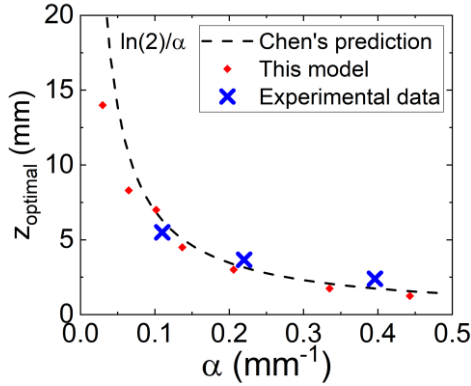Numerical modeling and experimental results are displayed in Fig. 3.12.

Fig. 3.12 Calculated optimal pump focusing position $z_{optimal}$ in the double-pass Yb:YAG amplifier (solid red circles), and experimental measurement data (blue marks). For the calculations, crystal length of $L = 30\ mm$, and pump beam diameter of $\omega_P = 0.4\ mm$ was chosen. Doping concentration was varied to match the tested pump absorption coefficient α. For the experiments, crystals were used: $2x2x12\ mm^3$ with Yb^{3+} doping concentration of 3.6% ($\alpha = 0.396\ mm^{-1}$), $2x2x20\ mm^3$ with Yb^{3+} doping concentration of 2% ($\alpha = 0.22\ mm^{-1}$), and $4x4x30\ mm^3$ with Yb^{3+} doping concentration of 1% ($\alpha = 0.11\ mm^{-1}$). Chen's prediction is displayed as the dashed curve.

Results of the numerical model and the experiments quite well match the prediction proposed by *Chen et al*. Slight visible mismatches in the model arise since pump absorption cross-sections are adjusted due to the change of temperature in the model, leading to a slightly different effective absorption coefficient across the crystal.

An interesting observation can be made that the focusing position of the pump beam is independent of the length of the gain material and the divergence of pump radiation if the pump absorption rate remains identical. To test this prediction made by *Chen et al.*, additional numerical modeling was performed in such cases: crystal length of $L = 10; 30\ mm$ and pump beam diameter of $\omega_p = 0.2; 0.4\ mm$, which sufficiently covers a significant change in pump beam divergence and crystal length. Pump beam focusing position inside the end-pumped gain medium was varied, and the resulting amplified signal power was recorded (normalized to the maximum value at each case). Results of such modeling are displayed in Fig. 3.13.
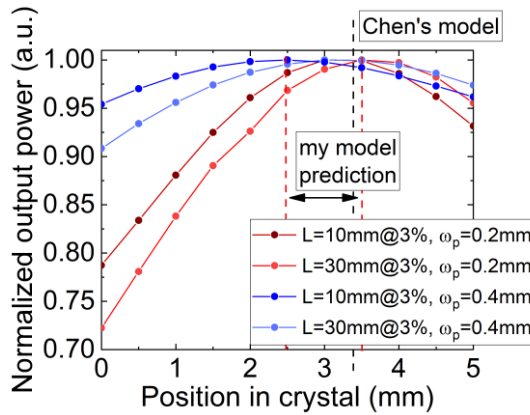
Fig. 3.13 Calculated amplified output power (normalized to maximum) dependency on pump beam focusing position in the crystal at pump absorption coefficient $\alpha \approx 0.2\ mm^{-1}$. The dashed black line indicates prediction by Chen's model, and the red dashed lines indicate the range of possible pump focusing positions, as predicted by my model. Investigated amplifier configurations are described in the legend of the graph.

Modeling results verify the proposed assumption. Slight discrepancies from the predicted value in Chen's model are explained due to slight differences in pump absorption rate across crystal due to varying temperature profiles, yielding differences in pump absorption cross-section. However, the error is within 20 %, proving such prediction satisfactory for the initial amplifier design.

The observable influence of pump beam divergence lies at the required precision of pump beam focusing within the gain medium – if pump beam divergence is high, more accurate positioning of pump beam waist in the crystal is required due to larger intensity variation along the crystal. However, the optimal focusing position is independent of the divergence of the pump beam.

In conclusion, using a simple expression in Eq. (3.5), as proposed by *Chen et. al.* [110], optimal pump beam focusing position in the gain medium could be retrieved. However, for more accurate results, modeling that includes pump absorption cross-section changes due to temperature gradient along crystal could prove useful, which would account for slight changes in effective pump absorption coefficient change.

3.5. Summary

In this chapter, basic guidelines for designing of an end-pumped double-pass Yb:YAG amplifier were presented, which are crucial for the experimental development of similar systems, presented later in Chapter 4 and Chapter 5.

At first, with the help of numerical modeling, guidelines for optimal crystal length and doping concentration combination were deduced, in the case of the end-pumped Yb:YAG gain medium pumped at $940\ nm$ wavelength, and seeded at $1030\ nm$ wavelength. Investigated pump intensity values were in the range of $I_p = 25 - 125\ \frac{kW}{cm^2}$, and pump diameter values were in the range of $\omega_P = 200 - 500\ \mu m$, covering a wide and practical range of possible amplifier scenarios. Numerical investigation showed that parameter $CDD = L \cdot X$ (where L is crystal length, and X is doping concentration) conveniently describes the optimal gain medium configuration, as it is only dependent on pump intensity. In investigated pump intensity range, this corresponds to $CDD = 30 - 51\ (\%\ mm)$ in the case when input signal power matches signal saturation power, and $CDD = 32 - 70\ (\%\ mm)$ in the case when input signal power is low (small-signal gain regime). Additionally, it was found that optimal crystal length correlates to the divergence of pump radiation. In the described scenarios, the optimal ratio of crystal length and pump radiation Rayleigh length was found to be in the range of $\frac{L}{z_R} \sim 2 - 3$. It was proposed that choosing parameter CDD based on pump intensity, and crystal length based on $\frac{L}{z_R} \sim 2 - 3$, would act as the initial parameters for designing the end-pumped Yb:YAG amplifier.

Amplified signal spectrum reduction (transform-limited pulse duration lengthening) due to the gain narrowing effect was also investigated numerically. It was deduced that the most straightforward way to reduce gain narrowing effect arising in Yb:YAG amplifier is to: (1) operate in low gain regime (e.g., choose sufficient initial signal intensity to operate in the highly saturated gain regime, by the use of pre-amplifiers), or (2) choose initial signal spectrum bandwidth as narrow as possible. In a more practical sense, to determine optimal initial signal spectral bandwidth for a wide range of gain regimes, transform-limited pulse duration of $< 1\ ps$ was chosen as a target, which is applicable in many areas within scientific and industrial environments (see Chapter 1). In such case, when the initial signal bandwidth is $\Delta\lambda = 4.0\ nm$ (corresponds to $\tau_{TL} = 390\ fs$), the amplified signal transform-limited pulse duration is still within $< 1\ ps$ – in high gain $g = 30\ dB$ regime $\tau_{TL} = 1000\ fs$, and in low gain $g = 5\ dB$ regime this value is $\tau_{TL} = 546\ fs$. This indicates that the initial signal bandwidth of $\Delta\lambda = 4.0\ nm$ is optimal for operation in the sub-ps regime.

Additionally, central signal wavelength shifting influence on the gain narrowing effect was investigated. Numerical modeling suggested that shifting central signal wavelength to lower wavelength region by $\sim 1\ nm$

would be a possible option to counter gain narrowing, at least to some extent. Total system gain would drop, but resulting transform-limited pulse duration would decrease, yielding practically the same resulting peak power. However, in this thesis, this scenario was not attempted due to the limited possibility of shifting the initial signal central wavelength.

In the end, an optimal (in terms of maximum efficiency) pump beam focusing position was investigated numerically and experimentally, and a simple solution was presented (originally proposed by *Chen et al.* [110]), which matched well with the results retrieved by the model and from the experiments.

4. Experimental development of the single cascade end-pumped Yb:YAG amplifiers

Material related to this Chapter was published in A1 and A4

4.1. Introduction

This chapter is dedicated to the discussion and experimental demonstration of the end-pumped Yb:YAG amplifier schematics. The strategy of laser system design was based on employing a hybrid laser approach, where initial signal pulses were generated in a fiber oscillator based on Yb^{3+} doped fiber and semiconductor saturable absorber mirror (SESAM), pre-amplified to moderate energy and power levels ($> 1\ \mu J$) using CPA technique, and further peak power scaling was performed in developed double-pass Yb:YAG DPSS amplifier. Signal stretching was performed by CFBG with specifically optimized dispersion values for each configuration under investigation. Relevant characterization of such seed sources (developed by *Ekspla*) and main parameters are presented in the following sections. All DPSS amplifier configurations were pre-modeled and optimized by techniques discussed in the previous chapter. Double-pass configuration was chosen, as discussed in Chapter 1, to prove a point that a rather simplistic approach could yield sufficiently similar or better laser parameters as compared to presented schematics in the literature review chapter of this thesis.

In the first section, a configuration capable of reaching $120\ \mu J$ energy pulses at $200\ kHz$ pulse repetition rate, with a pulse duration of $764\ fs$ is presented. Configuration operated in a moderate-gain regime when significant bandwidth narrowing of the initial signal was expected. Strategically, an all-in-fiber seed source with a relatively narrow initial signal bandwidth of $\Delta\lambda(FWHM) = 3.6\ nm$ was used to modestly mitigate the gain narrowing effect. All-in-fiber laser operated in CPA configuration, where pulse stretching was performed in CFBG. Pulse compression was performed in free-space with CVBG, with CFBG and CVBG dispersions matched.

In the second section, a similar approach was used to demonstrate $1\ mJ$ energy pulses at $14\ kHz$ pulse repetition rate, with pulse duration still below $1\ ps$. Dispersion matched pair of CFBG as pulse stretcher and 4-pass diffraction grating-based pulse compressor was employed.

In the third section, limiting factors of such configurations are discussed. Measurement of depolarization and beam circularity parameter of presented configurations was performed. A practical solution for improving beam circularity was proposed.

In the last section of this chapter, a different strategy in the choice of initial seed source was employed. An all-in-fiber seed source with a relatively broad initial signal bandwidth of $\Delta\lambda(FWHM) = 7.7\,nm$ was used, however, with sufficiently high initial signal power of $3.3\,W$, which significantly saturated Yb:YAG amplifier. Such configuration was operating in low-gain and high amplified signal power saturation regime, thus reducing the gain-narrowing effect. As a result, $32\,\mu J$ energy pulses at $1\,MHz$ pulse repetition rate, with pulse duration below $318\,fs$ were demonstrated at the output of the laser system. Dispersion matched pair of CFBG as a pulse stretcher and 4-pass diffraction grating-based pulse compressor was employed.

4.2. Realization of 104 μJ, 200 kHz, 764 fs hybrid laser system with dispersion matched pair of CFBG stretcher and CVBG compressor

To realize the hybrid laser configuration, an all-in-fiber seed source, and double-pass Yb:YAG amplifier configuration was employed. Initial configuration was based on the CPA technique, with dispersion matched CFBG as pulse stretcher (from *TeraXion*) and CVBG as pulse compressor (from *IPG Photonics*). The developed CPA laser system layout is shown in Fig. 4.1.

The all-in-fiber seed source was based on the architecture developed in *Ekspla* (based on commercially available fiber oscillator FFS100CHI) [15,112]. It consisted of SESAM based fiber oscillator, generating $1\,ps$ duration pulses with spectral bandwidth of $1.55\,nm$ at full width at half maximum (FWHM) level. The resulting pulse repetition rate was $47.4\,MHz$. Seed pulses were then linearly up-chirped to $4\,ps$, and spectral bandwidth broadened to $3.6\,nm$ at FWHM. The seed laser pulses were further chirped to $220\,ps$ duration using CFBG stretcher with group delay dispersion (GDD) of $\beta_2 = -33.7\,ps^2$. The pulse repetition rate was reduced using a fiber-coupled acousto-optic modulator (AOM) before the power amplifier. Additional fiber amplifier was used after AOM to increase the output energy. Initial chirped seed pulses were amplified to the maximum pulse energy of $\sim 7.8\,\mu J$ at the pulse repetition rate of $38\,kHz$, and with spectral bandwidth of $3.6\,nm$ (FWHM) at $1030\,nm$ central wavelength.
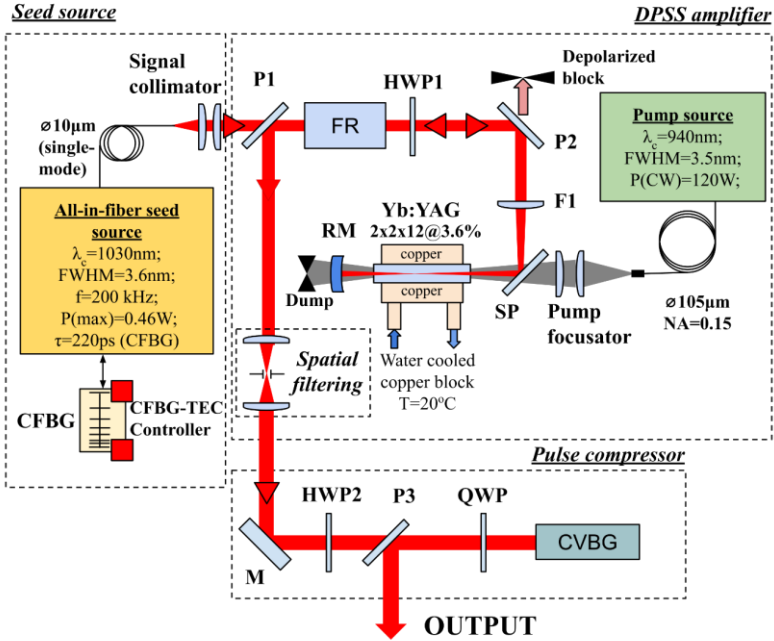
Fig. 4.1 The layout of the developed laser system, which consisted of an all-in-fiber seed source, free-space Yb:YAG amplifier ($2x2x12\ mm^3$ with Yb^{3+} doping concentration of 3.6%), and a pulse compressor. HWP1, HWP2 – half-wave phase retardation plates, FR – Faraday rotator, P1, P2, P3 – polarizers, SP – pump/signal wavelength separator, F1 – focusing lens for signal beam, RM – spherical mirror for signal beam double-pass realization, M – mirror, CFBG – chirped fiber Bragg grating, CVBG – chirped volume Bragg grating, QWP – quarter-wave phase retardation plate. Circulating water in crystal heatsink temperature was set to $20℃$.

By changing pulse repetition rate of the AOM, the average power that was fed to the last stage fiber amplifier was correspondingly varied, thus changing the resulting outcome in terms of achievable pulse energy. Measurement of the seed laser output power (and energy) dependency on pulse repetition rate is provided in Fig. 4.2.

Pulses originating from the small-mode area ($\sim 100\ \mu m^2$) fiber amplifier will inevitably be affected due to accumulated nonlinear phase shift if the resulting intensity is sufficiently high, leading to degraded recompressed pulse quality. Such effect for this seed source was investigated in the work of *Bartulevičius et al.* [112] and is not separately presented in this thesis. Relevant data from measurements indicated that accumulated B-integral, which describes accumulated nonlinear phase shift, amounts to $\sim 1.4\ \pi\ rad$ at the maximum pulse energy of $7.8\ \mu J$ ($38\ kHz$), and $\sim 0.5\ \pi\ rad$ at pulse energy of $2.3\ \mu J$ ($200\ kHz$). Such levels of pulse energies were used for experiments, as provided below.
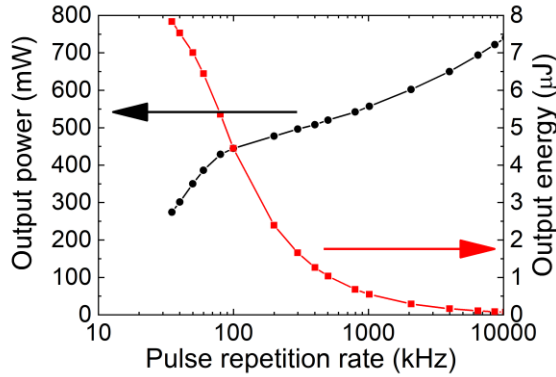
Fig. 4.2 Measured output power dependency on internal AOM pulse repetition rate of the all-in-fiber seed source. The pulse energy was estimated by dividing the measured output power by pulse repetition rate.

The output of the all-in-fiber seed source featured a single-mode (SM) polarization-maintaining (PM) fiber with a core diameter of $10\ \mu m$, spliced to angle-polished connector (APC) with an angle of 8° to minimize back-reflection. Output seed radiation was collimated with an aspheric lens from *Optizone*, with the focal length of $f = 6.2\ mm$. Collimated beam quality parameter M^2 was estimated via the z-scan technique. A focusing lens of $F = 200\ mm$ was placed on the beam path, and refocused beam diameter change was measured by translating a CCD camera (*Spiricon SP503U*) along the beam propagation direction. Measurement results are displayed in Fig. 4.3.
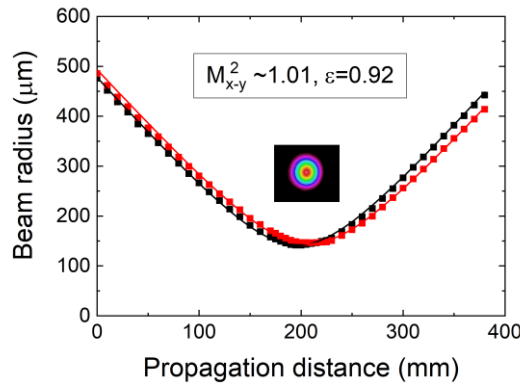

Fig. 4.3 Beam radius measurement along the propagation direction of focused seed beam (red and black dots). The beam quality parameter was estimated to be $M^2 \sim 1.01$ from the fit (red and black curves). The image of the beam profile at the focal position of the lens is shown as an inset. ε denotes the worst ratio of major and minor beam axis (beam ellipticity).

The beam quality of the seed source was measured to be diffraction-limited ($M^2 \sim 1$), with slight ellipticity present (worst ratio of beam diameters at major and minor axis was measured to be $\varepsilon = 0.92$). The origin of beam ellipticity can be traced to the beam propagating at an angle to the collimating lens (introducing offset), which was introduced by the APC connector. Additionally, the overall quality of the aspheric lens (its symmetry) was also found to introduce some portion of beam ellipticity. However, the resulting beam quality, including beam ellipticity, was satisfactory.

Chirped seed pulses were then directed to the DPSS Yb:YAG amplifier stage. The geometry of c-cut ([111]) Yb:YAG crystal was $2x2x12\ mm^3$ with Yb^{3+} doping concentration of 3.6%. Both facets of the crystal were coated with high laser-induced damage threshold (LIDT) coatings ($\sim 50\ J/cm^2$ for $10\ ns$ duration pulses). The input and output beams of the double-pass free-space amplifier were decoupled via polarization using a half-wave plate (HWP1), Faraday rotator (FR), and a pair of polarizers (P1 and P2), as shown in Fig. 4.1. In the amplifier, Yb:YAG crystal rod was end-pumped longitudinally by a continuous wave laser diode. Pump radiation was coupled to $105\ \mu m$ core (multimode) diameter and 0.22 numerical aperture (NA) fiber (although the actually measured pump radiation numerical aperture was estimated to be $NA = 0.15$, as was discussed in Chapter 2). The maximum measured laser diode (from *nLight*) power was $120\ W$ at $940\ nm$ central wavelength with $3.5\ nm$ bandwidth (FWHM). The laser diode was placed on the water-cooled heatsink, and its temperature was adjusted to shift the peak of laser diode emission to $940\ nm$ (laser diode was not wavelength-stabilized). The measured spectrum at the output of the laser diode, depending on water coolant temperature, is shown in Fig. 4.4. Power dependence on diode driver current is also provided.
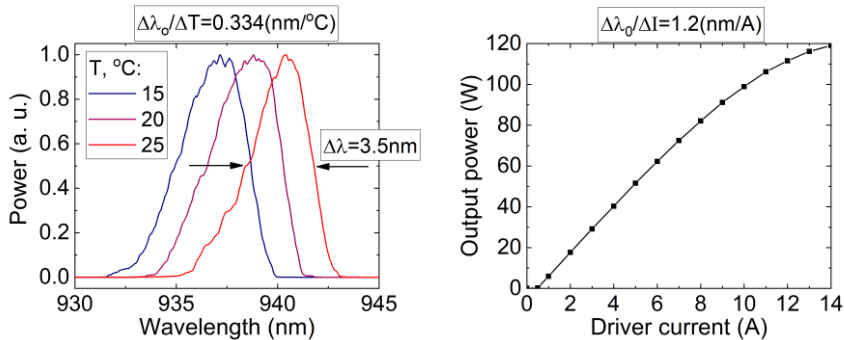

Fig. 4.4 <u>Left</u>: measured pump spectrum from nLight pump diode, with a maximum output power of $P_p = 120\ W$, measured at few different water coolant temperatures. The measured center wavelength-temperature coefficient was $\Delta\lambda_0/\Delta T = 0.334(nm/°C)$. <u>**Right:**</u> diode output

power dependence on driver current. Wavelength-current coefficient (measured, and according to datasheet) was $\Delta\lambda_0/\Delta I = 1.2 (nm/A)$.

The seed and pump beams were focused to respectively $\omega_p = 0.36\ mm$ and $\omega_s = 0.33\ mm$ diameters and overlapped in the amplifier crystal. Initial pump power of $84\ W$ (below maximum) was chosen for this amplifier stage due to limiting factors of depolarization and bi-focusing, both of which are discussed in more detail in Section 4.4 of this chapter. Here only the most optimal (in the author's opinion) configuration is discussed, and results are presented, which are not yet significantly limited by the mentioned detrimental effects.

The resulting pump beam intensity inside the crystal corresponded to $I_p = 82\ \frac{kW}{cm^2}$, which is almost four times above the pump saturation intensity of $I_{psat} = 22\ \frac{kW}{cm^2}$, and significantly larger than the minimum pump intensity required to reach transparency at laser wavelength ($I_{min} = 1.3\ \frac{kW}{cm^2}$), providing sufficient amplification level, which is not yet limited by bi-focusing and depolarization. Crystal length and doping concentration was based on optimum parameter CDD, as was presented in Chapter 3 of this thesis (see Fig. 3.5). In the experiments, this parameter was $CDD{\sim}43 - 46\ (\%\ mm)$, which is close to the proposed parameter from modeling of $CDD{\sim}47\ (\%\ mm)$. The variation is due to the length tolerance of the received crystal. However, according to preliminary modeling data, the result is not significantly different from what would optimally be possible.

Yb:YAG crystal was mounted into a water-chilled copper block, with high conductivity silicone as an interface layer between the gain medium and heatsink, with an experimentally estimated thickness of $\delta = 100\ \mu m$ (measurement was performed via microscope; estimated precision was $\delta{\sim}\pm 30\ \mu m$). The temperature of circulating cooling water was set to $T = 20°C$ (room temperature).

The second pass was realized by back reflecting the amplified signal by a concave spherical mirror (RM) with $R = 100\ mm$ radius of curvature, placed at the required distance to compensate the pump induced thermal lens. The required distance at which RM must be placed to compensate for a different thermal lens is plotted in Fig. 4.5 (with few different mirror radii of curvature). Gaussian beam propagation in principal amplifier scheme when the thermal lens of $F_{th} = 50\ mm$ is compensated is plotted in Fig. 4.6 for illustratory purposes. Modeling was performed with the *reZonator* software.
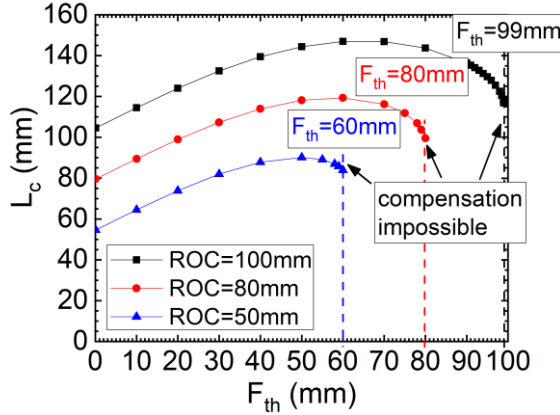
Fig. 4.5 Required distance L_c at which spherical mirror RM must be placed from Yb:YAG crystal to compensate pump induced thermal lens F_{th}. Scenarios for different radii of curvature $ROC = 50; 80; 100 \ mm$ are plotted. Dashed colored lines indicate the maximum thermal lens that could be optimally compensated with the corresponding ROC of the mirror.
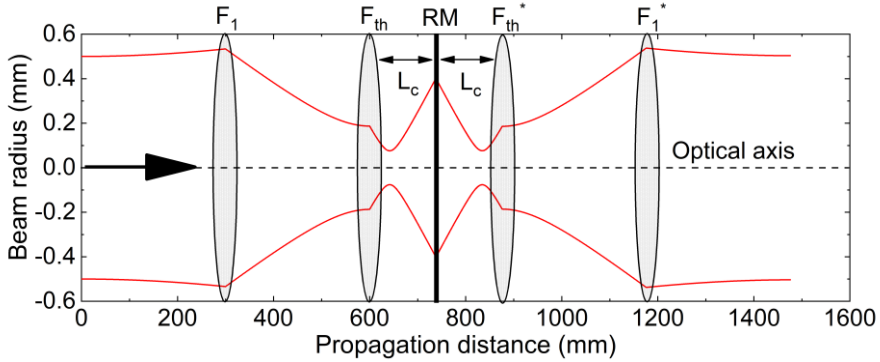

Fig. 4.6 Gaussian beam (signal) radius evolution as the beam propagates in the Yb:YAG amplifier system. The optical scheme is folded after spherical mirror RM. $F_1 = 300 \ mm$ corresponds to signal focusing lens (see Fig. 4.1 for the whole schematic), $F_{th} = 50 \ mm$ corresponds to the thermal lens (Yb:YAG crystal), RM is a spherical mirror with $ROC = 100 \ mm$. Asterix denotes identical optical elements in the folded schematic.

From presented modeling and following insights from Gaussian beam propagation nuances, the longest thermal lens that spherical mirror with a specific radius of curvature can compensate equals to the magnitude of the radius itself, e.g. $F_{th}(max) = ROC$. On the other hand, there are no limitations regarding the compensation of stronger thermal lens, except practicality. Spherical mirror with $ROC = 100 \ mm$ was chosen as it could be placed further from the gain medium to compensate identical thermal lens, as compared to spherical mirror with lower ROC. This provided sufficient freedom required for experimental measurements. However, the drawback of such an optical scheme that is worth mentioning is that even though the

Gaussian beam itself is backward propagated after the spherical mirror RM identically to forward propagation, the beam at crystal is not relay-imaged back to the crystal. In such case, beam amplitude modulations (degradation) due to the amplification and thermal effects arising in the end-pumped Yb:YAG crystal are not imaged back to the crystal after reflection from the RM, suggesting that the signal beam backward propagation in the Yb:YAG crystal is not exactly identical to forward propagation. This was not an important issue in the currently presented amplifier schematic. However, a situation where it becomes important and upgraded optical schematic is presented in Chapter 5.

Initially, pulse repetition rate was set to $200\ kHz$ by the fiber-coupled AOM (corresponding to a seed pulse energy of $E = 2.3\ \mu J$), and amplifier characteristics at the pump power of $P_p = 84\ W$ were measured by varying the input signal power with an external power attenuator, based on a half-waveplate and polarizer. Results are displayed in Fig. 4.7, with modeling predictions included.
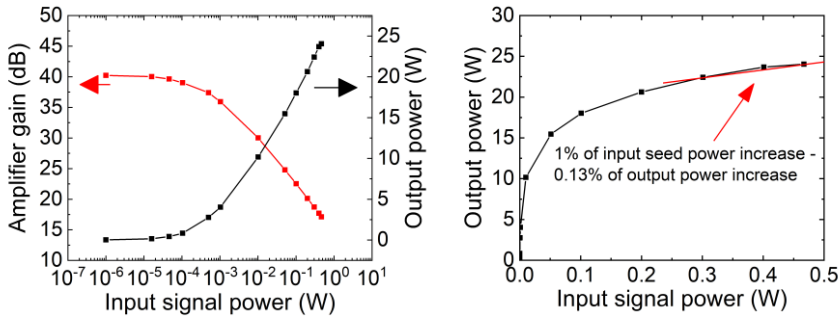

Fig. 4.7 <u>Left:</u> average output power (black curve, right axis) and total amplifier gain (red curve, left axis) of double-pass Yb:YAG amplifier versus input signal (seed) power (in logarithmic scale). The pulse repetition rate was 200 kHz. The amplifier was pumped by $P_p = 84\ W$ power. **<u>Right:</u>** average output power versus input signal power (linear scale), showing a significant power saturation level of the amplifier stage.

After double-pass through the amplifier, the signal was amplified from $460\ mW$ to an average output power of $\sim 24\ W$ at $200\ kHz$ pulse repetition rate ($120\ \mu J$ pulse energy). For $84\ W$ of pump power, it corresponded to $\eta = 28\ \%$ of amplifier efficiency. In the tested setup, a high amplified power saturation level was attained – $1\ \%$ change of input power transforms to $0.13\ \%$ of output power change when the amplifier is seeded with an average power higher than $0.3\ W$. Such level of saturation is beneficial for the overall power stability of the system as it becomes less sensitive to seed power fluctuations. On the other hand, at low seed power, $\sim 40\ dB$ of double pass

gain was achieved (small-signal gain regime). Experimental measurement of small signal gain was complicated due to the significant amount (compared to amplified signal) of fluorescence emitted from the pumped crystal, which interfered with amplified signal power measurement. To overcome this, a sensitive photodiode power sensor (*S130C*, from *Thorlabs*) was placed at $500\ mm$ from Yb:YAG amplifier output. The amplified signal was refocused with $F = +100\ mm$ lens with iris-type aperture placed in the vicinity of lens focal position. Aperture was closed to such extent as not to block the actual amplified signal but sufficiently to block background radiation. Additionally, measurement was performed in a darkened room, and residual background (measured power level) was subtracted. Furthermore, to subtract any additional remaining background emitted from the pumped Yb:YAG crystal, power level reaching photodiode sensor was measured when the crystal was pumped with input signal blocked. Afterward, the input signal was unblocked, and the resulting measured power was estimated by subtracting the measured background.

At maximum seed power, spectral bandwidth after amplification in Yb:YAG crystal was reduced from $3.6\ nm$ to $2.2\ nm$ FWHM due to gain narrowing effect. Consequently, chirped pulse duration was reduced from $220\ ps$ down to $150\ ps$ as measured by $20\ GHz$ bandwidth oscilloscope and photodetector with $35\ ps$ response time. The measured spectrum of chirped pulses before and after amplification at maximum output power is shown in Fig. 4.8.
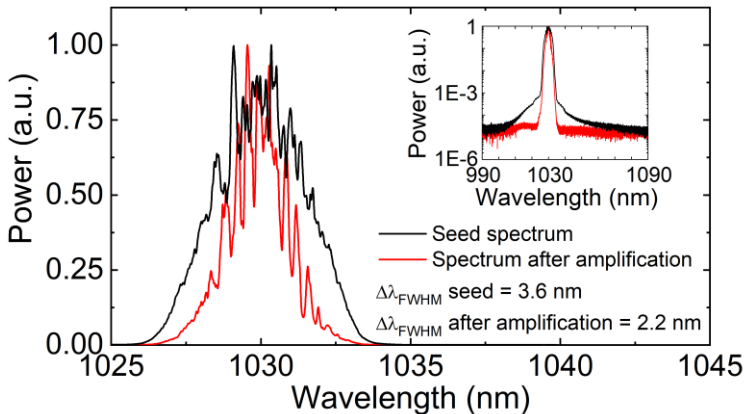

Fig. 4.8 Spectrum of the chirped seed pulses (black line) and spectrum of the chirped pulses after double-pass Yb:YAG amplifier (red line). Inset: the same spectra in logarithmic scale.

The initial spectral modulation, as seen from Fig. 4.8, could arise from group delay ripples of the CFBG stretcher or from the internal reflections in

micro-optical components used in all-in-fiber seed source [112]. It was previously shown that small initial spectral modulation leads to the appearance of small amplitude (~1%) satellite pulses in the range of $3 - 5\ ps$ from the main compressed pulse. The spacing of these pulses is related to the modulation frequency of the spectrum. However, overall temporal quality of the compressed pulse does not degrade significantly in this case [113,114].

At the output of the laser, besides the laser radiation bunched in ultrashort pulses, there unavoidably is a certain level of continuous wave (CW) amplified spontaneous emission (ASE) coming from the pumped amplifier stages. This CW background can be relatively separated into two components: one that comes from the Yb-doped fiber amplifiers and another added by the ASE from the pumped Yb:YAG crystal. ASE level from the fiber laser can be estimated from the broad spectral shoulders visible in the logarithmic scale (inset of Fig. 4.8). By smoothly extrapolating these shoulders, one can obtain ~$30\ dB$ ASE level at the central $1030\ nm$ wavelength. Because there is no temporal gating in this realization of the laser system, both CW background and pulsed radiation will be similarly amplified in Yb:YAG amplifier, resulting in ~$30\ mW$ of amplified background. The CW background that results from Yb:YAG amplifier was not directly measured, but the upper bound can be estimated from Fig. 4.7: when the input seed power is very small ($1\ \mu W$), total gain reaches ~$40\ dB$, which corresponds to the output power of ~$10\ mW$. A large part of this output power is still the actual amplified signal, as was measured with the method described earlier and according to provided modeling data. Furthermore, at high input seed power, the output power after the amplifier is $24\ W$, resulting in considerable Yb^{3+} upper-state depletion and reducing ASE. Conservatively one can estimate that ASE from Yb:YAG amplifier is $< 1\ mW$ at full output power, an insignificant amount compared to the ASE from the fiber amplifiers. Modeling prediction matched experimental data quite well, with visible minimal mismatches as described in Chapter 2 of this thesis.

Beam quality after amplification deteriorated (M^2 ~1.15) due to thermal lens aberrations, so spatial filtering was used to obtain diffraction-limited beam quality, as was discussed in Chapter 2. Spatial filtering was performed using an aperture near the focal plane of the focusing lens (shown in Fig. 4.1). Aperture size was chosen so that only the central lobe of the Gaussian beam was transmitted, with the aberrated part filtered out. Spatial filtering resulted in ~3% power loss of the amplified beam. After spatial filtering, beam quality parameter M^2 was measured using the standard z-scan technique by focusing the beam by a positive lens of well-defined focal length and tracing the beam

radius change along the propagation direction. The best fit yielded $M^2 \sim 1.0$, indicating a diffraction-limited beam quality, whereas beam ellipticity slightly degraded after the amplifier to $\varepsilon = 0.91$ (from initial $\varepsilon = 0.92$). The measurement graph before and after spatial filtering is shown in Fig. 4.9.
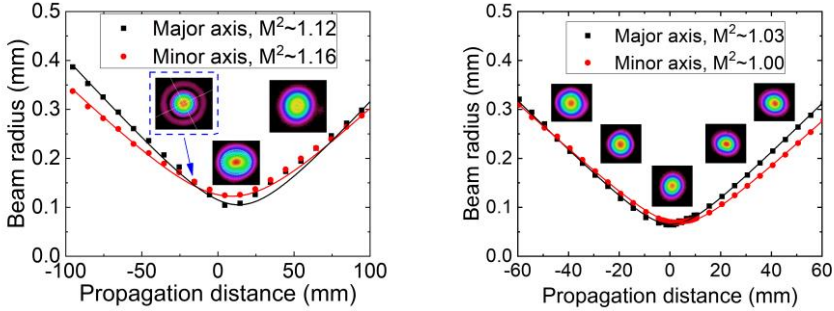

Fig. 4.9 Beam radius measurement along the propagation direction of focused amplified signal beam. **Left:** amplified signal beam without spatial filtering (red and black dots). The beam quality parameter was estimated to be $M^2 \sim 1.15$ from the fit (red and black curves). Images of the beam profile at several positions are shown as insets (beam size was normalized for clarity). A dashed blue box with a corresponding arrow indicates the position of spatial filtering, where the Gaussian beam lobe and aberrated part are well separated. **Right:** spatially filtered amplified beam (red and black dots). The beam quality parameter was estimated to be $M^2 \sim 1.0$ from the fit (red and black curves). Images of the beam profile at several positions are shown as insets (beam size was normalized for clarity).

After amplification and spatial filtering, chirped pulses were directed to CVBG compressor, with beam after spatial filtering expanded to the diameter of $\omega_s = 2\ mm$. CVBG stretching factor was $SF = 58\ \frac{ps}{nm}$, grating thickness $47\ mm$, and aperture $5\ mm\ x\ 5\ mm$, with a maximum spectral bandwidth of $\sim 8\ nm$. CVBG was mounted onto an aluminum heatsink with a silicone interface layer. CVBG was not subject to any mechanical forces other than its own weight since it was shown it could introduce beam ellipticity [115]. Output beam was separated from the input via polarization by using a polarizer (P3) and a quarter-wave plate (QWP), as shown in Fig. 4.1. The efficiency of the CVBG compressor was measured at full power, which yielded $87\ \%$ efficiency, corresponding to $20.8\ W$ of output power and $104\ \mu J$ pulse energy.

Dispersion of the CFBG stretcher was matched to the dispersion of the CVBG compressor accounting for the dispersion of $\sim 40\ m$ of fiber in the seed laser. Residual dispersion was compensated by applying a thermal gradient on the CFBG stretcher (for more details, see [15,112]). Optimally compressed pulses were characterized by the second-harmonic generation frequency-resolved optical gating (SHG-FROG) autocorrelation method. The pulse

duration retrieved by the FROG algorithm (*Swamp Optics*) using a 1024x1024 grid was $764\,fs$ (Fig. 4.10). Transform-limited pulse duration derived from the output spectrum was $644\,fs$. A mismatch between the measured and transform-limited pulses could be attributed to the accumulated nonlinear phase in the single-mode fiber seed laser due to a small mode area ($\sim100\,\mu m^2$) of the doped fiber, as was discussed earlier in this chapter. A residual spectral phase retrieved from FROG was $\sim2\,rad$ (corresponding to $\sim0.64\,\pi\,rad$) in the spectral range from $1026.5\,nm$ to $1032.7\,nm$ encompassing $99\,\%$ of total pulse energy. Strehl ratio of the compressed pulse, defined as the ratio of actual peak power of the pulse to the one of the transform limited pulse, was $76\,\%$.
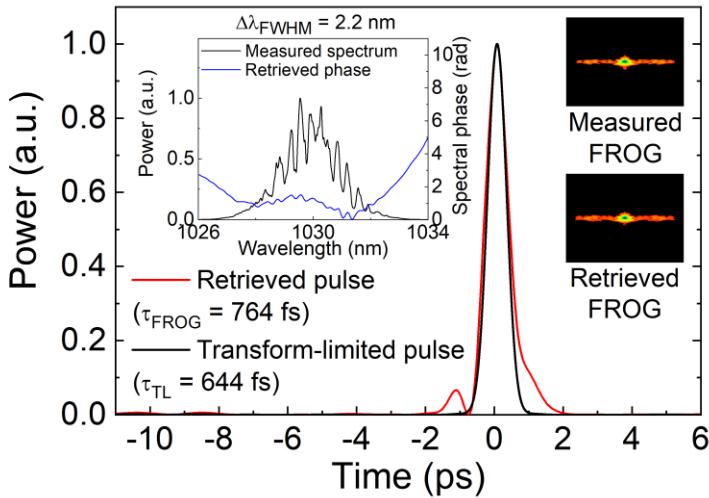

Fig. 4.10 Envelope of the compressed pulses retrieved from SHG FROG measurement compared to transform-limited pulse shape calculated from the measured spectrum. **Insets:** (left) measured amplified signal spectrum and retrieved spectral phase; (right) measured and retrieved FROG traces (0.15% retrieval error).

Beam quality after the CVBG compressor was characterized by the same z-scan technique of the focused beam (Fig. 4.11). Slight irregularities in the beam profile were observed near the focal position, the origin of which is not clear but is most likely related to manufacturing defects or irregularities in PTR glass present in CVBG [70]. Additionally, the beam quality parameter degraded to $M^2 < 1.2$, whereas beam ellipticity was unchanged ($\varepsilon = 0.91$). Similar beam quality degradation in CVBG manufactured from PTR glass was extensively studied in the work of *D. Stepankova et al.* [115] and *S. Cho et al.* [116] and is related to the thermal load generated by the residual beam absorption inside the CVBG. Longitudinal and transverse thermal gradients

are formed inside CVBG, leading to the formation of thermal lens, which values are slightly different for different spectral components (as they are reflected at different parts of CVBG), causing beam divergence variation across spectral components, and thus leading to beam quality degradation [115]. However, overall beam quality was good with the estimated beam quality parameter $M^2 < 1.2$.
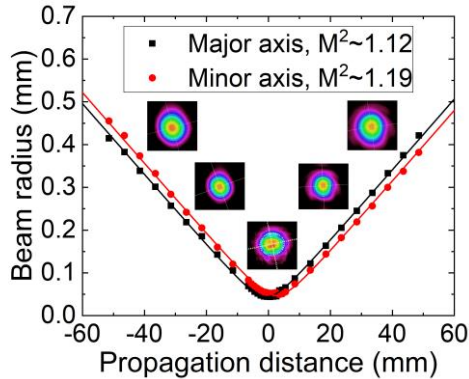

Fig. 4.11 Beam radius measurement along propagation direction after CVBG compressor via z-scan technique (red and black dots). Beam quality parameter $M^2 < 1.2$ was estimated from the fit (red and black curves). Images of the beam profile at a few positions are shown as insets (beam size was normalized for clarity).

According to the amplifier gain graph in Fig. 4.7 and seeder calibration curve in Fig. 4.2, there was a potential possibility to obtain pulses of $500\ \mu J$ energy from this configuration at lower repetition rates of $38\ kHz$ (corresponding to input signal energy of $7.8\ \mu J$ [$\sim 300\ mW$ input power], with corresponding Yb:YAG amplifier gain of $18\ dB$), or even $1\ mJ$ if pulse repetition rate is further reduced. However, the realization of such potential was impossible within the current setup, as beam quality significantly degraded when pulses with energy higher than $200\ \mu J$ were directed towards CVBG, even though beam quality prior to compression was diffraction limited. As mentioned before, such phenomena were mostly related to the quality of CVBG, which I used for the experiments. However, the technology of CVBG is very promising, as was presented in the work of *D. Stepankova et al.* [115], where Yb:YAG thin-disk configuration reaching $216\ W, 2\ ps$ compressed pulses at $92\ kHz$ pulse repetition rate ($\sim 2.3\ mJ$ pulse energy) was presented.

In conclusion, an ultrafast laser system based on fiber seed laser and Yb:YAG crystal rod power amplifier was developed. The key novelty of the system was the application of CFBG stretcher and CVBG compressor with

matched dispersion which enabled to obtain nearly bandwidth-limited compressed sub-picosecond pulses. The presented laser system produced pulses of $764\,fs$ duration and $104\,\mu J$ energy at $20.8\,W$ average power, which corresponds to the peak power of $P_p \sim 0.13\,GW$, with nearly diffraction-limited beam quality ($M^2 \sim 1.15$, beam ellipticity $\varepsilon = 0.91$), and amplifier efficiency of $\eta = 28\,\%$. In the tested setup, a high amplified power saturation level was attained – 1 % change of input power transforms to 0.13 % output power change when the amplifier is seeded with average power higher than $0.3\,W$. Such a level of saturation is beneficial for the overall power stability of the system as it becomes less sensitive to seed power fluctuations. The proposed relatively simplistic laser architecture enables the construction of high-energy ultrashort pulse lasers for a wide range of applications.

4.3. Realization of 1 mJ, 14 kHz, 815 fs hybrid laser system

To realize the full potential of the proposed hybrid laser configuration, similar to the previously presented all-in-fiber seed source and an identical double-pass Yb:YAG amplifier configuration was employed. Configuration was again based on the CPA technique, with CFBG as pulse stretcher (from *TeraXion*) and 4-pass diffraction grating as a pulse compressor (from *Gitterwerk*). A diffraction grating based pulse compressor was chosen to avoid beam quality limitations observed with CVBG. More information regarding pulse compressor can be found in Chapter 1 of this thesis. The developed CPA laser system layout is shown in Fig. 4.12.

The all-in-fiber seed source was developed in *Ekspla* (similar configuration as presented previously), with CFBG stretcher optimized for pulse compression in diffraction grating based pulse compressor (for diffraction grating with a groove density of $1842\,mm^{-1}$). The seed laser pulses were chirped to $220\,ps$ duration using CFBG stretcher with group delay dispersion (GDD) of $\beta_2 = -33.7\,ps^2$. The pulse repetition rate was reduced using a fiber-coupled acousto-optic modulator (AOM) before the power amplifier. Additional fiber amplifier was used after the AOM to increase the output energy. Initial chirped seed pulses were amplified to the maximum pulse energy of $\sim 3.9\,\mu J$ at the pulse repetition rate of $50\,kHz$, and with a spectral bandwidth of $3.75\,nm$ (FWHM) at $1030\,nm$ central wavelength. By changing the pulse repetition rate of the AOM, the average power that was fed to the last stage fiber amplifier was correspondingly varied, thus changing the resulting outcome in terms of achievable pulse energy. Measurement of seed laser output power (and energy) dependency on pulse repetition rate is provided in Fig. 4.13.
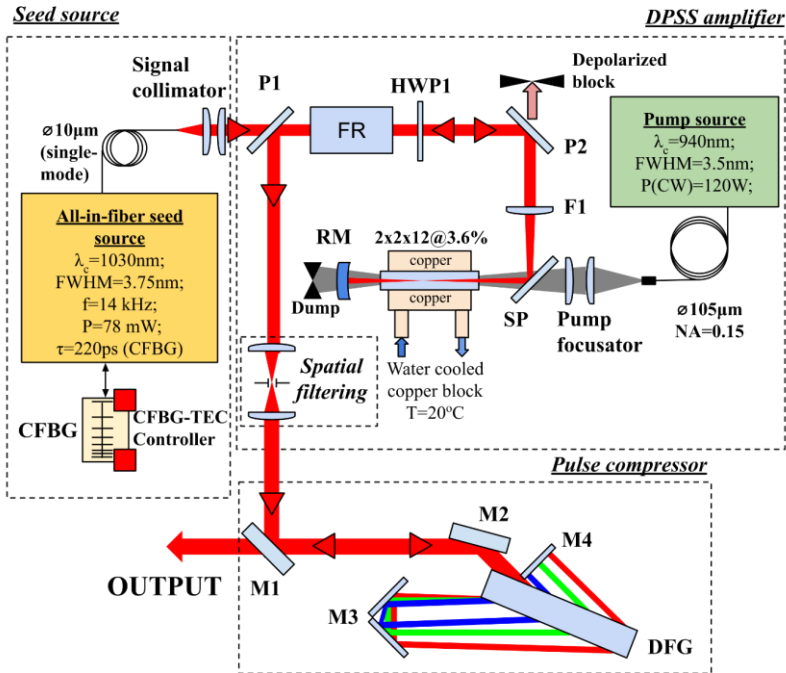
Fig. 4.12 Layout of the developed laser system, which consisted of an all-in-fiber seed source, free-space Yb:YAG amplifier ($2x2x12\ mm^3$ with Yb^{3+} doping concentration of 3.6%), and pulse compressor. HWP1 – half-wave phase retardation plate, QWP – quarter-wave phase retardation plates, FR – Faraday rotator, P1, P2 – polarizers, SP – pump/signal wavelength separator, F1 – focusing lens for signal beam, RM – spherical mirror for signal beam double-pass realization, M1-M4 – mirrors, CFBG – chirped fiber Bragg grating, DFG – diffraction grating with a groove density of $1842\ mm^{-1}$. Circulating water in crystal heatsink temperature was set to 20℃.
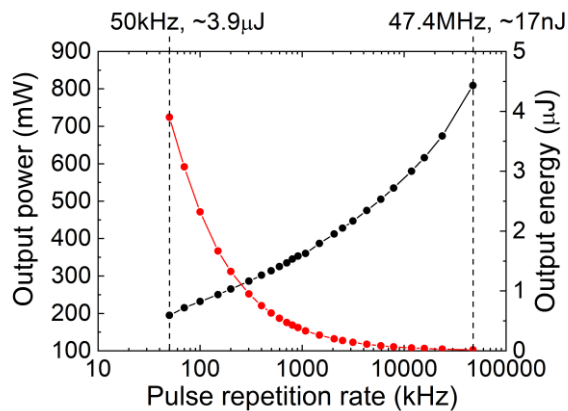

Fig. 4.13 Measured output power dependency on internal AOM pulse repetition rate of the all-in-fiber seed source. The pulse energy was estimated by dividing the measured output power by pulse repetition rate.

As mentioned previously, pulses originating from the small-mode area ($\sim 100\ \mu m^2$) fiber amplifier will inevitably be affected due to accumulated nonlinear phase shift if the resulting intensity is sufficiently high, leading to degraded recompressed pulse quality [112]. To examine this effect for the current seed source prior to amplifying pulses in Yb:YAG, the B-integral parameter [19] was experimentally estimated as follows. Chirped seeder pulses were directed to and compressed in $1842\ mm^{-1}$ diffraction grating pulse compressor, designed to compensate dispersion of used CFBG ($\beta_2 = -33.7\ ps^2$). At first, compressor length was adjusted for optimal compression of low-energy ($E \sim 0.1\ \mu J$) seeder pulses, where accumulated nonlinear phase is minimal. A low-energy regime was achieved by increasing pulse repetition rate to $\sim 10\ MHz$, thus significantly decreasing peak intensity. Afterward, pulse energy was increased by decreasing the AOM frequency to $50\ kHz$, corresponding to an output pulse energy of $3.9\ \mu J$. Pulse compressor length was then adjusted to accommodate for the induced nonlinear phase shift, which resulted in different optimal second-order dispersion value (compressor length) required for optimal pulse compression. B-integral value was estimated using the phase-compensation relation derived in the work of *Schimpf et al.* [117]:

$$\beta_{int}(rad) = \frac{\Delta\beta^{(2)}(\Delta\omega_{FWHM})^2}{4}, \tag{4.1}$$

where β_{int} is the resulting B-integral parameter, $\Delta\beta^{(2)}$ (in s^2) is the difference of second-order dispersion required for optimal pulse compression (between low and high energy in this case), $\Delta\omega_{FWHM}$ is the angular frequency bandwidth of pulses (in s^{-1}).

Experimental investigation indicated that pulse compressor length must be changed by $1\ mm$ for optimal pulse compression, corresponding to $\Delta\beta^{(2)} = 0.383 \times 10^{-24}\ s^2$. For the seed pulse bandwidth of $\Delta\lambda = 3.75\ nm$, this corresponds to $\sim 1.35\ \pi\ rad$ of accumulated nonlinear phase.

Compressed pulses were measured using a second harmonic non-collinear autocorrelator (*pulseCheck* from *APE*), and the resulting pulse compression quality due to non-negligible B-integral was estimated. Autocorrelation traces of optimally compressed pulses are displayed in Fig. 4.14. Measured corresponding pulse spectra are shown as the insets in each graph.
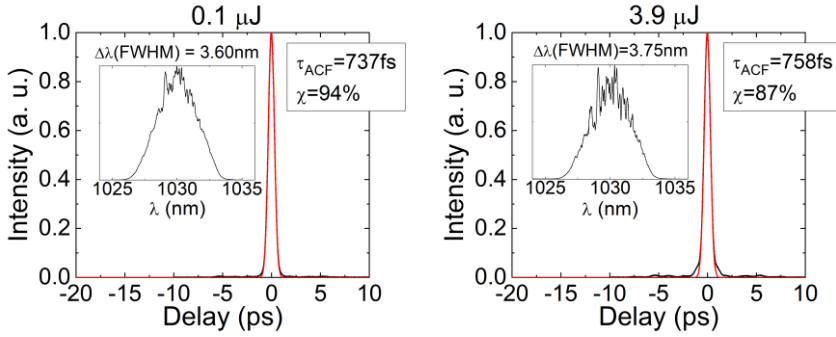
Fig. 4.14 Measured autocorrelation traces of optimally compressed seed pulses at **(left)** low energy of $E = 0.1 \, \mu J$ (minimal nonlinear phase shift), and **(right)** at relatively high energy of $E = 3.9 \, \mu J$. Measured spectra are displayed as insets on each graph. The width (FWHM) of the autocorrelation function is indicated at the top right corner of each graph. Red solid lines correspond to Gaussian fit of autocorrelation traces, serving as relative pulse quality estimation – χ corresponds to the ratio of area under autocorrelation trace and Gaussian fit curves.

Each autocorrelation trace was fitted with a Gaussian function for visual pulse quality estimation. The ratio χ (autocorrelation trace „contrast") of the area under autocorrelation trace and Gaussian fit curves was calculated. Results indicated that pulse quality visibly degraded when pulse energy was increased to $E = 3.9 \, \mu J$, which corresponded to accumulated B-integral of $\beta_{int} = 1.35 \, \pi \, rad$, and contrast degraded from $\chi = 94 \, \%$ to $\chi = 87 \, \%$. Additionally, visible spectral modulation most likely arose from group delay ripples of the CFBG stretcher or from internal reflections in micro-optical components used in all-in-fiber seed source [112]. Pulse duration, assuming Gaussian pulse shape, was estimated to be $\tau(Gaussian) = 538 \, fs$. Corresponding transform-limited pulse duration was estimated by applying Fourier transform on the measured spectrum, yielding $\tau(TL) = 512 \, fs$, indicating that measured pulse duration is close to transform-limited. Measurement of optimally compressed pulses at low energy also indicated an insignificant amount of pulse quality degradation (visible as features in autocorrelation trace at the delay values of $\pm 2 \, ps$ and $\pm 5 \, ps$) due to minimal dispersion mismatch between CFBG stretcher and diffraction grating pulse compressor. However, overall pulse quality is acceptable for further peak power scaling in Yb:YAG amplifier.

Pulse repetition rate (PRR) was further decreased to $13.9 \, kHz$ by fiber-coupled AOM, increasing seed source output pulse energy to $\sim 5.5 \, \mu J$, with a corresponding average power of $78 \, mW$. This was possible after optimization performed by *Ekspla*. The resulting B-integral value for such pulse repetition rate (PRR) was not separately investigated by the before-mentioned method, but extrapolation yielded B-integral $\sim 1.6 \, \pi \, rad$. The beam quality of seed

source was identical to the previous configuration - identical optical setup was used, yielding diffraction-limited beam quality of $M^2 \sim 1$.

Amplification characteristics dependence on input seed power were identical as presented in Fig. 4.7 (identical Yb:YAG amplifier configuration was used) and are not provided in this section separately.

The pulse repetition rate was set to $13.9\ kHz$ by the fiber-coupled AOM (corresponding to a seed pulse energy of $E = 5.5\ \mu J$). Amplified and outcoupled beam from the double-pass Yb:YAG amplifier (pumped with a pump power of $P_p = 84\ W$) was spatially filtered, resulting in $\sim 3\ \%$ power loss, totaling to the output power of $15.8\ W$, or the energy of $1.14\ mJ$. Amplifier efficiency resulted in $\eta = 19\ \%$, and beam quality was diffraction-limited with $M^2 \sim 1$. The extraction of higher pulse energy from the amplifier in this setup is limited by several things. First, higher pumping power would result in undesirable beam ellipticity and increased power loss due to depolarization (more on this in the next section). Secondly, even if such effects are diminished, amplified beam energy fluence on the coated surface of Yb:YAG crystal in this setup ($0.33\ mm$) reaches $2.7\ J/cm^2$, which is close to the observed damage threshold $\sim 5\ J/cm^2$ of the anti-reflection coating. A possible strategy, in this case, would be to increase both pump and signal beam size in the Yb:YAG crystal to avoid possible damage to the optical coating, but then increased pumping power would be required. Another option is to use a seed source with higher initial pulse energy. This could be done by either building a more powerful all-in-fiber seed source or building a dedicated free-space Yb:YAG amplifier stage to safely scale initial pulse energy. These strategies, however, were not implemented because, at the time of these experiments, a more powerful pumping source was not available, and there was no possibility to build an additional Yb:YAG amplifier stage. A more powerful all-in-fiber seed source was also not available.

The spatially filtered beam was then directed to a 4-pass diffraction grating pulse compressor. Measured diffraction and reflection losses in the pulse compressor were $\sim 10\ \%$, resulting in the output power of $\sim 14.4\ W$. Pulses were optimally compressed, where residual dispersion was compensated by applying a thermal gradient on the CFBG stretcher (for more details, see [15,112]). Compressed pulse quality was characterized using a second harmonic non-collinear autocorrelator (*pulseCheck* from *APE*), and autocorrelation trace of an optimally compressed pulse is displayed in Fig. 4.15. The measured corresponding pulse spectra are also shown before and after amplification in the end-pumped Yb:YAG amplifier.
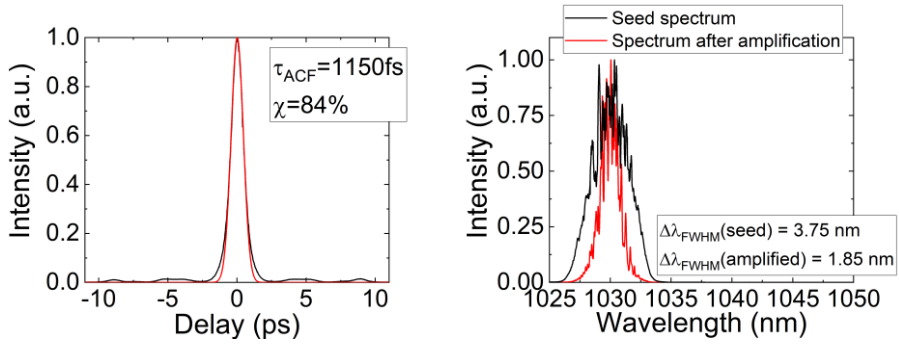
Fig. 4.15 <u>Left:</u> measured autocorrelation trace of optimally compressed seed pulse at the output of double-pass Yb:YAG amplifier and 4-pass diffraction grating compressor. The solid red line corresponds to the Gaussian fit of autocorrelation trace, serving as relative pulse quality estimation – χ corresponds to the ratio of area under autocorrelation trace and Gaussian fit curve. The width (FWHM) of the autocorrelation function is indicated at the top right corner of the graph. **<u>Right:</u>** measured initial and amplified signal spectrum.

The measured autocorrelation function FWHM was $\tau_{ACF} = 1150\,fs$, which corresponds to pulse duration of $\tau = 815\,fs$ (assuming Gaussian pulse shape). Transform-limited pulse duration derived from the output spectrum was $\tau_{TL} = 760\,fs$, indicating a good compression quality. A mismatch between the measured and transform-limited pulses could be attributed to the accumulated nonlinear phase in the single-mode fiber seed laser due to small mode area ($\sim 100\,\mu m^2$) of the doped fiber, as was discussed earlier in this chapter. Additionally, pulse quality was estimated from the measured pulse autocorrelation trace - autocorrelation trace was fitted with Gaussian function, and the ratio χ (autocorrelation trace „contrast") of the area under autocorrelation trace and Gaussian fit curves was calculated, with an estimated value of $\chi = 84\,\%$, indicating a relatively good pulse quality.

The resulting pulse energy was measured with energy meter *J-25MT-10KHZ* (*Coherent*), indicating $E = 1.01\,mJ$ pulse energy, which was similar to estimation by dividing the measured output power by pulse repetition rate ($E = 1.04\,mJ$). This yielded peak power of $P_p = 1.16\,GW$.

Beam quality after diffraction-grating based compressor was characterized by the same z-scan technique of focused beam (Fig. 4.16). The measured beam quality was diffraction-limited with estimated beam quality parameter $M^2 \sim 1$ and beam ellipticity $\varepsilon = 0.9$.
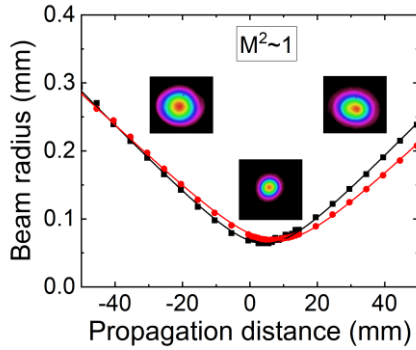
Fig. 4.16 Beam radius measurement along propagation direction after 4-pass diffraction grating based compressor via z-scan technique (red and black dots). Beam quality parameter M²~1 was estimated from the fit (red and black curves). Images of the beam profile at a few positions are shown as insets (beam size was normalized for clarity).

In conclusion, a compact ultrafast laser system based on fiber seed laser and Yb:YAG crystal rod power amplifier was developed. Nearly bandwidth-limited compressed sub-picosecond pulses were achieved by employing dispersion matched CFBG as the pulse stretcher and 4-pass diffraction grating pulse compressor. The presented laser system produced pulses of $815\,fs$ duration and $\sim 1\,mJ$ energy at $14.4\,W$ of average power, which corresponds to the peak power of $P_p \sim 1.16\,GW$, with diffraction-limited beam quality ($M^2 \sim 1$, beam ellipticity $\varepsilon = 0.9$), and amplifier efficiency of $\eta = 19\,\%$. The proposed relatively simplistic laser architecture enabled the construction of a truly compact and robust high-energy ultrashort pulse laser for a wide range of applications. The size of the free-space part of the laser system was $600x250x160\,mm^3$ (length, width, and height), whereas the fiber and electronics part was conveniently placed in an industry-standard rack-mountable unit, with the size of $436x449x140\,mm^3$. This high-energy ultrashort pulse laser is suitable for a wide range of applications, as was discussed in Chapter 1 of the thesis. The laser system at the prototyping stage is shown in Fig. 4.17.
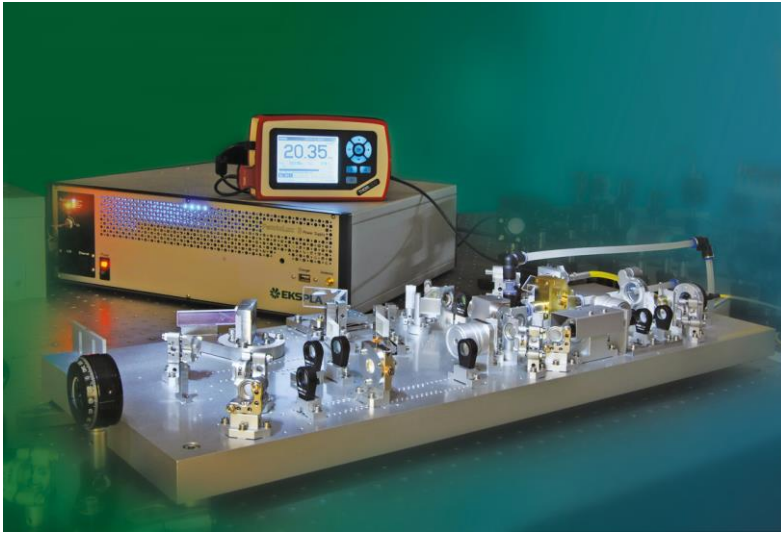
Fig. 4.17 Experimentally developed double-pass Yb:YAG amplifier at the prototyping stage. The size of the free-space part of the laser system was 600x250x160 mm^3 (length, width, and height), whereas the fiber and electronics part was conveniently placed in an industry-standard rack-mountable unit with the size of 436x449x140 mm^3. Courtesy of *Ekspla*.

4.4. Beam circularity degradation and depolarization loss investigation in end-pumped Yb:YAG amplifier

Thermal effects in the highly pumped gain medium cause significant power losses via depolarization if the laser system contains polarization-sensitive elements (e. g., Brewster plates, Faraday rotators, polarizers). In the end-pumped geometry and side cooling of such medium, a characteristic temperature distribution with its maximum in the center of element (which coincides with pumping region) and minimum at the medium outer surface results in axially symmetric temperature gradients. These gradients induce mechanical stresses in the pumped crystal, which lead to correlated to the gradient distribution of refractive indexes and birefringence over the cross-section of laser medium [35]. For [111]-cut Yb:YAG crystal, birefringence axes are oriented in the radial and tangential directions to gradient field (crystal axis of symmetry), leading to a common "cloverleaf" depolarized beam shape of initially linearly-polarized light at the input of amplifier [33]. Thermally-induced stresses not only affect spatial beam profile but result in bi-focusing, which spoils beam focusability [63].

This section is thus dedicated to the experimental investigation of such effects, which became prominent when investigated amplifiers were pumped with pump power higher than 84 W ($I_p > 82 \frac{kW}{cm^2}$).

114

Initially, beam bi-focusing due to thermal effects was estimated via the z-scan technique by measuring beam focusability change at the output of a single-pass Yb:YAG amplifier. The analyzed Yb:YAG amplifier was pumped with pump power up to $P_p = 110\ W$. Configuration was identical to the presented in previous sections, with input signal polarization oriented vertically to the lab reference plane (s-pol). Incident signal power was set to $P_s = 500\ mW$ (low gain regime), and pulse repetition rate was increased to $\sim 10\ MHz$ to avoid any measurement artifacts due to the possibility of the Kerr lens. The lens of $F = 300\ mm$ focal length was placed at a distance of $L = 2F$ from the crystal rod. Signal was reflected from a specially designed pump and signal beam separator, where a significant amount of pump is transmitted. Additional long-pass filter *FELH1000* (from *Thorlabs*) was placed in the signal path to block residual reflected pump radiation. Signal beam diameter evolution (at 4σ level) along propagation direction was measured in the vicinity of distance $L = 2F$ from the lens. At each z-scan position, the ratio of beam diameter along the major and minor axes was measured (defined as beam circularity, at 4σ level). The worst ratio ε was chosen as the figure of merit to define bi-focusing (beam ellipticity), with a lower value corresponding to stronger beam degradation. It was previously shown by *Ho W. Lo et al.* that this parameter is an invariant property of the Gaussian beam, and is not dependent on the optical scheme used for the measurement, as long as the scheme is stigmatic [118].

The initial ratio of seed source was measured to be $\varepsilon = 0.91$. Measurement scheme, signal beam characterization without any pump (for measurement illustration) and parameter ε dependence on absorbed pump power in the crystal are shown in Fig. 4.18, Fig. 4.19, and Fig. 4.20, respectively.
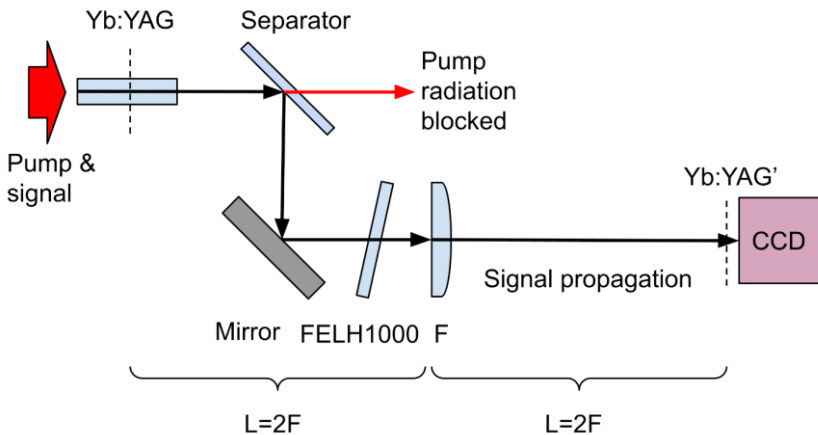
Fig. 4.18 Measurement scheme for beam diameter circularity ratio ε in the single-pass regime. Yb:YAG denotes the gain medium, whereas Yb:YAG' denotes the relayed image position of the crystal plane. A lens with a focal length of $F = 300\ mm$ was placed at a distance $L = 2F$ from the gain medium.

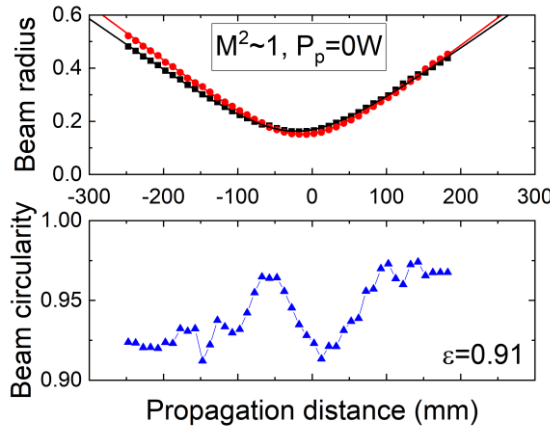**Beam radius**

$M^2 \sim 1,\ P_p = 0W$

Beam circularity

$\varepsilon = 0.91$

Propagation distance (mm)

Fig. 4.19 Measurement principle and results in case of no pump power ($P_P = 0\ W$), corresponding to the measured beam propagation quality of seed source after crystal. Beam radius along propagation direction was measured, and the ratio of major and minor beam axis was calculated. The worst ratio ε is displayed as an inset. Beam quality parameter M^2 was estimated from the fit (red and black curves).

15% beam circularity degradation with $P_p = 110W$

ε

Absorbed pump in crystal (W)
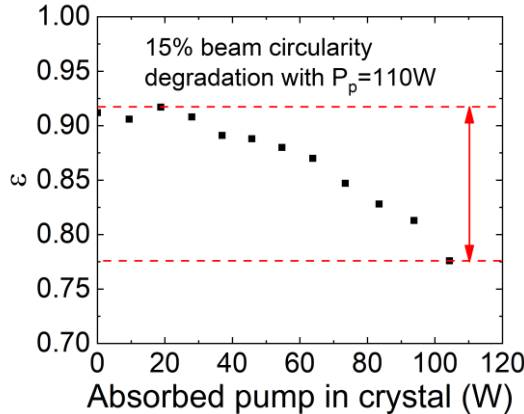
Fig. 4.20 Measurement results of bi-focusing effect. Parameter ε dependence on absorbed pump power in crystal. Maximum incident pump power was $P_P = 110\ W$ (corresponding to $\sim 105\ W$ of the absorbed pump), and pump power was varied in increments of $10\ W$.

Performed measurements indicated that the bi-focusing effect increased non-linearly with increasing incident pump power. In case of maximum tested incident pump power to the crystal $P_p = 110\ W$ (corresponding to the absorbed pump power of $\sim 105\ W$), beam circularity degraded by $\sim 15\ \%$, from $\varepsilon = 0.92$ (no pump) to $\varepsilon = 0.77$. This suggested that the bi-focusing

effect is significant at such incident pump intensity ($\sim 110\ \frac{kW}{cm^2}$), in part explaining why pumping power limit of $84\ W$ was chosen as the limit for previously presented schematics (corresponding to $\varepsilon \sim 0.85$, which in the author's opinion is reasonable).

To rule out the possibility that gain medium heatsink realization influenced the symmetry of heat removal from the crystal, thus introducing asymmetrical temperature gradients (also leading to beam circularity degradation), the following experiment was conducted. Crystal mount was rotated by 90°, and an identical measurement of parameter ε was performed. A comparison of measurement results for both cases is shown in Fig. 4.21.

Fig. 4.21 Measurement results of bi-focusing effect in the case when the crystal was placed horizontally and vertically (rotated by 90°)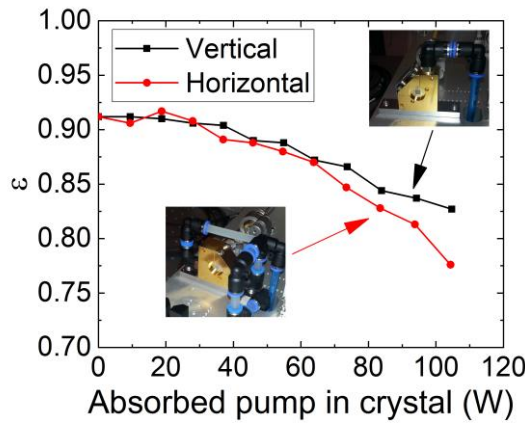. Parameter ε dependence on absorbed pump power in crystal. Maximum incident pump power was $P_P = 110\ W$ (corresponding to $\sim 105\ W$ of the absorbed pump), and pump power was varied in increments of $10\ W$.

Results indicated that heatsink realization had a measurable influence on the measured bi-focusing effect, suggesting that a slight asymmetry in temperature gradients of pumped crystal was present. At a maximum absorbed pump power of $P_p = 105\ W$, beam circularity degraded to $\varepsilon \sim 0.77$ in case of horizontal placement of crystal mount, and to $\varepsilon \sim 0.82$ in the case when crystal mount was rotated by 90°. However, the majority of beam circularity degradation can still be accounted to the bi-focusing effect.

To rule out the influence of initial signal beam circularity (and major/minor axis direction) on the bi-focusing effect, the following experiment was conducted at the maximum pump power of $P_p = 110\ W$. Identical z-scan measurement was performed but at the same time registering beam azimuth angle (angle between major beam axis and reference lab plane). Additionally, the signal beam collimator was rotated by 90°, thus introducing a modified

beam azimuth angle inside the crystal, and the same measurement was performed. Crystal mount was placed in the horizontal position. A comparison of the measured data for two cases is shown in Fig. 4.22. Measured beam spatial profiles in the case of the amplified signal beam are displayed in Fig. 4.23 for visualization purposes. Signal beam circularity evolution along beam propagation direction is depicted in Fig. 4.24.
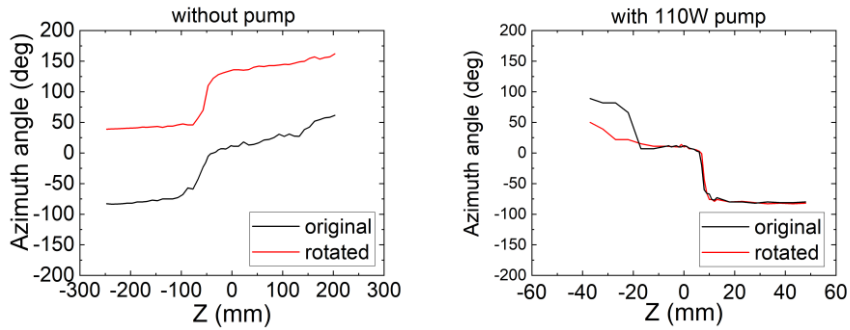
Fig. 4.22 <u>Left:</u> signal beam azimuth angle evolution of originally placed and rotated by 90° signal collimator. **<u>Right:</u>** amplified signal beam azimuth angle evolution. The azimuth angle of 0° degrees corresponds to the beam's major axis oriented horizontally.

| Z | -27 mm | -3 mm | 10 mm | 13 mm | 43 mm |
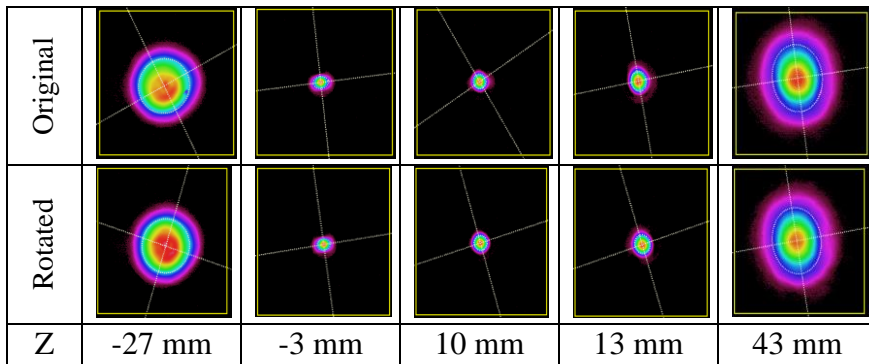
Fig. 4.23 Signal beam spatial profile evolution in the vicinity of the beam waist. The top row represents measurement at the original signal collimator position, whereas the middle row represents the case of the rotated signal collimator. The bottom row displays measurement position along beam propagation axis Z, as indicated in Fig. 4.24.

Fig. 4.24 Calculated (from the measurement data) beam circularity along the beam propagation direction when the crystal was pumped with a pump power of $P_p = 110\,W$. The solid red line corresponds to the original orientation of the signal beam (signal collimator), solid black line corresponds to the case when signal beam orientation was rotated by 90° signal (by rotating signal beam collimator).

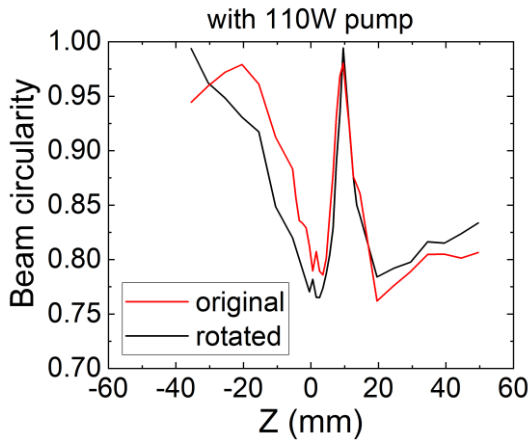Results clearly indicated that initial signal beam orientation inside the crystal rod had minimal effect on both: amplified signal principal axis orientation and resulting beam circularity degradation due to thermal effects inside Yb:YAG rod. Near beam waist, where measured beam circularity degradation was the highest (Fig. 4.24), beam orientation was practically identical (Fig. 4.22 right) despite initial signal beam orientation being significantly different (Fig. 4.22 left). Additionally, parameter $\varepsilon = 0.77$ was identical for both cases, although a slight mismatch of beam circularity at different propagation positions was seen. This suggests that in the current setup, the measured beam circularity degradation is in major part due to induced bi-focusing in crystal rather than possible systematic errors.

Retrieved results proved that beam circularity degradation in presented Yb:YAG amplifier configuration was mainly due to thermally induced bi-focusing. However, it also suggested that beam circularity degradation is most likely due to the incident signal beam polarization direction, which in the experiments was linear and oriented vertically (s-pol). In such configuration, different parts of the linearly polarized beam "see" different effective refractive index change due to different values of mechanical stresses in radial and tangential directions – for instance, the horizontal part of the beam experiences refractive index change due to mechanical stresses in the tangential direction, whereas vertical part is focused differently due to mechanical stresses in the radial direction, and remaining parts of beam

experience an effective refractive index change. Fig. 4.25 illustrates this effect.
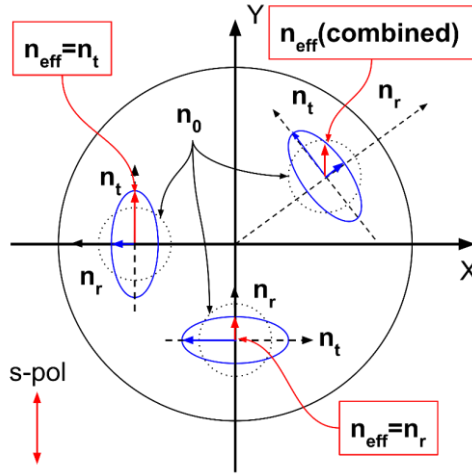
$n_{eff}=n_t$

n_{eff}(combined)

n_0

n_t

n_r

n_t

n_r

n_t

n_r

n_r

n_t

Y

X

s-pol

$n_{eff}=n_r$

Fig. 4.25 Orientation of refractive index indices in radial and tangential directions across pumped Yb:YAG gain medium. n_r denotes refractive index in the radial direction, n_t in the tangential direction, and n_{eff} denotes an effective refractive index that s-polarized signal beam experiences. Black dotted circles indicate the unperturbed refractive index n_0 ellipsoid, while blue ellipses indicate refractive index ellipsoid under thermal stress at different positions in pumped material.

Orienting the direction of linear polarization horizontally would yield differently oriented beam ellipticity, but beam circularity degradation would be similar. However, it was found that a rather simplistic approach would help alleviate the bi-focusing effect arising in the end-pumped Yb:YAG crystal rod. If the circularly polarized beam is amplified in the gain medium, every part of the beam will experience an identical effective refractive index induced by mechanical stresses, resulting in negligible ellipticity.

This assumption was tested experimentally. A quarter wave-plate was placed before the Yb:YAG crystal rod so that incident linearly polarized beam is transformed into the circularly polarized beam. Additional quarter wave-plate was placed after the Yb:YAG crystal to convert beam polarization back to linear. Z-scan measurement (as described previously) was performed. Results for the case of s-polarized, p-polarized, and circularly-polarized beam incident to the end-pumped Yb:YAG crystal rod with pump power $P_p = 110\ W$ are shown in Fig. 4.26.
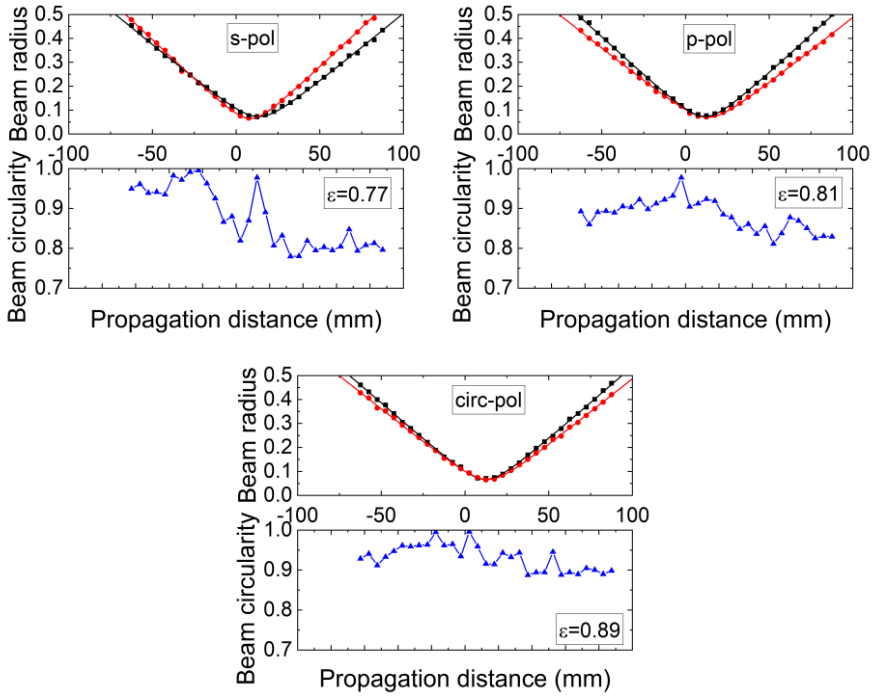
Fig. 4.26 Measurement of beam radius and circularity change along the beam propagation direction. Investigated cases are: (top-left) incident signal beam is s-polarized; (top-right) - incident signal beam is p-polarized; (bottom) incident signal beam is circularly-polarized. Input pump power to Yb:YAG amplifier was $P_p = 110\ W$, incident signal power $P_s = 0.5\ W$ (at $10\ MHz$ pulse repetition rate). Signal propagated in the single-pass regime. Initial signal beam circularity $\varepsilon = 0.91$.

Significant improvement in amplified beam circularity was measured in the case when the incident signal beam is circularly-polarized - merit parameter resulted in $\varepsilon = 0.89$. Slight degradation from the initial signal beam circularity of $\varepsilon = 0.91$ could be explained by uneven thermal gradients inside the crystal due to realization of crystal heatsink, as was discussed previously. Identically, the difference of the result in s-polarized and p-polarized beams can be explained.

However, such improvement comes at the price of increased depolarization loss. Depolarization loss in the end-pumped Yb:YAG single-pass amplifier configuration was measured by placing a high-contrast (1:1000) polarizing cube after the crystal, with pump radiation filtered out as described previously (Fig. 4.18). Depolarization loss dependence on absorbed pump power in the crystal is provided in Fig. 4.27.
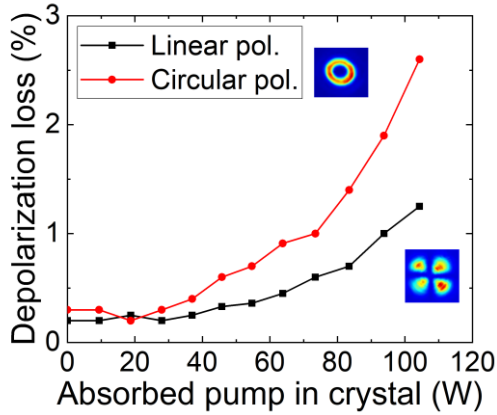
Fig. 4.27 Measurement of depolarization loss dependence on absorbed pump power in end-pumped Yb:YAG single-pass configuration. Cases of incident signal beam linear and circular polarization were investigated. Insets: depolarized beam profile in case of circular polarization (top) and in case of linear polarization (bottom).

Results indicated that depolarization loss increased almost two-fold in the case of the circularly-polarized beam. In the case of absorbed pump power of $105\,W$, depolarization loss resulted in $\sim 2.6\,\%$ (circular polarization) and $\sim 1.2\,\%$ (linear polarization).

In conclusion, the bi-focusing effect was shown to be a limiting factor in the end-pumped Yb:YAG amplifier configuration when the incident and absorbed pump power in the gain medium is sufficiently high. As a figure of merit parameter, the worst value of retrieved beam circularity ε during the z-scan measurement was evaluated. Measurements indicated that in the case of $105\,W$ of absorbed pump power, such parameter degraded from initial $\varepsilon = 0.91$ to $\varepsilon = 0.77$ (s-polarization) and to $\varepsilon = 0.81$ (p-polarization). As a practical remedy for such an effect, an optical configuration where the circularly-polarized signal beam is amplified in the gain medium was proposed. This yielded a significant improvement in beam circularity, reaching $\varepsilon = 0.89$. However, depolarization loss was measured to increase two-fold as compared to linear polarization case, resulting in $\sim 2.6\,\%$ power loss due to depolarization (in single-pass regime). It is expected that this loss would increase further in the double-pass regime (two times). However, in the author's opinion, the resulting beam quality is more important. Yb:YAG amplifier performance with proposed bi-focusing compensation setup in double-pass regime is presented in the next section.

4.5. Realization of 35 μJ, 1 MHz, 318 fs hybrid laser system

For the proposed hybrid laser realization, a different strategy in the choice of initial seed source was employed. An all-in-fiber seed source with a relatively broad initial signal bandwidth of $\Delta\lambda(FWHM) = 7.7\,nm$ was used with a sufficiently high output power of $3.3\,W$, corresponding to a pulse energy of $3.3\,\mu J$ at $1\,MHz$ of pulse repetition rate. Such choice of seed source parameters sufficiently saturated Yb:YAG amplifier, minimizing gain-narrowing effect, thus preserving broad signal spectral bandwidth after amplification. The design of the seed source was based on commercially available fiber laser *FemtoLux 3* from *Ekspla*.

Initial seed pulses were generated in the SESAM-based fiber oscillator, producing $1\,ps$ duration pulses with a spectral bandwidth of $1.55\,nm$ at full width half maximum (FWHM) level. These pulses were then linearly up-chirped to $10\,ps$, and spectral bandwidth broadened to $8\,nm$ at FWHM. Seed laser pulses were then further chirped to $\sim300\,ps$ duration pulses using chirped fiber Bragg grating (CFBG) stretcher with group delay dispersion (GDD) of $\beta_2 = -20.7\,ps^2$. Additional fiber amplifier was used after fiber-coupled acousto-optic modulator (AOM) to increase output power, generating $3\,W$ of average power, $1\,MHz$ repetition rate laser pulses (corresponding to a pulse energy of $3\,\mu J$) at $1030\,nm$ central wavelength and with a spectral bandwidth of $7.7\,nm$ at FWHM. CFBG was designed for pulse compression in a diffraction grating based pulse compressor with $1739\,mm^{-1}$ groove density diffraction grating. The developed CPA laser system layout is shown in Fig. 4.28.

The output of the all-in-fiber seed source featured a single-mode (SM) polarization-maintaining (PM) fiber with a core diameter of $15\,\mu m$ with a specially designed fiber-to-free-space collimator. The output beam from the fiber was collimated to a beam diameter of $1.5\,mm$, with diffraction-limited beam quality $M^2 \sim 1$, and beam circularity parameter $\varepsilon = 0.92$.

Chirped seed pulses were then directed to the identical DPSS Yb:YAG amplifier stage as described in previous sections. The geometry of c-cut ([111]) Yb:YAG crystal was $2x2x12\,mm^3$ with Yb^{3+} doping concentration of 3.6%. Both facets of the crystal were coated with high laser-induced damage threshold (LIDT) coatings ($\sim50\,J/cm^2$ for $10\,ns$ duration pulses). Additionally, two quarter waveplates were placed before and after Yb:YAG crystal to amplify circularly polarized signal beam in the gain medium, thus minimizing the bi-focusing effect. Seed and pump beams were focused to

respectively $\omega_p = 0.36 \ mm$ and $\omega_s = 0.33 \ mm$ diameters and overlapped in the amplifier crystal. Pump power up to $110 \ W$ was used.
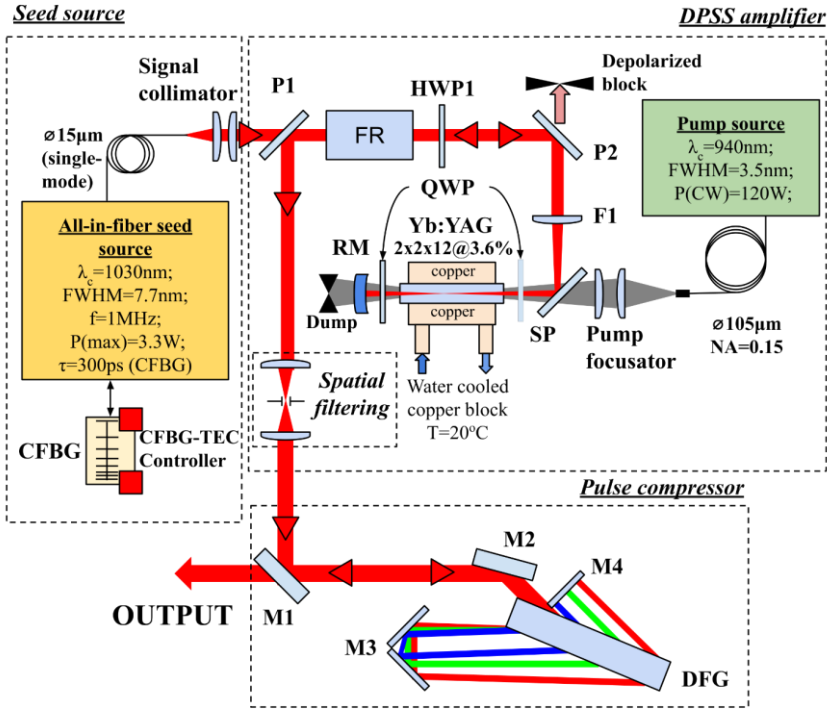

Fig. 4.28 Layout of the developed laser system, which consisted of an all-in-fiber seed source, free-space Yb:YAG amplifier ($2x2x12 \ mm^3$ with Yb^{3+} doping concentration of 3.6%), and pulse compressor. HWP1 – half-wave phase retardation plate, QWP – quarter-wave phase retardation plates, FR – Faraday rotator, P1, P2 – polarizers, SP – pump/signal wavelength separator, F1 – focusing lens for signal beam, RM – spherical mirror for signal beam double-pass realization, M1-M4 – mirrors, CFBG – chirped fiber Bragg grating, DFG – diffraction grating with a groove density of $1739 \ mm^{-1}$. Circulating water in crystal heatsink temperature was set to 20°C.

To evaluate seed pulse compression quality, pulses were compressed in $1739 \ mm^{-1}$ groove density 4-pass diffraction grating pulse compressor. Optimally compressed pulses were characterized by the second-harmonic generation frequency-resolved optical grating (SHG-FROG) autocorrelation method. The pulse duration retrieved by the FROG algorithm (*Swamp Optics*) using a 1024x1024 grid was $253 \ fs$ (Fig. 4.29). Transform-limited pulse duration derived from the output spectrum was $220 \ fs$. A slight mismatch between the measured and transform-limited pulses could be attributed to the accumulated nonlinear phase in the single-mode fiber, as was discussed earlier in this chapter. A residual spectral phase retrieved from FROG was $\sim 1.6 \ rad$ (corresponding to $\sim 0.5 \ \pi \ rad$) in the spectral range from $1022.3 \ nm$ to

1038.1 nm encompassing 98 % of total pulse energy. Strehl ratio of the compressed pulse, defined as the ratio of actual peak power of the pulse to the one of the transform-limited pulse, was 84 %, indicating high-quality femtosecond pulses.
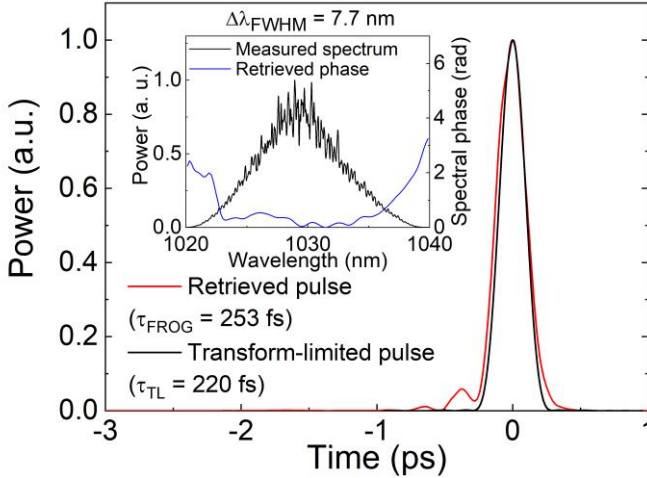
Fig. 4.29 Envelope of the compressed pulses retrieved from SHG FROG measurement compared to transform-limited pulse shape calculated from the measured spectrum. **Inset:** (left) measured amplified signal spectrum and retrieved spectral phase. FROG traces retrieval error was 0.15%.

Chirped seed pulses were amplified in a double-pass Yb:YAG amplifier. Input pump power was fixed to $P_p = 110\ W$, and input seed power was varied. The resulting amplifier characteristics are provided in Fig. 4.30.
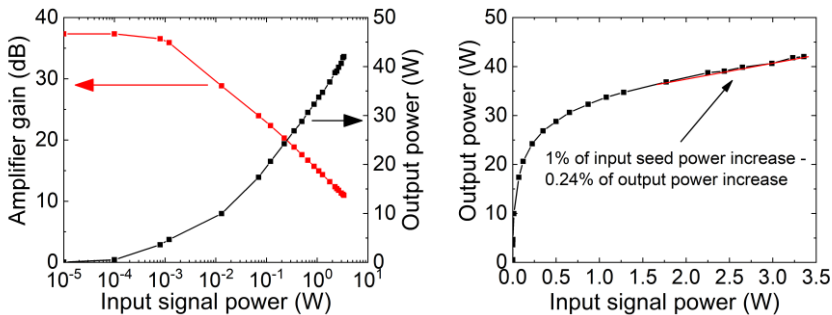
Fig. 4.30 Left: average output power (black curve, right axis) and total amplifier gain (red curve, left axis) of double-pass Yb:YAG amplifier versus input signal (seed) power (in logarithmic scale). The pulse repetition rate was 1 MHz. The amplifier was pumped by $P_p = 110\ W$ power. **Right:** average output power versus input signal power (linear scale), showing a significant power saturation level of the amplifier stage.

After double-pass through the amplifier, the crystal signal was amplified from $3.3\,W$ to an average output power of $\sim 42\,W$ at $1\,MHz$ of pulse repetition rate ($42\,\mu J$ pulse energy). For $110\,W$ of pump power, it corresponded to $\eta = 35.2\,\%$ of amplifier efficiency. Measured depolarization loss after double-pass was $8\,\%$, yielding total usable power of $38.3\,W$.

In the tested setup, a high amplified power saturation level was attained, similar to the case of the first presented configuration – $1\,\%$ change of input power transforms to $0.24\,\%$ output power change when the amplifier is seeded with average power higher than $2\,W$. Such a level of saturation is beneficial for the overall power stability of the system as it becomes less sensitive to seed power fluctuations. On the other hand, at low seed power, $\sim 37\,dB$ double-pass gain was achieved (small-signal gain regime).

At maximum seed power, spectral bandwidth after amplification in Yb:YAG crystal was reduced from $7.7\,nm$ to $3.3\,nm$ FWHM due to the gain narrowing effect. The measured spectra of chirped pulses before and after amplification at maximum output power are shown in Fig. 4.31.
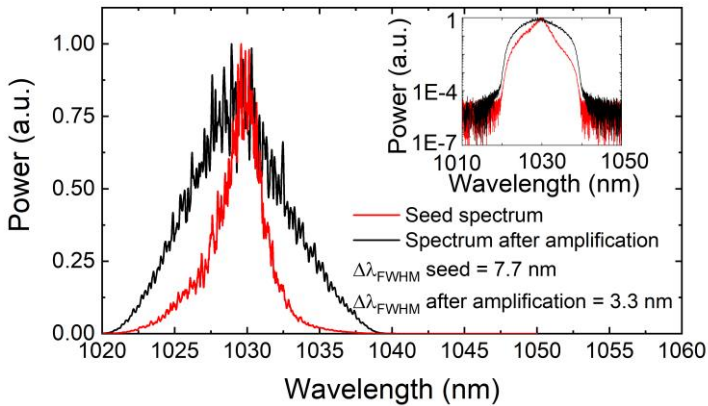
Fig. 4.31 Spectrum of the chirped seed pulses (black line) and spectrum of the chirped pulses after double-pass Yb:YAG amplifier (red line). Inset: the same spectra in logarithmic scale.

ASE level from the fiber laser was estimated from the broad spectral shoulders minimally visible in the logarithmic scale, as was discussed at the beginning of this chapter. By smoothly extrapolating these shoulders, one can obtain $\sim 35\,dB$ ASE level at the central $1030\,nm$ wavelength. Because there is no temporal gating in this realization of the laser system, both CW background and pulsed radiation were similarly amplified in Yb:YAG amplifier, resulting in $\sim 40\,mW$ of amplified background. The CW background that results from Yb:YAG amplifier was not directly measured, but the upper bound can be estimated from Fig. 4.30: when the input seed

power is very small ($10\ \mu W$), total gain reaches $\sim 37\ dB$, which corresponds to the output power of $\sim 54\ mW$. A large part of this output power was still the actual amplified signal. Furthermore, at high input seed power, output power after the amplifier is $42\ W$, resulting in considerable Yb^{3+} upper-state depletion and reducing ASE. Conservatively one can estimate that ASE from Yb:YAG amplifier is $< 10\ mW$ at full output power, an insignificant amount compared to the ASE from the fiber amplifiers.

The amplified signal beam was then spatially filtered, resulting in ~5% power loss of the amplified beam, yielding $36.4\ W$ average output power. After spatial filtering, beam quality parameter M^2 and beam circularity was measured using standard z-scan technique focusing the beam by a positive lens of well-defined focal length and tracing the beam radius change along the propagation direction. The best fit yielded M^2~1.0, indicating a diffraction-limited beam quality. The measurement graph after spatial filtering is shown in Fig. 4.32.
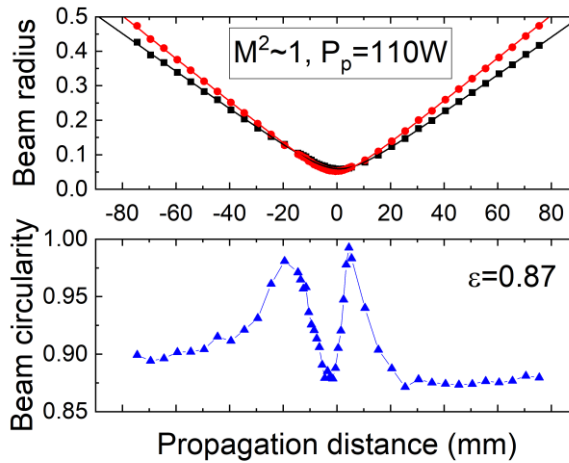
Fig. 4.32 Measurement of beam radius and circularity change along beam propagation direction after spatial filtering of the amplified signal beam. Measured beam circularity was $\varepsilon = 0.87$, and an initial signal was $\varepsilon = 0.92$. The beam quality parameter was estimated to be M^2~1.0 from the fit (red and black curves). Input pump power to Yb:YAG amplifier was $P_p = 110\ W$, incident signal power $P_s = 3.3\ W$ (at $1\ MHz$ pulse repetition rate).

Diffraction-limited beam quality was achieved (M^2~1), with minimal beam circularity degradation from the initial $\varepsilon = 0.92$ to $\varepsilon = 0.87$, proving that circularly-polarized beam amplification is significantly beneficial to minimize the bi-focusing effect as compared to amplification of linearly-polarized beam (in terms of resulting beam quality). The observed minimal

degradation was due to the realization of the crystal heatsink, as was discussed in the previous section.

The spatially filtered beam was then directed to a 4-pass diffraction grating pulse compressor, with $1739\ mm^{-1}$ groove density diffraction grating. The measured diffraction and reflection losses in the pulse compressor were $\sim 10\ \%$, resulting in the output power of $\sim 32.8\ W$. Pulses were optimally compressed, where residual dispersion was compensated by applying a thermal gradient on the CFBG stretcher (for more details, see [15,112]). Optimally compressed pulses were characterized by the second-harmonic generation frequency-resolved optical gating (SHG-FROG) autocorrelation method. The pulse duration retrieved by the FROG algorithm (*Swamp Optics*) using a 1024x1024 grid was $318\ fs$ (Fig. 4.33). Transform-limited pulse duration derived from the output spectrum was $315\ fs$, indicating an excellent pulse compression quality. The resulting comparatively short pulse duration is due to a broad range of remaining spectral components after amplification, which contains sufficient power to maintain short compressed pulse duration, even though spectral bandwidth at FWHM is narrow ($\Delta\lambda(FWHM) = 3.3\ nm$). Such effect was numerically investigated in Chapter 3 of this thesis. A residual spectral phase retrieved from FROG was $\sim 1.6\ rad$ (corresponding to $\sim 0.5\ \pi\ rad$) in the spectral range from $1021.5\ nm$ to $1033.8\ nm$ encompassing $98\ \%$ of total pulse energy. Strehl ratio of the compressed pulse, defined as the ratio of actual peak power of the pulse to the one of the transform-limited pulse, was $83\ \%$, indicating high-quality femtosecond pulses. Measurement results indicated that signal amplification in highly end-pumped Yb:YAG double-pass amplifier did not degrade the compressed pulse quality.
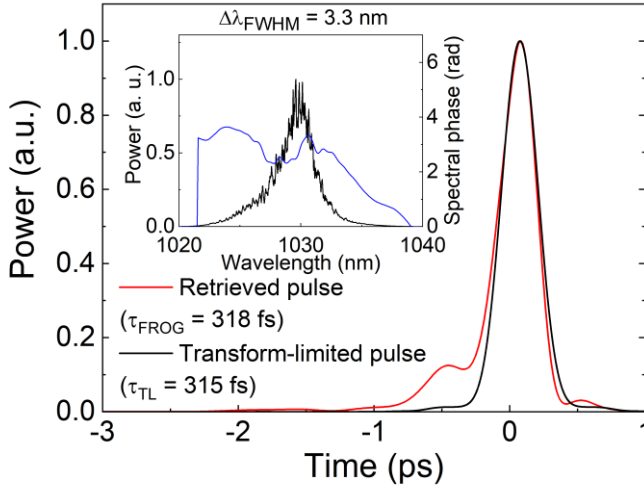
Fig. 4.33 Envelope of the compressed pulses at the output of hybrid laser system, retrieved from SHG FROG measurement compared to transform-limited pulse shape calculated from the measured spectrum. **Inset:** (left) measured amplified signal spectrum and retrieved spectral phase. FROG traces retrieval error was 0.15%.

Beam quality after pulse compressor was characterized by the same z-scan technique of focused beam (Fig. 4.34). Overall beam quality was diffraction-limited ($M^2 \sim 1$), with beam circularity parameter $\varepsilon = 0.87$, suggesting that pulse compression in 4-pass diffraction grating compressor did not introduce any beam quality degradation.
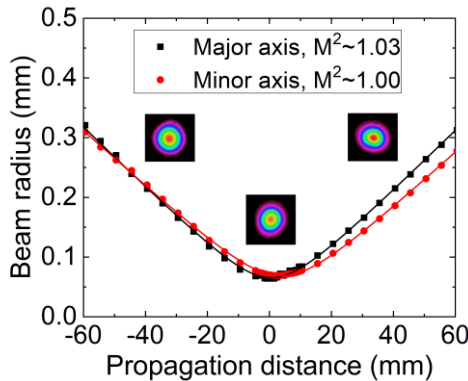
Fig. 4.34 Beam radius measurement along propagation direction after 4-pass diffraction grating based pulse compressor via z-scan technique (red and black dots). Beam quality parameter $M^2 \sim 1$ was estimated from the fit (red and black curves). Images of the beam profile at a few positions are shown as insets (beam size was normalized for clarity).

In conclusion, a compact ultrafast laser system based on fiber seed laser and Yb:YAG crystal rod power amplifier was developed. The key novelty of such configuration was the amplification of circularly-polarized input signal beam, which significantly mitigated the bi-focusing effect. Matched dispersion of CFBG as pulse stretcher and 4-pass diffraction grating pulse compressor enabled to obtain nearly bandwidth-limited compressed sub-picosecond pulses. The presented laser system produced pulses of $318\,fs$ duration and $32.8\,\mu J$ energy at $32.8\,W$ average power, which corresponds to the peak power of $P_p \sim 0.1\,GW$, with diffraction-limited beam quality with good beam circularity ($M^2 \sim 1, \varepsilon = 0.87$), and amplifier efficiency of $\eta = 35.2\,\%$ (without depolarization and spatial filtering losses). In the tested setup, a high amplified power saturation level was attained – $1\,\%$ change of input power transforms to $0.24\,\%$ output power change when the amplifier is seeded with average power higher than $2\,W$. Such a level of saturation is beneficial for the overall power stability of the system as it becomes less sensitive to seed power fluctuations. Proposed relatively simplistic laser architecture enables the construction of truly compact and robust high energy and high average power ultrashort pulse lasers for a wide range of applications.

4.6. Summary

In this chapter, various end-pumped Yb:YAG amplifier schematics were experimentally demonstrated. The strategy of laser system design was based on employing a hybrid laser approach, where initial signal pulses were generated in a fiber oscillator based on Yb^{3+} doped fiber and SESAM (developed by *Ekspla*), pre-amplified to moderate energy and power levels (> $1\,\mu J$) using CPA technique, and further peak power scaling was performed in developed double-pass Yb:YAG DPSS amplifier.

In the first section, a configuration that employed a CFBG stretcher and CVBG compressor with matched dispersion was presented, which enabled to obtain nearly bandwidth-limited compressed sub-picosecond pulses. The presented laser system produced pulses of $764\,fs$ duration and $104\,\mu J$ energy at $20.8\,W$ of average power, which corresponds to a peak power of $P_p \sim 0.13\,GW$, with nearly diffraction-limited beam quality ($M^2 \sim 1.15$, $\varepsilon = 0.91$), and free-space amplifier efficiency of $\eta = 28\,\%$. Configuration operated in a moderate-gain regime when significant bandwidth narrowing of the initial signal was expected. Strategically, an all-in-fiber seed source with a relatively narrow initial signal bandwidth of $\Delta\lambda(FWHM) = 3.6\,nm$ was

used to modestly mitigate the gain narrowing effect. In the tested setup, a high amplified power saturation level was attained – 1 % change of input power transforms to 0.13 % output power change when the amplifier is seeded with average power higher than $0.3\ W$. Such a level of saturation is beneficial for the overall power stability of the system as it becomes less sensitive to seed power fluctuations.

In the second section, a similar approach was used to demonstrate $1\ mJ$ energy pulses at $14\ kHz$ pulse repetition rate, with a pulse duration of $815\ fs$. Dispersion matched pair of CFBG as pulse stretcher and 4-pass diffraction grating based pulse compressor was employed. Nearly bandwidth-limited compressed sub-picosecond pulses were achieved after pulse compression. The presented laser system produced pulses of $815\ fs$ duration and $\sim 1\ mJ$ energy at $14.4\ W$ of average power, which corresponds to a peak power of $P_p \sim 1.16\ GW$, with diffraction-limited beam quality ($M^2 \sim 1, \varepsilon = 0.9$), and amplifier efficiency of $\eta = 19\ \%$.

In the third section, limiting factors of proposed configurations were discussed. Measurement of depolarization and beam circularity parameter of presented configurations was performed. A practical solution for improving beam circularity was proposed, which employed circularly-polarized signal beam amplification in the end-pumped Yb:YAG crystal rod.

In the last section of this chapter, a different strategy in the choice of initial seed source was employed. An all-in-fiber seed source with a relatively broad initial signal bandwidth of $\Delta\lambda(FWHM) = 7.7\ nm$ was used, however, with sufficiently high initial signal power of $3.3\ W$, which significantly saturated Yb:YAG amplifier. Such configuration operated in low-gain and high amplified signal power saturation regimes, thus reducing the gain-narrowing effect. As a result, $32\ \mu J$ energy pulses at $32\ W$ average power, and at $1\ MHz$ pulse repetition rate, with pulse duration below $318\ fs$ were demonstrated at the output of laser system, which corresponds to the peak power of $P_p \sim 0.1\ GW$, and amplifier efficiency of $\eta = 35.2\ \%$. Dispersion matched pair of CFBG as pulse stretcher and 4-pass diffraction grating based pulse compressor was employed. Additionally, a proposed amplifier schematic where the circularly-polarized signal beam is amplified was employed, which significantly mitigated the bi-focusing effect, resulting in diffraction-limited beam quality with good beam circularity ($M^2 \sim 1, \varepsilon = 0.87$). In the tested setup, a high amplified power saturation level was attained – 1 % change of input power transforms to 0.24 % output power change when the amplifier is seeded with average power higher than $2\ W$. Such a level of saturation is

beneficial for the overall power stability of the system as it becomes less sensitive to seed power fluctuations.

In conclusion, the proposed relatively simplistic laser architecture enabled the construction of truly compact and robust high energy and high average power ultrashort pulse lasers for a wide range of applications. The proposed double-pass Yb:YAG configuration is significantly less complicated than similar parameters laser systems based on *InnoSlab*, *Taranis* modules or multi-pass configurations while reaching similar or higher peak power in the range of $\sim 0.1 - 1\ GW$ in the sub-ps regime [30,74–77], but yet operating at room temperature ($T \sim 20°C$). Additionally, with the help of spatial beam filtering, diffraction limited beam quality $M^2 \sim 1$ was achieved, which is not always the case for other proposed systems.

The limiting factors for further peak power scaling are tied to increasing depolarization losses, beam quality degradation, or limitation induced by the damage threshold of optical coatings, as was briefly discussed in this chapter.

As a result, in the next chapter, a strategy of employing a two-cascade Yb:YAG amplifier system was chosen, where beam diameter was sufficiently expanded in the second cascade to avoid the optical damage of optical coatings. Significantly higher pumping power was thus needed, leading to unavoidably large depolarization losses. A novel depolarization compensation method was employed, which is presented in the last chapter of my thesis.

5. Experimental development of the two-cascade end-pumped Yb:YAG amplifier with depolarization compensation

Material related to this Chapter was published in A2 and A3

5.1. Introduction

Yb:YAG gain medium features high absorption and amplification cross-sections and high thermal conductivity, making it one of the most efficient Yb-doped material for application as a laser amplifier [22]. Though Yb-doped materials have a quite small quantum defect when pumped by $940\ nm$ laser diodes (and even lower when pumped by $969\ nm$, but such scenario is not investigated in this thesis), thermal effects in highly pumped gain medium cause significant power losses via depolarization if a laser system contains polarization-sensitive elements (e. g. Brewster plates, Faraday rotators, polarizers). In the end-pumped geometry and side cooling of a such medium, a characteristic temperature distribution with its maximum in the center of element (coincides with pumping region) and minimum at the medium outer surface, results in axially symmetric temperature gradients. These gradients induce mechanical stresses in the pumped crystal, which lead to correlated to gradient distribution of refractive indexes and birefringence over the cross-section of laser medium [33,35]. For the [111]-cut Yb:YAG crystal, birefringence axes are oriented in the radial and tangential directions to the gradient field (crystal axis of symmetry), leading to a common "cloverleaf" depolarized beam shape of initially linearly-polarized light at the input of the amplifier. Fig. 5.1 illustrates the impact of thermal stress on a linearly polarized beam propagating through the end-pumped isotropic Yb:YAG crystal.

Thermally-induced stresses not only affect spatial beam profile but result in polarization-dependent astigmatism (bi-focusing), which spoils beam focusability [63], as was discussed and experimentally investigated in the previous chapter. The illustration of polarization-dependent astigmatism is depicted in Fig. 5.2.
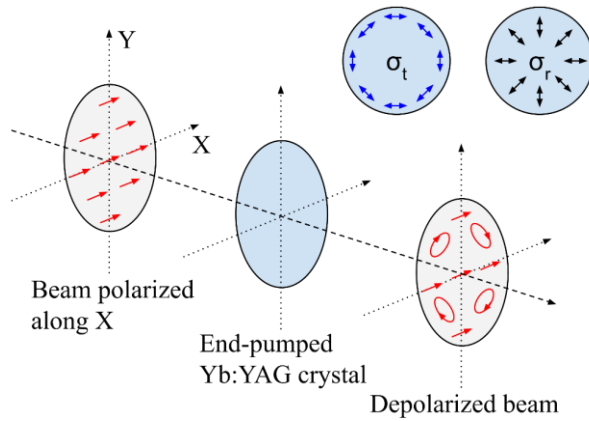
Fig. 5.1 Depolarization and bi-focusing illustration for a linearly polarized beam propagating through the end-pumped isotropic Yb:YAG crystal under thermal stress. σ_t and σ_r denote the principal stresses corresponding to tangential and radial directions (marked with blue and black arrows).
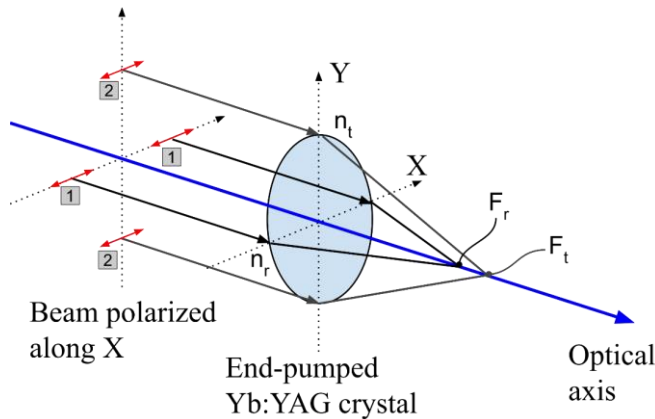
Fig. 5.2 Polarization-dependent astigmatism. A horizontally polarized ray propagates through the end-pumped Yb:YAG crystal. Rays 1 see radial refractive index n_r, whereas rays 2 see tangential refractive index n_t.

In principle, if depolarization and bi-focusing problems for the end-pumped Yb:YAG amplifier are solved, it would be preferable geometry compared to other geometries, e.g., thin disk or crystal fiber [43,44], mainly due to its simplicity. Crystal fiber-based amplifiers are usually arranged in the double-pass configuration for signal beam, whereas pump radiation propagates in the single-pass regime. Crystal fiber provides means for excellent thermal management due to the high surface-to-volume ratio, however, still suffering from depolarization losses. Additionally, crystal fiber is state-of-the-art technology, which might prove to be not cost-efficient in building independent amplifier systems. On the other hand, thin disk geometry

is less sensitive to depolarization losses, however, it requires multi-pass amplification arrangements due to relatively short gain length.

A very promising technology, which allows mimicking birefringence of thermally stressed Yb:YAG crystals is the technology of inscription by femtosecond laser of the so-called nano-gratings in optically transparent materials, e.g., fused silica [6,65–67]. The formation of self-assembled periodic sub-wavelength structures ("nanogratings") in a volume of bulk fused silica glass has been announced as one of the breakthroughs in photonics [119]. These modifications exhibit optical anisotropy with controllable birefringence, allowing the fabrication of different unique optical elements. Worth mentioning are the S-waveplates, linear to radial or azimuthal polarization converters, birefringent phase gratings and holograms, rewritable 5D optical memory, spatial beam formation tools, and many others, all exhibiting high damage threshold of bulk fused silica glass [5,120]. The main feature of these nano-gratings is that, by choosing certain parameters range of femtosecond laser, one can precisely point-by-point inscribe oriented birefringence in the volume of transparent material featuring no absorption and very low scattering [121], which in theory would allow to fully compensate depolarization and bi-focusing created in the end-pumped Yb:YAG gain medium.

Knowledge of depolarization level in Yb:YAG laser amplifier and amplified laser beam parameters (shape and initial polarization state) are then necessary to design an appropriate depolarization compensator (spatially variable waveplate or SVWP). This chapter is thus dedicated to upgrading the previously presented axis-symmetric modeling approach to full-3D, which would allow the extraction of necessary information (depolarization and beam shape) of the amplified beam in the end-pumped Yb:YAG gain medium for SVWP design. Additionally, a numerical description of depolarization compensator is also presented, and practical insights for using such element are provided.

In the experimental section of this chapter, for further peak-power scaling, an additional cascade of double-pass Yb:YAG amplifier was developed, seeded by the pulses generated from the hybrid laser presented in Chapter 4 of this thesis. Such configuration was pumped by $280\,W$ of power at $940\,nm$ and operated in low-gain and high amplified signal power saturation regime, thus reducing the gain-narrowing effect. $129\,\mu J$ energy pulses at $1\,MHz$ of pulse repetition rate were achieved at the output of the amplifier with high depolarization losses of $17.9\,\%$, and severe beam distortions. A novel approach of depolarization and bi-focusing compensation by SVWP allowed to reduce depolarization to $2.7\,\%$ with bi-focusing term minimized. Amplified

pulses were temporarily compressed in a 4-pass diffraction grating pulse compressor, yielding a pulse duration of $441\ fs$. The presented laser system produced $116\ \mu J$ energy pulses at $116\ W$ of average power at $1\ MHz$ of pulse repetition rate, totaling to the peak power of $0.25\ GW$. Such demonstration, in my opinion, provides sufficient proof that the end-pumped double-pass Yb:YAG amplifier configuration, together with SVWP, is a rather simplistic and efficient technology for peak power scaling, being more advantageous compared to other technologies.

5.2. Full-3D model of the end-pumped Yb:YAG amplifier

End-pumped Yb:YAG crystal in power amplifier layout introduces wavefront and polarization distortions in initially near-ideal Gaussian beam profile. Such distortions could be asymmetrical in nature (e.g., bi-focusing), so the axis-symmetric model, which was presented in Chapter 2 of the thesis, is insufficient for this task. In this section, I present differences in the numerical modeling approach, extending the axis-symmetric model case to a fully three-dimensional one.

In the updated model, the crystal rod was divided into a finite number of slices along the signal beam propagation direction. Each slice was then discretized into a finite number of elements in a two-dimensional grid. A number of elements in this grid was based on beam size to ensure fine sampling of the beam shape. The length of each slice dz was based on the Rayleigh length z_R of propagating signal beam, ensuring that $dz \ll z_R$, and additionally ensuring that the small-signal gain condition was satisfied [99]. Additional tuning of discretization parameters was completed for a balance of calculation speed and solution convergence.

Signal and pump beam in continuous-wave (CW) regime were launched along discretized crystal rod (end-pumping case). Modeling of signal beam propagation and amplification in crystal rod was based on an iterative procedure, iterating through slices consecutively in forward and backward directions to complete double-pass amplifier configuration, whereas pump beam propagated in the forward direction only (Fig. 5.3).
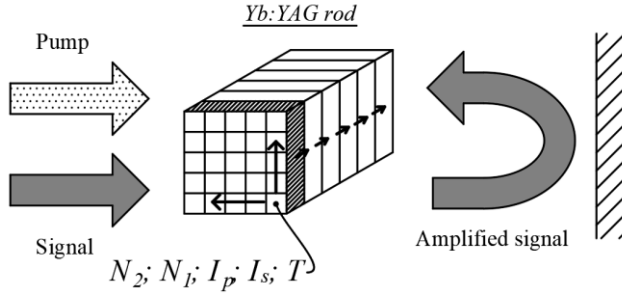
Fig. 5.3 Schematic of signal and pump radiation propagation in the double-pass amplifier configuration. The crystal rod was divided into slices, and each slice was discretized into a finite number of elements. At each element of slices population densities N_2, N_1, signal and pump intensities I_s, I_p and temperature values T were calculated.

Population density of the upper energy manifold N_2 was calculated independently at each element of the slice. A quasi-three level medium kinetics model which accounts for pumping, lasing, and fluorescence loss was used, determining a steady-state solution, as described in Chapter 2 of the thesis [109,122–124]:

$$N_2 = \frac{\dfrac{\sigma_a I_p}{h v_p} + \dfrac{\sigma_a I_s}{h v_s}}{\dfrac{1}{\tau} + \dfrac{(\sigma_a + \sigma_e) I_p}{h v_p} + \dfrac{(\sigma_a + \sigma_e) I_s}{h v_s}}, \tag{5.1}$$

where N_1, N_2 indicates the fractional level population of the ground and the upper level accordingly, σ_a, σ_e correspond to the effective absorption and emission cross-sections, I_s, I_p are the signal and pump optical intensities, $h v_s, h v_p$ indicate the signal and pump photon energies, τ is an upper-state lifetime. Gain $\Gamma = N_2 \sigma_e - N_1 \sigma_a$ and relative power change (signal amplification and pump absorption) $P_{out} = P_{in} \times \exp(\Gamma dz)$ at each element is then calculated with the given signal and pump optical intensities. Spectroscopic cross-sections are dependent on temperature $\sigma_a(T), \sigma_e(T)$, which is also accounted for in this model (data taken from *J. Koerner et al.* [47]).

Temperature distribution due to pump absorption (quantum defect) was calculated at each slice based on the semi-analytical solution [30,45,94] (more details can be found in Chapter 2 of this thesis):

$$T(r) = -\int_0^r \frac{h(r')}{k(T)} dr' + T_0, \tag{5.2 a}$$

$$r = \sqrt{x^2 + y^2}, \tag{5.2 b}$$

where h is the heat flux density (W/m²), k is the thermal conductivity coefficient (W/mK), r is the radial coordinate, x, y are the transverse coordinates in a two-dimensional grid, T_0 is the temperature at crystal/coolant interface (cooling temperature), and $T(r)$ is the temperature distribution. This equation takes into account pump beam shape but does not account for non-axis-symmetric temperature gradient case. Such an approach was chosen for calculation speed and, in my opinion, is a sufficient approximation, as temperature gradient asymmetry arising due to non-symmetrical pump beam shape or uneven heat removal between crystal and heatsink is negligible and was not investigated separately.

Calculation of pump beam shape and propagation within crystal rod was based on the ABCD matrix method, as was presented earlier in Chapter 2. Prior to the iterative procedure, the pump beam shape at each discretized slice was pre-calculated. Relative power was accordingly updated during iterations of the model, whereas propagation characteristics were left unchanged.

The signal beam was expressed as complex electric field amplitude, and its propagation in the crystal rod was based on the Fourier-transform method [99]. To account for the lensing effect, which arises within the Yb:YAG rod due to thermal effects, multiplication of propagated electric field by the corresponding phase factor $\exp(-i\varphi)$ was completed after each slice. Heat-induced thermal lens via thermo-optic coefficient, and stress-induced lens via photo-elastic effect were included in the model [125,126], with given expressions accordingly:

$$\exp\left(-i\frac{2\pi}{\lambda}\frac{dn}{dT}\Delta T dz\right), \tag{5.3 a}$$

$$\exp\left(-i\frac{2\pi}{\lambda}2n_0^3\alpha_T C_{r,\theta}\,\Delta T dz\right), \tag{5.3 b}$$

where λ is the seed wavelength, dn/dT is the thermo-optic coefficient, ΔT is the temperature difference between the crystal center and the crystal edge, dz is the propagation distance, n_0 is the unperturbed refractive index, α_T is the thermal expansion coefficient, $C_{r,\theta}$ is the photoelastic constant (for the radial and tangential direction, respectively). In the model, plane-stress approximation is used (end-pumping case) - values of photoelastic constants are then $C_r = +0.0032$ and $C_\theta = -0.011$. More information can be found in the work of *S. Chenais et al.* [45].

The initial electric field was split into two orthogonal principal electric fields E_x and E_y to account for polarization-sensitive lensing due to stress-induced birefringence:

$$E_0 = \begin{pmatrix} E_x \\ E_y \end{pmatrix} = \begin{pmatrix} \cos\beta \, E_{0x} \\ \sin\beta \, E_{0y} e^{i\Delta\varphi} \end{pmatrix}, \tag{5.4}$$

where E_{0x}, E_{0y} are the amplitudes of the electric field in the horizontal and vertical plane, $\Delta\varphi$ is the phase difference between two polarized fields, β is the orientation of linearly polarized light direction with respect to the horizontal plane.

Each component was propagated individually. Using Jones matrix formalism, polarization components were coupled via the off-diagonal element of the stress-index matrix at each slice [33,125]. Electric field E_x and E_y values were then recalculated at each slice during iterative procedure, based on birefringence induced at each element of slice:

$$E_x = E_{x0}\left(e^{-i\frac{2\pi}{\lambda}\frac{dn_r}{dT}\Delta T \, dz}\cos^2\theta + e^{-i\frac{2\pi}{\lambda}\frac{dn_\theta}{dT}\Delta T \, dz}\sin^2\theta\right)$$
$$+ E_{y0}\left(e^{-i\frac{2\pi}{\lambda}\frac{dn_r}{dT}\Delta T \, dz}\sin\theta\cos\theta - e^{-i\frac{2\pi}{\lambda}\frac{dn_\theta}{dT}\Delta T \, dz}\sin\theta\cos\theta\right), \tag{5.5 a}$$

$$E_y = E_{x0}\left(e^{-i\frac{2\pi}{\lambda}\frac{dn_r}{dT}\Delta T \, dz}\sin\theta\cos\theta - e^{-i\frac{2\pi}{\lambda}\frac{dn_\theta}{dT}\Delta T \, dz}\sin\theta\cos\theta\right)$$
$$+ E_{y0}\left(e^{-i\frac{2\pi}{\lambda}\frac{dn_r}{dT}\Delta T \, dz}\sin^2\theta + e^{-i\frac{2\pi}{\lambda}\frac{dn_\theta}{dT}\Delta T \, dz}\cos^2\theta\right), \tag{5.5 b}$$

where E_{x0}, E_{y0} are input electric fields in the horizontal and vertical plane, θ is the angle between reference polarization axis and local birefringence axis, $\frac{dn_{r,\theta}}{dT} = 2n_0^3\alpha_T C_{r,\theta}$ is the coefficient of stress-induced refractive index change in radial (r) and tangential (θ) directions.

By combining included lensing and polarization-dependent effects and following Jones matrix formalism, we can write the final expression for the signal beam that passed the pumped gain medium:

$$E = e^{-i\frac{2\pi}{\lambda}n_0 dz}e^{-i\frac{2\pi}{\lambda}\left[\frac{dn}{dT}\Delta T\right]dz}\begin{pmatrix} E_x \\ E_y \end{pmatrix}. \tag{5.6}$$

The modeling algorithm of signal beam propagation through gain media was based on an iterative procedure, where the algorithm convergence parameter was crystal rod temperature (see Fig. 5.4). First, initial modeling parameters were set – initial temperature of crystal $T(x, y, z)$, pre-calculated pump beam intensity profile $I(x, y, z)$ at each slice of crystal, gain media parameters (thermal conductivity k, upper-state lifetime τ, crystal doping concentration, unperturbed refractive index of gain media, crystal geometry, initial spectroscopic absorption, and emission cross-sections) and the initial signal and pump beam parameters (power and beam size, polarization state for seed beam). The iterative procedure started with the first pass through the

gain media. Initial parameters were used to calculate population densities N_2 and N_1, gain coefficients Γ_s and Γ_p, and amplified (or absorbed) power P at the initial slice within each element separately. The amplified signal beam was then propagated through a slice with resulting lensing effects. With updated power values and beam parameters of signal and pump, the procedure was repeated for the next consecutive slice. Such iterative procedure was repeated until the last slice was reached. Then resulting temperature map $T(x, y, z)$ of the crystal rod was retrieved. The algorithm repeated the first-pass iterative procedure until the difference between newly and previously retrieved temperature values within each slice and element were below convergence value.

Second-pass modeling was started by retrieving the calculated signal and pump intensity values $I(x, y, z)$ across the crystal rod slices and elements. Then signal beam was relay-imaged from and back to crystal to compensate for the lensing effect that resulted in the first-pass through the gain medium. The iterative procedure with slices where population density, gain, and fractional power change at each element was calculated was then started until the last slice was reached. Retrieved signal and pump intensity values from the first-pass were used as additional input parameters to accommodate for population density change due to first-pass propagation. The output power of signal after the second-pass was then compared with previously retrieved value – if the difference was above convergence value, the algorithm was repeated starting with first-pass, but with signal and pump intensity values from second-pass used as additional input parameters with updated spectroscopic coefficients due to newly retrieved temperature distribution map. When convergence was reached, the algorithm stopped, and the solution of beam output was determined.
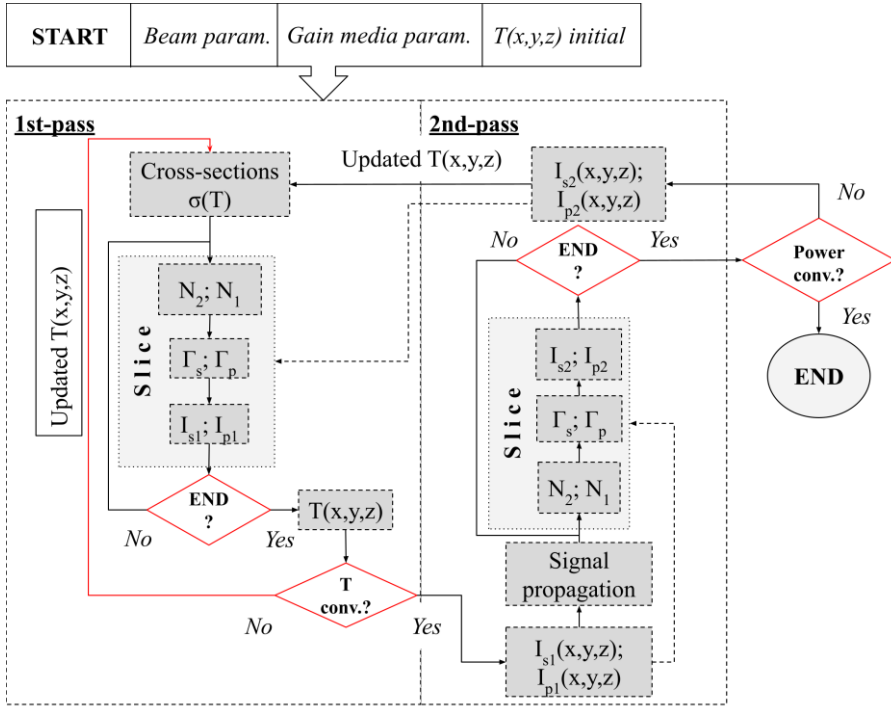
Fig. 5.4 Schematic drawing of iteration algorithm for solving signal beam amplification in Yb:YAG gain media. $T(x, y, z)$ corresponds to calculated temperature distribution map of end-pumped Yb:YAG crystal, N_1, N_2 correspond to population densities of ground and upper energy levels, respectively, Γ_s, Γ_p are calculated gain coefficients for signal and pump radiation, I_s, I_p correspond to signal and pump intensity, with subscript numbers indicating values retrieved in first-pass (1) and second-pass (2) regimes.

5.3. Spatially variable waveplate model and discussion

Spatially variable waveplates can be designed for incident beams with either linear or circular polarization. In both cases, a continuously varying fast and slow axis orientation is constructed, with a fast axis aligned to tangential direction, as is shown in Fig. 5.5. A radially varying birefringence value is continuously formed at each point, where phase retardance δ between the fast and slow axes (coinciding with tangential and radial respectively) can be expressed as:

$$\delta(r) = \frac{\lambda}{2}\left(\frac{r}{R}\right)^2,$$ (5.7)

where λ - wavelength, r – radial coordinate, R – radial coordinate of an element where phase retardance reaches a value of $\lambda/2$.
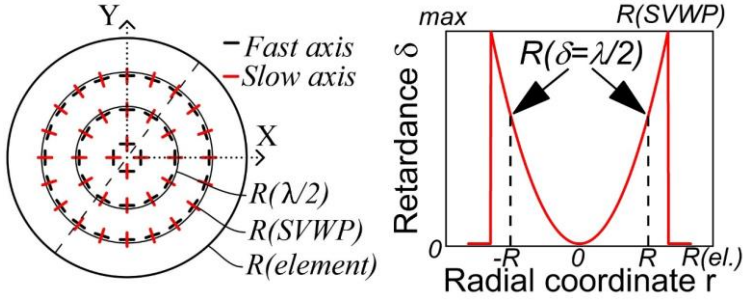
Fig. 5.5 Left: two-dimensional fast and slow axis orientation distribution map. $R(\lambda/2)$ marks the contour of SVWP where phase retardance is $\lambda/2$, $R(SVWP)$ marks the edge of the inscribed birefringence map, $R(element)$ marks radius of the glass substrate of the element. **Right:** retardance profile across the dashed line within SVWP element.

Following Jones matrix formalism, the SVWP element can be expressed as a phase retarder with arbitrary retardation along the radial and tangential axis [33,125]. The polarized electric field that passed this element is then defined as:

$$E = \begin{pmatrix} E_x \\ E_y \end{pmatrix}, \tag{5.8 a}$$

$$
\begin{aligned}
E_x = \cos\beta \, E_{0x}\left(\cos^2\theta + e^{-i\frac{2\pi}{\lambda}\delta}\sin^2\theta\right) + \ldots \\
\sin\beta \, E_{0y}e^{i\Delta\varphi}\left(\sin\theta\cos\theta - e^{-i\frac{2\pi}{\lambda}\delta}\sin\theta\cos\theta\right),
\end{aligned}
\tag{5.8 b}
$$

$$
\begin{aligned}
E_y = \cos\beta \, E_{0x}\left(\sin\theta\cos\theta - e^{-i\frac{2\pi}{\lambda}\delta}\sin\theta\cos\theta\right) + \ldots \\
\sin\beta \, E_{0y}e^{i\Delta\varphi}\left(\sin^2\theta + e^{-i\frac{2\pi}{\lambda}\delta}\cos^2\theta\right),
\end{aligned}
\tag{5.8 c}
$$

where E_{x0}, E_{y0} are the input electric fields in the horizontal and vertical plane, θ is the angle between reference polarization axis and local birefringence axis, β is the angle of linearly polarized light with respect to the horizontal plane (x-axis), $\Delta\varphi$ is the phase difference between electric fields in the horizontal and vertical plane, δ is the induced phase retardance between polarization components. Such parabolic birefringence distribution in SVWP mimics the thermally induced birefringence of the end-pumped gain medium [126]. In theory, if the birefringence profile is inversed in SVWP, it would be capable of compensating for thermally induced depolarization and bi-focusing in the pumped gain medium.

The case when linear or circular input Gaussian beam polarization propagates through the SVWP element was investigated. Depolarization level η dependence on the phase retardance δ induced by the SVWP element was calculated and presented in Fig. 5.6 bottom graph. The ratio of beam radius to

compensator radius r/R required to compensate for the induced phase retardance is plotted in Fig. 5.6 top. Few cases of required r/R ratio for different retardance δ values are displayed as a reference. Analytical expressions to calculate the required parameters of SVWP for certain depolarization value for the ideal Gaussian beam are depicted too. It is important to note that depolarization for circular polarization case is two times larger than for linear polarization with the same phase retardance, but the required compensation ratio r/R stays the same.
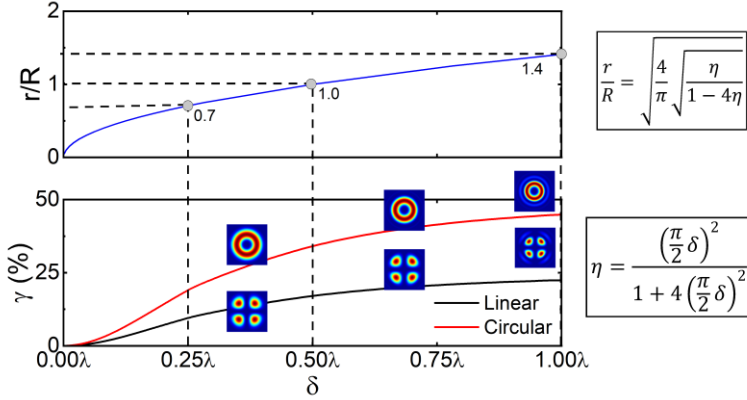

$$\frac{r}{R} = \sqrt{\frac{4}{\pi}\sqrt{\frac{\eta}{1-4\eta}}}$$

$$\eta = \frac{\left(\frac{\pi}{2}\delta\right)^2}{1 + 4\left(\frac{\pi}{2}\delta\right)^2}$$

Fig. 5.6 <u>Top:</u> the ratio of beam radius to compensator radius r/R required for compensation of induced phase retardance by SVWP element. <u>Bottom:</u> beam depolarization level γ dependence on induced phase retardance by SVWP element. Dashed lines indicate the values of ratio r/R required to compensate for corresponding phase retardance in the laser beam. <u>Insets:</u> depolarized beam profiles for circular (top) and linear (bottom) polarization at different phase retardance induced by SVWP element. Corresponding analytical expressions for linear polarization cases are provided, based on derivations from [40].

Another aspect of the SVWP element is intrinsic astigmatism that it produces for linearly polarized beam passing through it, or symmetrical focusing induced for circularly polarized beam. Naturally, this effect is fully compensated when depolarization itself is compensated with this element. However, SVWP element errors or beam size difference from the designed value lead to residual uncompensated focusing when the beam passes through this element. Modeling was performed by propagating the ideal Gaussian beam through SVWP using Fourier transform method and Eq. (5.8) and calculating the resulting beam wavefront radius, from which lens power was derived. Results are shown in Fig. 5.7.
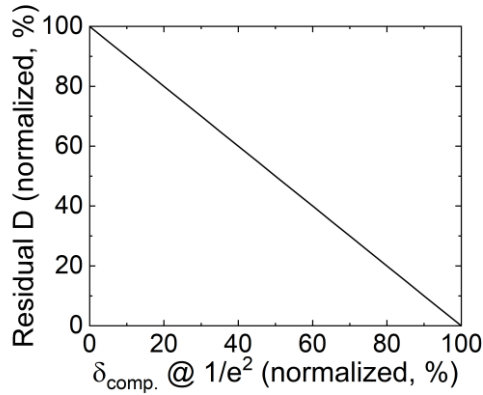
Fig. 5.7 Dependence of uncompensated lensing power D in SVWP element on induced phase retardance δ in SVWP element. Induced phase retardance δ is normalized to value when depolarization is fully compensated, whereas uncompensated lensing is expressed in diopters, normalized to maximum lens power without compensation.

Modeling results indicate that every percent of deviation in inscribed phase retardance from design value translates to the same amount of uncompensated bi-lens power. For example, if we take $r = 1\ mm$, and $R = 1\ mm$, for initially linearly polarized beam, bi-lens power produced by SVWP would be $D = 1.03\ m^{-1}$. If SVWP element compensates depolarization as designed, but with the error of 5%, uncompensated lensing power would be $D = 0.05\ m^{-1}$ (or $F = 20\ m$). Moreover, an increase of beam size reduces absolute lensing sensitivity by the power of 2 (whereas compensated depolarization sensitivity drops linearly). This suggests that it is practical to have a relatively large beam passing through the SVWP element.

5.4. Realization of 116 μJ, 1 MHz, 441 fs hybrid laser system with depolarization compensation – experiment and modeling

As described in Chapter 4 concluding remarks, a strategy of employing a two-cascade Yb:YAG amplifier system is necessary to further increase laser system peak power. Beam diameter in the second cascade is sufficiently expanded to avoid the optical damage of optical coatings. Significantly higher pumping power is thus needed, leading to unavoidably large depolarization losses.

In this section, the performance of an additional cascade of end-pumped Yb:YAG double-pass amplifier is thus investigated experimentally and theoretically based on the simulation algorithm described previously. The difference to the first cascade is also that the double-pass optical setup is arranged in a way that the signal beam is relay-imaged back to the crystal. The

reasoning behind this is provided later in this section. Additionally, specially designed SVWP is experimentally applied to reduce depolarization. All experimental data is compared to modeling predictions for model validation. Table 5.1 summarizes the basic parameters used in the experiment and for the model, whereas other parameters are the same as presented in Chapter 2 of this thesis.

Table 5.1 Modelling parameters and material properties for double-pass Yb:YAG amplifier under consideration. *Thermal expansion coefficient is taken from [48].

	Symbol	Value	Unit
Signal wavelength	λ_s	1030	nm
Signal power	P_s	37	W
Signal beam diameter @ $1/e^2$ level	ω_s	0.83	mm
Pump wavelength	λ_p	940	nm
Pump power	P_p	280	W
Pump beam diameter @ FWHM	ω_p	0.78	mm
Stress-induced birefringence term (radial)	C'_r	0.0032	
Stress-induced birefringence term (tangential)	C'_θ	-0.011	
Thermal expansion coefficient (10^{-6} K)*	α_T	6.15+0.01·T (in ℃)	
Yb^{3+} ions doping concentration	N_t	1	%
Crystal length	L	30	mm
Crystal width & height	a	4	mm

Experimental setup of the second-cascade double-pass Yb:YAG end-pumped amplifier is seeded by the developed hybrid laser system, described in Chapter 4. It featured an output power of 37 W at 1 MHz pulse repetition rate, pulses chirped to ~220 ps duration and bandwidth of $\Delta\lambda = 3.3\ nm$ (at FWHM), centered at 1030 nm. The full laser system layout is shown in Fig. 5.8.
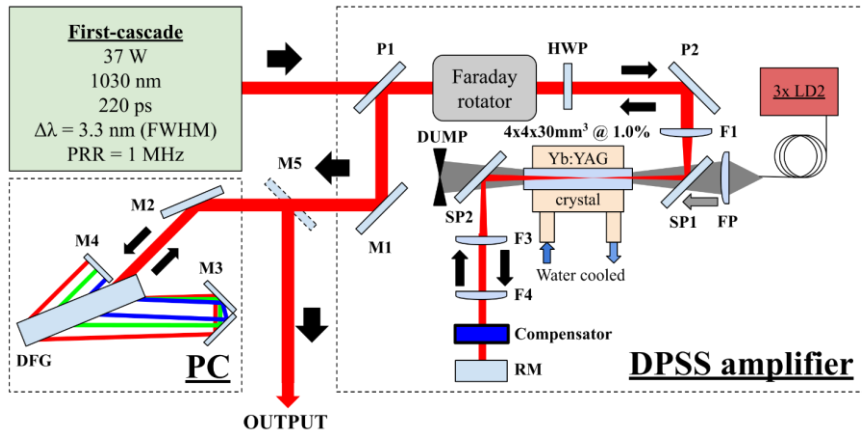
Fig. 5.8 Layout of the developed laser system consisting of first-cascade double-pass Yb:YAG amplifier, diode-pumped solid-state (DPSS) Yb:YAG power amplifier ($4x4x30\ mm^3$ with Yb^{3+} doping concentration of 1.0%), and 4-pass diffraction grating pulse compressor. LD2 – CW laser diode (130 W, NA = 0.22, D = 200 μm; set of 3 diodes used, coupled via fiber combiner), HWP – half wave-plate, F1 – focusing lens system to Yb:YAG crystal, P1, P2 – polarizers, SP1, SP2 – signal and pump beam separating mirrors, F3 and F4 – pair of focusing lenses for thermal lensing compensation, RM – flat mirror for beam back reflection, FP – pump beam focusing optics, DUMP – beam block of unabsorbed pump radiation after a single pass, M1, M2 – mirrors, M3 – mirror pair for pulse compressor optical path folding, M4 – mirror for beam returning in pulse compressor, M5 – output mirror, DFG – diffraction grating with 1739 mm^{-1} groove density. PC corresponds to a 4-pass diffraction grating based pulse compressor. Circulating water in crystal heatsink temperature was set to 20℃.

Chirped seed pulses from the first cascade were directed to the second DPSS Yb:YAG double-pass amplifier stage. The geometry of c-cut ([111]) Yb:YAG crystal was $4x4x30\ mm^3$ with Yb^{3+} doping concentration of 1.0%. Both facets of the crystal were coated with high laser-induced damage threshold (LIDT) coatings ($\sim 50\ J/cm^2$ for $10\ ns$ duration pulses). Yb:YAG crystal was mounted into a water-cooled copper block, with high thermal conductivity silicone as a thermal interface between the gain medium and heatsink. The temperature of circulating water was set to T=20 °C. The input and output beams of the double-pass amplifier were decoupled via polarization using a half-wave plate (HWP), Faraday rotator, and a pair of polarizers (P1 and P2) as shown in Fig. 5.8. The Yb:YAG crystal was end-pumped by a continuous wave laser diode. Three identical pumping diodes (output power 130 W, *nLight*), each coupled to 105 μm core diameter and 0.22 numerical aperture (NA) fiber, were combined using a high-power fiber combiner (*ITF Technologies*), featuring 200 μm core diameter and 0.22 numerical aperture (NA) output. The maximum measured pump power was 280 W at 940 nm central wavelength featuring 3.5 nm bandwidth (FWHM).

Each diode block was placed on a water-cooled heatsink, with temperatures adjusted to center output wavelength at 940 nm (diodes were not wavelength-stabilized). The seed and pump beams were focused by the F1 and FP lenses to spots of 0.83 mm and 0.78 mm diameters, respectively, and overlapped in the amplifier crystal (Fig. 5.8). Unabsorbed pump power was separated from the seed beam by SP2 wavelength separator and dumped.

Precise compensation of depolarization with SVWP requires that the beam is not elliptical in the compensation plane. It is possible, yet impractical, to put this element exactly at the output of Yb:YAG crystal and compensate the induced depolarization. In the case of circular polarization, this requirement is satisfied at any plane outside of the gain medium as there is no theoretical beam ellipticity. I have chosen an optical layout after the Yb:YAG gain medium that would work as a compensator for all polarization states. Relay imaging of crystal plane (where the beam is not elliptical) to compensation plane with ~2.3 times magnification was implemented, using two spherical lenses $F_1 = 75mm$ and $F_2 = 200mm$ telescope. The first lens was placed at a distance of $L_1 = F_1$ from crystal. Distance between lenses L_x was adjusted to compensate for the lensing effect F_{th} in the Yb:YAG crystal. Compensator could then be placed at a distance $L_2 = F_2$ from the second lens in its focal plane where both wavefront and beam shape from crystal (with magnification) were imaged. This setup also served for 2-pass configuration, when a flat back reflecting mirror is placed in compensation plane to return the beam using relay imaging to the crystal. Such an optical setup is shown in Fig. 5.9.
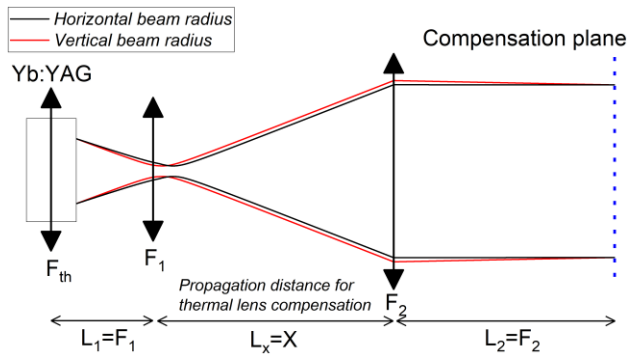

Fig. 5.9 Afocal imaging system used to image the end face of the crystal to the compensation plane with 2.3 times magnification (varies with thermal lens value). $F_1 = 75\ mm$, $F_2 = 200\ mm$. In case when the crystal is pumped with 280 W power and seeded with 37 W power, the distance between lenses is $L_x = 155\ mm$.

Results of amplification and induced depolarization after a single pass in Yb:YAG crystal are shown in Fig. 5.10.
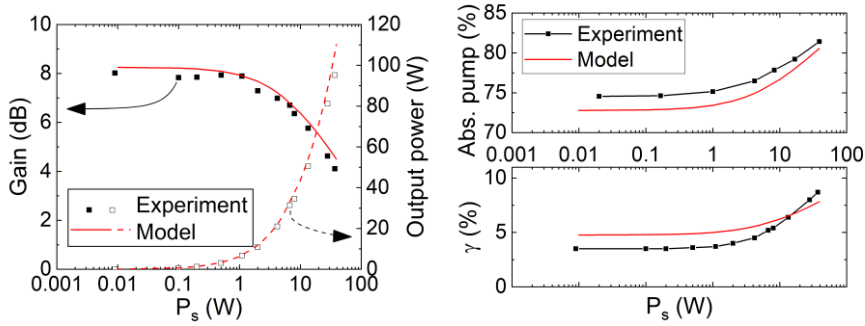
Fig. 5.10 1-pass end-pumped Yb:YAG experimental amplification results, with an incident pump power of 280 W. Modelling results are displayed in red. **Left:** average output power (hollow square marks, right axis) and total amplifier gain (full square marks, left axis) versus input signal power. **Right:** absorbed pump power and induced depolarization γ dependence on input seed power.

The signal after single-pass through the crystal rod was amplified from $37\,W$ to average output power of $95.2\,W$ ($110\,W$ modeling) at $1\,MHz$ pulse repetition rate. For $280\,W$ pump power, it corresponded to 21% amplifier efficiency (26% modeling). Furthermore, at low signal power, $8\,dB$ ($8.3\,dB$ modeling) gain was achieved. These results are in good agreement with modeling data, as it can be seen in Fig. 5.10 (left graph).

Depolarization rate at different input signal power levels was measured by placing a polarizer after the single-pass behind lenses $F3$ and $F4$. The beam power transmitted and reflected from the polarizer was measured. Results are presented in Fig. 5.10 bottom-right graph. At small-signal gain regime depolarization level was 3.5% (model 4.7%), at $37\,W$ of input power depolarization level reached 8.7% (model 7.8%). It is interesting that depolarization level depends on input power to the amplifier. Such dependence could be explained as follows. As it can be seen in Fig. 5.10 top-right graph, the absorbed pump power is dependent on the input seed power too, which correlates well with induced depolarization level – when absorbed pump power increases, induced depolarization level also increases. At high input seed power, considerable Yb^{3+} upper-state manifold depletion happens, leading to an increase of pump power absorption due to the three-level nature of Yb^{3+} ions. Increased pump absorption results in increased heat generation due to quantum defect and depolarization level increase since the change in temperature gradients leads to the change in induced depolarization due to the photoelastic effect. The second factor is caused by beam profile modification. At high input seed power level, considerable amplification saturation leads to different effective gain across beam profile – wings of Gaussian input beam are amplified relatively better than the central lobe, resulting in beam intensity

distribution that starts resembling flat-top beam shape [63]. Additionally, beam intensity redistribution is also influenced by thermal aberrations of the end-pumped gain medium. Beam profile deviation from Gaussian one, when more power is redistributed into the wings of Gaussian beam, leads to increased depolarization level, as phase retardance created by the end-pumped gain medium increases mostly parabolically from the center of the beam (Fig. 5.5 partly illustrates this).

There is a slight mismatch between the experimental and modeling data. In a small-signal gain regime, this discrepancy could be explained by the inaccuracy of the thermal expansion coefficient α_T and thermal conductivity k values used for modeling. Different sources provide slightly different measured values of such coefficients, suggesting that modeling results would also depend on the choice of references. Furthermore, in high input power amplification regime steeper increase of depolarization level was observed in the experiment compared to the model. Though this effect correlates well to an increase of absorbed pump power leading to temperature increase within the crystal, the dependence of α_T and k parameters on the temperature used in the model could differ from real material parameters, which in part explain this difference. Additionally, other parameters, e.g., stress-induced birefringence terms C', might also depend on temperature what was not accounted for in the model. However, the predicted depolarization level and its dependence on the seed power trend are satisfactory.

The spatially variable wave-plates for depolarization compensation in experimental tests were designed for several maximum retardances. As the law of retardance is parabolic, by combining elements with different maximum retardances, it is possible to get different values of total retardance. Additionally, due to the same parabolic retardance profile, by changing seed beam diameter incident on the SVWP element, one could change the phase retardance induced by the SVWP element, thus adjusting to different pumping conditions. This approach is convenient for experimental flexibility to compensate for different depolarization values. A set of SVWP with maximum retardances of $\lambda/2$, $\lambda/4$, $\lambda/8$, $\lambda/16$ and $\lambda/32$ for the central wavelength of $1030\ nm$ was fabricated in fused silica (UVFS) glass substrate by a *femtoLAB* micromachining system, produced by *Workshop of Photonics, Lithuania.*

After experiments and modeling, the necessary value of retardation for use in amplifier was determined and manufactured. To compensate depolarization arising in single-pass configuration, an SVWP with retardance of $\delta = 0.44\ \lambda$ (at $R = 1.5\ mm$) was placed at amplifier layout as it is shown in Fig. 5.8. The

signal beam was imaged to compensator from crystal and magnified to the diameter of $1.9\ mm$. To check how the compensator modifies beam spatial and polarization properties, a back reflecting mirror was removed, and a beam z-scan was performed. The signal beam was focused by $F = 200\ mm$ lens placed at $1\ m$ distance from SVWP, and the beam radius (at 4-sigma level) z-scan profile was captured by a CMOS camera. Results of z-scan without depolarization compensation are shown in Fig. 5.11. Modeling predictions are also included.
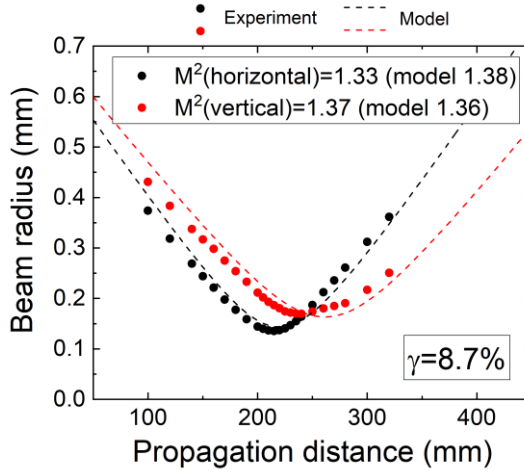
Experiment							
Model							
Z (mm)	150	210	215	220	230	240	300

Fig. 5.11. Z-scan of amplified beam demonstrating profile evolution (lower table) and caustic radius along propagation direction (axis Z) without depolarization compensation. The calculated beam quality parameter was $M^2 = 1.33$ and $M^2 = 1.37$, corresponding to horizontal and vertical beam cross-sections. The calculated caustics are presented by dashed lines.

Insertion of SVWP in the amplified beam resulted in that depolarization level was reduced from 8.7 % (7.8 % modeling) to 2.3 % (1.8 % modeling), and bi-focusing nearly vanished, restoring initial signal beam ellipticity present prior to amplification. Beam quality parameter after amplification degraded to $M^2 = 1.3 - 1.4$ due to thermal aberrations and gain saturation influence and was not affected by depolarization compensator. Captured and modeled beam profiles matched quite well, demonstrating model validity, as is shown in Fig. 5.12.
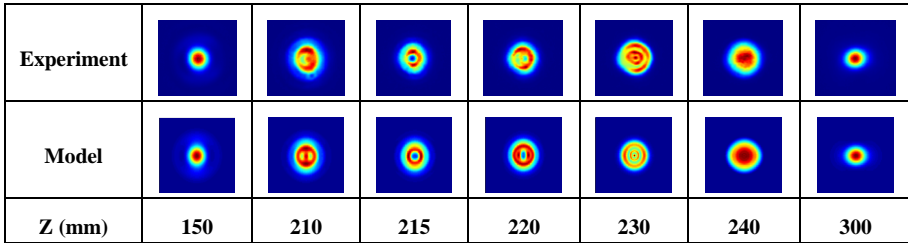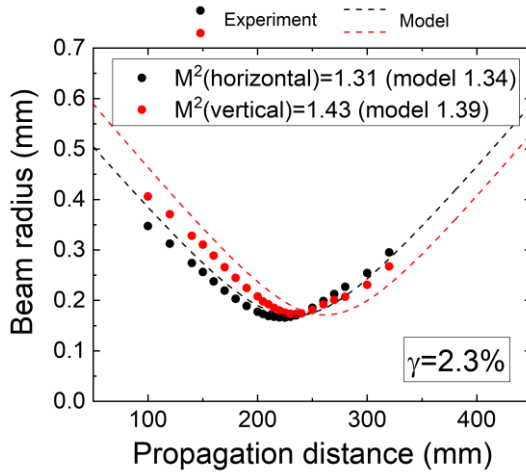
Fig. 5.12 The same as in Fig. 5.11 parameters and profiles in the case when depolarization is compensated by SWWP.

At the next step, a back reflector RM was installed in place. The beam was imaged back to the amplifier crystal and after the second pass outcoupled by the polarizer P1 (Fig. 5.8). Two-pass amplification and depolarization level were measured and compared to modeling data. Results are displayed in Fig. 5.13.
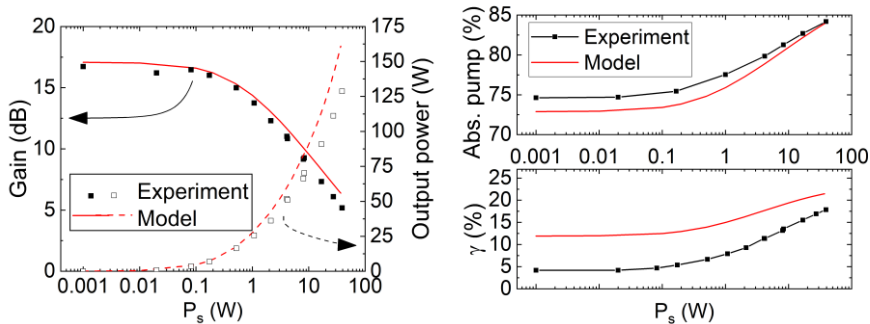

Fig. 5.13 Results of amplification in a 2-pass amplifier at 280 W pump level. Modeled graphs are plotted in red. **Left:** average output power (hollow square marks, right axis) and total amplifier gain (full square marks, left axis) versus input signal power. **Right:** absorbed pump and induced depolarization η versus input seed power.

The maximum output power of 129 W (161 W modeling) at 1 MHz pulse repetition rate was achieved for 37 W seed power. For 280 W pump power, it corresponded to 32% amplifier efficiency (43% modeling). At low seed power, 16.7 dB gain was achieved (17.1 dB modeling). These results are also in reasonable agreement with modeling data, as shown in Fig. 5.13 (left graph). The mismatch between experimental and modeling data could be further explained by optical losses in the used optical components, which were not considered during the modeling.

In Fig. 5.13 bottom-right graph dependence of depolarization change at different input signal power levels is plotted. At the small-signal gain regime, the depolarization level was 4.2% (model 11.9%), and at 37 W of input signal power, the depolarization level reached 17.9% (model 21.4%). Again, it is interesting that the depolarization level depends on the input power to the amplifier. Such dependence could be explained identically as the single-pass case. As it can be seen in Fig. 5.13 top graph, the absorbed pump power is dependent on the input seed power too, which correlates well with the induced depolarization level – when the absorbed pump power increases, induced depolarization level also increases. At high input seed power, considerable Yb^{3+} upper-state manifold depletion happens, leading to increase of pump power absorption due to the three-level nature of Yb^{3+} ions. Increased absorption results in increased heat generation due to the quantum defect and depolarization level increase. Additionally, at high input seed power level, considerable amplification saturation leads to different effective gain across beam profile – wings of input Gaussian beam are amplified relatively better than the central lobe, resulting in beam intensity redistribution [63]. Additionally, beam intensity redistribution is also influenced by thermal aberrations of the end-pumped gain medium. Beam profile deviation from Gaussian one, when more power is redistributed into the wings of Gaussian beam, leads to increased depolarization level, as phase retardance created by end-pumped gain medium increases parabolically from the center of beam.

To illustrate this effect, amplified seed beam intensity distribution was modelled at the output of end-pumped Yb:YAG crystal when input seed power is $P_s = 0.001\ W$ (corresponding to low amplification saturation case) and $P_s = 37\ W$ (corresponding to high amplification saturation case). Additionally, phase retardance δ created by end-pumped gain medium was extracted from model. Results of modelling are displayed in Fig. 5.14.
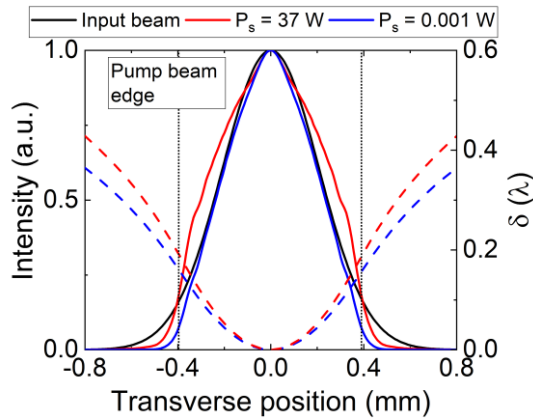
Fig. 5.14 2-pass modeling results of amplified beam intensity distribution (left vertical axis) in case of low amplification saturation ($P_s = 0.001\,W$, blue) and high amplification saturation ($P_s = 37\,W$, blue). The black curve corresponds to the input beam intensity distribution. Phase retardance δ for 1-pass (right vertical axis) is plotted with dashed lines.

Modeling confirms the proposition – in the case of high input seed power, when considerable amplification saturation is present, increased pump absorption leads to higher retardance δ created by the end-pumped gain medium. Additionally, due to amplification and thermal effects, more power is distributed to the wings of the beam, where larger retardance happens. This leads to a larger depolarization level as compared to a low amplification saturation regime, where beam distortions are considerably lower.

Though the depolarization dependence behavior is similar to the modeled one, there is a considerable mismatch between the experimental and modeling data. I can guess that this difference may be linked to the difference in real and modeled pump absorption and due to saturation of amplification which caused beam intensity distribution change. Such mismatch, especially at low input signal power, could be caused by experimental configuration. I have used a half-wave phase retardation plate and 45° angle of incidence thin film polarizers for signal attenuation. As seed was produced after two reflections, some uncontrolled mix of polarizations possibly was present in the seed. Phase retardation plate introduced depolarization in the seed, which possibly partially compensated amplifier depolarization, causing an observed difference between the experimental and modeled figures. At high input seed power level, the depolarization level difference between experimental and modeling data becomes lower, suggesting that laser crystal depolarization starts to dominate.

To compensate for depolarization arising in double-pass configuration, SVWP was placed at the same compensation plane as in the single-pass configuration. Beam characterization was done using a z-scan of the amplified

output beam with installed depolarization compensator and without it. Results are shown in Fig. 5.16 and Fig. 5.15, respectively, together with the modeled graphs.
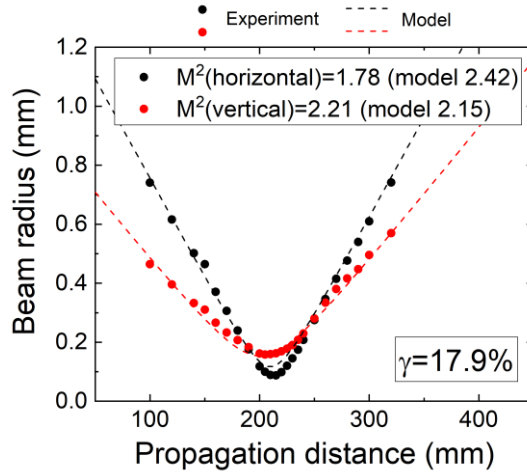
Experiment							
Model							
Z (mm)	150	210	215	220	230	240	300

Fig. 5.15 Z-scan of the amplified beam without depolarization compensation by SVWP. Beam quality parameter was $M^2 = 1.78$ and $M^2 = 2.21$ for horizontal and vertical projections of cross-section correspondingly. The dashed lines depict the modeling results. Experimental and modeled images of the beam cross-section profiles at several positions along the propagation axis are shown in the table below, illustrating the amplitude and phase of the amplified beam, severally affected by the induced birefringence.
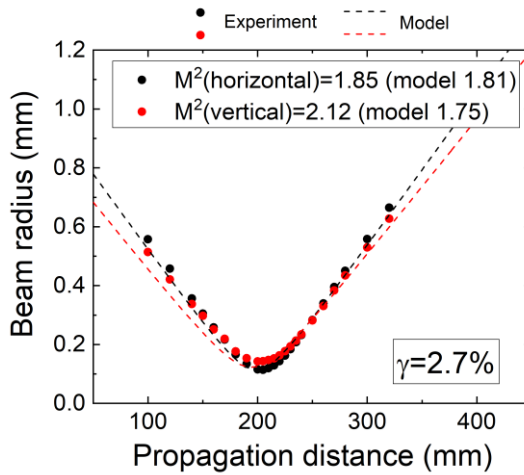
Fig. 5.16 The same as in Fig. 5.14 but with installed SVWP depolarization compensator. Beam quality parameter was evaluated as $M^2=1.85$ and $M^2=2.12$ for horizontal and vertical cross-section axes. Dashed lines depict modeled caustics. Experimental and modeled images of the beam cross-section profiles at several positions along the propagation axis are shown in the table below, illustrating compensation of induced birefringence and restoring of amplitude and phase of the amplified beam.

With an installed depolarization compensator depolarization level was reduced from 17.9 % (21.4 % modeling) to 2.7 % (0.3 % modeling), and the bi-focusing term was minimized to the level I was unable to measure. The resulting depolarization compensation and bi-focusing reduction were significant due to the correct choice of compensator parameters, saving a lot of output power and preserving symmetrical beam shape. There were several reasons for residual uncompensated depolarization. The first, when pump power was switched off, the "cold" depolarization in the system was around 0.5% due to the stress induced by the crystal mount. Second, a small amount of uncompensated depolarization could arise due to the manufacturing errors of the SVWP element itself. The third, maximum phase retardation inscribed in the SVWP of 4 mm diameter was not enough for full compensation of the induced depolarization. The compensation could be enhanced by adding one more SVWP in which a small amount of phase retardance is inscribed. As

phase retardation could be summed up, the set of several SVWPs could serve any heat load to amplifier crystal.

Beam quality parameter degradation in double-pass configuration was more severe compared to single-pass, resulting in $M^2 = 1.9 - 2.2$, mainly due to the thermal aberrations arising in the end-pumped Yb:YAG crystal and gain saturation.

Improvement of resulting beam quality is possible via spatial filtering, however, it was not implemented experimentally – at the time of investigating this problem, an experimental setup was not available anymore. For the sake of demonstration, I present a theoretical prediction of beam quality improvement, which should be valid as previous experiments showed (in the single-cascade amplifier case). Beam at $1\ m$ distance from the output of the amplifier was refocused with $F = 200\ mm$ lens (identical setup as before). Theoretical spatial filtering was performed using an aperture at the z-scan position where the aberrated part was fully blocked, and the central lobe was transmitted. Such position corresponded to near focal position $z = 192\ mm$ of focusing lens. Beam cross-section at filtering position with and without aperture (AP) is shown in Fig. 5.17. Additionally, beam radius evolution as it propagates is shown.

Without AP							
With AP							
Z (mm)	192	210	215	220	230	240	300
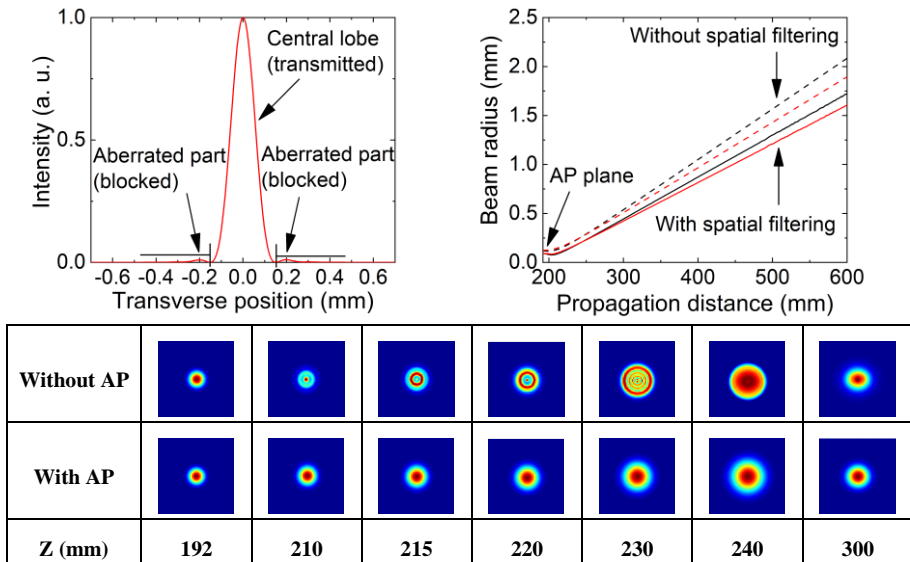
Fig. 5.17 Beam radius evolution with and without spatial filtering. The left graph depicts beam intensity cross-section at the filtering plane. The right graph depicts modeled beam radius evolution with (solid lines) and without (dashed lines) spatial filtering. Modeled images of the beam cross-section profiles at several positions along the propagation axis are shown in the table below, illustrating beam improvement by spatial filtering.

Results indicate a significant beam quality improvement – severely aberrated beam intensity cross-sections returned to Gaussian-like. Estimated spatial filtering losses were ~12%.

To estimate the improved beam quality, an additional lens with a focal length of $F = 200\ mm$ was placed at $300\ mm$ distance from waist position, and the beam was refocused. The resulting M^2 parameter was estimated from the fit of beam radius evolution. Results are shown in Fig. 5.18.
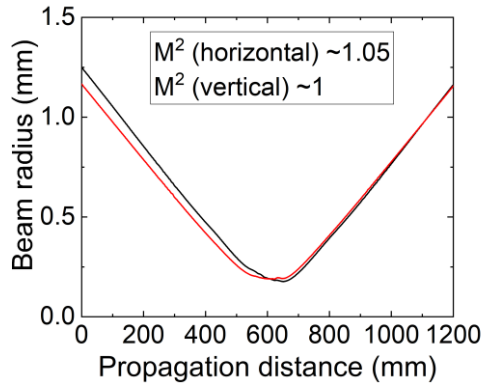

Fig. 5.18 Numerically evaluated from z-scan beam quality parameter after theoretical spatial filtering. Numerical estimation yielded M^2~1.05 and M^2~1 for horizontal and vertical cross-section axes.

Modeling results showed that beam quality could be significantly improved by applying spatial filtering – beam quality improved to M^2~1.05 (horizontal) and M^2~1 (vertical), indicating nearly diffraction-limited beam quality. Residual slightly degraded beam quality is the result of initial beam ellipticity (from seed source), resulting in optimal spatial filtering for only one plane (vertical in this case). In case the initial beam is stigmatic, beam quality would be diffraction limited in both directions.

After amplification in double-pass Yb:YAG amplifier pulses were experimentally compressed in a 4-pass diffraction grating pulse compressor. Temporally compressed pulses were characterized by the second-harmonic generation frequency-resolved optical gating (SHG-FROG) autocorrelation method. The pulse duration was retrieved by the FROG algorithm (Swamp Optics) using a 1024x1024 grid was $441\ fs$ (Fig. 5.19). Transform-limited pulse duration derived from the output spectrum was $415\ fs$. A residual spectral phase retrieved from FROG was $\sim2.3\ rad$ in the spectral range from $1024.3\ nm$ to $1033.8\ nm$ encompassing 98% of total pulse energy. The temporal Strehl ratio of the compressed pulse, defined as the ratio of actual peak power of the pulse to one of the bandwidth-limited pulse, was 81%,

indicating high amplified pulse quality. Pulse quality minimally degraded compared to the initial seed pulse temporal Strehl ratio of 83%, whereas pulse bandwidth narrowed from 3.3 nm (at FWHM) to 2.3 nm (at FWHM) due to gain narrowing effect. Measured diffraction and reflection losses in pulse compressor were ~10%, resulting in total output power of ~116 W, whereas beam quality did not degrade further and remained at $M^2 = 1.9 - 2.2$.
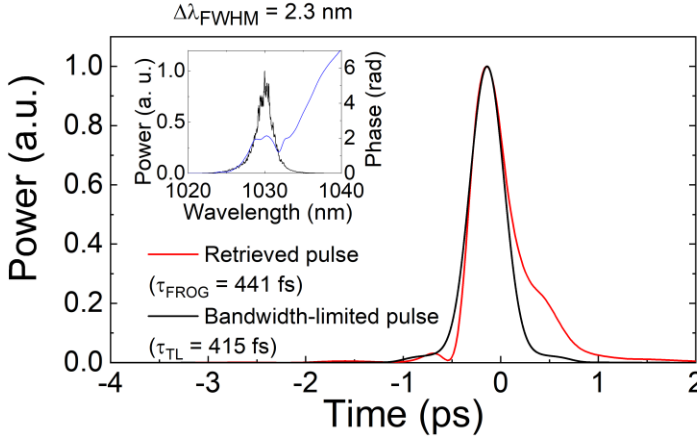

Fig. 5.19 Envelope of the compressed pulses at the output of the two-pass amplifier, retrieved from SHG FROG measurement compared to bandwidth-limited pulse shape calculated from the measured spectrum. Inset: (left) measured amplified signal spectrum and retrieved spectral phase. FROG traces retrieval error was 0.15%. The estimated temporal Strehl ratio of the pulse was 81%.

5.5. Summary

In this chapter, a hybrid laser system consisting of fiber-CPA seed source and two cascades of the end-pumped double-pass Yb:YAG amplifiers was demonstrated experimentally. The key novelty of the system was the application of depolarization compensation in the second cascade using specially designed SVWP, which allowed to extract nearly maximum power from such an amplifier without additional beam quality degradation. To the best of my knowledge, this method was applied for the first time. In the author's opinion, the proposed method is more beneficial compared to the others (reviewed in Chapter 1), such as intracavity quarter-wave plate [37,39], intracavity Faraday rotator [64], classical depolarization compensation layout with two identically pumped and relay-imaged gain media [38], and different crystal cut directions [40–42]. The reasons are: (1) the substrate of SVWP is fused-silica, providing low bulk absorption of laser radiation and featuring significantly lower nonlinear refractive index, as compared to Faraday rotator,

thus minimizing thermals effects and nonlinear interaction in high-intensity lasers, (2) the SVWP element is compact ($6\ mm$ in thickness, usually 1-inch in diameter), whereas Faraday rotator material is usually at least $20\ mm$ in length, (3) possibility to compensate depolarization in the highly pumped gain medium, which is not the case using a simplistic approach with quarter-wave plate, (4) is not overly sensitive to alignment and specific configuration, (5) very practical as induced/compensated depolarization level can be tuned by either changing incident laser beam size or stacking a few SVWPs in the same optical layout.

The presented laser system produced pulses of $441\ fs$ duration, $116\ \mu J$ pulse energy at $116\ W$ average power with a beam quality of $M^2 \sim 2.1$, featured optical-to-optical efficiency of 32% at room temperature ($T = 20°C$) and residual depolarization level of 2.7%. The resulting system peak power was $0.25\ GW$. Possible beam quality improvement by spatial filtering was demonstrated theoretically, yielding diffraction-limited beam quality of $M^2 \sim 1$ with Gaussian intensity distribution with power loss due to spatial filtering of $\sim 12\%$. In my opinion, such laser system demonstration provides sufficient proof that the end-pumped double-pass Yb:YAG amplifier configuration, together with SVWP, is a rather simplistic and efficient technology for peak power scaling, being more advantageous compared to other technologies, such as thin-disk or crystal fiber [43,44].

Additionally, comprehensive amplifier modeling was performed using the code written in *Matlab*. Modeling results matched well experimental, providing the tool to build and predict the performance of similar systems prior to the experimental phase.

6. The presented laser systems parameters – a comparison to the other systems

The advances in the performance of the amplifiers based on Yb:YAG as a gain media have been significant in the past two decades, noticeably accelerated by the introduction of the commercially available high-brightness ($NA <$ 0.22) pump diodes [32]. The single-crystal fiber and slab crystal amplifier configurations have shown promising results in amplifying laser pulses to high average power levels [30,43,74–78], whereas multi-pass geometries, employing cryogenic cooling technology, enabled reaching multi-Joule pulse energies, featuring mind-blowing peak powers of TW level [84–88]. The goal of this chapter is thus to compare the achieved parameters of the amplifier schematics presented in this work to the other configurations. In the author's opinion, this would provide a more general picture of the presented laser systems and highlight the results and key areas where the presented systems stand out in terms of the achieved parameters. A merit parameter, accounting for beam quality parameter M^2, beam ellipticity, amplifier efficiency and pulse compression quality (depicting the ratio of the compressed and bandwidth-limited pulse duration), is introduced, and compared to the other systems. Additionally, the applicability of the laser systems with achieved parameters is presented. It must be noted that not all of the authors in the reviewed literature provide all the parameters of interest, as is shown in Table 6.1 below.

Table 6.1 Summary of main parameters achieved in different Yb:YAG DPSS amplifier systems. SCF – single crystal fiber, IS – InnoSlab, MP – multipass, HEC-DPSLL – high energy class DPSLL, P_{peak} – the achieved maximum pulse peak power, M^2 – the beam quality parameter, ε – the beam ellipticity, η_{eff} – the optical-to-optical efficiency, $\tau_{meas.}/\tau_{BL}$ – the ratio of the compressed and bandwidth-limited pulse duration. In the case of different units for parameters, they are specified separately.

	Technology	P_{peak} (GW)	M^2	ε	η_{eff} (%)	$\dfrac{\tau_{meas.}}{\tau_{BL}}$	Ref.
This work	Bulk Yb:YAG (CPA)	0.13	1.15	0.91	28	0.85	Ch. 4.2
	Bulk Yb:YAG (CPA)	1.16	1	0.9	19	0.93	Ch. 4.3
	Bulk Yb:YAG (CPA)	0.1	1.01	0.87	35.2	0.99	Ch. 4.5
	Bulk Yb:YAG (CPA)	0.25	1.99 (1.03)	0.92	32	0.94	Ch. 5
Other	SCF (non-CPA)	0.006	1.3	0.8	22.7	0.88	[76]
	SCF (CPA)	0.069	1.24	0.89	15	0.73	[74]
	SCF (CPA)	2.5	1.1	0.9	28.5	0.98	[75]
	SCF (non-CPA)	0.002	1.9	0.8	36.8	0.83	[43]
	IS (non-CPA)	0.007	1.4	0.6	49	0.91	[30]
	IS (non-CPA)	0.084	2.1	0.63	43	0.9	[77]
	IS (CPA)	22.65	1.25	0.79	40	0.67	[78]

MP (thin-disk, regen., CPA)	26	1.5	0.9	42	0.91	[44]
MP (bulk, cryogenic CPA)	11	1.17	0.92	21	0.66	[80]
MP (bulk, CPA)	136	-	0.7	7.5	0.72	[79]
MP (thin-disk, non-CPA)	0.31	2.3	0.85	30	0.29	[81]
MP (bulk, non-CPA)	0.001	1.95	0.42	40	0.67	[82]
HEC-DPSLL (CPA, thin-disk, cascaded multi-pass)	1270	-	-	21	0.98	[84]
HEC-DPSLL (CPA, slab, cascaded cryogenic multi-pass)	0.95	-	-	22	-	[85]
HEC-DPSLL (CPA, thin disk, cascaded multi-pass)	1.65	-	-	17	-	[86]
HEC-DPSLL (CPA, thin-disk, cascaded regen. + multi-pass)	150	1.1	0.91	14	0.98	[87]
HEC-DPSLL (CPA, cascaded cryogenic regen.)	94 TW	-	-	-	-	[88]

The demand for high peak power femtosecond lasers has been investigated in various fields of science and industry, as was reviewed in the introductory section of this thesis [1–8]. The dependency of peak power versus pulse repetition rate of the reviewed laser systems is presented in Fig. 6.1, with the red numbered dots representing the laser systems demonstrated in this work ("1" – Chapter 4.2, "2" – Chapter 4.3, "3" – Chapter 4.5, "4" – Chapter 5). It can be seen from the graph that all the presented laser systems in this thesis feature relatively similar achieved peak power within the covered pulse repetition rate. While there is no distinguishable difference in terms of the achieved peak power (within similar pulse repetition rates), one can conclude that a double-pass amplifier, based on a bulk Yb:YAG crystal as a gain medium (presented in this thesis), is comparable and at some instances showing even higher achievable peak power, as compared to the state-of-the-art single-crystal fiber technology (exploiting the pump-guiding feature inside the gain medium) [74–76] and multi-pass slab or thin-disk [78,81] amplifier geometries. In principle, it was enabled by the precise dispersion parameters control of the pulse stretcher and the pulse compressor, achieving nearly bandwidth-limited pulse duration of the compressed pulses, as demonstrated in this work. Additionally, optimization of the gain medium parameters (gain medium length and doping concentration), which was enabled by the developed modeling tool, allowed to achieve record-high small-signal gain value as compared to similar systems (40 dB demonstrated in this thesis, the

highest value found in similar pulse repetition rate systems was 32.5 dB [43]), as well as power-extraction efficiency on the higher side ($> 35\%$ demonstrated in this work, more details later). However, peak power alone is not sufficient to fully describe the laser system, so additional parameters, such as beam quality parameter M^2, beam ellipticity, pulse compression quality and amplifier efficiency are reviewed further.
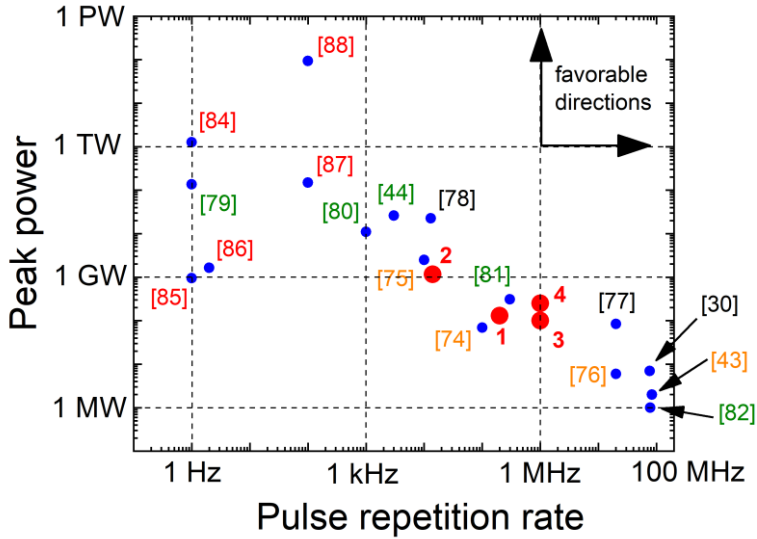

Fig. 6.1 Summarized graph showing peak power and pulse repetition rate for different Yb:YAG DPSS amplifier systems as reviewed in the literature (see Chapter 1 for more information). Numbered insets correspond to the literature as indicated in the bibliography of this thesis. Different colors correspond to used technology/type: red – HEC-DPSSL, green – MP, orange – SCF, black – IS (see Table 6.1). The red dots highlight the achieved peak power in this work, with numbers indicating the presented amplifier schematic (in the order in which they were presented in this thesis).

The comparison of the beam characteristics as described by the beam quality parameter M^2 and the worst-case beam ellipticity of the refocused beam is shown in Fig. 6.2 and Fig. 6.3.
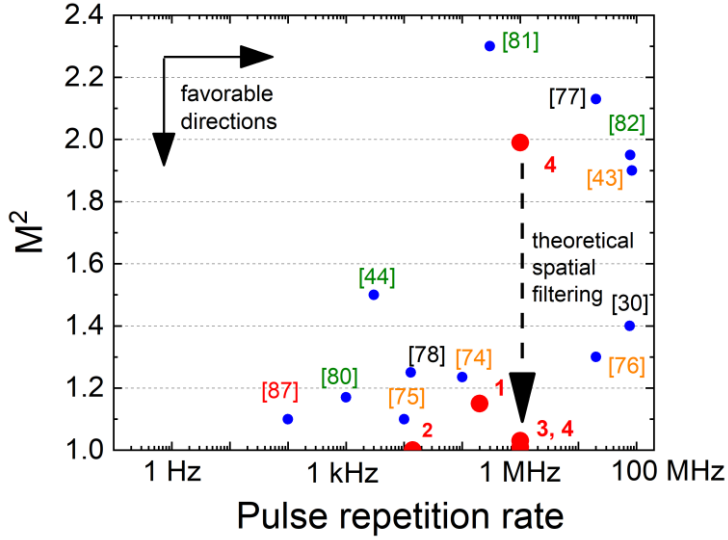
Fig. 6.2 Summarized graph showing beam quality parameter and pulse repetition rate for different Yb:YAG DPSS amplifier systems as reviewed in the literature. Theoretical spatial filtering indicates the improvement of the beam quality parameter if spatial filtering was applied in the system presented in Chapter 5.
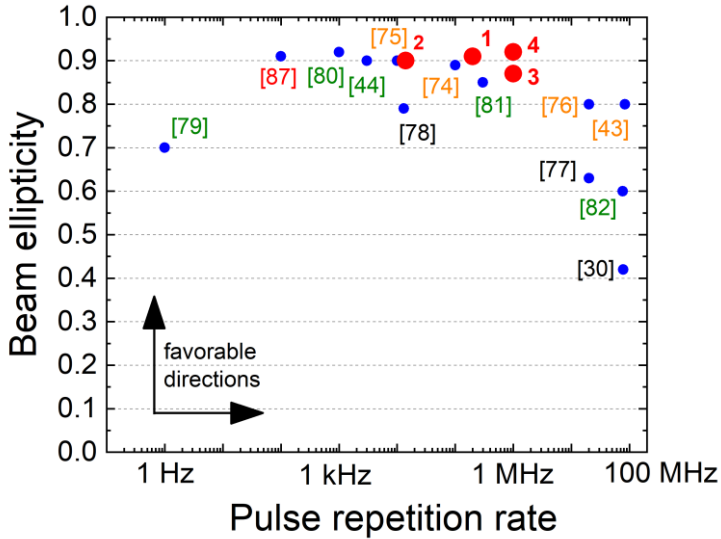

Fig. 6.3 Summarized graph showing the beam ellipticity and the pulse repetition rate for different Yb:YAG DPSS amplifier systems as reviewed in the literature. Beam ellipticity value of 1 corresponds to the perfectly circular beam shape.

These graphs clearly state that the presented laser systems and amplifier geometries in this thesis featured a superior beam quality parameter M^2

(diffraction-limited) and beam ellipticity $(0.87 - 0.92)$ as compared to the results of the other presented laser systems. This is highly beneficial for applications such as eye surgery by the femtosecond laser pulses, precise hard materials processing, semiconductor substrate processing, and others [127–129]. As an example, in the work of *V. Stankevič et al.* [127], they have shown that the beam ellipticity variation in the focal plane had a significant influence on the ablation rate of tungsten carbide material (due to the variation in the pulse overlap), which in their work changed about 4 times, when the beam ellipticity changed from 0.96 to 0.73. Another example was the case shown in the work of *T. Tetz et al.* [128], where the experiments were performed by the irradiation of silicon wafers using two different ultrafast laser systems. One of the observations (from the measurement data) was that the ablation threshold differed almost two times due to the different beam ellipticity of the different laser systems. Additionally, it was discussed that a deviation of the beam profile from the ideal Gaussian also influenced the ablation threshold.

As was discussed in the previous chapters of this thesis, the main reasons for the beam distortions in the described amplifiers are due to the thermally-induced stresses, which not only affect spatial beam profile but result in the polarization-dependent astigmatism (bi-focusing), which spoils beam focusability [63]. These effects were successfully mitigated in this thesis by using the spatial-filtering technique (filtering out the pump-induced thermal aberrations, which spoil beam quality parameter M^2 and beam intensity distribution), amplifying circularly polarized beam in the amplifier and implementing a novel compensator element (SVWP), which compensates both, induced depolarization and bi-focusing of the thermally-stressed Yb:YAG gain medium. Thus, the used techniques allowed to achieve significantly improved beam quality as compared to the other amplifier geometries.

Another important aspect that describes the performance of the femtosecond laser systems is the pulse compression quality. The quality was estimated by calculating the ratio of the compressed and the bandwidth-limited pulse duration $\frac{\tau_{meas.}}{\tau_{BL}}$. The results are shown in Fig. 6.4.

All the presented laser systems in this work are on the leading side in terms of the pulse compression quality, which was mainly enabled by a careful control and fine-tuning of the temporal dispersion parameters. Additionally, the system presented in Chapter 4.5 (numbered as 3 in Fig. 6.4), featuring $32.8\,\mu J$ energy at $1\,MHz$ of pulse repetition rate, with diffraction-limited beam quality, and amplifier efficiency of $\eta = 35.2\,\%$, also featured a compressed pulse duration of $318\,fs$, coinciding to bandwidth-limited pulse

duration (ratio 0.99, as seen in Fig. 6.4), which makes this system stand out from the others not only in terms of the pulse compression quality but also in the fact that the compressed pulse duration is quite short from the Yb:YAG based amplifiers. This was made possible by employing a hybrid laser architecture – a fiber seed source with a sufficiently high average output power ($3.3\ W$) and bandwidth ($7.7\ nm$) enabled the Yb:YAG crystal rod amplifier to operate in the low-gain regime (which was optimized for efficiency), thus minimizing the gain-narrowing effect, yet the system still produced relatively high output energy pulses ($32.8\ \mu J$).
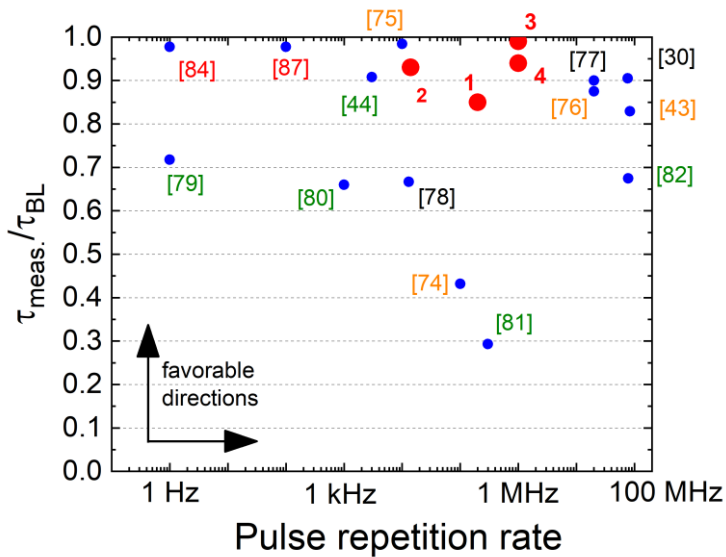

Fig. 6.4 Summarized graph showing the pulse compression quality (ratio of measured $\tau_{meas.}$ and bandwidth-limited τ_{BL} pulse duration) and pulse repetition rate for different Yb:YAG DPSS amplifier systems as reviewed in the literature. The ratio value of 1 corresponded to the case when the bandwidth-limited pulse duration was achieved.

The last considered aspect of the amplifier was its optical-to-optical efficiency. The results are shown below in Fig. 6.5.
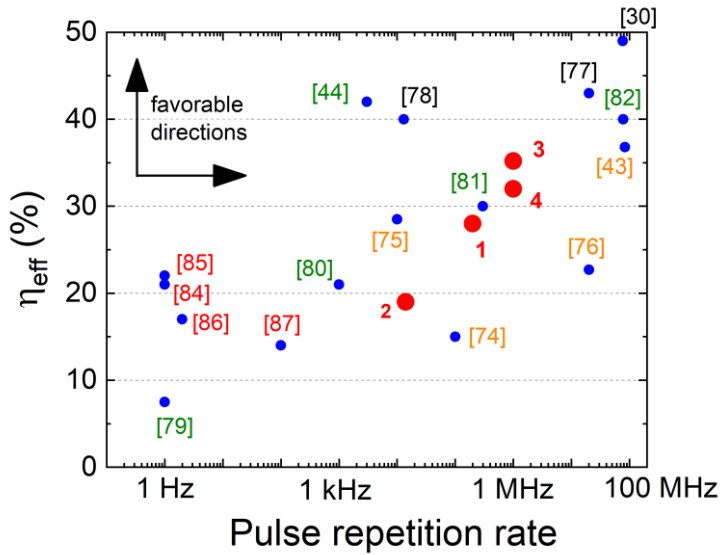
Fig. 6.5 Summarized graph showing the Yb:YAG amplifier efficiency and pulse repetition rate for different Yb:YAG DPSS amplifier systems as reviewed in the literature.

The results indicate that higher efficiency is naturally extracted from the amplifier geometries using multi-pass approach (black and green marked in Fig. 6.5), whereas if compared to the single-crystal fiber geometry, also featuring double-pass approach (for the signal beam), the majority of Yb:YAG amplifiers presented in this work feature higher optical-to-optical efficiency. As a specific example, if we compare the system presented by *F. Lesparre et al.* [76], where they also employed a hybrid laser architecture, with a fiber seed source providing average output power of $1.5\,W$, to the system presented in this work (Chapter 5), where I used a fiber seed source with an average output power of $3.3\,W$, they have managed to extract $100\,W$ of output power with three amplifier cascades (total pump power of $440\,W$), whereas in this thesis an output power of $116\,W$ (with $390\,W$ of total pump power) was achieved in two amplifier cascades. In the author's opinion, this was made possible by the optimization of gain medium parameters and by employing a novel depolarization compensation technique by SVWP, allowing efficient extraction of amplified power from the presented amplifier geometry (by reducing depolarization losses). As a side note, the presented system by *F. Lesparre et al.* is CPA-free, whereas, in this work, it is CPA-based. However, this fact wouldn't change the efficiency of the amplifiers presented in this work (only lower the output energy to the levels of their work by, for example, increasing the pulse repetition rate of the pulses emitted by the fiber seed source) since the seed beam sizes and gain medium lengths are comparable or

even larger in this thesis - at the last amplifier stage, I have used the seed beam size of $830\ \mu m$, whereas, in the work of *F. Lesparre et al.*, the seed beam size was $400\ \mu m$, suggesting that nonlinear effects wouldn't be an issue.

To provide a more general picture of the performance of the laser system, a merit parameter was derived by combining amplifier efficiency η (in the range of $0-1$, with 1 corresponding to 100% efficiency), beam ellipticity ε (in the range of $0-1$, with 1 corresponding to a perfectly circular beam), beam quality parameter M^2 and pulse compression quality ratio $\frac{\tau_{meas.}}{\tau_{BL}}$ (in the range of $0-1$, with 1 corresponding to a bandwidth-limited compressed pulse duration) in such a relation:

$$MP = \frac{\eta\varepsilon\frac{\tau_{meas.}}{\tau_{BL}}}{M^2}. \tag{6.1}$$

All the considered parameters are multiplied, except for the beam quality parameter M^2, since by increasing its value, the performance of the laser system decreases. The results are shown in Fig. 6.6.
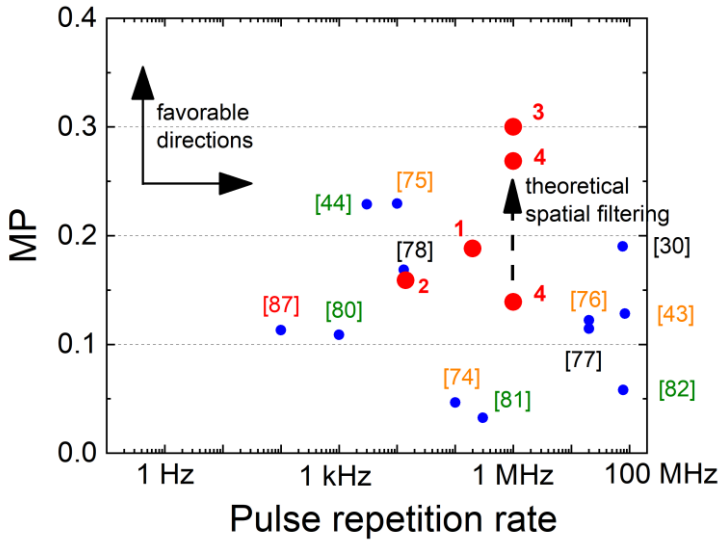

Fig. 6.6 Summarized graph showing the merit parameter and the pulse repetition rate for different Yb:YAG DPSS amplifier systems as reviewed in the literature. Theoretical spatial filtering indicates the improvement of the merit parameter if spatial filtering was applied in the system presented in Chapter 5.

The results indicate that even though some systems featured a higher optical-to-optical efficiency, they suffered from degraded beam quality or un-

optimal pulse compression, producing an overall lower score in terms of the merit parameter MP.

In conclusion, in this work, by improving the beam quality by the spatial filtering technique, by employing a spatially-variable waveplate for thermally induced astigmatism and depolarization compensation, by optimizing the end-pumped Yb:YAG amplifier for efficiency, and by choosing correct temporal dispersion parameters for an excellent pulse compression, a considerably higher merit parameter MP was reached (especially in the system presented in Chapter 4.5), indicating that the overall performance of the presented laser systems is higher than those reviewed in the literature. This is highly beneficial for various fields of applications, as was discussed earlier in this chapter, especially where a high quality of the laser beam is required [127–129].

Conclusions

1. Axis-symmetric (1D) numerical model for three-level gain medium continuous-wave amplifier, which incorporates signal beam propagation description by Hankel transform, pump beam shape calculation by ABCD matrix method, gain medium parameters – thermal conductivity, thermo-optic coefficient, spectroscopic cross-sections – dependency on temperature, spectroscopic cross-section value dependency on wavelength, and operates in the iterative algorithm, where convergence parameters are end-pumped gain medium temperature (single-pass) and output power (double-pass), is capable to accurately predict amplifier output power, gain narrowing effect, amplified beam shape, and wave-front distortions.

2. Application of CFBG as pulse stretcher and CVBG as matched dispersion pulse compressor in the hybrid laser system, consisting of FCPA laser as a seed source and a double-pass end-pumped Yb:YAG amplifier for further peak-power scaling, enables to construct a compact hybrid laser system, delivering nearly bandwidth-limited compressed femtosecond pulses.

3. Incorporation of a pair of quarter-wave plates to the end-pumped double-pass Yb:YAG amplifier, placed before and after gain medium, and oriented in a way that enables amplification of circularly polarized signal beam inside the gain medium, in addition to spatial filtering technique, where the spatial aperture is placed near the focal plane of the refocused beam to filter out thermally-induced aberrations, provides practical means to significantly minimize bi-focusing and restore original beam quality, enabling to achieve diffraction-limited beam quality after amplification in the end-pumped Yb:YAG amplifier.

4. Implementation of the SVWP enables significant reduction of the thermally-induced depolarization and astigmatism in the double-pass end-pumped Yb:YAG amplifier configuration.

SANTRAUKA

Įvadas

Femtosekundinės didelės smailinės galios (TW/cm^2) ir didelio impulsų pasikartojimo dažnio (MHz) lazerinės sistemos yra plačiai naudojamos mokslo, pramonės ir kariniuose sektoriuose. Femtosekundiniai lazeriai pasižymi puikiomis skaidrių terpių tūrinio apdirbimo galimybėmis (pvz. lydyto kvarco, safyro ir kt.) dėl daugiafotonės sugerties ir neterminių procesų [1,2]. Lazerinio mikroapdirbimo pasiekimai teikia galimybę ultratrumpųjų impulsų lazerius taikyti eilėje taikymų, tokių kaip difrakcinių gardelių formavimas optinėse skaidulose, safyro padėklų, ant kurių suformuotos puslaidininkinės struktūros, pjaustymas, ar formuojant plačiai pritaikomus fazinius optinius elementus, iš kurių galima paminėti S-fazines-plokšteles (angl. *S-waveplate*), šviesos pluošto poliarizacinės būsenos keitiklius (pvz. iš tiesinės poliarizacinės būsenos į radialinę ar azimutinę), dvejopalaužes fazines gardeles, hologramas, penkiamatę optinę atmintį, erdvinius pluošto formavimo įrankius ir daug kitų [3–6]. Buvo pastebėta, kad specifinis saulės elementų paviršiaus apdirbimas panaudojant femtosekundinius lazerių impulsus leidžia reikšmingai padidinti šių elementų efektyvumą [7]. Femtosekundiniai lazeriai taip pat plačiai pritaikomi žadinimo-zondavimo spektroskopijoje - biologinėje medžiagoje realiuoju laiku galima stebėti greitą fotofizinių ir fotocheminių reakcijų evoliuciją panaudojant ultratrumpuosius zondavimo impulsus [8]. Tai tik kelios taikymo sritys, kurios buvo reikšmingai išplėtotos panaudojant femtosekundinių impulsų lazerines sistemas, tačiau pateikti pavyzdžiai, mano manymu, pakankamai iliustruoja tokių sistemų plačias pritaikymo galimybes.

Femtosekundinių impulsų generavimas yra iššūkis - tiesioginį didelės smailinės galios femtosekundinių impulsų stiprinimą riboja netiesinės sąveikos efektai, tokie kaip fazės savimoduliacija, pluošto savifokusacija, Ramano sklaida ir kt. [9,10]. Šiuos nepageidaujamus ir ribojančius veiksnius galima efektyviai minimizuoti įgyvendinant čirpuotų impulsų stiprinimo (angl. *chirped pulse amplification*, CPA) metodą [11], kuomet lazerio impulsai prieš juos stiprinant yra išplečiami laike (angl. *temporarily chirped*), sustiprinami ir vėliau vėl suspaudžiami iki pradinės impulso trukmės. Impulsų laikinė plėtra ir spūda paprastai realizuojama difrakcinių gardelių impulsų plėstuve/spaustuve, kurių chromatinės aberacijos profiliai yra tiksliai suderinti [12,13]. Visgi, jeigu impulsai plečiami laike iki trukmės, kuri siekia ir viršija kelis šimtus pikosekundžių, tuomet tokios difrakcinių gardelių sistemos tampa nepraktiškos vien dėl reikalingo gardelės dydžio.

Ši ganėtinai praktinė problematika gali būti sprendžiama, pavyzdžiui, panaudojant skaidulinių lazerių technologiją. Čirpuotų impulsų stiprinimo sistemoje skaidulinis lazeris gali būti panaudojamas kaip impulsų užkrato šaltinis, kuriame impulsų plėtimas vykdomas čirpuotoje skaidulinėje Brego gardelėje (angl. *chirped fiber Bragg grating*, CFBG) – tokiu atveju sistemos dydžio problematika, bent jau impulsų plėtimo atveju, yra išsprendžiama [14,15]. Siekiant spręsti praktinę impulsų spūdos sistemų problematiką, pastarąjį dešimtmetį didelio susidomėjimo mokslininkų ir lazerinių sistemų kūrėjų tarpe susilaukė čirpuotos tūrinės Brego gardelės (angl. *chirped volume Bragg gratings*, CVBG) [16–18]. Technologiniai patobulinimai šių gardelių gamyboje leido pasiekti itin aukštą impulsų spūdos efektyvumą, išsaugant gerą, neretais atvejais ir difrakciškai ribotą lazerinio pluošto kokybę [16,17]. Be to, CVBG pagrindu pagamintas impulsų spaustuvas yra labai kompaktiškas, lengvai optiškai suderinamas ir daug mažiau jautrus optiniams išderinimams nei difrakcinių gardelių impulsų spaustuvai. Šios savybės yra pageidautinos kuriant pramoninius ultratrumpųjų impulsų lazerius. Šios technologijos, derinant su skaidulinių lazerių technologijomis, suteikia lazerių kūrėjams itin daug galimybių kuriant kompaktiškus ir tvirtus lazerius, kurie reikalauja minimalios priežiūros. Be to, jeigu skaiduliniai lazeriai paremti Yb^{3+} jonais legiruotomis lydyto kvarco skaidulomis, plati iterbio emisijos juosta suteikia galimybę generuoti ir stiprinti ultratrumpuosius impulsus.

Pagrindinis skaidulinių lazerinių sistemų trūkumas norint pasiekti didelę smailinę galią yra santykinai mažas vienamodžių skaidulų šerdies plotas ($\sim 95\ \mu m^2$) bei ilgas sąveikos ilgis, sukeliantis reikšmingą netiesinių efektų poveikį. Net ir plečiant impulsus laike iki praktinės $1\ ns$ trukmės, pasiekiamą didžiausią smailinę galią vis dar riboja dominuojantis netiesinis reiškinys - fazės savimoduliacija (angl. *self-phase modulation*, SPM). Buvo ištirta, kad SPM sukeltas netiesinis fazės postūmis per daugiau nei $1\ rad$ jau daro pastebimą įtaką suspaustų impulsų kokybei [19]. Vienas iš sprendimo būdų yra naudoti didelio šerdies ploto (angl. *large mode area*, LMA) skaidulas (iki $30\ \mu m$). Visgi, norint, kad skaidulose būtų sužadinta ir sklistų tik fundamentalioji moda (kaip vienamodžių skaidulų atveju), reikia panaudoti pažangias skaidulų dizaino technologijas, kaip antai fotoninių kristalų skaidulas, kurios yra iš esmės sudėtingesnės, brangesnės ir mažiau patrauklios kuriant industrinius lazerius lyginant su vienamodėmis skaidulomis [20,21]. Visa tai rodo, kad, nors skaiduliniai lazeriai suteikia aibę pranašumų, vien tik jų nepakanka norint kurti praktiškas itin didelės smailinės galios lazerines sistemas. Vienas iš patrauklių būdų yra kombinuoti skaidulines ir kietojo kūno lazerinių stiprintuvų sistemas – laisvos erdvės kietojo kūno stiprinimo

pakopose lazerinio pluošto plotas yra pakankamai padidinamas, o sąveikos ilgis yra pakankamai sumažinamas, kad būtų išvengta ribojančių netiesinės sąveikos efektų.

Puslaidininkiniais diodais kaupinamų kietojo kūno (angl. *diode-pumped solid-state*, DPSS) stiprinimo pakopų kokybiškas dizainas priklauso nuo tinkamos stiprinimo terpės pasirinkimo. Norint tinkamai stiprinti plačiajuosčius lazerio impulsus (kuriuos vėliau būtų galima suspausti laike iki šimtų femtosekundžių trukmės), reikalinga stiprinimo terpė, kurios stiprinimo juostos plotis yra didesnis nei stiprinamų lazerio impulsų spektro plotis. Be to, labai svarbios yra stiprinimo terpės termo-optinės ir mechaninės savybės. Iterbio Yb^{3+} jonais legiruoti kristalai, kaip pavyzdžiui Yb:YAG, Yb:KGW, Yb:CaF$_2$ ir kt., yra patrauklūs kandidatai DPSS stiprintuvų panaudojime. Šios terpės turi eilę pageidaujamų savybių – mažas kvantinis defektas, plati stiprinimo juosta, maža sužadintos būsenos sugertis, - kurios leidžia efektyviai stiprinti plačiajuosčius lazerio impulsus [22–24]. Visgi, šiems kristalams kaupinti yra reikalinga santykinai didelė smailinė kaupinimo galia dėl trijų energijos lygmenų sistemos (kurią lemia kristalų legiravimas Yb^{3+} jonais), norint pasiekti didelį optinį stiprinimo efektyvumą kambario temperatūroje. Viena iš alternatyvų yra kristalus aušinti iki itin žemų temperatūrų (kriogeninės sistemos), tačiau toks metodas yra sudėtingas, didelių gabaritų bei reikalaujantis santykinai didelių išlaidų, o tai yra nepalanku konstruojant lazerines sistemas pramoniniam panaudojimui [25–27]. Kita alternatyva yra diodais kaupinamų plonojo disko regeneratyvinių stiprintuvų konstrukcijos, kurios užtikrina reikiamą stiprinamo lazerio impulso praėjimų skaičių per stiprintuvinę terpę, taip pasiekiant pakankamai didelį stiprinimo efektyvumą kambario temperatūroje [28,29]. Tačiau pagrindinis tokio metodo trūkumas yra tas, kad, norint stiprinamą impulsą įvesti ir išvesti iš stiprintuvo, reikalinga Pokelso celė (angl. *Pockels cell*) ir Pokelso celės valdiklis su maža perjungimo trukme (kuri yra mažesnė už impulso apėjimo rezonatoriuje laiką) ir pakankamu perjungimo tikslumu. Netinkamo perjungimo atveju stiprintuvo išėjime gali atsirasti šalutiniai impulsai, kurie iš principo yra nepageidaujami daugelyje taikymų. Tokiu atveju reikalingos papildomos impulsų moduliavimo sistemos, kurios lemia bendrai išaugusį sistemos sudėtingumą. Be to, išvadinę stiprintuvo galią gali pradėti riboti ir vidutinė galia, kurią „atlaiko" ir pati Pokelso celė. Dar viena alternatyva yra daugialėkis DPSS stiprintuvas, kuriame optinė sistema išdėstyta taip, kad stiprinamas impulsas sklistų per stiprintuvo terpę daugelį kartų vis kitu optiniu keliu [30,31]. Tačiau toks dizainas vėlgi yra sudėtingas ir sunkiai optiškai suderinamas, jeigu lėkių skaičius per stiprintuvo terpę yra didelis. Palyginti neseniai atsiradę itin didelio optinio ryškio/skaisčio kaupinimo diodai, kurių skaitinė apertūra

siekia $NA < 0.22$ [32], iš principo turėtų leisti pasiekti pakankamą stiprinimo efektyvumą kambario temperatūroje net ir esant minimaliam stiprinamų impulsų praėjimo skaičiui per stiprintuvo kristalą.

Viena iš kylančių problematikų intensyviai kaupinamuose kietojo kūno stiprintuvuose yra santykinai didelis galios praradimas dėl depoliarizacijos reiškinio [33–37]. Šiluminiai gradientai atsirandantys stiprinimo terpėje lemia stiprinamo pluošto degradaciją dėl terminių aberacijų bei dėl atsirandančių mechaninių įtempių sukelto medžiagos dvejopalaužiškumo (kristalas tampa optiškai astigmatinis). Yra pasiūlyta nemažai būdų šiai problematikai spręsti. Optiškai izotropinėje stiprinimo terpėje, tokioje kaip Yb:YAG, depoliarizacinius nuostolius galima sumažinti panaudojus klasikinę depoliarizacijos kompensavimo schemą, kurioje du identiški ir vienodai kaupinami stiprintuvo moduliai yra išdėstomi vienas po kito su atitinkamu poliarizacijos pasukimu ir vaizdo pernešimu tarp jų [38,39]. Pagrindinė tokio metodo idėja yra ta, kad pirmajame modulyje sustiprinto pluošto poliarizacinė būsena yra apgręžiama prieš jam patenkant į antrąjį aktyvųjį elementą, taip iš principo panaikinant sukauptą fazės poslinkį tarp radialinės ir tangentinės poliarizacijos krypties stiprintuvo išėjime. Taip pat buvo atlikta rezultatyvių depoliarizacijos kompensavimo tyrimų, kuomet aktyviosios terpės kristalinės plokštumos orientacija buvo keičiama parenkant skirtingas kristalo pjūvio kryptis, pavyzdžiui Yb:YAG ir Nd:YAG atvejais [40–42]. Visi šie metodai tam tikru mastu veikia, tačiau kelia nemažai iššūkių – depoliarizacija nėra visiškai sukompensuojama, metodas yra bendrai jautrus šiluminiams efektams, reikalauja tikslaus optinio suderinimo ir identiškų kaupinimo sąlygų stiprinimo terpėse, metodas yra ribojamas netiesinės sąveikos (savifokusacijos, spektrinių iškraipymų) arba yra sąlyginai jautrus kristalinei konfigūracijai bei optiniam suderinimui.

Atsižvelgiant į siūlomų skaidulinių ir kietojo kūno stiprintuvų privalumus ir trūkumus, *hibridinis* čirpuotų impulsų stiprinimo metodas atrodo perspektyvus variantas, kuriant kompaktišką ir ekonomišką femtosekundinių impulsų lazerinę sistemą. Įvestas terminas *hibridinis lazeris* šio mano disertacinio darbo kontekste reiškia lazerinę sistemą, kurią sudaro skaidulinis užkrato šaltinis su papildomomis kietojo kūno stiprinimo pakopomis (t. y. lazerinė sistema susideda iš bent poros skirtingų technologijų kombinacijos, sintezės).

Pagrindinis mano disertacijos tikslas buvo suprojektuoti ir eksperimentiškai bei skaitmeniškai pademonstruoti kietojo kūno stiprinimo pakopų konfigūracijas bei jų galimybes, siekiant išlaikyti tiriamos konfigūracijos paprastumą, praktiškumą, bei patrauklumą kuriant pramonines

lazerines sistemas. Užkrato šaltiniai šioms pakopoms buvo specialiai suprojektuoti ir pagaminti kompanijos *Ekspla*, UAB.

Prieš pradedant DPSS stiprintuvo projektavimą, buvo atlikta įvairių stiprinimo terpių, legiruotų Yb^{3+} jonais, teorinė analizė - perspektyviausia medžiaga buvo pasirinkta Yb:YAG. Taip pat buvo sukurta skaitmeninio modeliavimo programinė įranga, leidžianti modeliuoti iš galo kaupinamų kristalų kietojo kūno stiprintuvus, bei eksperimentiškai patvirtinta ašinės-simetrijos atveju (1D). Ši programinė įranga buvo panaudota siekiant optimizuoti stiprintuvo parametrus (kaip antai terpės ilgį, aktyviųjų jonų koncentraciją, kt.) įvairiems praktiniams scenarijams. Taikant skaitmeniniu modeliavimu sukauptas žinias, buvo eksperimentiškai ištirtos bei pademonstruotos trys hibridinės lazerinės sistemos, skirtos generuoti didelės energijos ir didelės vidutinės galios lazerinius impulsus. Skaitmeninis modelis buvo papildomai išplėstas į trimatę (3D) situaciją, kad būtų atsižvelgta į nesimetrinius efektus (astigmatizmą, depoliarizaciją), kylančius iš galo kaupinamų kristalų stiprintuvuose. Modeliavimo metu surinktos žinios buvo panaudotos kuriant novatorišką depoliarizacijos kompensavimo metodą intensyviai kaupinamo dvigubo lėkio DPSS stiprintuvo konfigūracijoje. Galiausiai, visa sukaupta patirtis buvo realizuota kuriant ir eksperimentiškai pademonstruojant didelės vidutinės galios hibridinę sub-pikosekundinių impulsų lazerinę sistemą, kuri galėtų būti plačiai pritaikyta pramonėje ir moksle.

Mokslinis naujumas

Pagrindinis skaidulinių lazerinių sistemų trūkumas norint pasiekti didelę smailinę galią yra palyginti mažas vienamodžių skaidulų šerdies plotas ($\sim 95\,\mu m^2$) bei ilgas stiprinimo sąveikos ilgis, sukeliantis reikšmingą netiesinių efektų poveikį [19]. Dėl to reikalingos papildomos laisvos erdvės kietojo kūno stiprinimo pakopos, kuomet atsiranda galimybė nesunkiai padidinti stiprinamo pluošto plotą bei sumažinti stiprinimo sąveikos ilgį, taip išvengiant ribojančių netiesinės sąveikos reiškinių. Kita vertus, intensyviai iš galo kaupinami Yb:YAG stiprintuvai (pasirinkti šiame darbe) neišvengiamai susiduria su reikšmingais galios nuostoliais dėl depoliarizacijos reiškinio, nuo poliarizacijos priklausomo sustiprinto pluošto eliptiškumu ir pluošto degradacija dėl šiluminio poveikio [33–37]. Šie reiškiniai riboja tokiuose stiprintuvuose pasiekiamą maksimalią vidutinę galią. Be to, efektyvus stiprinimas yra sudėtingesnis kambario temperatūroje net ir esant nemažam stiprinamo pluošto praėjimų skaičiui per stiprinimo terpę. Taip pat impulsų plėtimas ir suspaudimas laike femtosekundinėse lazerinėse sistemose tampa

nepraktiškas, jeigu CPA schemoje impulsai plečiami laike iki kelių šimtų pikosekundžių ar ilgesnės impulsų trukmės [12,13]. Taigi, atsižvelgiant į skaidulinių lazerių ir DPSS stiprintuvų privalumus ir trūkumus, hibridinė čirpuotų impulsų stiprinimo lazerinė sistema yra perspektyvus būdas, kuriant kompaktišką ir ekonomišką femtosekundinę lazerinę sistemą. Mano disertacinio darbo mokslinis naujumas yra praktinė jau vystomų skaidulinių lazerinių sistemų ir kietojo kūno stiprintuvų technologijų sintezė, siekiant išspręsti minėtą problematiką, papildomai pritaikant skaitmeninio modeliavimo metodus:

1. Sukurtas ir eksperimentiškai patvirtintas novatoriškas ir efektyvus skaitmeninis trijų energijos lygmenų stiprintuvinis modelis, gebantis modeliuoti stiprinimo dinamiką nuolatinės veikos režime. Kiek man žinoma, tokia modeliavimo metodika anksčiau pristatyta nebuvo.

2. Buvo sukurta ir eksperimentiškai pademonstruota kompaktiška ir novatoriška ultratrumpųjų impulsų lazerinė sistema, paremta skaiduliniu užkrato lazeriu ir Yb:YAG dvigubo lėkio lazeriniu stiprintuvu, kuris veikė kambario temperatūroje. Pagrindinė sistemos naujovė buvo čirpuotos skaidulinės Brego gardelės (angl. *chirped fiber Bragg grating*, CFBG) kaip impulsų plėstuvo ir čirpuotos tūrinės Brego gardelės (angl. *chirped volume Bragg grating*, CVBG) kaip impulsų spaustuvo su suderinta dispersija pritaikymas, kuri leido pasiekti beveik spektriškai ribotos trukmės femtosekundinius impulsus. Pasiūlyta lazerio architektūra leido sukonstruoti kompaktišką santykinai didelės energijos ultratrumpųjų impulsų lazerį.

3. Buvo pritaikytas depoliarizacijos ir poliarizacinių efektų sukelto astigmatizmo eliminavimo metodas, panaudojant specialią fazinę plokštelę, kurios tūryje suformuotas erdvėje paraboliškai kintantis fazinis skirstinys (angl. *spatially variable wave-plate*, SVWP), atkartojantis ir invertuojantis fazinius iškraipymus, sukuriamus iš galo kaupinamo Yb:YAG kristalo stiprintuve. Mano turimomis žiniomis, šis metodas buvo skaitmeniškai ištirtas bei eksperimentiškai pademonstruotas pirmą kartą. Pademonstruota lazerinė sistema su iš galo kaupinamu Yb:YAG kristalu bei depoliarizacijos kompensavimu su SVWP yra santykinai paprastas ir efektyvus būdas smailinės lazerio galios didinimui. Daugeliu atveju pritaikyta technologija yra pranašesnė už alternatyvias technologijas, tokias kaip plonojo disko ar kristalinių skaidulų stiprintuvų [43,44].

Praktinė vertė

Kompaktiškos, tvirtos ir ekonomiškos femtosekundinės lazerinės sistemos sparčiai tobulėja, o tokių lazerių pritaikymo sritys plačios, ir apimančios mokslo bei pramonės rinkas. Femtosekundiniai lazeriai pasižymi puikiomis įvairių terpių tūrinio bei paviršinio apdirbimo galimybėmis – tūrinis skaidrių terpių modifikavimas (pvz. Lydyto kvarco, safyro ir kt.), safyro padėklų, ant kurių suformuotos puslaidininkinės struktūros, pjaustymas, ar formuojant plačiai pritaikomus fazinius optinius elementus, iš kurių galima paminėti S-fazines-plokšteles (angl. *S-waveplate*), šviesos pluošto poliarizacinės būsenos keitiklius (pvz. iš tiesinės poliarizacinės būsenos į radialinę ar azimutinę), dvejopalaužes fazines gardeles, hologramas, penkiamatę optinę atmintį, erdvinius pluošto formavimo įrankius ir daug kitų [1–6]. Hibridinės lazerinės sistemos architektūros panaudojimas, kuri sudaryta iš skaidulinio lazerio kaip impulsų užkrato šaltinio (kuris taipogi paremtas čirpuotų impulsų stiprinimo metodu), ir papildomų kietojo kūno laisvos erdvės stiprinimo pakopų, yra, mano įsitikinimu, praktinis būdas kuriant tokias, didelės smailinės galios, femtosekundines lazerines sistemas. Taigi, mano disertacinis darbas turi reikšmingą praktinę vertę keliais aspektais:

1. Sukurtas skaitmeninis trijų energijos lygmenų stiprintuvinis modelis, gebantis modeliuoti stiprinimo dinamiką nuolatinės veikos režime, leido greitai suprojektuoti, optimizuoti ir išbandyti įvairias iš galo kaupinamų Yb:YAG kristalų stiprintuvines konfigūracijas, kurios tinkamos kuriant femtosekundines lazerines sistemas. Sukurta modeliavimo programinė įranga šiuo metu naudojama įmonėje *Ekspla*, UAB.

2. Buvo sukurta ir eksperimentiškai pademonstruota kompaktiška ultratrumpųjų impulsų lazerinė sistema, paremta skaiduliniu užkrato lazeriu ir Yb:YAG dvigubo lėkio lazeriniu stiprintuvu, kuris veikė kambario temperatūroje. Pagrindinė sistemos naujovė buvo čirpuotos skaidulinės Brego gardelės (angl. *chirped fiber Bragg grating*, CFBG) kaip impulsų plėstuvo ir čirpuotos tūrinės Brego gardelės (angl. *chirped volume Bragg grating*, CVBG) kaip impulsų spaustuvo su suderinta dispersija pritaikymas, kuri leido pasiekti beveik spektriškai ribotos trukmės femtosekundinius impulsus. Pasiūlyta lazerio architektūra leido sukonstruoti kompaktišką santykinai didelės energijos ultratrumpųjų impulsų lazerį.

3. Hibridinėje lazerinėje sistemoje, kurioje kaip impulsų užkrato šaltinis panaudojamas skaidulinis lazeris, o tolimesniam smailinės galios didinimui panaudojamas iš galo kaupinamas stiprintuvas Yb:YAG

kristalo pagrindu, pritaikius CFBG kaip impulsų plėstuvą ir CVBG kaip impulsų spaustuvą (arba keturių-lėkių difrakcinės gardelės pagrindu sukurtą impulsų spaustuvą), bei suderinus jų dispersiją, atsiveria praktinė galimybė generuoti spektriškai ribotus didelės smailinės galios femtosekundinius impulsus. Tokios eksperimentiškai pademonstruotos koncepcijos panaudojimas prisidėjo prie komercinės femtosekundinės lazerinės sistemos *FemtoLux 30* išvystymo kompanijoje *Ekspla*, UAB.

4. Hibridinėje lazerinėje sistemoje, kurioje kaip impulsų užkrato šaltinis panaudojamas skaidulinis lazeris, o tolimesniam smailinės galios didinimui panaudojamos dvi pakopos iš galo kaupinamų stiprintuvų Yb:YAG kristalų pagrindu, ir kurioje buvo pritaikytas depoliarizacijos ir poliarizacinių efektų sukelto astigmatizmo eliminavimo metodas, panaudojant specialią fazinę plokštelę SVWP, įgalino eksperimentiškai pademonstruoti tokios sistemos galimybes generuojant didelės smailinės galios femtosekundinius impulsus. Praktiniu požiūriu pritaikyta technologija yra pranašesnė už alternatyvias technologijas, tokias kaip plonojo disko ar kristalinių skaidulų stiprintuvų [43,44].

Ginamieji teiginiai

S1. Vienmatis, ašinės simetrijos (1D) skaitmeninis trijų energijos lygmenų stiprintuvinis modelis, skirtas modeliuoti spinduliuotės stiprinimą nuolatinės veikos režime, taipogi aprašantis signalo pluošto sklidimą per Hankelio transformaciją, kaupinimo pluošto sklidimą per ABCD matricų metodą, įskaitantis stiprinančiosios terpės parametrus, tokius kaip šiluminį laidumą, termo-optinį koeficientą, spektroskopinius sugerties ir emisijos skerspjūvius, bei šių parametrų priklausomybę nuo temperatūros, skerspjūvių priklausomybę nuo bangos ilgio, ir kurio veikimas pagrįstas iteraciniu algoritmu, kurio išeities parametras iš galo kaupinamo kristalo atveju yra temperatūrinio skirstinio (vieno lėkio atveju) ir sustiprintos spinduliuotės vidutinės galios (dvigubo lėkio atveju) nusistovėjimas, yra tikslus ir eksperimentiškai pagrįstas metodas, įgalinantis modeliuotoją apskaičiuoti spinduliuotės stiprinimą aprašytos konfigūracijos stiprintuve, įskaityti spektro siaurėjimo reiškinį dėl stiprinimo, numatyti stiprinamos spinduliuotės pluošto kokybės bei skirstinio pokyčius ir banginio fronto degradaciją.

S2. Ultratrumpųjų impulsų hibridinė lazerinė sistema, kurią sudaro skaidulinis užkrato lazeris ir iš galo kaupinamo Yb:YAG kristalo dvigubo lėkio

laisvos erdvės stiprintuvas, kurioje impulsų plėtimas ir spaudimas laike įgyvendinamas dispersiškai suderintoje CFBG ir CVBG poroje, leidžia pasiekti beveik spektriškai ribotus, laike suspaustus santykinai didelės smailinės galios femtosekundinius impulsus.

S3. Praktinis būdas sumažinti stiprinamos spinduliuotės pluošto degradaciją iš galo kaupinamo Yb:YAG kristalo dvigubo lėkio stiprintuve, kylančią dėl šiluminių ir poliarizacinių reiškinių stiprintuvinėje terpėje, yra panaudojant porą ketvirčio bangos ilgio fazinių plokštelių, kurios talpinamos prieš ir po Yb:YAG kristalą, ir orientuotos taip, kad aktyviojoje terpėje būtų stiprinama apskritiminė poliarizacija, bei įgyvendinant pluošto erdvinio filtravimo metodą, kuomet sustiprintas pluoštas yra perfokusuojamas su teigiamo židinio lęšiu, kurio židinio plokštumoje yra pastatoma apertūra, nufiltruojanti šiluminių reiškinių kristale sukeltas pluošto aberacijas. Toks praktiškas metodas leidžia atstatyti pradinę pluošto kokybę ir daugeliu atveju pasiekti difrakciškai ribotą pluošto kokybę po stiprinimo iš galo kaupinamo Yb:YAG kristalo dvigubo lėkio stiprintuve.

S4. SVWP fazinio elemento panaudojimas suteikia galimybę reikšmingai sumažinti šiluminių reiškinių sukeltą depoliarizaciją ir sustiprinto pluošto eliptiškumą dvigubo lėkio iš galo kaupinamo Yb:YAG kristalo stiprintuvo konfigūracijoje.

Publikacijos ir asmeninis indėlis

Disertacijoje remiamasi keturiomis mokslinėmis publikacijomis, kurių sąrašas pateiktas žemiau:

A1. **L. Veselis**, T. Bartulevičius, K. Madeikis, A. Michailovas, and N. Rusteika, "Compact 20 W femtosecond laser system based on fiber laser seeder, Yb:YAG rod amplifier and chirped volume Bragg grating compressor", Opt. Express **26**(24), 31873-31879 (2018). https://doi.org/10.1364/OE.26.031873

A2. **L. Veselis**, R. Burokas, A. Michailovas, "Numerical model of end-pumped Yb:YAG double-pass laser amplifier experimentally validated at 129 W output power", Lith. J. Phys. **61**(4), accepted, will be published in 2021.

A3. **L. Veselis**, R. Burokas, O. Ulčinas, T. Gertus, K. Michailovas, and A. Michailovas, "Depolarization compensation with spatially variable waveplate in 116 W, 441 fs, 1 MHz Yb:YAG double-pass laser amplifier", Appl. Opt. **60**, 7164-7171 (2021). https://doi.org/10.1364/AO.432573

A4. **L. Veselis**, T. Bartulevičius, K. Madeikis, and A. Michailovas, „Generation of 40 W, 400 fs pulses at 1 MHz repetition rate from efficient, room temperature Yb:YAG double-pass amplifier seeded by fiber CPA system", Proc. SPIE 11259, Solid State Lasers XXIX: Technology and Devices, 1125925 (2020).
https://doi.org/10.1117/12.2545473

Doktorantūros studijų metu autorius taip pat prisidėjo prie trijų mokslinių publikacijų, kurios nėra tiesiogiai susijusios su disertacijos tematika. Studijuojant doktorantūroje disertacijos tematika taip pat buvo pristatyta 10 konferencijų pranešimų ir 19 pranešimų, kurie nėra tiesiogiai susiję su disertacijos tema. Pilnas sąrašas pateikiamas disertacijoje anglų kalba.

Visus darbe pateiktus tyrimus atliko autorius, išskyrus darbus, minimus bendraautorių indėlio skyriuje. Autorius sukūrė modeliavimo programinę įrangą, aprašytą šio darbo 2 ir 5 skyriuose, ir atliko visus skaitinius skaičiavimus ir teorinę analizę, pateiktus 3 skyriuje ir A3 straipsnyje. Be to, autorius suprojektavo, sukonstravo ir eksperimentiškai realizavo lazerines sistemas, aprašytas disertacijos darbe ir A1, A2 ir A4 straipsniuose. Autorius sukūrė ir eksperimentiškai realizavo dviejų stiprinimo pakopų iš galo kaupinamų Yb:YAG kristalų stiprintuvo lazerinę sistemą ir pradėjo pirminius depoliarizacijos kompensavimo eksperimentus, kurie publikuoti A3 straipsnyje. Autorius pilnai parengė rankraščius A1-A4.

Disertacijos sandara

Disertaciją (anglų kalba) sudaro įvadas, autoriaus publikacijų sąrašas, šeši skyriai, išvados ir panaudotos literatūros sąrašas. Disertacija pradedama literatūros apžvalga, kurioje aptariamos iterbio jonais legiruotų kristalų savybės, bei apžvelgiamos įvairios Yb:YAG stiprintuvinės konfigūracijos. Kiti du skyriai skirti tiesinių stiprintuvų modeliavimo metodikos aprašymui, eksperimentiniam pagrindimui, bei pateikiamos naudingos praktinės įžvalgos tokių stiprintuvų parametrų optimizavime. Ketvirtajame skyriuje eksperimentiškai pademonstruojamos įvairios iš galo kaupinamų Yb:YAG kristalų dvigubo lėkio stiprinimo pakopos hibridinėje lazerinėje sistemoje, skirtoje femtosekundinių impulsų generavimui. Penktasis skyrius skirtas depoliarizacijos kompensavimo metodo teorinei analizei bei eksperimentiniam pagrindimui dviejų pakopų, dvigubo lėkio Yb:YAG stiprintuve. Paskutiniajame skyriuje yra pristatomi pagrindiniai pasiekti lazerinių sistemų parametrai (apibendrinimas). Pristatytos lazerinės sistemos palyginamos su rastomis literatūroje.

Literatūros apžvalga

Šiame skyriuje trumpai apžvelgiamos iterbio jonais legiruotų kristalinių medžiagų (Yb:YAG, Yb:KGW, Yb:KYW, Yb:BOYS, Yb:CALGO, Yb:CaF$_2$, Yb:YVO$_4$, Yb:Y$_2$O$_3$, Yb:Sc$_2$O$_3$, Yb:Lu$_2$O$_3$, Yb:LuAG ir Yb:YLF) savybės ir jų pritaikymas ultratrumpųjų impulsų lazerinėse sistemose. Lyginamos stiprintuvinių medžiagų savybės yra:

1. sugerties ir emisijos skerspjūvių vertės σ_a ir σ_e;
2. stiprinimo juostos plotis $\Delta\lambda$;
3. netiesinis lūžio rodiklis n_2;
4. šiluminio laidumo koeficientas k;
5. sužadintos būsenos gyvavimo trukmė τ_f;
6. šiluminio plėtimosi koeficientas α_T;
7. šiluminio atsparumo parametras R_s;
8. stiprinamos spinduliuotės soties intensyvumas I_{sat};
9. minimalus kaupinimo spinduliuotės intensyvumas I_{min}, reikalingas pasiekti medžiagos skaidrumą lazerinei spinduliuotei.

Palyginus šiuos parametrus buvo prieita prie išvados, kad Yb:YAG yra perspektyvi ir labai praktiška (bei plačiai prieinama) kristalinė medžiaga, kuri tinkama naudoti kaip aktyvioji terpė kietojo kūno stiprintuvuose, norint pasiekti aukštą stiprinimo efektyvumą kambario temperatūroje, bei kuriant ultratrumpųjų impulsų lazerius.

Šiame skyriuje taip pat apžvelgiama viena iš opiausių problematikų – galios nuostoliai dėl depoliarizacijos - iš galo kaupinamų Yb:YAG kristalų stiprintuvuose, kurie buvo pasirinkti kaip pagrindas šiame disertaciniame darbe. Trumpai apžvelgiamos literatūroje pateiktos depoliarizacijos kompensavimo metodikos, tokios kaip: (a) klasikinė, kurioje du identiški ir identiškai kaupinami aktyvūs elementai išdėstyti optinėje schemoje vienas po kito taip, kad būtų pernešamas pluošto vaizdas iš vienos aktyviosios terpės į kitą, bei invertuojama pluošto poliarizacinė būsena prieš jam patenkant į antrąjį aktyvųjį elementą [33,38,39], (b) metodas su ketvirčio bangos ilgio fazine plokštele ir plokščiuoju veidrodžiu, kuris apgręžia stiprinamą spinduliuotę ir nukreipia ją atgal į aktyvųjį elementą, (c) panaudojant Faradėjaus rotatorių, kuris invertuoja pluošto poliarizacinę būseną [36], (d) parenkant skirtingos kristalografinės plokštumos orientacijos kristalines medžiagas [40–42]. Skyriuje diskutuojama, kad šios metodikos nėra labai praktiškos, kadangi reikia idealiai suderintų aktyviųjų terpių, metodas su ketvirčio bangos ilgio fazine plokštele tinkamai veikia tik iki santykinai mažo depoliarizacijos lygio, Faradėjaus rotatorių panaudojimas yra problematiškas

dėl šio elemento jautrumo šiluminiams reiškiniams, dėl kurių jis negali būti naudojamas didelės vidutinės galios sistemose, ir skirtingų kristalografinių plokštumų orientacijų kristalų panaudojimas ir atkartojamumas yra problematiškas, kadangi reikia pakankamai tiksliai pataikyti kristalografinės plokštumos orientaciją. Trumpai aprašomas siūlomas novatoriškas depoliarizacijos kompensavimo metodas, kuris taipogi pagrįstas pluošto poliarizacinės būsenos invertavimu, tačiau panaudojant iki šiol šiam tikslui nenaudotos specialios fazinės plokštelės su specialiai įrašytu faziniu skirstiniu, atkartojančiu tokį, koks yra sukuriamas iš galo kaupinamuose Yb:YAG kristaluose (tik su invertuotu fazės ženklu).

Šiame skyriuje taip pat pristatomos impulsų laikinio plėtimo ir spaudimo metodikos, kurios naudojamos eksperimentinėje šio disertacinio darbo dalyje – impulsų laikinis plėtimas čirpuotoje skaidulinėje Brego gardelėje (CFBG) [68], impulsų laikinė spūda čirpuotoje tūrinėje Brego gardelėje (CVBG) [70] bei impulsų laikinė spūda keturių lėkių per difrakcinę gardelę impulsų spaustuve [13].

Paskutinis šio skyriaus poskyris skirtas apžvelgti kelioms pagrindinėms laisvos erdvės kietojo kūno stiprintuvų konfigūracijomis, kurios yra lyginamos su pasiūlyta ir vystyta mano disertaciniame darbe. Iš jų galima išskirti:

1. viengubos kristalinės skaidulos konfigūracija (angl. *single crystal fiber*, SCF) [43,74–76], kurioje aktyvioji terpė yra pakankamai ilga ir siaura (jos diametras yra 1 mm eilės, o ilgis 10 mm eilės). Dėl aktyviosios terpės matmenų ir didelio paviršiaus ploto ši technologija leidžia efektyviai nuvesti šilumą iš aktyviosios terpės, sugeneruotą kaupinimo spinduliuotės.

2. plokščios kristalinės aktyviosios terpės konfigūracija (angl. *InnoSlab*, IS) [30,77,78], kurioje aktyviosios terpės įėjimo ir išėjimo plokštuma (optinė apertūra) yra stačiakampio formos, kuri įgalina optinę grandinę formuoti taip, kad stiprinama spinduliuotė sklistų per aktyviąją terpę per vis kitą, naujai užkaupintą, kristalo segmentą.

3. plonojo disko daugelio lėkių per aktyviąją terpę konfigūracija (MP), kurioje stiprinama spinduliuotė sklinda per užkaupintą aktyviąją terpę daugelį kartų, kiekvieno sklidimo metu pataikantį į aktyviąją terpę su tam tikru kampiniu nuokrypiu nei prieš tai buvusio sklidimo [44,79–82].

4. išskiriamas atskiras segmentas stiprintuvinių sistemų, skirtų stiprinti impulsus iki itin didelės energijos (1 J lygio), bet mažo impulsų

pasikartojimo dažnio (~1 Hz) (angl. *The-High-Energy-Class Diode-Pumped-Solid-State-Lasers*, HEC-DPSSL).

Skyrius užbaigiamas pateikiant aptariamų sistemų santrauką parametrų žemėlapyje, kuriame pateikiamos sistemos priklausomai nuo jų pademonstruotos smailinės galios ir impulsų pasikartojimo dažnio. Pateikiamos parametrų rinkinio ribos, kurį buvo siekiama pademonstruoti šiame disertaciniame darbe. Šis grafikas pateiktas Pav. S.1.
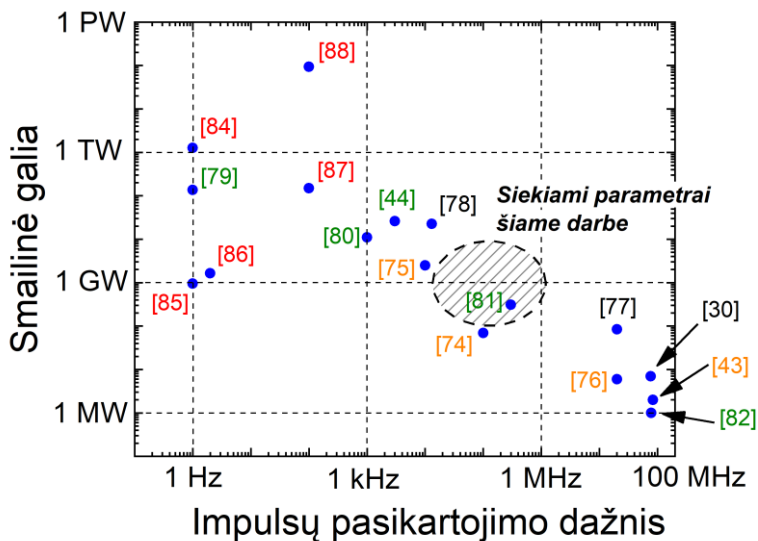
Pav. S.1 Apibendrintysis grafikas, parodantis skirtingų Yb:YAG kietojo kūno laisvos erdvės stiprintuvinių sistemų pademonstruotą smailinę galią ir impulsų pasikartojimo dažnį. Skaičiai žymi nuorodas į sistemas, kurių numeracija atitinka pateiktas literatūros sąraše (bibliografijoje). Skirtingos spalvos atitinka naudojamą technologiją bei jos tipą: raudona - HEC-DPSSL, žalia - MP, oranžinė - SCF, juoda - IS (žr. aprašymą aukščiau). Brūkšninė sritis parodo parametrų diapazoną, kuriuos buvo siekta pademonstruoti šioje disertacijoje.

Iš galo kaupinamos trijų energijos lygmenų terpės skaitmeninis modelis

Šiame skyriuje pristatomas iš galo kaupinamų Yb:YAG kristalų stiprintuvų skaitmeninis modelis, modeliuojantis spinduliuotės stiprinimą nuolatinės veikos režime. Modelis buvo parašytas *Matlab* terpėje.

Skyrius suskaidytas į poskyrius, kurie skirti aprašyti skirtingus modelio aspektus:

1. trijų energijos lygmenų lygtys, skirtos apskaičiuoti užpildos apgrąžą nuostovioje būsenoje. Pateikiame esminę išraišką, kuri naudojama užpildos apgrąžai skaičiuoti:

$$N_2 = \frac{\dfrac{\sigma_{12}I_p}{h\nu_p} + \dfrac{\sigma_{12}I_s}{h\nu_s}}{A_{21} + \dfrac{(\sigma_{12}+\sigma_{21})I_p}{h\nu_p} + \dfrac{(\sigma_{12}+\sigma_{21})I_s}{h\nu_s}}, \qquad \text{(S.1)}$$

kur N_2 santykinį aktyviosios terpės sužadinimo lygį, I_p, I_s žymi kaupinimo ir stiprinamosios spinduliuotės intensyvumą, $h\nu_p, h\nu_s$ žymi jų fotonų energijas, σ_{12}, σ_{21} atitinka pereinamųjų virsmų (sugerties ir išspinduliavimo) skerspjūvius, A_{21} žymi atvirkštinę priverstinės spinduliuotės spartą.

2. temperatūrinio skirstinio skaičiavimo išraiškos iš galo kaupinamame Yb:YAG kristale. Pagrindinė naudojama išraiška:

$$T(r,z) = -\int_0^r \frac{h(r_1,z)}{k(T)}\,dr_1 + T_0, \qquad \text{(S.2)}$$

kur h žymi šilumos srautą (W/m^2), L yra aktyviosios terpės ilgis, r yra radialinė koordinatė, I žymi kaupinimo spinduliuotės intensyvumą, k yra šiluminio laidumo koeficientas ($W/(m \cdot K)$), T_0 žymi aktyviosios terpės temperatūrą ties aktyviosios terpės ir aušinimo bloko sandūra (kraštinė sąlyga) bei T žymi skaičiuojamą temperatūros skirstinį aktyviojoje terpėje.

3. kaupinimo pluošto formos sklidimas, remiantis ABCD matricų metodu.

4. stiprinamosios spinduliuotės sklidimas pasinaudojant Hankelio transformacijų metodu.

5. aprašomos ir pateikiamos aktyviosios terpės savybės, tokios kaip sugerties ir emisijos skerspjūvių priklausomybė nuo bangos ilgio bei aktyviosios terpės temperatūros, bei šiluminio laidumo ir termo-optinio koeficiento priklausomybė nuo temperatūros.

Kiti du poskyriai skirti modelio algoritmo aprašymui. Modelyje aktyvioji terpė yra sudalinama erdvėje į pasirinktą kiekį pjūvių. Kiekvienas pjūvis yra dargi sudalinamas į baigtinį skaičių tūrinių erdvinių ląstelių radialine kryptimi, kiekviena iš kurių savyje laiko informaciją apie stiprinamosios ir kaupinimo spinduliuotės spektro skirstinį (t. y., kiekviena ląstelė yra taipogi sudalinama į baigtinį skaičių spektrinių ląstelių). Toks aktyviosios terpės suskaidymas į tinklinę struktūra leidžia, be pačio stiprinimo, taipogi modeliuoti ir spektro formos pokyčius, jo siaurėjimą stiprinimo metu, pluošto banginio fronto iškraipymus ir kt. Modeliuojamos aktyviosios terpės struktūra pateikta Pav. S.2.
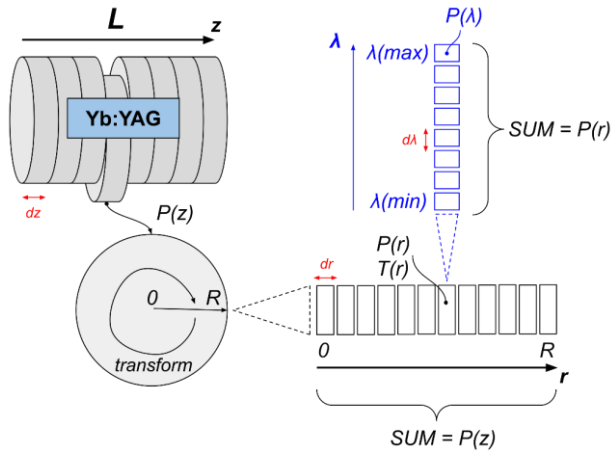
Pav. S.2 Modeliuojamos aktyviosios terpės tinklinė struktūra radialinės simetrijos atveju. L atitinka Yb:YAG kristalo ilgį, $P(z)$ atitinka stiprinamosios ir kaupinimo spinduliuotės pilną galią nagrinėjamame pjūvyje sklidimo atstume z, dz yra kristalo pjūvio storis, R žymi aktyviosios terpės spindulį, $transform$ žymi spinduliuotės galios skirstinio transformaciją iš dviejų matmenų plokštumos į radialinės simetrijos atvejį, r žymi radialinę koordinatę, dr yra tūrinės erdvinės ląstelės storis, $P(r)$ žymi pilną spinduliuotės galią šioje ląstelėje, $T(r)$ yra temperatūros vertė šioje ląstelėje, $\lambda(\text{min})$ ir $\lambda(\text{max})$ žymi modeliuojamą spektrinį diapazoną, $d\lambda$ yra spektrinio diapazono žingsnis, λ žymi bangos ilgių skanavimo kryptį modelyje, $P(\lambda)$ yra pilna galia spektrinėje ląstelėje.

Šiame darbe nagrinėjama dvigubo lėkio Yb:YAG stiprintuvo konfigūracija, kuomet stiprinamoji spinduliuotė per aktyviąją terpę sklinda du kartus (yra apgręžiama), o kaupinimo spinduliuotė sklinda tik viena kryptimi. Modelio algoritmas paremtas iteraciniu metodu, kurio išeities parametrai yra aktyviosios terpės temperatūros nusistovėjimas (po pirmo praėjimo per aktyviąją terpę) ir sustiprintos spinduliuotės vidutinės galios nusistovėjimas (po antrojo praėjimo). Pilnas modelio aprašymas pateiktas disertacijoje anglų kalba.

Skyrius užbaigiamas modelio eksperimentiniu patvirtinimu dvigubo lėkio iš galo kaupinamo Yb:YAG kristalo stiprintuve. Eksperimentams buvo panaudoti du skirtingų parametrų Yb:YAG kristalai: $2x2x20\ mm^3$ su 2% Yb^{3+} jonų legiravimo laipsniu ir $2x2x13\ mm^3$ su 3.6% Yb^{3+} jonų legiravimo laipsniu. Stiprintuvas buvo kaupinamas $64\ W$ nuolatinės veikos kaupinimo diodais, o stiprinamosios spinduliuotės ir kaupinimo pluošto diametrai aktyviosios terpės plokštumoje buvo parinkti $0.4\ mm$. Stiprinamosios spinduliuotės įvadinė galia siekė $0.46\ W$.

Eksperimentiniai rezultatai atitiko modeliavimo rezultatus su 7% paklaida mažo signalo stiprinimo režime ir su mažesne nei 12% paklaida esant pilnai įvadinio signalo pradinei galiai į stiprintuvą. Kaip pavyzdį šioje santraukoje

pateikiu eksperimentinius ir stiprinimo rezultatus vienu iš nagrinėjamų atvejų, kuomet aktyvioji terpė buvo $2x2x13\ mm^3@3.6\%$ Yb:YAG kristalas (Pav. S.3).
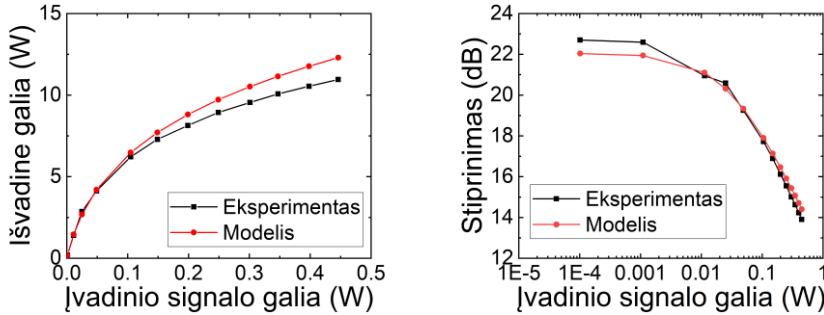

Pav. S.3 Eksperimentiniai ir modeliavimo stiprinimo duomenys dviejų lėkių iš galo kaupinamo $2x2x13\ mm^3@3.6\%$ Yb:YAG kristalo atveju. Kairėje – išvadinės galios priklausomybė nuo įvadinės signalo galios, dešinėje – signalo stiprinimo priklausomybė nuo įvadinės signalo galios.

Buvo pastebėta, kad išmatuotas neatitikimas greičiausiai lemtas parametrų verčių, pateiktų literatūroje, neidealaus atitikimo eksperimentiškai naudotiems kristalams. Taipogi buvo pastebėta, kad sumodeliuotas pluošto sklidimas ir jo skirstinio degradacija, bei stiprinamosios spinduliuotės spektro formos pokyčiai beveik idealiai atitiko modeliavimo prognozes. Pristatytas modeliavimo paketas leidžia gerai prognozuoti iš galo kaupinamų stiprintuvų elgseną.

Dvigubo lėkio diodais kaupinamų kietojo kūno stiprintuvų, kuriuose Yb:YAG naudojamas kaip stiprintuvinė terpė, skaitmeninis optimizavimas

Šiame skyriuje, pasinaudojant antrajame skyriuje pristatytu modeliu, yra pateikiama iš galo kaupinamo dvigubo lėkio Yb:YAG stiprintuvo parametrų optimizacija. Principinė modeliuojama konfigūracija pateikiama Pav. S.4.
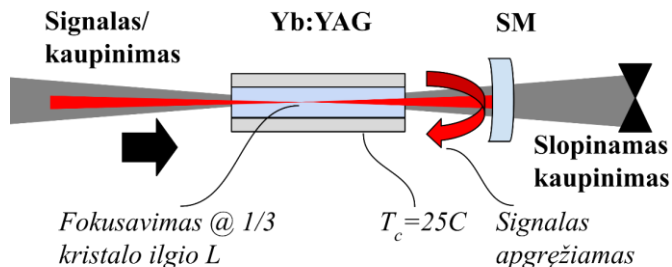
Pav. S.4 Principinė modeliuojamos dvigubo lėkio iš galo kaupinamo Yb:YAG kristalo stiprintuvo schema. Raudona rodyklė žymi stiprinamosios spinduliuotės sklidimą, juoda – kaupinimo spinduliuotės. *SM* žymi sferinį veidrodį, skirtą stiprinamosios spinduliuotės apgrąžai. Signalo ir kaupinimo spinduliuotės buvo fokusuojamos į pirmąjį trečdalį aktyviosios terpės ilgio *L*. Aktyviosios terpės aušinimo temperatūra buvo parinkta $T_c = 20\text{℃}$ (kraštinės sąlygos).

Vienas iš svarbesnių šio optimizavimo aspektų – tinkamo konfigūracijai kristalo ilgio *L* ir aktyvių jonų legiravimo laipsnio *X* parinkimas, vertinant šių parametrų įtaką spinduliuotės stiprinimui. Modeliuojant buvo pastebėta, kad šių parametrų sandaugos $CDD = L \cdot X$ vertė yra fiksuota ties fiksuotu kaupinimo intensyvumu, nepriklausomai nuo kaupinimo pluošto diametro. Toks sutapimas gerai koreliuoja su pastebėjimais kituose moksliniuose darbuose, kuomet šiam parametrui net įvedamas atskiras terminas, kuris naudojamas ir mano disertaciniame darbe – skiltinis legiravimo tankis (angl. *columnar doping density*, CDD) [104]. Sumodeliuota šio parametro priklausomybė nuo kaupinimo intensyvumo pateikiama žemiau, Pav. S.5.
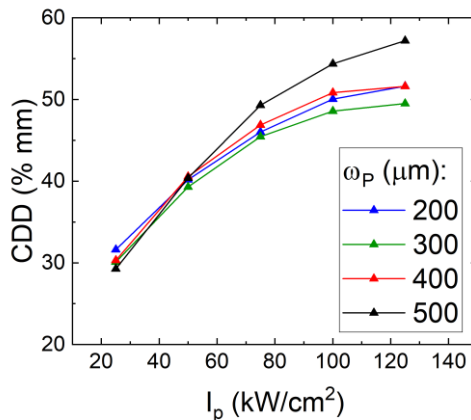
Pav. S.5 Skiltinio legiravimo tankio (CDD) parametrų priklausomybė nuo kaupinimo spinduliuotės intensyvumo esant skirtingiems kaupinimo ir signalo pluošto diametrams (kiekvienu modeliuotu atveju jie sutapo). Įvadinė signalo galia sutapo su signalo soties galia: $P_{sat} = 1.3; 2.9; 5.2; 8.1\,W$ esant signalo/kaupinimo pluošto diametrams $\omega = 200; 300; 400; 500\,\mu m$.

Taip pat buvo sumodeliuota, kad, nors parametras CDD nepriklauso nuo kaupinimo pluošto diametro, tačiau optimalus kristalo ilgis priklauso (kuris įeina į minėtą parametrą) – kuo kaupinimo pluošto diametras mažesnis, tuo kristalo ilgis turi būti parenkamas trumpesnis, norint pasiekti maksimalų stiprinimą. Šis pastebėjimas koreliuoja su kaupinimo spinduliuotės skėstimi – esant mažam pluošto diametrui, skėstis santykinai didelė, todėl, jei aktyvioji terpė parenkama per ilga, jos galiniame segmente kaupinimo spinduliuotė

išplinta dėl difrakcijos tiek, kad likutinio intensyvumo nebepakanka efektyviam stiprinimui. Modeliavimo rezultatai rodo, kad optimalus kristalo ilgio ir kaupinimo spinduliuotės Relėjaus ilgio (kuris aprašo skėstį) santykis yra $L/z_R \sim 2-3$.

Kitame šio skyriaus poskyryje aptariama įvadinio signalo spektro pločio įtaka spektro pločio pokyčiui esant skirtingam signalo stiprinimui Yb:YAG stiprintuve. Kaip parametras įvedamas santykis $\frac{\tau_{in}}{\tau_{out}}$, kuris parodo, kiek pakito spektriškai riboto įvadinio impulso trukmė lyginant su spektriškai ribota impulso trukme po stiprinimo. Tokio modeliavimo duomenys pateikti Pav. S.6.
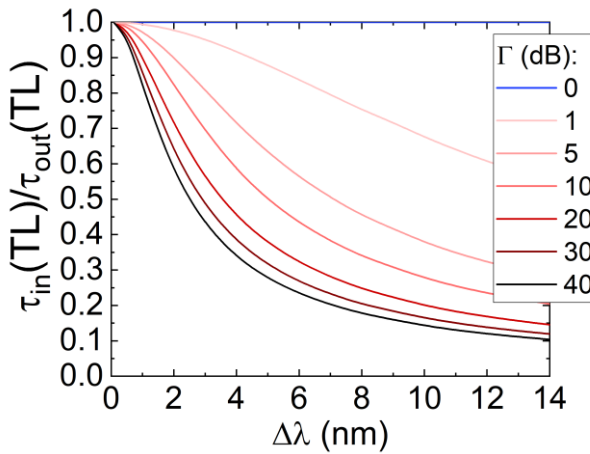
Pav. S.6 Santykio tarp įvadinio signalo spektriškai ribotos impulso trukmės ir sustiprinto signalo spektriškai ribotos impulso trukmės priklausomybė nuo įvadinio signalo spektro pločio, vertinamo pusės maksimalaus intensyvumo aukštyje esant skirtingiems stiprinimo koeficientams Γ (išreikštais dB).

Žvelgiant iš praktinės pusės, iš gautų rezultatų buvo padaryta išvada, kad įvadinio signalo spektro plotis $\Delta\lambda = 4.0\ nm$ (atitinka spektriškai riboto impulso trukmę $\tau_{TL} = 390\ fs$) yra geras pasirinkimas, norint, kad po stiprinimo spektriškai riboto impulso trukmė būtų mažesnė nei 1 ps. Tokia impulsų trukmė, kaip buvo minėta ankstesniuose skyriuose, yra tinkama daugelyje taikymų.

Paskutiniame šio skyriaus poskyryje buvo skaitmeniškai išanalizuota, bei eksperimentiškai patvirtinta, kaupinimo pluošto sąsmaukos fokusavimo padėties aktyvioje terpėje įtaka stiprinimui. Buvo patikrinta prielaida, pateikta literatūroje, kad optimali (optinio stiprinimo prasme) kaupinimo pluošto sąsmaukos fokusavimo padėtis aprašoma [110,111]:

$$z_{optimalus} = \frac{\ln(2)}{\alpha},\qquad\qquad (S.3)$$

kur α yra kaupinimo spinduliuotės sugerties koeficientas (mm^{-1}), kuris apytikriai gali būti įvertinamas iš $\alpha = N_d \sigma_a$ (čia N_d yra aktyvių jonų koncentracija aktyvioje terpėje, σ_a yra kaupinimo spinduliuotės sugerties skerspjūvis). Šios analitinės išraiškos rezultatai buvo palyginti su modeliavimo ir eksperimentiniais rezultatais, žr. Pav. S.7.
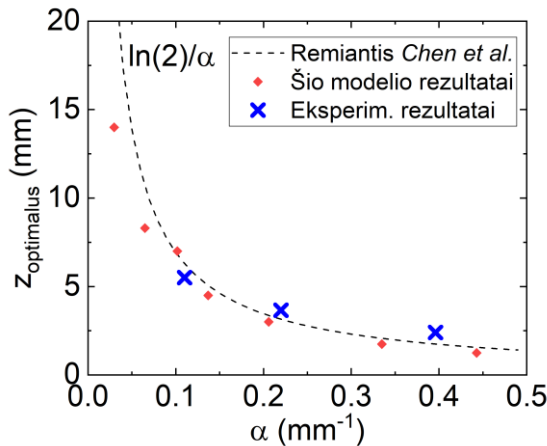

Pav. S.7 Skaitmeniškai sumodeliuotos ir eksperimentiškai išmatuotos optimalios (stiprinimo prasme) kaupinimo pluošto sąsmaukos padėties $z_{optimalus}$ kristale priklausomybė nuo kaupinimo spinduliuotės sugerties koeficiento α (raudoni taškai – modeliavimo rezultatai, mėlyni kryželiai – eksperimentiniai rezultatai). Modeliavimams naudotas Yb:YAG kristalas, kurio ilgis $L = 30\ mm$, kaupinimo pluošto diametras $\omega_P = 0.4\ mm$ (varijuotas legiravimo laipsnis, kad atitiktų modeliuojamą α). Eksperimentams naudoti kristalai: $2x2x12\ mm^3$ su 3.6% legiravimo laipsniu ($\alpha = 0.396\ mm^{-1}$), $2x2x20\ mm^3$ su 2% legiravimo laipsniu ($\alpha = 0.22\ mm^{-1}$), ir $4x4x30\ mm^3$ su 1% legiravimo laipsniu ($\alpha = 0.11\ mm^{-1}$). *Chen et al.* prielaida pateikta punktyrine linija.

Modeliavimo bei eksperimentiniai rezultatai gerai atitiko pasiūlytą analitinę išraišką, pateiktą literatūroje [110,111]. Esminis pastebėjimas buvo toks, kad kuo didesnis kaupinimo sugerties koeficientas aktyviojoje terpėje (arba kitaip – kaupinimo sugerties sparta kristale), tuo arčiau prie kristalo įvadinės plokštumos turi būti fokusuojama kaupinimo spinduliuotė, norint pasiekti maksimalų stiprinimą.

Vienos pakopos iš galo kaupinamų Yb:YAG stiprintuvų eksperimentinė plėtra

Šiame skyriuje pristatomos ir eksperimentiškai pademonstruojamos hibridinės lazerinės sistemos galimybės, kuriose kaip užkrato šaltinis naudojamas skaidulinis lazeris (pagamintas kompanijoje *Ekspla*, UAB), o tolimesniam stiprinimui naudojamas dvigubo lėkio iš galo kaupinama Yb:YAG kristalo stiprintuvinė pakopa. Stiprinimo pakopos buvo optimizuotos panaudojant sukurtą modeliavimo paketą, kuris aprašytas ankstesniuose skyriuose.

Pirmosios eksperimentiškai pademonstruotos sistemos principinė schema pateikta Pav. S.8, kurios esminis naujumas buvo impulso plėtimas ir suspaudimas laike dispersiškai suderintoje CFBG ir CVBG poroje.
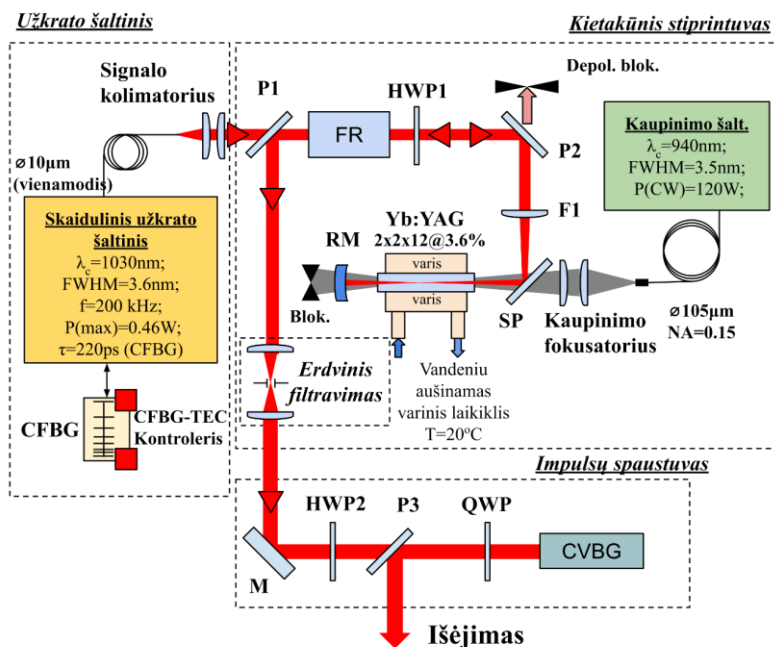
Pav. S.8 Principinė hibridinio lazerio optinė schema. Ją sudarė visiškai skaidulinis užkrato šaltinis, laisvos erdvės dvigubo lėkio iš galo kaupinamas Yb:YAG stiprintuvas ir impulsų spaustuvas CVBG pagrindu. HWP1, HWP2 – pusės bangos ilgio fazinės plokštelės, FR – Faradėjaus rotatorius, P1, P2, P3 – poliarizatoriai, SP – kaupinimo/signalo pluoštų separatorius, F1 – fokusuojantysis lęšis, RM – signalą apgręžiantis sferinis veidrodis, M – veidrodis, CFBG – čirpuota skaidulinė Brego gardelė, CVBG – čirpuota tūrinė Brego gardelė, QWP – ketvirčio bangos ilgio fazinė plokštelė. Kristalas buvo įstatytas į varinį laikiklį, kuris buvo aušinamas vandeniu 20°C temperatūroje.

Skaidulinis užkrato šaltinis generavo $2.3\,\mu J$ energijos impulsus ties $200\,kHz$ impulsų pasikartojimo dažniu. Užkrato šaltinio spinduliuotės

spektro plotis buvo 3.6 nm (pusės maksimalaus intensyvumo aukštyje), centruotas ties 1030 nm bangos ilgiu. Stiprintuvas buvo kaupinamas nuolatinės veikos lazeriniu diodu su 84 W vidutinės galios spinduliuote, kurios spektro plotis buvo 3.5 nm (pusės maksimalaus intensyvo aukštyje) ties 940 nm centriniu bangos ilgiu nuolatinės. Kaupinimo ir signalo pluoštai buvo sufokusuoti į $\omega_p = 0.36\ mm$ and $\omega_s = 0.33\ mm$ pluošto diametrus atitinkamai ir idealiai perkloti aktyvioje terpėje. Sustiprinta spinduliuotė buvo apgręžiama su $R = 100\ mm$ kreivumo radiuso sferiniu veidrodžiu, pastatytu reikiamu atstumu nuo aktyviosios terpės, kad būtų sukompensuota termo-lęšio įtaka, ir toliau stiprinama per antrąjį lėkį per aktyviąją terpę. Kaupinimo spinduliuotė po pirmojo lėkio buvo atskirta nuo optinės stiprintuvo grandinės su dichroiniu veidrodžiu, ir toliau nebenaudojama (žr. Pav. S.8). Sustiprintos spinduliuotės pluoštas buvo išvedamas iš stiprintuvo atskiriant įeinančią ir išeinančią spinduliuotę per poliarizaciją. Tokio stiprintuvo stiprinimo rezultatai pateikti Pav. S.9.
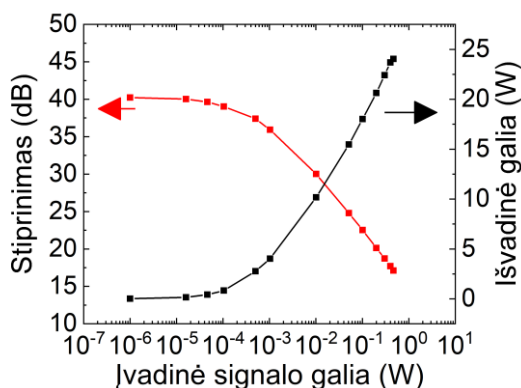
Pav. S.9 Vidutinės išvadinės galios (juoda kreivė, dešinioji ašis) ir stiprinimo (raudona kreivė, kairioji ašis) priklausomybė nuo įvadinės signalo galios (logaritminė skalė). Impulsų pasikartojimo dažnis buvo 200 kHz. Stiprintuvas kaupinamas 84 W vidutine galia nuolatinės veikos režime.

Šioje konfigūracijoje buvo pasiekta 24 W išvadinė vidutinė galia (atitinka 120 μJ impulso energiją ties 200 kHz impulsų pasikartojimo dažniu) esant 460 mW įvadinei signalo galiai, kas atitinka $\eta = 28\ \%$ stiprintuvo optinį efektyvumą, o mažo signalo stiprinimas siekė rekordiškai didelį ~40 dB. Sustiprinto pluošto kokybė po erdvinio filtravimo siekė difrakciškai ribotą su kokybės parametru M^2~1.0. Sustiprinti impulsai buvo suspausti CVBG impulsų spaustuve. Impulsų gaubtinė buvo charakterizuota antrosios harmonikos generacijos dažninės skyros optinio moduliavimo metodu (angl.

second harmonic generation frequency-resolved optical gating, SHG-FROG).
Rezultatai pateikti Pav. S.10.
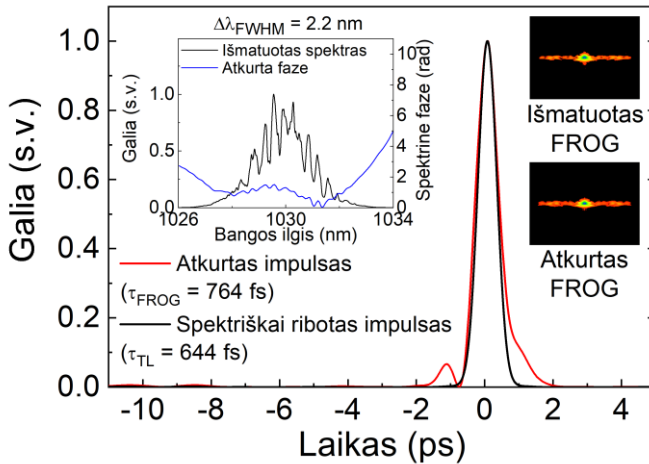
Pav. S.10 Laike suspaustų ir SHG-FROG metodu atkurtų impulsų gaubtinė (raudona kreivė). Juoda kreivė atitinka spektriškai riboto impulso gaubtinę.. Įsiuvai: (kairėje) išmatuotas sustiprinto impulso spektras ir atkurta spektrinė fazė; (dešinėje) išmatuotas ir atkurtas FROG užrašas (0.15% atkūrimo paklaida).

Suspaustų impulsų trukmė beveik sutapo su spektriškai ribota impulso trukme (764 fs ir 644 fs atitinkamai). Buvo išsiaiškinta, kad minimalus neatitikimas buvo didžiąja dalimi nulemtas netiesinių reiškinių sukeltų fazinių impulso iškraipymų skaiduliniame lazeryje. Pluošto kokybė po impulsų spūdos CVBG buvo artima difrakciškai ribotai ($M^2 \sim 1.15$) su minimaliais pluošto iškraipymais, nulemtais CVBG kokybės – šis efektas išsamiai aprašytas literatūroje [115]. Tokio impulsų spaustuvo optinis efektyvumas siekė 87 %. Esminis ribojimas norint pasiekti didesnę impulso energiją iš tokios konfigūracijos buvo nulemtas CVBG elemento – eksperimentiškai buvo pastebėta, kad impulso energijai, patenkančiai į impulsų spaustuvą, viršijus 200 μJ, pluošto kokybė drastiškai suprastėja, todėl buvo pasirinkta sąlyginai konservatyvi, bet praktiška konfigūracijos realizacija. Įskaičius visus optinius sistemos nuostolius, tokios sistemos išėjime buvo pasiekti 764 fs trukmės ir 104 μJ energijos impulsai su 20.8 W vidutine galia išėjime – tai atitinka $P_p \sim 0.13\ GW$ smailinę galią. Pluošto kokybė sistemos išėjime buvo beveik difrakciškai ribota ($M^2 \sim 1.15$), kaip parodyta Pav. S.11.
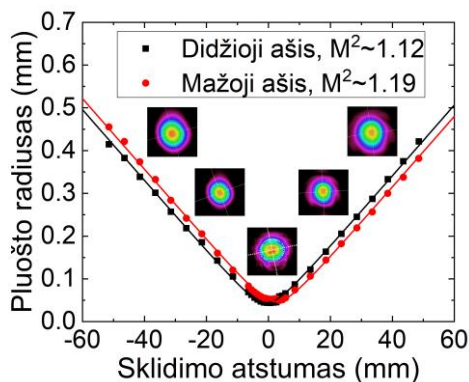
Pav. S.11 Pluošto kokybės matavimo rezultatai lazerinės sistemos išėjime. Pluoštas buvo perfokusuotas su teigiamu F=200 mm židinio ilgio lęšiu ir išmatavus pluošto dydžio evoliuciją jam sklindant. Pluošto kokybės parametras buvo įvertintas z-scan metodu, aproksimavus eksperimentinius rezultatus kokybės funkcija, kuri davė vidutinę reikšmę M²~1.15. Grafike pateikti pluošto intensyvumo skerspjūviai keliose matavimo vietose.

Atsižvelgus į pasiekiamos impulso energijos apribojimus, kuriuos lėmė eksperimentams panaudoto CVBG kokybė, buvo nuspręsta pakeisti impulsų spaustuvo konfigūraciją. Tam tikslui buvo suprojektuota ir eksperimentiškai realizuota impulsų spaustuvo optinė schema, kurią sudarė difrakcinė gardelė, kurios rėžių tankis $1842\ mm^{-1}$. Optinė impulsų spaustuvo grandinė buvo sulankstyta taip, kad spaudžiamas laike impulsas per gardelę sklistų 4 kartus, taip išlaikant vieną iš pagrindinių lazerinės sistemos koncepcijų – kompaktiškumą. Stiprinimo charakteristikos Yb:YAG stiprintuve yra identiškos pateiktoms anksčiau, kaip parodyta Pav. S.9, todėl atskirai nepateikiamos.

Laike suspaustų impulsų kokybė po Yb:YAG stiprintuvo buvo charakterizuota išmatavus impulsų autokoreliacinę funkciją su *pulseCheck* (*APE*) impulsų autokoreliatoriumi ties $13.9\ kHz$ impulsų pasikartojimo dažniu ir $E = 5.5\ \mu J$ užkrato šaltinio impulsų energija – tai atitiko maksimalią galimą impulso energiją iš skaidulinio lazerio, beigi maksimalią pasiekiamą impulsų energiją iš Yb:YAG stiprintuvo. Yb:YAG stiprintuvo kaupinimo sąlygos liko tos pačios, t. y., kristalas buvo kaupinamas $84\ W$ vidutinės galios spinduliuote. Tokiu atveju, maksimali išmatuota impulsų energija po Yb:YAG stiprintuvo, įskaičius nuostolius dėl erdvinio filtravimo, buvo $1.14\ mJ$ (stiprintuvo optinis efektyvumas siekė $\eta = 19\ \%$). Laikinės spūdos rezultatai pateikti Pav. S.12.
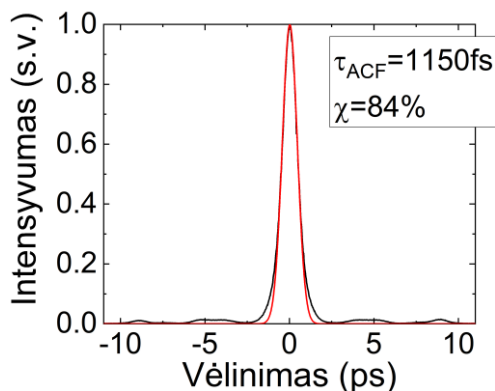
Pav. S.12 Eksperimentiškai išmatuota laike suspaustų impulsų autokoreliacinė funkcija po Yb:YAG stiprintuvo. Impulsai buvo spaudžiami laike keturių lėkių difrakcinės gardelės impulsų spaustuve. Difrakcinės gardelės rėžių tankis atitiko $1842~mm^{-1}$. Juoda kreivė atitinka išmatuotą autokoreliacinę funkciją, raudona – išmatuotos funkcijos apkroksimacija Gauso funkcija. Parametras χ atitinka plotų santykį, kurį užima šios funkcijos laikinėje skalėje. τ_{ACF} atitinka išmatuotos funkcijos plotį pusės maksimalaus intensyvo aukštyje.

Išmatuotų impulsų autokoreliacinės funkcijos plotis pusės maksimalaus intensyvumo aukštyje atitiko $\tau_{ACF} = 1150~fs$. Laikant, kad impulsų laikinė gaubtinė artima Gausiniam impulsui (o tokia aproksimacija galima, kaip parodė ankstesni rezultatai), buvo įvertinta, kad išmatuotų impulsų trukmė atitinka $\tau = 815~fs$. Spektriškai ribotų impulsų trukmė įvertinta $\tau_{TL} = 760~fs$, kas rodo, kad impulsų laikinės spūdos kokybė yra labai gera. Vėlgi, minimalus neatitikimas buvo didžiąja dalimi nulemtas netiesinių reiškinių sukeltų fazinių impulso iškraipymų skaiduliniame lazeryje. Impulsų kokybė taipogi buvo įvertinta iš parametro $\chi = 84~\%$, kuris atitinka plotų santykį, kurį užima eksperimentiškai išmatuota autokoreliacinė funkcija ir jos aproksimacija Gauso funkcija laikinėje skalėje, kas vėlgi indikavo labai gerą impulso laikinę kokybę.

Optiniai nuostoliai, patirti impulsų spaustuve, siekė $\sim 10~\%$, kas lėmė, kad sistemos išėjime impulsų energija siekė $E = 1.01~mJ$ (ties $13.9~kHz$ impulsų pasikartojimo dažniu), kuri buvo išmatuota su energijos matuokliu *J-25MT-10KHZ* (*Coherent*). Tai atitiko smailinę spinduliuotės galią $P_p = 1.16~GW$, su difrakciškai ribota pluošto kokybe $M^2 \sim 1$, kaip parodyta Pav. S.13.
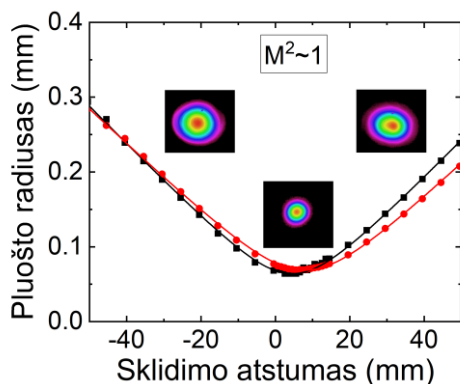
Pav. S.13 Pluošto kokybės matavimo rezultatai lazerinės sistemos išėjime. Pluoštas buvo perfokusuotas su teigiamu F=200 mm židinio ilgio lęšiu ir išmatavus pluošto dydžio evoliuciją jam sklindant. Pluošto kokybės parametras buvo įvertintas z-scan metodu, aproksimavus eksperimentinius rezultatus kokybės funkcija, kuri davė vidutinę reikšmę M^2~1. Grafike pateikti pluošto intensyvumo skerspjūviai keliose matavimo vietose.

Kitame šio skyriaus poskyryje yra aptariamos problematikos, kylančios iš galo kaupinamo Yb:YAG kristalo stiprintuve, kurios ribojo didesnę pasiekiamą vidutinę galią bei impulsų energiją pristatytose konfigūracijose. Pagrindinės priežastys – terminių reiškinių sąlygotas sustiprinto pluošto astigmatizmas bei galios nuostoliai dėl depoliarizacijos.

Buvo išsiaiškinta ir eksperimentiškai pademonstruota, kad sustiprinto pluošto astigmatizmo prigimtis yra sąlygota kaupinimo spinduliuotės sukeltų šiluminių efektų, ir priklausoma nuo stiprinamos spinduliuotės poliarizacinės būsenos. Tuo atveju, kai kristale sklinda ir yra stiprinama tiesinės poliarizacinės būsenos spinduliuotė, pluošto dalys, atitinkančios horizontaliąją ir vertikaliąją ataskaitines ašis, „mato" skirtingus kristalo lūžio rodiklio pokyčius dėl kaupinimo spinduliuotės sąlygotų šiluminių efektų ir iš jų atsirandančių mechaninių įtempimų kristale, kurių principinės ašys yra orientuotos radialine ir tangentine ašimis (šis efektas yra stebimas pvz. Yb:YAG kristaluose, kurių kristalografinės ašys yra orientuotos [111] kryptimi [33,35]).

Eksperimentiškai pademonstruota, kad sustiprinto pluošto astigmatizmą galima praktiškai minimizuoti stiprinant apskritiminės poliarizacinės būsenos pluoštą Yb:YAG kristale. Tai buvo įgyvendinta prieš ir po Yb:YAG kristalą pastačius ketvirčio bangos ilgio plokšteles, kurių optinės ašys buvo orientuotos taip, kad į kristalą sklindančios tiesinės poliarizacinės būsenos pluoštas būtų konvertuotas į apskritiminės poliarizacinės būsenos pluoštą, o už kristalo poliarizacinė pluošto būsena būtų vėl atversta į tos pačios krypties tiesinę poliarizacinę būseną (t. y., likusioje sistemos dalyje poliarizacinės

194

būsenos kryptis išliktų nepakitusi). Sustiprinto pluošto astigmatizmo pokytis dėl kaupinimo spinduliuotės sąlygotų terminių efektų buvo vertinamas per pluošto apvalumo pokytį, kuris randamas perfokusuojant sustiprintą pluoštą su teigiamo židinio lęšiu, bei surandant tokią padėtį, kurioje pluoštas yra eliptiškiausias (parametras ε) [118]. Daugiau informacijos galima rasti pilnoje disertacijos versijoje anglų kalba.

Visgi, toks astigmatizmo minimizavimo metodas turi trūkumą – stiprinant apskritiminės poliarizacinės būsenos pluoštą Yb:YAG kristale, nuostoliai dėl depoliarizacijos išaugo beveik du kartus – išmatuota, kad galios nuostoliai dėl depoliarizacijos išaugo nuo $\sim 1.2\,\%$ (tiesinė poliarizacija) iki $\sim 2.6\,\%$ (apskritiminė poliarizacija) vieno lėkio per Yb:YAG kristalą atveju (su $P_p = 110\,W$ kaupinimo spinduliuotės galia). Autoriaus nuomone, šie papildomi nuostoliai dėl depoliarizacinių reiškinių Yb:YAG kristale yra šiuo atveju mažiau svarbūs nei pluošto kokybės blogėjimas dėl astigmatizmo, kadangi, žvelgiant iš praktinės pusės, tokiu atveju galima kaupinti kristalą su didesne kaupinimo galia, ir taip pasiekti absoliutine prasme didesnę išėjimo galią su geresne pluošto kokybe, negu netaikant šio metodo.

Toks astigmatizmo minimizavimo metodas buvo pritaikytas eksperimentiškai pademonstruojant hibridinę lazerinę sistemą paskutiniame šio skyriaus poskyryje. Šios sistemos išskirtinumas buvo dvejopas. Viena vertus, buvo pasirinktas impulsų užkrato šaltinis, generuojantis sąlyginai aukštos vidutinės galios spinduliuotę ($P_S = 3.3\,W$), bet su pakankamai plačiu impulsų spektro pločiu ($\Delta\lambda(FWHM) = 7.7\,nm$). Didelė signalo spinduliuotės vidutinė galia lėmė tai, kad Yb:YAG stiprintuvas buvo pakankamai įsotintas stiprinimo prasme, taip išvengiant reikšmingo stiprinamų impulsų spektro siaurėjimo dėl siauros Yb:YAG stiprinimo juostos bei stiprinimo efekto. Tai leido pasiekti $330\,fs$ trukmės impulsus, kaip pademonstruojama vėliau. Antra vertus, pasirinktas sustiprinto pluošto astigmatizmo minimizavimo metodas su ketvirčio bangos ilgio plokštelėmis leido pasiekti itin gerą pluošto kokybę, kaip pademonstruojama vėliau. Principinė demonstruojamos konfigūracijos schema pateikta Pav. S.14, kurioje kaip impulsų spaustuvas buvo pasirinktas keturių lėkių difrakcinės gardelės (rėžių tankis $1739\,mm^{-1}$) impulsų spaustuvas, siekiant išvengti pluošto kokybės blogėjimo, kaip buvo matyti su CVBG tipo impulsų spaustuvu.
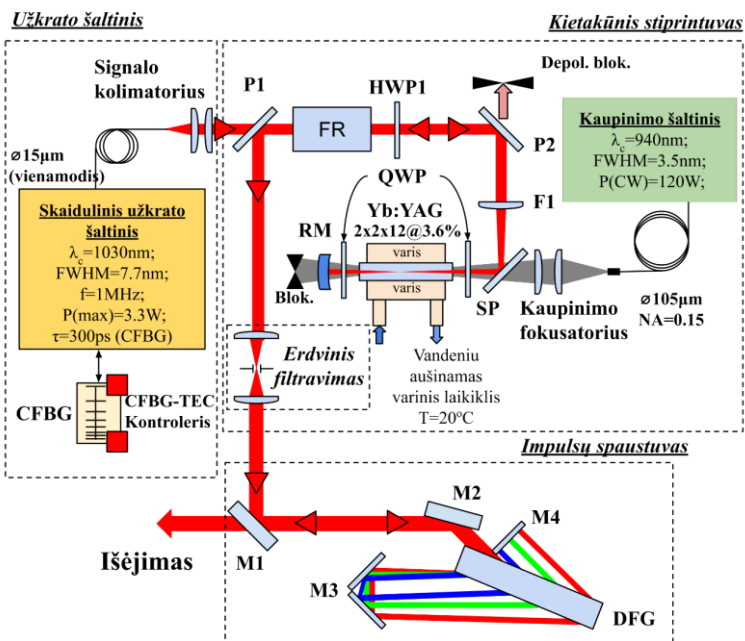
Pav. S.14 Principinė hibridinio lazerio optinė schema. Ją sudarė visiškai skaidulinis užkrato šaltinis, laisvos erdvės dvigubo lėkio iš galo kaupinamas Yb:YAG stiprintuvas ir impulsų spaustuvas difrakcinės gardelės (rėžių tankis 1739 mm^{-1}) pagrindu. HWP1 – pusės bangos ilgio fazinė plokštelė, QWP – ketvirčio bangos ilgio fazinė plokštelė, FR – Faradėjaus rotatorius, P1, P2 – poliarizatoriai, SP – kaupinimo/signalo pluoštų separatorius, F1 – fokusuojantysis lęšis, RM – signalą apgręžiantis sferinis veidrodis, M1-M4 – veidrodžiai, CFBG – čirpuota skaidulinė Brego gardelė, DFG – difrakcinė gardelė. Kristalas buvo įstatytas į varinį laikiklį, kuris buvo aušinamas vandeniu 20℃ temperatūroje.

Skaidulinis užkrato šaltinis generavo 3.3 μJ energijos impulsus ties 1 MHz impulsų pasikartojimo dažniu (atitiko 3.3 W vidutinę galią). Užkrato šaltinio spinduliuotės spektro plotis buvo 7.7 nm (pusės maksimalaus intensyvumo aukštyje), centruotas ties 1030 nm bangos ilgiu. Stiprintuvas buvo kaupinamas nuolatinės veikos lazeriniu diodu su 110 W vidutinės galios spinduliuote (maksimali galima galia iš naudoto kaupinimo diodo), kurios spektro plotis buvo 3.5 nm (pusės maksimalaus intensyvo aukštyje) ties 940 nm centriniu bangos ilgiu. Kaupinimo ir signalo pluoštai buvo sufokusuoti į $\omega_p = 0.36\ mm$ and $\omega_s = 0.33\ mm$ pluošto diametrus atitinkamai ir idealiai perkloti aktyvioje terpėje. Prieš ir po Yb:YAG kristalą buvo pastytos ketvirčio bangos ilgio plokšteles, kurių optinės ašys buvo orientuotos taip, kad į kristalą sklindančios tiesinės poliarizacinės būsenos pluoštas būtų konvertuotas į apskritiminės poliarizacinės būsenos pluoštą, o už kristalo poliarizacinė pluošto būsena būtų vėl atversta į tos pačios krypties tiesinę poliarizacinę būseną (t. y., likusioje sistemos dalyje poliarizacinės

būsenos kryptis išliktų nepakitusi). Sustiprinta spinduliuotė buvo apgręžiama su $R = 100\,mm$ kreivumo radiuso sferiniu veidrodžiu, pastatytu reikiamu atstumu nuo aktyviosios terpės, kad būtų sukompensuota termo-lęšio įtaka, ir toliau stiprinama per antrąjį lėkį per aktyviąją terpę. Kaupinimo spinduliuotė po pirmojo lėkio buvo atskirta nuo optinės stiprintuvo grandinės su dichroiniu veidrodžiu, ir toliau nebenaudojama (žr. Pav. S.14). Sustiprintos spinduliuotės pluoštas buvo išvedamas iš stiprintuvo atskiriant įeinančią ir išeinančią spinduliuotę per poliarizaciją. Tokio stiprintuvo stiprinimo rezultatai pateikti Pav. S.15.
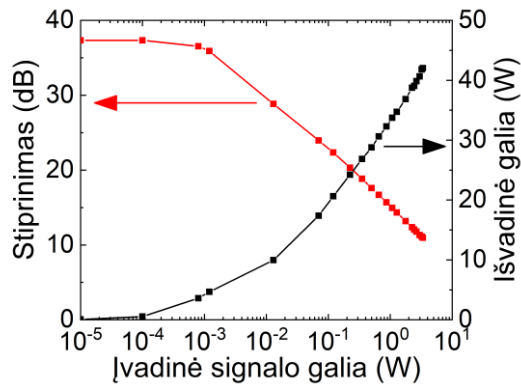
Pav. S.15 Vidutinės išvadinės galios (juoda kreivė, dešinioji ašis) ir stiprinimo (raudona kreivė, kairioji ašis) priklausomybė nuo įvadinės signalo galios (logaritminė skalė). Impulsų pasikartojimo dažnis buvo 1 MHz. Stiprintuvas kaupinamas 110 W vidutine galia nuolatinės veikos režime.

Šioje konfigūracijoje buvo pasiekta $42\,W$ išvadinė vidutinė galia (atitinka $42\,\mu J$ impulso energiją ties $1\,MHz$ impulsų pasikartojimo dažniu) esant $3.3\,W$ įvadinei signalo galiai, kas atitinka $\eta = 40\,\%$ stiprintuvo optinį efektyvumą, o mažo signalo stiprinimas siekė $\sim 37\,dB$. Nuostoliai dėl depoliarizacijos bei erdvinio filtravimo siekė 8 % ir 5 % atitinkamai, kas lėmė išvadinės galios sumažėjimą iki $36.4\,W$, tačiau pluošto kokybė buvo difrakciškai ribota su minimaliu šiluminių reiškinių sukeltu astigmatizmu, kaip parodyta Pav. S.16.
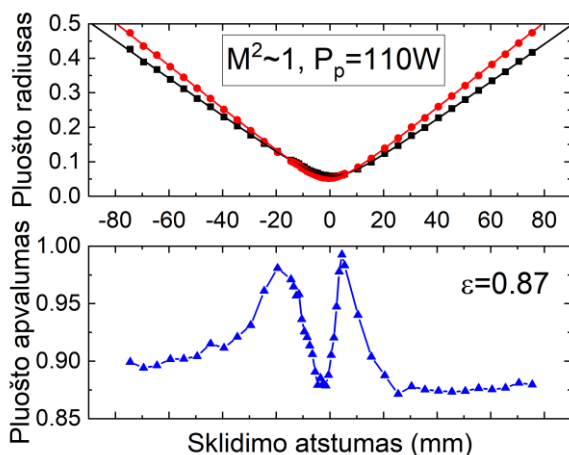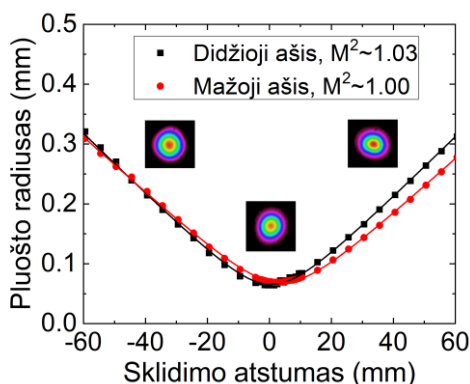
Pav. S.16 Pluošto kokybės matavimo rezultatai po Yb:YAG stiprintuvo bei erdvinio filtravimo. Pluoštas buvo perfokusuotas su teigiamu F=200 mm židinio ilgio lęšiu ir išmatavus pluošto dydžio evoliuciją jam sklindant. Pluošto kokybės parametras buvo įvertintas z-scan metodu, aproksimavus eksperimentinius rezultatus kokybės funkcija, kuri davė vidutinę reikšmę $M^2 \sim 1$. Apatiniame grafike pateiktas pluošto apvalumo pokytis jam sklindant, o pluošto apvalumo parametras blogiausioje vietoje atitiko $\varepsilon = 0.87$ (be kaupinimo atitiko $\varepsilon = 0.92$).

Impulsų gaubtinė buvo charakterizuota antrosios harmonikos generacijos dažninės skyros optinio moduliavimo metodu (angl. *second harmonic generation frequency-resolved optical gating*, SHG-FROG). Rezultatai pateikti Pav. S.17.
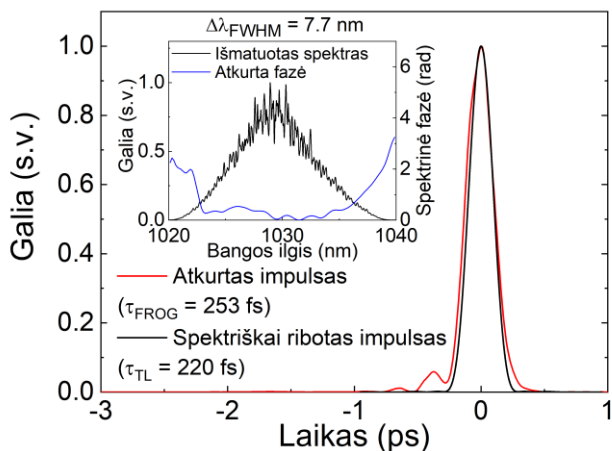
Pav. S.17 Laike suspaustų ir SHG-FROG metodu atkurtų impulsų gaubtinė (raudona kreivė). Juoda kreivė atitinka spektriškai riboto impulso gaubtinę.. Įsiuvai: (kairėje) išmatuotas sustiprinto impulso spektras ir atkurta spektrinė fazė; (dešinėje) išmatuotas ir atkurtas FROG užrašas (0.15% atkūrimo paklaida).

Suspaustų impulsų trukmė beveik sutapo su spektriškai ribota impulso trukme (318 fs ir 315 fs atitinkamai). Minimalus neatitikimas buvo didžiąja dalimi nulemtas netiesinių reiškinių sukeltų fazinių impulso iškraipymų skaiduliniame lazeryje. Pluošto kokybė po impulsų spūdos keturių lėkių difrakcinės gardelės impulsų spaustuve buvo difrakciškai ribota ($M^2 \sim 1$, Pav. S.18). Tokio impulsų spaustuvo optinis efektyvumas siekė 90 %. Įskaičius visus optinius sistemos nuostolius, tokios sistemos išėjime buvo pasiekti 318 fs trukmės ir 32.8 μJ energijos impulsai su 32.8 W vidutine galia išėjime – tai atitinka $P_p \sim 0.1 \, GW$ smailinę galią.

Pav. S.18 Pluošto kokybės matavimo rezultatai lazerinės sistemos išėjime. Pluoštas buvo perfokusuotas su teigiamu F=200 mm židinio ilgio lęšiu ir išmatavus pluošto dydžio evoliuciją jam sklindant. Pluošto kokybės parametras buvo įvertintas z-scan metodu, aproksimavus eksperimentinius rezultatus kokybės funkcija, kuri davė vidutinę reikšmę $M^2 \sim 1$. Grafike pateikti pluošto intensyvumo skerspjūviai keliose matavimo vietose.

Dviejų pakopų iš galo kaupinamų Yb:YAG stiprintuvų eksperimentinė plėtra pritaikant novatorišką depoliarizacijos kompensavimo metodą

Šis skyrius skirtas papildomos Yb:YAG stiprinimo pakopos, kuri kaupinama 280 W vidutinės galios kaupinimo spinduliuote ties 940 nm bangos ilgiu, eksperimentinei realizacijai. Pagrindinis tikslas buvo praplėsti jau eksperimentiškai pademonstruotos 4 skyriaus paskutiniame poskyryje sistemos galimybes, t. y., pasiekti reikšmingai didesnį spinduliuotės smailinį intensyvumą lazerinės sistemos išėjime. Būtent ši paskiausiai pademonstruota lazerinė sistema, tik be impulsų laikinės spūdos difrakcinės gardelės impulsų spaustuve, buvo panaudota kaip užkrato šaltinis papildomai Yb:YAG stiprinimo pakopai.

Norint pasiekti didelį optinio stiprinimo efektyvumą kambario temperatūroje, stiprinimo terpė neišvengiamai turėjo būti kaupinama didelio

intensyvumo bei vidutinės galios kaupinimo spinduliuote, kuri savo ruožtu iššaukė nepageidaujamus reiškinius, tokius kaip stiprinamo pluošto kokybės degradacija, astigmatizmas bei stiprinamos spinduliuotės galios nuostoliai dėl depoliarizacijos reiškinio [33,63]. Siekiant geriau suprasti ir prognozuoti šiuos reiškinius, buvo išplėstas skaitmeninis modelis, kuris geba modeliuoti depoliarizacinius ir pluošto astigmatizmo reiškinius. Šis modelis buvo pritaikytas tokios sistemos skaitmeniniam modeliavimui ir pagrįstas eksperimentiškai. Jos aprašymas yra pateiktas pilnoje disertacijos versijoje anglų kalba, o pati eksperimento schema pateikta žemiau (Pav. S.19).
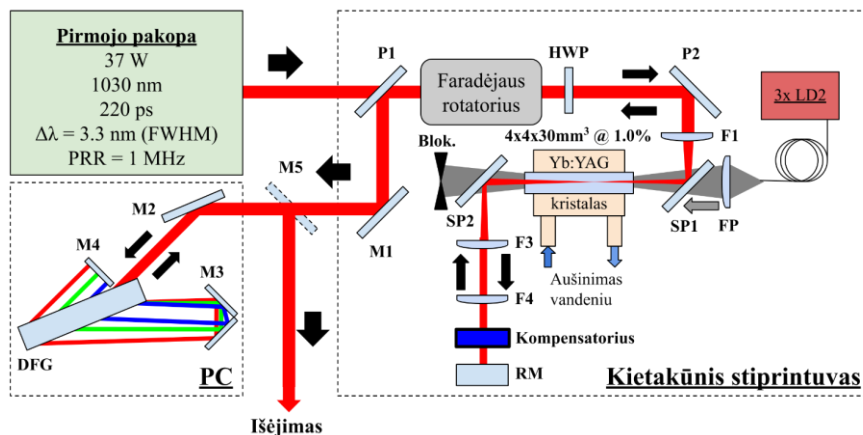
Pav. S.19 Principinė hibridinio lazerio optinė schema. Ją sudarė visiškai skaidulinis užkrato šaltinis, dvi laisvos erdvės dvigubo lėkio iš galo kaupinamų Yb:YAG stiprintuvų pakopos (pirmosios aprašymas praeitame skyriuje) ir impulsų spaustuvas difrakcinės gardelės (rėžių tankis 1739 mm^{-1}) pagrindu. HWP – pusės bangos ilgio fazinė plokštelė, QWP – ketvirčio bangos ilgio fazinė plokštelė, FR – Faradėjaus rotatorius, P1, P2 – poliarizatoriai, SP1, SP2 – kaupinimo/signalo pluoštų separatorius, F1 – signalo spinduliuotę į kristalą fokusuojantysis lęšis, FP – kaupinimo spinduliuotės fokusatorius, F3, F4 – lęšių pora, skirta signalo spinduliuotės formavimui ir vaizdo pernešimui atgal į kristalą, RM – signalą apgręžiantis plokščiasis veidrodis, KOMP. – depoliarizacijos ir astigmatizmo kompensatorius, M1-M5 – veidrodžiai, DFG – difrakcinė gardelė. Kristalas buvo įstatytas į varinį laikiklį, kuris buvo aušinamas vandeniu 20℃ temperatūroje.

Užkrato šaltinis generavo laike čirpuotus iki $220\,ps$, $37\,\mu J$ energijos impulsus ties $1\,MHz$ impulsų pasikartojimo dažniu (atitiko $37\,W$ vidutinę galią). Užkrato šaltinio spinduliuotės spektro plotis buvo $3.3\,nm$ (pusės maksimalaus intenstyvumo aukštyje), centruotas ties $1030\,nm$ bangos ilgiu. Spinduliuotė buvo stiprinama $30\,mm$ ilgio, 1 % legiravimo laipsnio Yb:YAG kristale. Stiprintuvas buvo kaupinamas $280\,W$ vidutinės galios spinduliuote, gauta apjungus trijų nuolatinės veikos lazerinių diodų spinduliuotes per skaidulinį apjungėją (angl. *high-power fiber combiner*). Šios spinduliuotės spektro plotis buvo $3.5\,nm$ (pusės maksimalaus intensyvo aukštyje) ties

940 nm centriniu bangos ilgiu, o skaidulos, iš kurios buvo išvedama kaupinimo spinduliuotė, diametras buvo 200 μm, o skaitinė apertūra atitiko $NA = 0.22$. Kaupinimo ir signalo pluoštai buvo sufokusuoti į $\omega_p = 0.78\ mm$ and $\omega_s = 0.83\ mm$ pluošto diametrus atitinkamai ir idealiai perkloti aktyvioje terpėje. Sustiprinta spinduliuotė buvo apgręžiama su lęšiais $F_3 = 75\ mm$ ir $F_4 = 200\ mm$ bei plokščiuoju veidrodžiu RM. Lęšis F_3 buvo pastatytas židinio atstumu nuo aktyviosios terpės, o atstumas tarp lęšio F_4 ir veidrodžio RM atitiko pastarojo lęšio židinio atstumą. Atstumas tarp lęšių F_3 ir F_4 buvo suderintas taip, kad būtų sukompensuota termo-lęšio įtaka. Tokia optinė schema leido „pernešti" aktyviosios terpės vaizdą ant plokščiojo veidrodžio RM ir atgal į aktyviąją terpę. Kaupinimo spinduliuotė po pirmojo lėkio buvo atskirta nuo optinės stiprintuvo grandinės su dichroiniu veidrodžiu, ir toliau nebenaudojama (žr. Pav. S.20). Sustiprintos spinduliuotės pluoštas buvo išvedamas iš stiprintuvo atskiriant įeinančią ir išeinančią spinduliuotę per poliarizaciją. Tokio stiprintuvo stiprinimo rezultatai pateikti Pav. S.16.

Depoliarizacijos ir astigmatizmo kompensavimui tokioje sistemoje buvo suprojektuotas ir eksperimentiškai panaudotas novatoriškas depoliarizacijos kompensatorius, pagamintas iš lydyto kvarco, kuriame buvo „įrašytas" dvejopalaužiškumo profilis [6,65–67,119], pasižymintis ašine simetrija, ir atkartojantis pobūdį tokio profilio, kuris atsiranda kaupinamose lazerinėse terpėse [126]. Šis elementas angliškoje literatūroje turi savo pavadinimą, kurį pažodžiui galima išversti kaip „banginė plokštelė su erdvėje kintančiu fazės profiliu" (angl. *spatially variable waveplate*, SVWP), tačiau toliau vietomis bus naudojama santrumpa SVWP.

Fazinio vėlinimo profilis tarp greitosios ir lėtosios poliarizacinių ašių, ir šių ašių orientacija įrašytame depoliarizacijos kompensavimo elemente pateikti Pav. S.21. Verta pabrėžti, kad greitoji ir lėtoji poliarizacijos ašys yra suorientuotos taip, kad sutaptų su tangentine ir radialine ašimis, kadangi aktyviojoje terpėje, kuri pasižymi [111] kristalografine simetrija (šiame darbe naudojami tokie Yb:YAG kristalai), sugertos kaupinimo spinduliuotės sukeltų mechaninių įtempių ašys yra orientuotos būtent taip, o šie įtempiai savo ruožtu sukelia dvejopalaužiškumo reiškinį dėl foto elastinio efekto [33,35]. Šių efektų sukeltą depoliarizacijos ir astigmatizmo reiškinį ir siekiama sukompensuoti, sukuriant identišką aktyviojoje terpėje atsirandantį dvejopalaužiškumo profilį kompensuojančiame elemente, tik su priešinga faze. Taipogi, įrašytas fazinio vėlinimo δ profilis yra parabolinis, kas vėlgi atitinka minėtų medžiagų specifiką, kaip tai aprašyta klasikinėje literatūroje šia tematika, bei pateikta formulėje žemiau [126]:
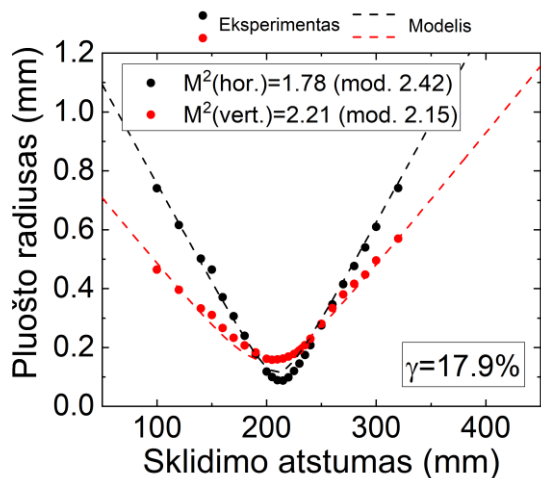
$$\delta(r) = \frac{\lambda}{2}\left(\frac{r}{R}\right)^2, \tag{S.4}$$

čia λ -spinduliuotės bangos ilgis, r – radialinė koordinatė coordinate, R – radialinė koordinatė, ties kuria įrašytas fazinis vėlinimas yra $\lambda/2$ (pusė bangos ilgio). Šis elementas buvo statomas prieš pat plokščiąjį veidrodį RM, kaip tai parodyta Pav. S.20.
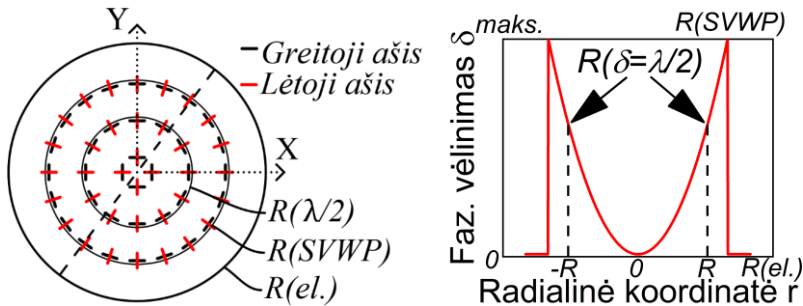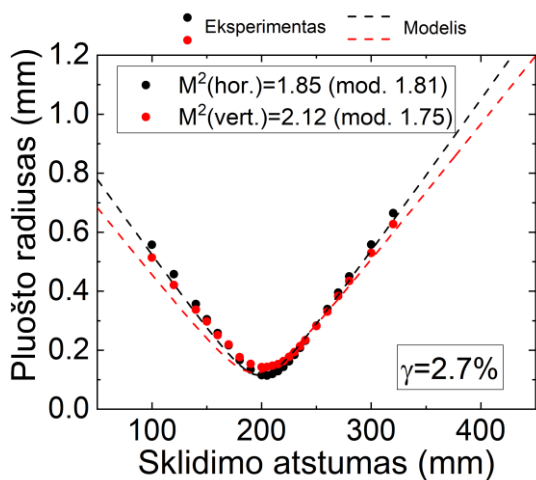

Pav. S.20 <u>Kairėje</u> – dvimatis greitosios ir lėtosios poliarizacinių ašių pasiskirstymas depoliarizaciją kompensuojančiame elemente. $R(\lambda/2)$ žymi elemento kontūrą, ties kuriuo fazinis vėlinimas yra $\lambda/2$ (pusė bangos ilgio), $R(SVWP)$ žymi elemento kontūrą, nuo kurio toliau dvejopalaužiškumo nėra (neįrašyta lydyto kvarco zona), $R(el.)$ žymi fizinį elemento kraštą. <u>Dešinėje:</u> parabolinis fazinio vėlinimo profilis išilgai punktyrinės linijos
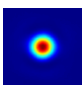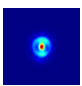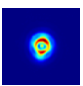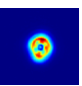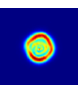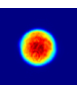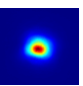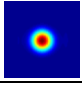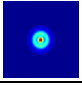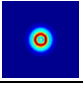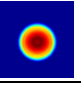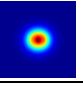
Nagrinėjamame stiprintuve maksimali pasiekta išvadinė vidutinė galia buvo $129\,W$ (ties $1\,MHz$ impulsų pasikartojimo dažniu), esant $280\,W$ kaupinimo vidutinei galiai ir $37\,W$ įvadinės spinduliuotės galiai. Tai atitiko $32\,\%$ optinį stiprintuvo efektyvumą. Pluošto kokybės parametras po stiprinimo įvertintas $M^2 = 1.9 - 2.2$. Esant tokioms sąlygoms, nuostoliai dėl depoliarizacijos siekė net $17.9\,\%$, kas taipogi sąlygojo itin prastą pluošto skirstinį po stiprinimo bei ryškų astigmatizmą. Buvo įvertinta, kad tokiomis sąlygomis yra reikalingas depoliarizacijos kompensatorius, kuriame įrašytas fazinis vėlinimas 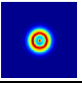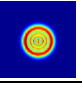$\delta = 0.44\,\lambda$ ties radiusu $R = 1.5\,mm$ (sustiprinto pluošto diametras kompensacijos plokštumoje buvo $\sim 2.2\,mm$). Įstačius SVWP pozicijoje, kaip parodyta Pav. S.20, depoliarizacijos lygis buvo sumažintas iki $2.7\,\%$, o pluošto astigmatizmas dėl cilindrinio termolęšio kristale buvo praktiškai eliminuotas, kaip rodo rezultatai, pateikti Pav. S.21 (be kompensavimo) ir Pav. S.22 (su kompensavimu).

Pav. S.21 Viršuje - pluošto kokybės matavimo rezultatai be kompensatoriaus SVWP. Taškai atitinka eksperimentinius rezultatus, o punktyrinės linijos – modeliavimo rezultatus. Apačioje - skerspjūvio matavimo eksperimentiniai ir modeliavimo rezultatai. Z atitinka sklidimo atstumą, kaip parodyta viršuje.

|							
Eksperimentas							
Modelis							
Z (mm)	150	210	215	220	230	240	300

Pav. S.22 Analogiški rezultatai Pav. S.21, tik įstačius kompensatorių SVWP.

Gauti rezultatai parodė tokio novatoriško depoliarizacijos kompensatoriaus pranašumą, lyginant su kitomis technologijomis, aptartomis kituose darbuose. Pirma, šis pritaikomas metodas praktiškai pilnai kompensuoja depoliarizaciją bei pluošto astigmatizmą dėl terminių reiškinių intensyviai užkaupintose aktyviose terpėse, ko neatlieka itin paprastas metodas, panaudojant ketvirčio bangos ilgio plokštelę [39]. Antra, šis metodas iš principo nėra apribotas terminių ir netiesinių efektų pačioje kompensatoriaus medžiagoje, lyginant su metodu, kuomet depoliarizacijos kompensavimui panaudojamas Faradėjaus rotatorius – tiek stiprinamos spinduliuotės sugertis, tiek netiesinis lūžio rodiklis (kuris sąlygoja netiesinių efektų stiprumą medžiagoje) yra gerokai didesnis magneto-optinėje medžiagoje (Faradėjaus rotatoriuose) negu lydytame kvarce [130–133]. Trečia, aktyviosios terpės kristalografinės plokštumos orientacija yra tipinė rinkoje ([111]), ir nereikalauja ypatingo tikslumo, priešingai negu metodas su kitomis kristalų pjūvio orientacijomis [40,41]. Galiausiai, tiek pati derinimo procedūra, tiek optinės konfigūracijos išpildymas nėra toks sudėtingas, lyginant su klasikiniu depoliarizacijos kompensavimo metodu, kuriame panaudojami du identiški ir identiškai kaupinami kristalai su vaizdo pernešimu tarp jų [38]. Verta pabrėžti, kad pats metodas dargi yra lankstus – kadangi fazinio vėlinimo profilis yra parabolinis (žr. Pav. S.21), tai parenkant skirtingą stiprinamo pluošto dydį, sklindantį per SVWP elementą, galima padidinti arba sumažinti sukuriamą fazinį vėlinimą, taip prisitaikant prie skirtingų kaupinimo sąlygų. Taipogi galima šiuos elementus kombinuoti, t. y., pridėjus papildomą elementą, sukuriamas fazinis vėlinimas sumuojasi (arba minusuojasi, priklausomai nuo fazės ženklo). Modeliavimo rezultatai taip pat parodė gerą atitikimą eksperimentiniams rezultatams, įrodydami skaitmeninio modelio galimybes.

Kaip buvo minėta, pluošto kokybė po stiprinimo suprastėjo nuo difrakciškai ribotos iki $M^2 = 1.9 - 2.2$. Panaudotas depoliarizacijos ir astigmatizmo kompensatorius šios kokybės nepagerino, kadangi jo funkcija ne tokia – jis nekompensuoja termo-lęšio aberacijų. Visgi, teoriškai buvo

įvertinta, kad erdvinis filtravimas (aptartas praeitame skyriuje) šią kokybę gali pagerinti iki difrakciškai ribotos, su 12 % optiniais nuostoliais.

Siekiant pasiekti maksimalų smailinę galią tokioje konfigūracijoje, laike čirpuoti impulsai buvo eksperimentiškai suspausti difrakcinės gardelės impulsų spaustuve, kaip parodyta Pav. S.19. Laikinės spūdos rezultatai pateikti Pav. S.23.
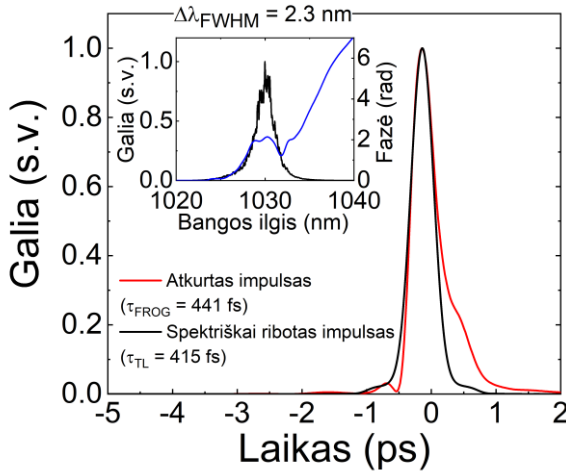
Pav. S.23 Laike suspaustų ir SHG-FROG metodu atkurtų impulsų gaubtinė (raudona kreivė). Juoda kreivė atitinka spektriškai riboto impulso gaubtinę.. Įsiuvai: (kairėje) išmatuotas sustiprinto impulso spektras ir atkurta spektrinė fazė; (dešinėje) išmatuotas ir atkurtas FROG užrašas (0.15% atkūrimo paklaida).

Suspaustų impulsų trukmė beveik sutapo su spektriškai ribota impulso trukme (441 fs ir 415 fs atitinkamai). Vėlgi, minimalus neatitikimas buvo didžiąja dalimi nulemtas netiesinių reiškinių sukeltų fazinių impulso iškraipymų skaiduliniame lazeryje. Pluošto kokybė po impulsų spūdos keturių lėkių difrakcinės gardelės impulsų spaustuve nepakito. Tokio impulsų spaustuvo optinis efektyvumas siekė 90 %. Įskaičius visus optinius sistemos nuostolius, tokios sistemos išėjime buvo pasiekti 441 fs trukmės ir 116 μJ energijos impulsai su 116 W vidutine galia išėjime – tai atitinka $P_p \sim 0.25\ GW$ smailinę galią.

Apibendrinant, panaudojant papildomą Yb:YAG stiprinimo pakopą, smailinė galia buvo padidinta net 2.5 karto, lyginant su vienos Yb:YAG stiprinimo pakopos atveju. Tokia galimybė atsirado pritaikius novatorišką depoliarizacijos ir astigmatizmo kompensavimo metodą su SVWP. Mano manymu, tokia šiame disertaciniame darbe pademonstruota hibridinė lazerinė sistema yra pranašesnė, nei kitos lazerinės sistemos, paremtos Yb:YAG

aktyviąja stiprinimo terpę, tokios kaip plonojo disko ar kristalinės skaidulos technologijos [43,44]. Viena vertus, konfigūracija yra gerokai paprastesnė negu plonojo disko technologija, kadangi stiprinama spinduliuotė, sklisdama per aktyviąją terpę tik du kartus (kas yra lengvai įgyvendinama), patiria pakankamai efektyvų stiprinimą, ko nepakanka plonojo disko atveju – tuo atveju spinduliuotė turi sklisti per santykinai trumpą terpę daugelį kartų, taip apsunkinant optinės grandinės išpildymą bei suderinimą. Kita vertus, tokios konfigūracijos Yb:YAG kristalai, kurie panaudoti šiame darbe, yra plačiai prieinami rinkoje, todėl pakankamai pigūs, lyginant su kristalinės skaidulos technologija. Galiausiai, santykinai paprastas ir efektyvus depoliarizacijos kompensavimas su SVWP įgalina šią technologiją tobulėti toliau, kadangi vienas iš esminių šios technologijos apribojimų yra įveiktas.

<div style="text-align:center">

**Pristatytų lazerinių sistemų parametrų palyginimas
su kitomis sistemomis**

</div>

Paskutiniame disertacijos skyriuje buvo trumpai apžvelgtos literatūroje sutinkamos lazerinės sistemos ir palygintos su pasiektais parametrais šiame darbe. Lyginami parametrai buvo smailinė galia, stiprintuvo optinis efektyvumas, pluošto kokybės parametras M^2, pluošto eliptiškumas bei impulsų spūdos kokybė. Sukombinavus šiuos parametrus, buvo įvestas lyginamasis parametras MP, kuris apibūdinamas:

$$MP = \frac{\eta \varepsilon \frac{\tau_{išmat.}}{\tau_{SR}}}{M^2}, \tag{S.5}$$

kur η – optinis stiprintuvo efektyvumas (maksimali vertė 1, atitinkanti stiprintuvo efektyvumą 100%), ε – lazerinio pluošto eliptiškumas (maksimali vertė 1, atitinkanti idealiai apvalų pluoštą), M^2 – pluošto kokybės parametras, $\frac{\tau_{išmat.}}{\tau_{SR}}$ – suspaustų (išmatuotų) ir spektriškai ribotų impulsų trukmės santykis (maksimali vertė 1, atitinkanti spektriškai ribotą impulsų trukmę). Rezultatai pateikti Pav. S.24.
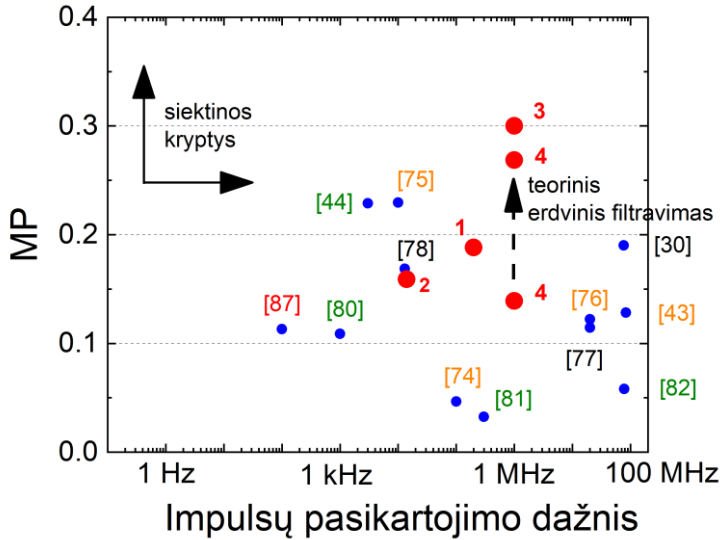
Pav. S.24 Apibendrintysis grafikas, parodantis skirtingų Yb:YAG kietojo kūno laisvos erdvės stiprintuvinių sistemų lyginamąjį parametrą MP ir impulsų pasikartojimo dažnį. Skaičiai žymi nuorodas į sistemas, kurių numeracija atitinka pateiktas literatūros sąraše (bibliografijoje). Skirtingos spalvos atitinka naudojamą technologiją bei jos tipą: raudona - HEC-DPSSL, žalia - MP, oranžinė - SCF, juoda - IS (žr. aprašymą aukščiau). Raudoni sunumeruoti taškai atitinka sistemas, pademonstruotas šiame darbe (1 – skyriuje 4.2, 2 – skyriuje 4.3, 3 – skyriuje 4.5, 4 – skyriuje 5).

Lyginamoji analizė parodė, kad šiame darbe pademonstruotos sistemos pasižymėjo itin aukštu įvertinimu. Tą leido įgyvendinti keli esminiai dalykai: pirma, erdvinio filtravimo pritaikymas, leidęs pasiekti difrakciškai ribotą pluošto kokybę; antra, depoliarizacijos ir terminių reiškinių sukelto astigmatizmo kompensavimas su novatorišku SVWP elementu; trečia, pasiekta itin aukšta impulsų spūdos kokybė dėl tinkamų sistemos laikinės dispersijos parametrų parinkimo bei suderinimo.

Išvados

1. Vienmatis, ašinės simetrijos (1D) skaitmeninis trijų energijos lygmenų stiprintuvinis modelis, skirtas modeliuoti spinduliuotės stiprinimą nuolatinės veikos režime, taipogi aprašantis signalo pluošto sklidimą per Hankelio transformaciją, kaupinimo pluošto sklidimą per ABCD matricų metodą, įskaitantis stiprinančiosios terpės parametrus, tokius kaip šiluminį laidumą, termo-optinį koeficientą, spektroskopinius sugerties ir emisijos skerspjūvius, bei šių parametrų priklausomybę nuo temperatūros, skerspjūvių priklausomybę nuo bangos ilgio, ir kurio veikimas pagrįstas iteraciniu

algoritmu, kurio išeities parametras iš galo kaupinamo kristalo atveju yra temperatūrinio skirstinio (vieno lėkio atveju) ir sustiprintos spinduliuotės vidutinės galios (dvigubo lėkio atveju) nusistovėjimas, yra tikslus ir eksperimentiškai pagrįstas metodas, leidžiantis apskaičiuoti spinduliuotės stiprinimą Yb:YAG tiesiniame stiprintuve, įskaityti spektro siaurėjimo reiškinį dėl terpės stiprinimo juostos formos, numatyti stiprinamos spinduliuotės pluošto kokybės bei skirstinio pokyčius ir banginio fronto degradaciją.

2. Ultratrumpųjų impulsų hibridinė lazerinė sistema, kurią sudaro skaidulinis užkrato lazeris ir iš galo kaupinamo Yb:YAG kristalo dvigubo lėkio laisvos erdvės stiprintuvas, kurioje impulsų plėtimas ir spaudimas laike įgyvendinamas dispersiškai suderintoje CFBG ir CVBG poroje, leidžia pasiekti beveik spektriškai ribotus, laike suspaustus santykinai didelės smailinės galios femtosekundinius impulsus.

3. Praktinis būdas sumažinti stiprinamos spinduliuotės pluošto degradaciją iš galo kaupinamo Yb:YAG kristalo dvigubo lėkio stiprintuve, kylančią dėl šiluminių ir poliarizacinių reiškinių stiprintuvinėje terpėje, yra panaudojant porą ketvirčio bangos ilgio fazinių plokštelių, kurios talpinamos prieš ir po Yb:YAG kristalą, ir orientuotos taip, kad aktyviojoje terpėje būtų stiprinama apskritiminė poliarizacija, bei įgyvendinant pluošto erdvinio filtravimo metodiką, kuomet sustiprintas pluoštas yra perfokusuojamas su teigiamo židinio lęšiu, kurio židinio plokštumoje yra pastatoma apertūra, nufiltruojanti šiluminių reiškinių kristale sukeltas pluošto aberacijas. Toks praktiškas metodas leidžia atstatyti pradinę pluošto kokybę ir daugeliu atveju pasiekti difrakciškai ribotą pluošto kokybę po stiprinimo iš galo kaupinamo Yb:YAG kristalo dvigubo lėkio stiprintuve.

4. SVWP fazinio elemento panaudojimas suteikia galimybę reikšmingai sumažinti šiluminių reiškinių sukeltą depoliarizaciją ir sustiprinto pluošto astigmatizmą dvigubo lėkio iš galo kaupinamo Yb:YAG kristalo stiprintuvo konfigūracijoje.

About the author

Laurynas Veselis was born in May 5th, 1990, in Klaipėda, Lithuania.

The author studied Applied Physics at Vilnius University in 2009-2013, where he received his Bachelor's degree in Physics. He received his Master's degree in Laser Technology in 2015, at Vilnius University. In 2016 he started doctoral studies in the Center for Physical Sciences and Technology.

In 2012-2015 he worked as a researcher in the laser microfabrication company *Evana Technologies*, where he completed majority of the work related to his Bachelor's and Master's degree. From 2015 to 2020 he worked as a research and developement engineer in the laser manufacturing company *Ekspla*. Majority of the work related to doctoral studies was completed in this company. From 2020 the author works as a junior scientist in the Center for Physical Sciences and Technology. Current area of interest consists of solid state laser amplifiers, numerical modeling and ultrashort pulse generation.

Apie autorių

Laurynas Veselis gimė 1990 m. gegužės 5 d. Klaipėdoje, Lietuvoje.

2009-2013 m. studijavo taikomąją fiziką Vilniaus Universitete, Fizikos Fakultete ir įgijo bakalauro laipsnį apsigynęs mokslinį tiriamąjį darbą, pavadinimu „Optinio pramušimo safyre formavimas čirpuotais femtosekundinio lazerio impulsais. Pažeidimų pobūdžio priklausomybės nuo pluošto tiesinės poliarizacijos orientavimo tyrimas". 2013-2015 studijavo magistrantūrą Vilniaus Universitete, pasirinkęs Lazerinės Technologijos studijų programą, ir įgijo magistro laipsnį, apsigynęs mokslinį tiriamąjį darbą, pavadinimu „Puslaidininkinių prietaisų padėklų lazerinio raižymo metodų tyrimas ir vystymas". Nuo 2016 metų autorius pradėjo doktorantūros studijas Fizinių ir Technologijos mokslų centre.

2012-2015 metais autorius dirbo tyrėju privačioje lazerinio apdirbimo įmonėje *Evana Technologies*, UAB, kurioje ir atliko didžiąją dalį mokslinių tyrimų bakalauro ir magistro studijų tematika. Taip pat nuo 2015 m. iki 2020 m. jis dirbo privačioje lazerinių sistemų kūrėjų kompanijoje *Ekspla*, UAB, kurioje dirbo lazerių inžinieriumi tyrimų padalinyje bei atliko didžiąją dalį tyrimų doktorantūros tematika. Nuo 2020 m. iki dabar autorius dirba jaunesniuoju mokslo darbuotoju Fizinių ir technologijos mokslų centro Lazerinių technologijų skyriuje, Skaidulinių lazerių laboratorijoje. Dabartinė autoriaus mokslinės veiklos interesų sritis apima kietojo kūno stiprintuvus, jų skaitmeninį modeliavimą, ultratrumpųjų impulsų generavimą.

Bibliography

1. E. Toyserkani and N. Rasti, *Ultrashort Pulsed Laser Surface Texturing* (Elsevier Ltd., 2015).
2. S. K. Sundaram and E. Mazur, "Inducing and probing non-thermal transitions in semiconductors using femtosecond laser pulses," Nat. Mater. **1**(4), 217–224 (2002).
3. D. N. Wang, Y. Wang, and C. R. Liao, *Femtosecond Laser Micromachining on Optical Fiber* (Elsevier Ltd., 2015).
4. A. Yadav, H. Kbashi, S. Kolpakov, N. Gordon, K. Zhou, and E. U. Rafailov, "Stealth dicing of sapphire wafers with near infra-red femtosecond pulses," Appl. Phys. A Mater. Sci. Process. **123**(5), 1–7 (2017).
5. L. Sudrie, M. Franco, B. Prade, and A. Mysyrowicz, "Writing of permanent birefringent microlayers in bulk fused silica with femtosecond laser pulses," Opt. Commun. **171**(4), 279–284 (1999).
6. M. Beresna, M. Gecevičius, and P. G. Kazansky, "Ultrafast laser direct writing and nanostructuring in transparent materials," Adv. Opt. Photonics **6**(3), 293 (2014).
7. T. R. Rublack, S. Krause, S. Schweizer, and G. S. Seifert, "Increasing solar-cell efficiency by femtosecond laser microstructuring," SPIE Newsroom (September), (2012).
8. R. Berera, R. van Grondelle, and J. T. M. Kennis, "Ultrafast transient absorption spectroscopy: Principles and application to photosynthetic systems," Photosynth. Res. **101**(2–3), 105–118 (2009).
9. J. Limpert, F. Röser, D. N. Schimpf, E. Seise, T. Eidam, S. Ḧdrich, J. Rothhardt, C. J. Misas, and A. Tünnermann, "High repetition rate gigawatt peak power fiber laser systems: Challenges, design, and experiment," IEEE J. Sel. Top. Quantum Electron. **15**(1), 159–169 (2009).
10. S. Backus, C. G. Durfee, M. M. Murnane, and H. C. Kapteyn, "High power ultrafast lasers," Rev. Sci. Instrum. **69**(3), 1207–1223 (1998).
11. D. Strickland and G. Mourou, "Compression of amplified chirped optical pulses," Opt. Commun. **56**(3), 219–221 (1985).
12. E. B. Treacy, "Optical Pulse Compression with Diffraction Gratings," IEEE J. Quantum Electron. **5**(9), 454–458 (1969).
13. O. E. Martinez, J. P. Gordon, and R. L. Fork, "Negative group-velocity dispersion using refraction," J. Opt. Soc. Am. A **1**(10), 1003 (1984).
14. G. Imeshev, I. Hartl, and M. E. Fermann, "Chirped pulse amplification with a nonlinearly chirped fiber Bragg grating matched to the Treacy compressor," Opt. Lett. **29**(7), 679 (2004).
15. T. Bartulevicius, S. Frankinas, A. Michailovas, R. Vasilyeu, V. Smirnov, F. Trepanier, and N. Rusteika, "Compact fiber CPA system based on a CFBG stretcher and CVBG compressor with matched dispersion profile," Opt. Express **25**(17), 19856 (2017).

16. G. Chang, M. Rever, V. Smirnov, L. Glebov, and A. Galvanauskas, "Femtosecond Yb-fiber chirped-pulse-amplification system based on chirped-volume Bragg gratings," Opt. Lett. **34**(19), 2952 (2009).

17. G. Sobon, K. Krzempek, J. Taka, and J. Sotor, "Compact, all-PM fiber-CPA system based on a chirped volume Bragg grating," Laser Phys. **26**(1), (2016).

18. M. Smrž, M. Chyla, O. Novák, T. Miura, A. Endo, and T. Mocek, "Amplification of picosecond pulses to 100 W by an Yb:YAG thin-disk with CVBG compressor," High-Power, High-Energy, High-Intensity Laser Technol. II **9513**, 951304 (2015).

19. M. Perry and G. Atomics, "Self-phase modulation in chirped-pulse amplification," (December 1994), (2016).

20. J. Limpert, F. Stutzki, F. Jansen, H. J. Otto, T. Eidam, C. Jauregui, and A. Tünnermann, "Yb-doped large-pitch fibres: Effective single-mode operation based on higher-order mode delocalisation," Light Sci. Appl. **1**(APRIL), (2012).

21. T. T. Alkeskjold, M. Laurila, L. Scolari, and J. Broeng, "Single-mode ytterbium-doped large-mode-area photonic bandgap rod fiber amplifier," Opt. Express **19**(8), 7398 (2011).

22. A. Brenier and G. Boulon, "Overview of the best Yb3+-doped laser crystals," J. Alloys Compd. **323**–**324**, 210–213 (2001).

23. C. Hönninger, R. Paschotta, M. Graf, F. Morier-Genoud, G. Zhang, M. Moser, S. Biswal, J. Nees, A. Braun, G. A. Mourou, I. Johannsen, A. Giesen, W. Seeber, and U. Keller, "Ultrafast ytterbium-doped bulk lasers and laser amplifiers," Appl. Phys. B Lasers Opt. **69**(1), 3–17 (1999).

24. F. Druon, F. Balembois, and P. Georges, "New laser crystals for the generation of ultrashort pulses," Comptes Rendus Phys. **8**(2), 153–164 (2007).

25. D. C. Brown, S. Tornegård, J. Kolis, C. McMillen, C. Moore, L. Sanjeewa, and C. Hancock, "The application of cryogenic laser physics to the development of high average power ultra-short pulse lasers," Appl. Sci. **6**(1), 1–74 (2016).

26. D. C. Brown, J. M. Singley, E. Yager, J. W. Kuper, B. J. Lotito, and L. L. Bennett, "Innovative high-power CW Yb:YAG cryogenic laser," Laser Source Technol. Def. Secur. III **6552**(May), 65520D (2007).

27. T. Y. Fan, S. Member, D. J. Ripin, R. L. Aggarwal, J. R. Ochoa, B. Chann, M. Tilleman, and J. Spitzberg, "Cryogenic Yb 3 + -Doped Solid-State Lasers," **13**(3), 448–459 (2007).

28. C. Hönninger, I. Johannsen, M. Moser, G. Zhang, A. Giesen, and U. Keller, "Diode-pumped thin-disk Yb: YAG regenerative amplifier," Appl. Phys. B Lasers Opt. **65**(3), 423–426 (1997).

29. A. Alismail, H. Wang, J. Brons, and H. Fattahi, "20 mJ, 1 ps Yb:YAG thin-disk regenerative amplifier," J. Vis. Exp. **2017**(125), 1–9 (2017).

30. P. Russbueldt, T. Mans, G. Rotarius, and J. Weitenberg, "400 W Yb :

YAG Innoslab fs-amplifier," Opt. Express **17**(15), 1013–1023 (2009).

31. M. Siebold, M. Loeser, U. Schramm, J. Koerner, M. Wolf, M. Hellwing, J. Hein, and K. Ertel, "High-efficiency, room-temperature nanosecond Yb:YAG laser," Opt. Express **17**(22), 19887 (2009).

32. K. Price, S. Karlsen, P. Leisher, and R. Martinsen, "High Brightness Fiber Coupled Pump Laser Development," (n.d.).

33. A. Starobor and O. Palashov, "Peculiarity of the thermally induced depolarization and methods of depolarization compensation in square-shaped Yb:YAG active elements," Opt. Commun. **402**(February), 468–471 (2017).

34. M. De Vido, P. D. Mason, M. Fitton, R. W. Eardley, G. Quinn, D. Clarke, K. Ertel, T. J. Butcher, P. Jonathan Phillips, S. Banerjee, J. Smith, J. Spear, C. Edwards, and J. L. Collier, "Modelling and measurement of thermal stress-induced depolarisation in high energy, high repetition rate diode-pumped Yb:YAG lasers," Opt. Express **29**(4), 5607 (2021).

35. H. J. Eichler, A. Haase, R. Menzel, and A. Siemoneit, "Thermal lensing and depolarization in a highly pumped nd:Yag laser amplifier," J. Phys. D. Appl. Phys. **26**(11), 1884–1891 (1993).

36. E. Khazanov, A. Anastasiyev, N. Andreev, A. Voytovich, and O. Palashov, "Compensation of birefringence in active elements with a novel Faraday mirror operating at high average power," Appl. Opt. **41**(15), 2947 (2002).

37. R. Kandasamy, M. Yamanaka, Y. Izawa, and S. Nakai, "Analysis of birefringence compensation using a quarter-wave plate in solid-state lasers," Opt. Rev. **7**(2), 149–151 (2000).

38. K. Michailovas, V. Smilgevičius, and A. Michailovas, "High average power effective pump source at 1 kHz repetition rate for OPCPA system," Lith. J. Phys. **54**(3), 150–154 (2014).

39. W. A. Clarkson, N. S. Felgate, and D. C. Hanna, "Simple method for reducing the depolarization loss resulting from thermally induced birefringence in solid-state lasers," Opt. Lett. **24**(12), 820 (1999).

40. H. Tünnermann, O. Puncken, P. Weßels, M. Frede, D. Kracht, and J. Neumann, "Intrinsic reduction of the depolarization in Nd: YAG crystals," Opt. InfoBase Conf. Pap. **18**(19), 5496–5501 (2010).

41. H. Tünnermann, O. Puncken, P. Weßels, M. Frede, J. Neumann, and D. Kracht, "Linearly polarized single-mode Nd:YAG oscillators using [100]- and [110]-cut crystals," Opt. Express **19**(14), 12992 (2011).

42. D. Albach and J.-C. Chanteloup, "Large size crystalline vs co-sintered ceramic Yb^3+:YAG disk performance in diode pumped amplifiers," Opt. Express **23**(1), 570 (2015).

43. V. Markovic, A. Rohrbacher, P. Hofmann, W. Pallmann, S. Pierrot, and B. Resan, "160 W 800 fs Yb:YAG single crystal fiber amplifier without CPA," Opt. Express **23**(20), 25883 (2015).

44. J. Fischer, A.-C. Heinrich, S. Maier, J. Jungwirth, D. Brida, and A.

Leitenstorfer, "615 fs pulses with 17 mJ energy generated by an Yb:thin-disk amplifier at 3 kHz repetition rate," Opt. Lett. **41**(2), 246 (2016).

45. S. Chénais, F. Druon, S. Forget, F. Balembois, and P. Georges, "On thermal effects in solid-state lasers: The case of ytterbium-doped materials," Prog. Quantum Electron. **30**(4), 89–153 (2006).

46. J. Dong, A. Rapaport, M. Bass, F. Szipocs, and K. I. Ueda, "Temperature-dependent stimulated emission cross section and concentration quenching in highly doped Nd 3+: YAG crystals," Phys. Status Solidi Appl. Mater. Sci. **202**(13), 2565–2573 (2005).

47. J. Koerner, C. Vorholt, H. Liebetrau, M. Kahle, D. Kloepfel, R. Seifert, J. Hein, and M. C. Kaluza, "Measurement of temperature-dependent absorption and emission spectra of Yb:YAG, Yb:LuAG, and Yb:CaF_2 between 20 °C and 200 °C and predictions on their influence on laser performance," J. Opt. Soc. Am. B **29**(9), 2493 (2012).

48. H. Furuse, R. Yasuhara, and K. Hiraga, "Thermo-optic properties of ceramic YAG at high temperatures," Opt. Mater. Express **4**(9), 1794 (2014).

49. D. C. Brown, J. M. Singley, K. Kowalewski, J. Guelzow, and V. Vitali, "High sustained average power cw and ultrafast Yb:YAG near-diffraction-limited cryogenic solid-state laser," Opt. Express **18**(24), 24770 (2010).

50. D. Albach, "Amplified Spontaneous Emission and Thermal Management on a High Average-Power Diode-Pumped Solid-State Laser - The Lucia Laser System," Ecole Polytechnique X (2010).

51. A. Major, J. S. Aitchison, P. W. E. Smith, F. Druon, P. Georges, B. Viana, and G. P. Aka, "Z-scan measurements of the nonlinear refractive indices of novel Yb-doped laser crystal hosts," Appl. Phys. B Lasers Opt. **80**(2), 199–201 (2005).

52. J. Körner, M. Krüger, J. Reiter, A. Münzer, J. Hein, and M. C. Kaluza, " Temperature dependent spectroscopic study of Yb 3+ -doped KG(WO 4) 2 , KY(WO 4) 2 , YAlO 3 and YLiF 4 for laser applications ," Opt. Mater. Express **10**(10), 2425 (2020).

53. S. Chénais, F. Druon, F. Balembois, P. Georges, R. Gaumé, P. H. Haumesser, B. Viana, G. P. Aka, and D. Vivien, "Spectroscopy and efficient laser action from diode pumping of a new broadly tunable crystal: Yb^3+:Sr_3 Y(BO_3)_3," J. Opt. Soc. Am. B **19**(5), 1083 (2002).

54. R. Gaumé, B. Viana, D. Vivien, J. P. Roger, D. Fournier, J. P. Souron, G. Wallez, S. Chénais, F. Balembois, and P. Georges, "Mechanical, thermal and laser properties of Yb:(Sr1-xCa x)3Y(BO3)3 (Yb:CaBOYS) for 1 μm laser applications," Opt. Mater. (Amst). **24**(1–2), 385–392 (2003).

55. F. Pirzio, S. D. D. D. Cafiso, M. Kemnitzer, A. Guandalini, F. Kienle,

S. Veronesi, M. Tonelli, J. Aus der Au, and A. Agnesi, "Sub-50-fs widely tunable Yb:CaYAlO_4 laser pumped by 400-mW single-mode fiber-coupled laser diode," Opt. Express **23**(8), 9790 (2015).

56. J. Boudeile, F. Druon, M. Hanna, P. Georges, Y. Zaouter, E. Cormier, J. Petit, P. Goldner, and B. Viana, "Continuous-wave and femtosecond laser operation of Yb:CaGdAlO_4 under high-power diode pumping," Opt. Lett. **32**(14), 1962 (2007).

57. A. Rudenkov, V. Kisel, V. Matrosov, and N. Kuleshov, "200 kHz 55 W Yb^3+: YVO_4-based chirped-pulse regenerative amplifier," Opt. Lett. **40**(14), 3352 (2015).

58. B. Le Garrec, V. Cardinali, and G. Bourdet, " Thermo-optical measurements of ytterbium doped ceramics (Sc 2 O 3 , Y 2 O 3 , Lu 2 0 3 , YAG) and crystals (YAG, CaF 2) at cryogenic temperatures ," High-Power, High-Energy, High-Intensity Laser Technol. Res. Using Extrem. Light Enter. New Front. with Petawatt-Class Lasers **8780**(March 2014), 87800E (2013).

59. M. Tokurakawa, A. Shirakawa, K. Ueda, H. Yagi, M. Noriyuki, T. Yanagitani, and A. A. Kaminskii, "Diode-pumped ultrashort-pulse generation based on Yb^3+:Sc_2O_3 and Yb^3+:Y_2O_3 ceramic multi-gain-media oscillator," Opt. Express **17**(5), 3353 (2009).

60. R. Peters, C. Kränkel, K. Petermann, and G. Huber, "Broadly tunable high-power Yb:Lu_2O_3 thin disk laser with 80% slope efficiency," Opt. Express **15**(11), 7075 (2007).

61. R. Peters, C. Kränkel, S. T. Fredrich-Thornton, K. Beil, K. Petermann, G. Huber, O. H. Heckl, C. R. E. Baer, C. J. Saraceno, T. Südmeyer, and U. Keller, "Thermal analysis and efficient high power continuous-wave and mode-locked thin disk laser operation of Yb-doped sesquioxides," Appl. Phys. B Lasers Opt. **102**(3), 509–514 (2011).

62. J. Petit, B. Viana, P. Goldner, J. P. Roger, and D. Fournier, "Thermomechanical properties of Yb3+ doped laser crystals: Experiments and modeling," J. Appl. Phys. **108**(12), (2010).

63. P. Albrodt, X. Delen, M. Besbes, F. Lesparre, and P. Georges, "Simulation and experimental investigation of beam distortions in end-pumped laser rod amplifiers," J. Opt. Soc. Am. B **35**(12), 3004 (2018).

64. M. Ostermeyer, G. Klemz, P. Kubina, and R. Menzel, "Quasi-continuous-wave birefringence-compensated single- and double-rod Nd:YAG lasers," Appl. Opt. **41**(36), 7573 (2002).

65. Y. Shimotsuma, P. G. Kazansky, J. Qiu, and K. Hirao, "Self-organized nanogratings in glass irradiated by ultrashort light pulses," Phys. Rev. Lett. **91**(24), (2003).

66. S. Richter, M. Heinrich, S. Döring, A. Tünnermann, S. Nolte, and U. Peschel, "Nanogratings in fused silica: Formation, control, and applications," J. Laser Appl. **24**(4), 042008 (2012).

67. E. Bricchi, B. G. Klappauf, and P. G. Kazansky, "Form birefringence and negative index change created by femtosecond direct writing in

transparent materials," Opt. Lett. **29**(1), 119 (2004).

68. D. Tosi, "Review of chirped fiber bragg grating (CFBG) fiber-optic sensors and their applications," Sensors (Switzerland) **18**(7), (2018).

69. B. R. Dionne, M. Morin, and D. Ph, *Pulse Stretching Using High Accuracy Chirped Fiber Bragg Grating* (2015).

70. L. Glebov, V. Smirnov, E. Rotari, I. Cohanoschi, L. Glebova, O. Smolski, J. Lumeau, C. Lantigua, and A. Glebov, "Volume-chirped Bragg gratings: monolithic components for stretching and compression of ultrashort laser pulses," Opt. Eng. **53**(5), 051514 (2014).

71. K. Osvay, A. P. Kovács, Z. Heiner, G. Kurdi, J. Klebniczki, and M. Csatári, "Angular dispersion and temporal change of femtosecond pulses from misaligned pulse compressors," IEEE J. Sel. Top. Quantum Electron. **10**(1), 213–220 (2004).

72. I. V Yakovlev, "Stretchers and compressors for ultra-high power laser systems," Quantum Electron. **44**(5), 393–414 (2014).

73. R. Danilevičius, "Fiber laser based technologies for high energy femtosecond wavelength-tunable optical parametric chirped pulse amplification systems," Vilnius University (2017).

74. F. Li, Z. yang, Y. Wang, Z. Lv, Q. Li, X. Yang, X. Wang, X. Hu, and W. Zhao, "Hybrid high energy femtosecond laser system based on Yb:YAG single crystal fiber amplifier," Optik (Stuttg). **156**, 155–160 (2018).

75. X. Délen, Y. Zaouter, I. Martial, N. Aubry, J. Didierjean, C. Hönninger, E. Mottay, F. Balembois, and P. Georges, "Yb:YAG single crystal fiber power amplifier for femtosecond sources," Opt. Lett. **38**(2), 109 (2013).

76. F. Lesparre, J. T. Gomes, X. Délen, I. Martial, J. Didierjean, W. Pallmann, B. Resan, M. Eckerle, T. Graf, M. A. Ahmed, F. Druon, F. Balembois, and P. Georges, "High-power Yb:YAG single-crystal fiber amplifiers for femtosecond lasers in cylindrical polarization," Opt. Lett. **40**(11), 2517 (2015).

77. P. Russbueldt, T. Mans, H.-D. Hoffmann, and R. Poprawe, "1100 W Yb:YAG femtosecond Innoslab amplifier," Solid State Lasers XX Technol. Devices **7912**(0), 79120R (2011).

78. M. Schulz, R. Riedel, A. Willner, T. Mans, C. Schnitzler, P. Russbueldt, J. Dolkemeyer, E. Seise, T. Gottschall, S. Hädrich, S. Duesterer, H. Schlarb, J. Feldhaus, J. Limpert, B. Faatz, A. Tünnermann, J. Rossbach, M. Drescher, and F. Tavella, "Yb:YAG Innoslab amplifier: efficient high repetition rate subpicosecond pumping system for optical parametric chirped pulse amplification," Opt. Lett. **36**(13), 2456 (2011).

79. G. Figueira, J. Alves, J. M. Dias, M. Fajardo, N. Gomes, V. Hariton, T. Imran, C. P. Joaõ, J. Koliyadu, S. Künzel, N. C. Lopes, H. Pires, F. Ruaõ, and G. Williams, "Ultrashort pulse capability at the L2I high

intensity laser facility," High Power Laser Sci. Eng. **5**, 1–5 (2017).

80. C.-L. Chang, P. Krogen, K.-H. Hong, L. E. Zapata, J. Moses, A.-L. Calendron, H. Liang, C.-J. Lai, G. J. Stein, P. D. Keathley, G. Laurent, and F. X. Kärtner, "High-energy, kHz, picosecond hybrid Yb-doped chirped-pulse amplifier," Opt. Express **23**(8), 10132 (2015).

81. A. Loescher, J.-P. Negel, T. Graf, and M. Abdou Ahmed, "Thin-disk multipass amplifier emitting radially polarized beam with 635 W of average power and 2.1 mJ of pulse energy," Laser Sources Appl. III **9893**, 98930N (2016).

82. K.-H. Hong, C.-J. Lai, A. Siddiqui, and F. X. Kärtner, "130-W picosecond green laser based on a frequency-doubled hybrid cryogenic Yb:YAG amplifier," Opt. Express **17**(19), 16911 (2009).

83. J. Pouysegur, B. Weichelt, F. Guichard, Y. Zaouter, C. Hönninger, E. Mottay, F. Druon, and P. Georges, "Simple Yb:YAG femtosecond booster amplifier using divided-pulse amplification," Opt. Express **24**(9), 9896 (2016).

84. C. Wandt, S. Klingebiel, S. Keppler, M. Hornung, M. Loeser, M. Siebold, C. Skrobol, A. Kessel, S. A. Trushin, Z. Major, J. Hein, M. C. Kaluza, F. Krausz, and S. Karsch, "Development of a Joule-class Yb:YAG amplifier and its implementation in a CPA system generating 1 TW pulses," Laser Photonics Rev. **8**(6), 875–881 (2014).

85. S. Banerjee, K. Ertel, P. D. Mason, P. J. Phillips, M. Siebold, M. Loeser, C. Hernandez-Gomez, and J. L. Collier, "High-efficiency 10 J diode pumped cryogenic gas cooled Yb:YAG multislab amplifier," Opt. Lett. **37**(12), 2175 (2012).

86. T. Gonçalvès-Novo, D. Albach, B. Vincent, M. Arzakantsyan, and J.-C. Chanteloup, "14 J / 2 Hz Yb^3+:YAG diode pumped solid state laser chain," Opt. Express **21**(1), 855 (2013).

87. J. Tümmler, R. Jung, H. Stiel, P. V. Nickles, and W. Sandner, "High-repetition-rate chirped-pulse-amplification thin-disk laser system with joule-level pulse energy," Opt. Lett. **34**(9), 1378 (2009).

88. J. Kawanaka, K. Yamakawa, K. Tsubakimoto, T. Kanabe, T. Kawashima, H. Nakano, M. Yoshida, T. Yanagitani, F. Yamamura, M. Fujita, Y. Suzuki, N. Miyanaga, and Y. Izawa, "Generation of Energetic Beam Ultimate (GENBU) Laser - Main Laser," Rev. Laser Eng. **36**(APLS), 1056–1058 (2008).

89. M. Geissler, J. Schreiber, and J. Meyer-ter-Vehn, "Bubble acceleration of electrons with few-cycle laser pulses," New J. Phys. **8**, (2006).

90. A. Buck, M. Nicolai, K. Schmid, C. M. S. Sears, A. Sävert, J. M. Mikhailova, F. Krausz, M. C. Kaluza, and L. Veisz, "Real-time observation of laser-driven electron acceleration," Nat. Phys. **7**(7), 543–548 (2011).

91. O. Svelto, *Principles of Lasers* (Springer US, 2010), **53**(2).

92. N. P. Barnes and B. M. Walsh, "Amplified spontaneous emission - Application to Nd : YAG lasers," IEEE J. Quantum Electron. **35**(1),

101–109 (1999).

93. J. B. Trenholme, "Fluorescence Amplification and Parasitic Oscillation Limitations in Disc Lasers," Nav. Res. Lab. Memo. Rep. 2480 (August), (1972).

94. F. P. Incropera and D. P. DeWitt, "Fundamentals of Heat and Mass Transfer," 890 (1996).

95. L. Yu, M. Huang, M. Chen, W. Chen, W. Huang, and Z. Zhu, "Quasi-discrete Hankel transform.," Opt. Lett. **23**(6), 409–411 (1998).

96. M. Guizar-Sicairos and J. C. Gutiérrez-Vega, "Computation of quasi-discrete Hankel transforms of integer order for propagating optical wave fields," J. Opt. Soc. Am. A **21**(1), 53 (2004).

97. B. E. A. Saleh and M. C. Teich, *Fundamentals of Photonics*, Wiley Series in Pure and Applied Optics (John Wiley & Sons, Inc., 1991).

98. O. L. Antipov, E. A. Anashkina, and K. A. Fedorova, "Electronic and thermal lensing in diode end-pumped Yb:YAG laser rods and discs," Quantum Electron. **39**(12), 1131–1136 (2009).

99. A. Siegman, *Lasers* (University Science Books, 1986).

100. J. Dong, M. Bass, Y. Mao, P. Deng, and F. Gan, "Dependence of the Yb^3+ emission cross section and lifetime on temperature and concentration in yttrium aluminum garnet," J. Opt. Soc. Am. B **20**(9), 1975 (2003).

101. Y. Y. Kalisky, *The Physics and Engineering of Solid State Lasers* (2006).

102. T. Kasamatsu, H. Sekita, and Y. Kuwano, "Temperature dependence and optimization of 970-nm diode-pumped Yb:YAG and Yb:LuAG lasers," Appl. Opt. **38**(24), 5149 (1999).

103. D. C. Brown, R. L. Cone, Y. Sun, and R. W. Equall, "Yb:YAG absorption at ambient and cryogenic temperatures," IEEE J. Sel. Top. Quantum Electron. **11**(3), 604–611 (2005).

104. K. Ertel, S. Banerjee, P. D. Mason, P. J. Phillips, M. Siebold, C. Hernandez-Gomez, and J. C. Collier, "Optimising the efficiency of pulsed diode pumped Yb:YAG laser amplifiers for ns pulse generation," Opt. Express **19**(27), 26610 (2011).

105. D. F. Hotz, "Gain Narrowing in a Laser Amplifier," Appl. Opt. **4**(5), 527 (1965).

106. L. W. Casperson and A. Yarint, "Spectral narrowing in High-Gain Lasers," IEEE J. Quantum Electron. **8**(2), 80–85 (1972).

107. S. Uemura and K. Torizuka, "Center-Wavelength-Shifted Passively Mode-Locked Diode-Pumped Ytterbium(Yb):Yttrium Aluminum Garnet(YAG) Laser," Jpn. J. Appl. Phys. **44**(No. 12), L361–L363 (2005).

108. O. Casagrande, N. Deguil-Robin, B. Le Garree, and G. L. Bourdet, "Time and spectrum resolved model for quasi-three-level gain-switched lasers," IEEE J. Quantum Electron. **43**(2), 206–212 (2007).

109. G. L. Bourdet, "Theoretical investigation of quasi-three-level

longitudinally pumped continuous wave lasers," Appl. Opt. **39**(6), 966 (2000).

110. Y. F. Chen, C. F. Kao, and S. C. Wang, "Analytical model for the design of fiber-coupled laser-diode end-pumped lasers," Opt. Commun. **133**(1–6), 517–524 (1997).

111. K. N. Kim, H. J. Seo, H. N. Kim, J. W. Ryu, Y. G. Kim, and D. H. Kim, "Study on the focusing position effects in a diode end-pumped Nd:YAG laser," J. Korean Phys. Soc. **57**(21), 349–354 (2010).

112. T. Bartulevičius, L. Veselis, K. Madeikis, A. Michailovas, and N. Rusteika, "Compact high energy femtosecond fiber laser with a CFBG Stretcher and CVBG Compressor," Proc. - Int. Conf. Laser Opt. 2018, ICLO 2018 17 (2018).

113. D. Schimpf, E. Seise, J. Limpert, and A. Tünnermann, "Decrease of pulse-contrast in nonlinear chirped-pulse amplification systems due to high-frequency spectral phase ripples," Opt. Express **16**(12), 8876 (2008).

114. D. N. Schimpf, E. Seise, J. Limpert, and A. Tünnermann, "The impact of spectral modulations on the contrast of pulses of nonlinear chirped-pulse amplification systems," Opt. Express **16**(14), 10664 (2008).

115. D. Štěpánková, J. Mužík, O. Novák, L. Roškot, V. Smirnov, L. Glebov, M. Jelínek, M. Smrž, A. Lucianetti, and T. Mocek, "Experimental study on compression of 216-W laser pulses below 2 ps at 1030 nm with chirped volume Bragg grating," Appl. Opt. **59**(26), 7938 (2020).

116. S. Cho, O. Novák, M. Smrž, A. Lucianetti, T. J. Yu, and T. Mocek, "Numerical analysis of beam distortion induced by thermal effects in chirped volume Bragg grating compressors for high-power lasers," J. Opt. Soc. Am. B **37**(12), 3874 (2020).

117. D. Schimpf, E. Seise, J. Limpert, and A. Tünnermann, "Self-phase modulation compensated by positive dispersion in chirped-pulse systems," Opt. Express **17**(7), 4997 (2009).

118. H. W. Lo, J. Kleinert, and M. Kleinert, "Conservation of extremal ellipticity and analytical expressions for astigmatism and asymmetry in Gaussian beam transformations," Appl. Opt. **56**(9), 2523 (2017).

119. F. Burmeister, S. Richter, D. Richter, C. Voigtlander, A. Heisterkamp, and S. Nolte, "Breakthroughs in photonics 2012: Femtosecond-laser nanomachining," IEEE Photonics J. **5**(2), (2013).

120. J. Adamonis, A. Aleknavičius, K. Michailovas, S. Balickas, V. Petrauskienė, T. Gertus, and A. Michailovas, "Implementation of a SVWP-based laser beam shaping technique for generation of 100-mJ-level picosecond pulses," Appl. Opt. **55**(28), 8007 (2016).

121. M. Beresna, M. Gecevičius, P. G. Kazansky, and T. Gertus, "Radially polarized optical vortex converter created by femtosecond laser nanostructuring of glass," Appl. Phys. Lett. **98**(20), 1–4 (2011).

122. R. J. Beach, "Optimization of quasi-three level end-pumped Q-switched lasers," IEEE J. Quantum Electron. **31**(9), 1606–1613 (1995).

123. R. J. Beach, "CW Theory of quasi-three level end-pumped laser oscillators," Opt. Commun. **123**(1–3), 385–393 (1996).

124. D. A. Copeland, "Optical extraction model and optimal outcoupling for a CW quasi-three level thin disk laser," Solid State Lasers XX Technol. Devices **7912**, 79120D (2011).

125. J. J. Morehead, "Compensation of Laser Thermal Depolarization Using Free Space," IEEE J. Sel. Top. Quantum Electron. **13**(3), 498–501 (2007).

126. W. Koechner, *Solid-State Laser Engineering*, Springer Series in Optical Sciences (Springer New York, 2006), **1**.

127. V. Stankevič, A. Čermák, S. Mikalauskas, P. Kožmín, S. Indrišiūnas, and G. Račiukaitis, "Processing of ultra-hard materials with picosecond pulses: From research work to industrial applications," J. Laser Appl. **30**(3), 032202 (2018).

128. T. Tetz, I. Mingareev, S. Berger, C. Fornaroli, M. Richardson, and A. Gillner, "Comparison of different ultra-short pulsed laser sources used for semiconductor substrate processing," **73**, 73–78 (2018).

129. A. Heisterkamp, T. Ripken, U. Oberheide, O. Kermani, T. Mamom, W. Drommer, W. Ertmer, and H. Lubatschowski, "Applications of Ultrafast Lasers in Ophthalmology," **5142**, 5142–146 (2013).

130. I. Snetkov, I. Mukhin, O. Palashov, and E. Khazanov, "Compensation of thermally induced depolarization in Faraday isolators for high average power lasers," Opt. Express **19**(7), 6366 (2011).

131. F. Nürnberg, B. Kühn, A. Langner, M. Altwein, G. Schötz, R. Takke, S. Thomas, and J. Vydra, "Bulk damage and absorption in fused silica due to high-power laser applications," in *Laser-Induced Damage in Optical Materials: 2015*, G. J. Exarhos, V. E. Gruzdev, J. A. Menapace, D. Ristau, and M. Soileau, eds. (2015), **9632**(November), p. 96321R.

132. D. Milam, "Review and assessment of measured values of the nonlinear refractive-index coefficient of fused silica," Appl. Opt. **37**(3), 546 (1998).

133. K. T. Stevens, W. Schlichting, G. Foundos, A. Payne, and E. Rogers, "Promising Materials for High Power Laser Isolators," Laser Tech. J. **13**(3), 18–21 (2016).

COPIES OF PUBLICATIONS

A1

COMPACT 20 W FEMTOSECOND LASER SYSTEM BASED ON FIBER LASER SEEDER, YB:YAG ROD AMPLIFIER AND CHIRPED VOLUME BRAGG GRATING COMPRESSOR

L. Veselis, T. Bartulevičius, K. Madeikis, A. Michailovas, and N. Rusteika

A2

NUMERICAL MODEL OF END-PUMPED YB:YAG DOUBLE-PASS LASER AMPLIFIER EXPERIMENTALLY VALIDATED AT 129 W OUTPUT POWER

L. Veselis, R. Burokas, A. Michailovas

A3

DEPOLARIZATION COMPENSATION WITH SPATIALLY VARIABLE WAVEPLATE IN 116 W, 441 FS, 1 MHZ YB:YAG DOUBLE-PASS LASER AMPLIFIER

L. Veselis, R. Burokas, O. Ulčinas, T. Gertus, K. Michailovas, and A. Michailovas

A4

GENERATION OF 40 W, 400 FS PULSES AT 1 MHZ REPETITION RATE FROM EFFICIENT, ROOM TEMPERATURE YB:YAG DOUBLE-PASS AMPLIFIER SEEDED BY FIBER CPA SYSTEM

L. Veselis, T. Bartulevičius, K. Madeikis, and A. Michailovas